

Award Number: W81XWH-09-1-0698

TITLE: Hybrid Nanotechnologies for Detection and Synergistic Therapies for Breast Cancer

PRINCIPAL INVESTIGATOR: Erkki Ruoslahti, M.D., Ph.D.

CONTRACTING ORGANIZATION: Sanford-Burnham Medical Research Institute, La Jolla, CA 92037

REPORT DATE: October 2012

TYPE OF REPORT: Annual

PREPARED FOR: U.S. Army Medical Research and Materiel Command
Fort Detrick, Maryland 21702-5012

DISTRIBUTION STATEMENT:

Approved for public release; distribution unlimited

The views, opinions and/or findings contained in this report are those of the author(s) and should not be construed as an official Department of the Army position, policy or decision unless so designated by other documentation.

REPORT DOCUMENTATION PAGE				Form Approved OMB No. 0704-0188	
Public reporting burden for this collection of information is estimated to average 1 hour per response, including the time for reviewing instructions, searching existing data sources, gathering and maintaining the data needed, and completing and reviewing this collection of information. Send comments regarding this burden estimate or any other aspect of this collection of information, including suggestions for reducing this burden to Department of Defense, Washington Headquarters Services, Directorate for Information Operations and Reports (0704-0188), 1215 Jefferson Davis Highway, Suite 1204, Arlington, VA 22202-4302. Respondents should be aware that notwithstanding any other provision of law, no person shall be subject to any penalty for failing to comply with a collection of information if it does not display a currently valid OMB control number. PLEASE DO NOT RETURN YOUR FORM TO THE ABOVE ADDRESS.					
1. REPORT DATE (DD-MM-YYYY) 1 October 2012		2. REPORT TYPE Annual		3. DATES COVERED (From - To) Sept. 21, 2011 - Sept. 20, 2012	
4. TITLE AND SUBTITLE Hybrid Nanotechnologies for Detection and Synergistic Therapies for Breast Cancer				5a. CONTRACT NUMBER	
				5b. GRANT NUMBER W81XWH-09-1-0698	
				5c. PROGRAM ELEMENT NUMBER	
6. AUTHOR(S) Erkki Ruoslahti, M.D., Ph.D. twqurcj vB ucphqtf dwtpj co Qti				5d. PROJECT NUMBER	
				5e. TASK NUMBER	
				5f. WORK UNIT NUMBER	
7. PERFORMING ORGANIZATION NAME(S) AND ADDRESS(ES) Sanford-Burnham Medical Research Institute, 10901 North Torrey Pines Rd., La Jolla, CA 92037 [AND] UCSB Bio II, Rm. 3119 Santa Barbara, CA 93106-9610				8. PERFORMING ORGANIZATION REPORT NUMBER	
9. SPONSORING / MONITORING AGENCY NAME(S) AND ADDRESS(ES) WUOCto { "O gf lecnT gugctej "cpf "O cvgtlgnEgo o cpf HqtvF gtleM"OF "4924" " "				10. SPONSOR/MONITOR'S ACRONYM(S)	
				11. SPONSOR/MONITOR'S REPORT NUMBER(S)	
12. DISTRIBUTION / AVAILABILITY STATEMENT Approved for public release; distribution unlimited					
13. SUPPLEMENTARY NOTES					
14. ABSTRACT This is a joint project by two Innovator Awardees and a Scholar to develop a novel nanotechnology platform for the diagnosis and treatment of breast cancer. The prevalence of breast cancer and the large number of deaths from this disease underscore the need for a paradigm shift in the strategies towards developing a cure for breast cancer. Nanotechnology has the potential of causing such a paradigm shift. Current work focuses on the development of novel peptide probes and probe strategies for the targeting of breast cancers, including very early pre-malignant lesions. Another focus is development of drug conjugates, nanomedicines and diagnostic nanosystems for therapeutic and theranostic targeting of breast cancers.					
15. SUBJECT TERMS anti-angiogenesis, phage display, tumor homing peptides					
16. SECURITY CLASSIFICATION OF:			17. LIMITATION OF ABSTRACT UU	18. NUMBER OF PAGES 152	19a. NAME OF RESPONSIBLE PERSON USAMRCC
a. REPORT U	b. ABSTRACT U	c. THIS PAGE U			19b. TELEPHONE NUMBER (include area code)

Table of Contents

	<u>Page</u>
Introduction.....	1
Body.....	2
Key Research Accomplishments.....	3
Reportable Outcomes.....	27
Conclusion.....	28
References.....	28
Appendices.....	30

Attachments:

Sanchez-Martin, D., Cuesta, A.M., Fogal, V., Ruoslahti, E., and Alvarez-Vallina, L. The multi-compartmental p32/gCiqR as a new target for antibody based tumor targeting strategies. *J Biol Chem* 286:5197-5203 (2011) PMC:3037632

Roth, L., Agemy, L., Kotamraju, V.R., Braun, G., T. Teesalu, T, Sugahara, K.N., Hamzah, J., and Ruoslahti E. Transtumoral targeting enabled by a novel neuropilin-binding peptide. *Oncogene*, 31: 3754-3763(2012). PMID: 22179825

Ruoslahti, E. Peptides as targeting elements and tissue penetration devices for nanoparticles. *Adv. Mat.* (review article) 24:3747-3756. (2012). [Epub ahead of print] PMID: 22550056.

Braun G B., Friman, T., Pang H-B., Kotamraju, VR, Pallaoro, A., Reich, NO., Teesalu, T. and Ruoslahti, E. Etchable and bright silver nanoparticle probes for cell internalization assays. Submitted

Chen, R., Braun, G.B., Luo, X. Sugahara, K.N., Teesalu, T., Ruoslahti, E. Application of a proapoptotic peptide for an intratumoral-spreading cancer therapy. (2012). Cancer Research, Provisionally accepted.

Alberici L., Roth, L., Sugahara, K.N., Agemy, L., Kotamraju, V.R., Teesalu, T., Bordignon, C., Traversari, C., Rizzardi, G.-P., Ruoslahti, E. De Novo Design of a Tumor Penetrating Peptide (2012) Cancer Research, Provisionally accepted.

Collaborative Innovator Grant – W81XWH-09-1-0698

Hybrid Nanotechnologies for Detection and Synergistic Therapies for Breast Cancer

Principal Investigator: Dr. Erkki Ruoslahti; Project PIs: Dr. Roger Tsien and Dr. Shiladitya Sengupta

Progress Report Year 03

INTRODUCTION

This is a joint project by two Innovator Awardees and a Scholar to develop a novel nanotechnology platform for the diagnosis and treatment of breast cancer. The prevalence of breast cancer and the large number of deaths from this disease underscore the need for a paradigm shift in the strategies towards developing a cure for breast cancer. Nanotechnology has the potential of causing such a paradigm shift.

Some clinically used anti-cancer drugs (e.g. Abraxane, Doxil) and imaging agents are already nanoparticle-based. While highly effective, these first generation products do not utilize the full power of nanotechnology; nanoparticles can be “smart,” not just passive carriers of a drug. One such function, which is central to this project, is endowing nanoparticles with an ability to seek out tumors and selectively accumulate in them. This can be accomplished by incorporating a tumor-homing molecule, such as a peptide, aptamer, or antibody to the nanoparticle. A significant recent development has been the realization that nanoparticles can be best targeted into tumors by making use of molecular targets in the vasculature of tumors because these targets, unlike the extravascular tumor tissue, are readily available for circulating nanoparticles. There are numerous targets in tumor vasculature, and they are highly versatile in that they can be pan-tumor markers, or specific to a tumor type (such as breast cancer, specific for a certain stage in tumor development); metastases may have their own markers that depend on the tissue the metastasis resides in. We are making use of the versatility of nanoparticles and vascular homing peptides in developing a seamless, synergistic nanotechnology platform for early detection, monitoring, and therapy of breast cancer.

Synergistic therapies that combine inhibitors of oncogenic signal transduction pathways with cytotoxic chemotherapies have proven effective as nanoparticle-based formulations in animal models. Targeting can then concentrate the therapeutic agent in the tumor, improving the efficacy of the treatment and reducing damage to healthy tissues. The diagnostic and therapy functions will be synergistic in that the diagnostic methods will provide information on the efficacy of individual homing peptides in targeting the tumor. This information makes it possible to select the most effective targeting mechanism for each patient. Incorporating diagnostic and treatment functions into the same particle will enhance the ability to monitor the treatment and reduce the number of procedures the patient is subjected to.

Specifically, we are assembling a panel of breast cancer-homing peptides, which will be then used as recognition elements for nanoparticles. The diagnostic platform technology under development is based on nanoparticles that, when injected into the blood stream, bind to tumor vessels and undergo a change as a result of the binding. This change is then detected in blood samples. We are developing and testing nanoparticles based on polymer and other chemistries to serve as tumor-targeted drug carriers. Cell-penetrating and tumor-penetrating properties of certain homing peptides will be made use of in delivering the drugs-carrying nanoparticles deep into tumor tissue and inside tumor cells. If possible we will distill a single, optimized theranostic nanosystem from these studies. We expect these advances to have a major beneficial effect on the cure rates and quality of life of breast cancer patients.

We are working on a number of biotechnology and pharmaceutical companies that have licensed various aspects of our technologies from our institutions. Thus, there is a high probability that this project will bring advanced nanotechnology closer to clinical reality in breast cancer management (while also creating well-paying jobs).

BODY

The approved Tasks for this grant are:

Task 1.

Establish a panel of homing ligands for the project. (Months 1-36) Investigators:

Ruoslahti, Tsien, Soh, Sengupta

1a. Screen an existing panel of tumor-homing peptides for peptides that selectively recognize the vasculature of pre-malignant breast lesions, fully malignant carcinomas, or metastatic lesions.

Months 1-18. Investigators: Ruoslahti, Tsien

1b. Screen phage libraries for new peptides that selectively recognize the vasculature of early breast cancer lesions and breast cancer metastases in a given organ. Months 1-36; Investigators: Ruoslahti

1c. Screen aptamer libraries for aptamers that bind to a receptor in tumor vessels where the binding leads to a stable change in conformation that eliminates receptor binding and can be monitored in the blood. Months 1-36; Investigators: Ruoslahti, Soh

Task 2.

Engineer chimeric nanoparticles that deploy signal transduction inhibitors and cytotoxic chemotherapies for synergistic antitumor outcome. (Months 1-30) Investigators:

Sengupta, Ruoslahti

2a. Engineer a chimeric nanoparticle from the drug-polymer conjugates. Investigator: Sengupta
Chemically conjugate PD98059 to PLGA. (Months 1-6)

Engineer a polymaleic acid-cisplatin complex (Months 1-24)

Chemically conjugate Doxorubicin-(7KDa) PLGA carbamate conjugate. (Months 1-6)

Engineer a chimeric NP entrapping LY294002 in matrix. (Months 1-24)

2b. Physicochemically characterize the chimeric nanoparticles for size, morphology, and release kinetics of the therapeutic agents. (Months 1-30) Investigator: Sengupta

2c. *In vitro* and *in vivo* characterization of the chimeric nanoparticle in 4T1 and MDA-MB-231 tumor models (Months 6-30) Investigators: Sengupta, Ruoslahti

Task 3.

Validate a minimally invasive bar-coded nanoparticle-based in vivo diagnostic platform for breast cancer detection and staging, and monitoring of therapy. (Months 12-42)
Investigators: Ruoslahti, Reich, Tsien, Sengupta

3a. Test a prototype assay in which a mixture of nanoparticles coated with either a tumor-homing peptide or a control peptide is injected into a tumor-bearing mouse and a change in the ratio of the particles in the circulation is monitored. (Months 12-36). Investigators: Ruoslahti, Sengupta

1. Functionalization of magnetic nanoparticles with cleavable Homing-CENDR peptide chimera and physicochemical characterization. (Months 12-30) Investigators: Ruoslahti

2. In vivo evaluation of the prototype nanoparticle (Months 24-42). Investigators: Ruoslahti,

Sengupta

3b. Examine the suitability of surface enhanced Raman spectroscopy (SERS) for *in vivo* detection of barcoded nanoparticles. (Months 18-42) Investigators: Ruoslahti, Reich, Sengupta

3c. Test an alternative prototype in which the nanoparticles are coated with a bipartite tumor homing peptide that is susceptible to proteolytic cleavage by a tumor protease that generates a tumor-binding fragment and a free fragment. The ratio of labels attached to the ends of the peptide is monitored. (Months 12-42). Investigators: Tsien, Ruoslahti, Sengupta

Task 4.

Specific Aim 4. Develop a multifunctional nanoparticle that delivers a drug to tumor vessels and tumor cells, while releasing a diagnostic component into the circulation

(Months: 24-60)

Investigators: Sengupta, Ruoslahti, Tsien

4a. Adapt the barcoded diagnostic technology onto polymer-based drug-loaded multifunctional nanoparticles, and characterize for physicochemical properties. Months 24-48 Investigators: Sengupta, Ruoslahti, Tsien

4b. Characterization of multifunctional nanoparticle in *in vivo* tumor models, including testing for tumor homing, penetration and uptake into tumor cells. Months 36-60 Investigators: Sengupta, Ruoslahti, Tsien

4c. Characterize the antitumor efficacy and mechanism of action of the multifunctional bar-coded nanoparticles *in vivo*. Months 42-60 Investigators: Sengupta

KEY RESEARCH ACCOMPLISHMENTS

We have:

- Used phage library screening to identify a new peptide that detects early changes in the extracellular matrix of premalignant transgenic mouse breast lesions.
- Identified a peptide from our panel of tumor-homing peptides that specifically recognizes the fibroblasts that reside in early premalignant breast lesions.
- Developed (in the Soh laboratory) a new method that may revolutionize aptamer screening and may also allow *in vivo* screening for breast cancer-recognizing aptamers, which has turned out not to be possible with the current technology.
- Shown in a collaborative project between the Sengupta and Ruoslahti laboratories that coating of nanoparticles carrying a platinum compound with the tumor-penetrating peptide iRGD peptide increases the anti-tumor activity of the nanoparticles in a breast cancer model.
- Constructed a functioning hit-and-run assay for tumor detection using iron oxide nanoparticles doped with radiostable gadolinium isotopes.
- Developed a new silver nanoparticle-based assay for accurate measurement of nanoparticle uptake by cells.
- Engineered Cisplatin, Doxorubicin and taxane-based self assembled nanoparticles.
- Engineered PI-828 and PI-103 nanoparticles.
- Extended activatable cell penetrating peptides (ACPPs) to proteases other than matrix metalloproteinases-2 and -9 (elastase and thrombin).

- Shown that RACPPs enable detection of metastases into liver and lymph nodes in a mouse breast cancer model.
- Developed a RACPP-targeted drug conjugates and shown efficacy in a breast cancer model.
- Published and submitted for publication several papers acknowledging this grant and filed patent applications on new inventions.

Task 1. Establish a panel of homing ligands for the project

1a. Screen an existing panel of tumor-homing peptides for peptides that selectively recognize the vasculature of pre-malignant breast lesions, fully malignant carcinomas, or metastatic lesions

Extracellular matrix alteration in pre-malignant lesions

We used phage library screening to identify a new peptide that detects early changes in the extracellular matrix of premalignant transgenic mouse breast lesions in genetically engineered PyMT-MMTV breast cancer mice. The screen that yielded this peptide was based on phage binding to matrigel, which is a basement membrane extract from a mouse tumor. The next and final step was an *in vivo* screen for tumor homing, where we used the MDA-MB-435 xenograft model. We are well aware of the controversy regarding the origin of this tumor, and although the balance seems to have shifted back to this tumor being of breast cancer origin, as shown below, we carefully validate all results using other breast cancer models.

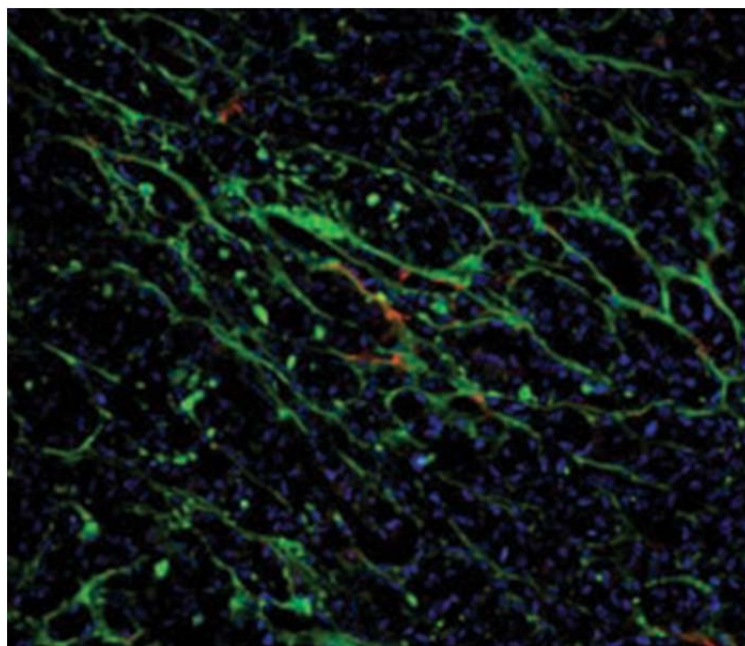


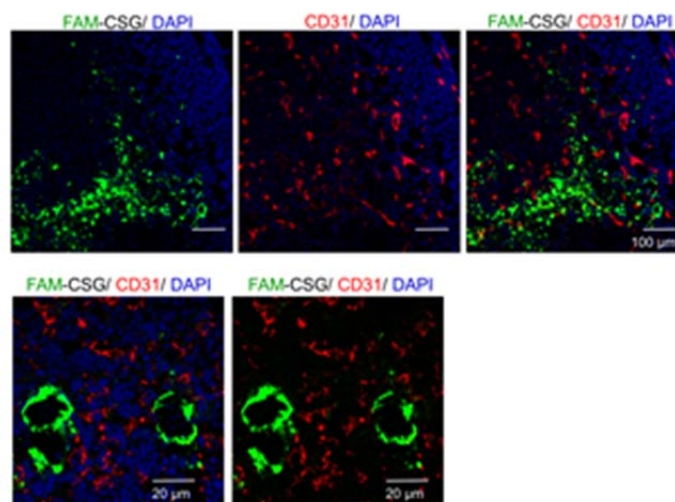
Fig. 1. Specific tumor accumulation of CSG peptide in the MDA-MB-435 breast cancer model.

A. Mice bearing MDA-MB-435 xenograft tumors were intravenously injected with fluorescein-conjugated CSG peptide (150 ug/mouse). The mice were anesthetized 2 hours later, perfused through the heart with 4% paraformaldehyde, and the tumors were examined microscopically. B. CSG phage was intravenously injected into MDA-MB-435 tumor-bearing mice, and the phage titers recovered from the tissues after 10 min in circulation were determined. The titers are expressed as fold over control insertless phage.

The peptide, dubbed CSG, is a 9-amino acid peptide with a cyclizing disulfide bond between cysteines at the first and last positions. It avidly and specifically homes to the MDA-MB-435 tumors used to

identify it (Fig. 1), and it also homes to mouse 4T1 transplantable, orthotopic breast cancers (Fig. 2). The pattern of homing coincides with extracellular matrix, rather than cells in the tumors.

Fig. 2. CSG specifically homes to orthotopic 4T1 mouse breast cancer tumors. FAM-CSG peptide (0.1 μmol) was intravenously injected into tumor-bearing mice and tissues were collected 2 hours later and the peptide was detected in tumor sections by fluorescence microscopy (Green). CSG shows no co-localization with tumor blood vessels (CD31; red). Nuclei were stained with DAPI (blue). Original magnification $\times 20$; scale bars 100 μm (upper panels), and $\times 40$; scale bars, 20 μm (lower panels).



The target molecule for CSG appears to be the basement membrane component nidogen, because affinity chromatography on immobilized CSG peptide identifies nidogen-1 as a specific binder of CSG (Fig. 3). This agrees with the matrix localization in tumor-homing studies and its matrigel binding. The identification of nidogen as the relevant receptor will still need to be confirmed with knockdown and antibody inhibition experiments. And it will also be important to determine whether the cancer specificity of CSG comes from over-expression of nidogen-1 in cancer, its abnormal exposure, or some modification of the molecule.

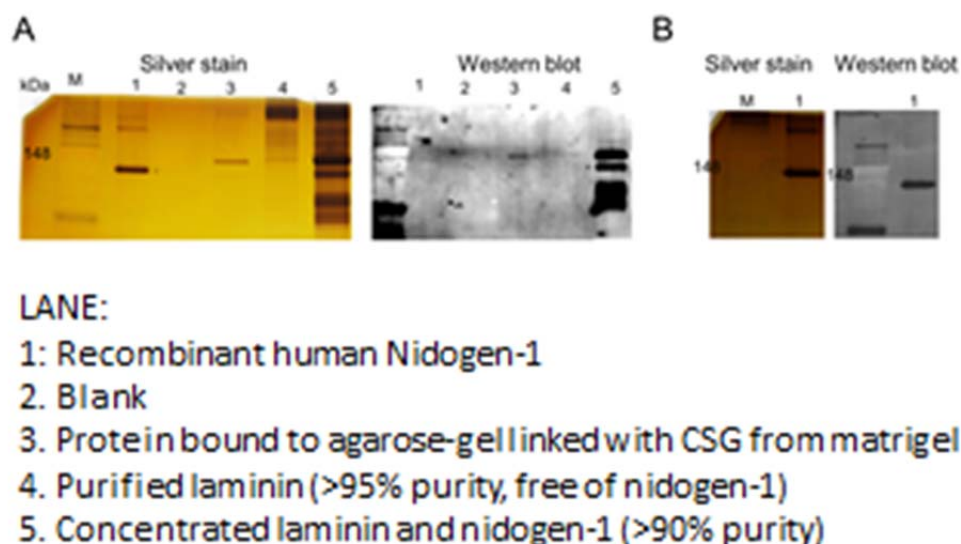


Fig. 3. CSG binds to basement membrane protein, nidogen-1/entactin. A. CSG peptide coupled to agarose gel linked with CSG peptide from A. Silver-stained PAGE gel showing the 140-kDa band and immunoblot identification identifying the isolated protein (lane 3) is nidogen-1 using an antibody against mouse nidogen-1. This antibody did not work on recombinant human nidogen-1. B. Silver staining and western blot analysis of recombinant human nidogen-1 using polyclonal antibody raised against human nidogen-1.

A feature of CSG that is particularly relevant to this grant project is that it recognizes early, premalignant breast cancer lesions. We used the well-known PyMT-MMTV models (Fig. 4) for the study of premalignant lesions. Systemically injected CSG recognized the extracellular matrix of the developing mammary glandular tree in the PYMT mice already at a stage where only hypertrophy of the epithelium was evident (Fig. 5), whereas there was no homing to the mammary gland of normal mice of the same strain. We will conduct additional studies on lactating glands, inflamed tissue and, when possible, non-malignant tumors to determine the specificity of this promising peptide for premalignant lesions and fully developed cancer.

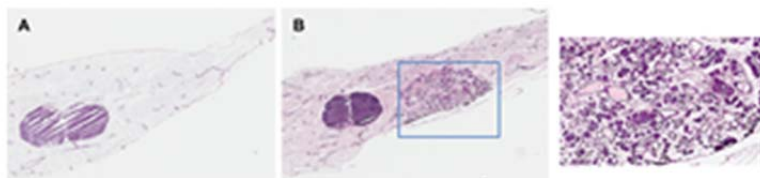


Fig. 4. PyMT-MMTV is a useful model for studying early premalignant breast tumors. H&E images of whole mount sections of mammary fat pad isolated from normal mouse (A) or 60-day-old PyMT-MMTV (B). Inset shows the hyperplastic lesion in the mouse mammary fat pad.

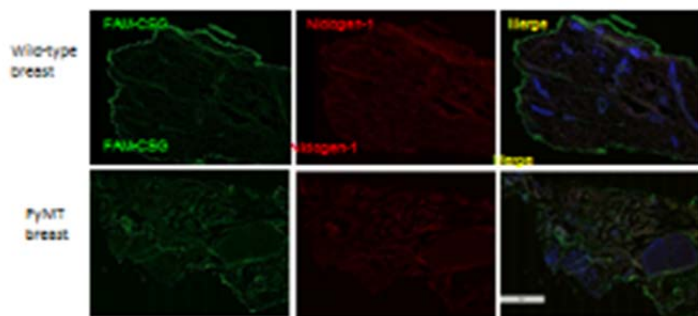


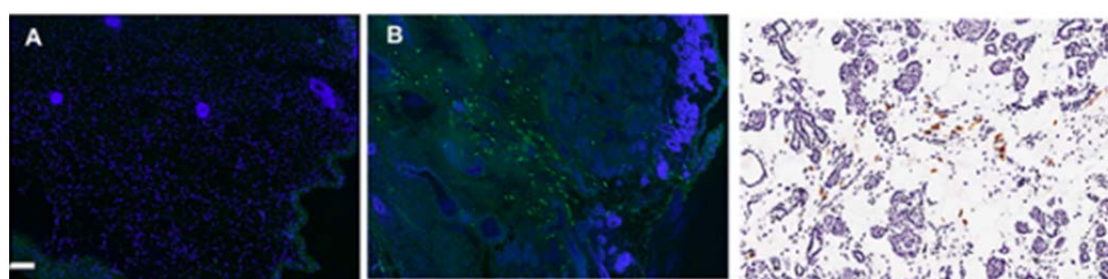
Fig. 5. CSG peptide homes to premalignant hyperplastic lesions in mammary fat pad isolated from PyMT-MMTV animals. Immunofluorescence staining on whole mount sections of mammary fat pad isolated following 1 hour in-vivo circulation of FAM-CSG in normal Blk6 mouse (A) or PyMT-MMTV mouse (B). Green - anti-FAM; Red - anti-nidogen-1, Blue - nuclear stain. Scale bar is 2 microns. The fluorescence around the margins of the sections is non-specific.

Peptide recognizing fibroblasts in premalignant lesions. We have identified a peptide in our panel of tumor-homing peptides that specifically recognizes the fibroblasts that reside in early premalignant breast lesions. This peptide, iRGD, is prototype compound among the tumor-penetrating peptides we have described recently (Sugahara et al., 2009; 2010; Roth et al., 2012; Alberici et al., 2012). Systemically injected iRGD homes to individual cells around the premalignant PyMT glands (Fig. 6). These cells appear to be tumor fibroblasts based on three lines of evidence: They are clearly not tumors cells, their morphology is not that of immune cells, and the iRGD staining co-localizes with the fibroblast marker vimentin (Fig. 6). Moreover, we have found that tumor fibroblasts are strongly positive for iRGD uptake in fully malignant breast cancers (Sugahara et al., unpublished results). Interestingly, iRGD did not home to the blood vessels in the hyperplastic lesions, although it strongly recognizes the blood vessels in breast cancers. This may be an indication that the angiogenic switch (Hanahan and Folkman) has not been turned on at this stage. Even more strikingly, the hyperplastic glandular cells were also not positive for iRGD uptake at this stage. This result indicates that α_v integrin and/or neuropilin expression (to be further studied with antibody probes) has not been turned on in the tumor cells or endothelial cells at a stage, when the fibroblasts are already activated.

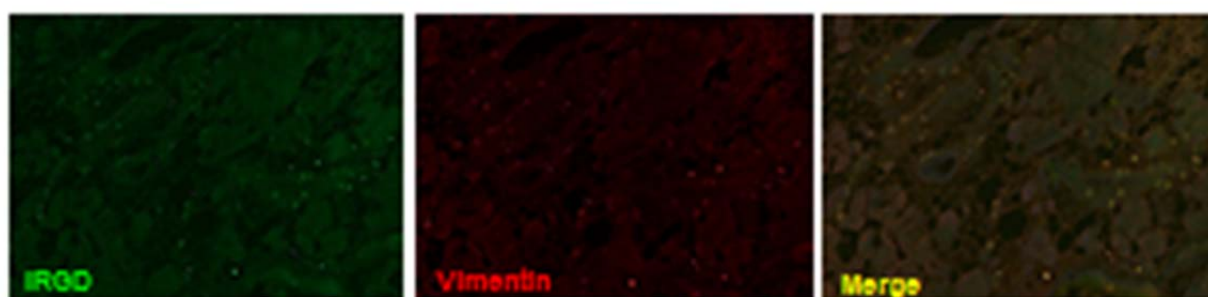
Fig. 6. iRGD homes to early (pre-malignant) hyperplastic lesions in mammary fat pad isolated from PyMT-MMTV animals. Immunofluorescence staining on whole mount sections of mammary fat pad isolated following 1 hour in-vivo circulation of 0.15 μ mol FAM-iRGD in normal Blk6 mouse (A) or day 48 PyMT-MMTV mouse (B). Green – anti-FAM; Blue – DAPI nuclear stain. Scale Bar is 100 micron. (C) Immunohistochemistry staining for FAM on sections of mammary fat pad isolated following FAM-CSG injection in PyMT-MMTV mouse. Note the rare positive cells in the tissue interspersed among the tumor cells.

Fig. 7. iRGD colocalizes with fibroblasts in early (pre-malignant) hyperplastic lesions in mammary fat pad isolated from PyMT-MMTV mice. Immunofluorescence staining on whole mount sections of mammary fat pad isolated following FAM-iRGD injection in PyMT-MMTV mouse. Green - anti-FAM-CSG; Red - anti-vimentin-1, Blue - nuclear stain.

Our results show, to our knowledge for the first time, that changes in the extracellular matrix and resident fibroblasts



already occur at the stage of early hyperplasia in breast cancer development, preceding detectable changes in the vasculature. We have initiated phage library screen for peptides that recognize the earliest changes in to-be-breast-cancer tumor cells. The CSG and iRGD peptides may be useful in the diagnosis of early breast cancer. Thus, targeting of nanoparticles with iRGD, such as the nanoparticles carrying a platinum compound developed in a collaborative study between the Sengupta and Ruoslahti laboratories



(Task 2) will attack the earliest changes in breast cancer development, in addition to the fully developed cancers. At the other end of the tumor development spectrum, we are working on metastasis targeting and expect to describe the results in the next report.

1b. Screen phage libraries for new peptides that selectively recognize the vasculature of early breast cancer lesions and breast cancer metastases in a given organ.

As described above, we have discovered probes that detect early changes in the extracellular matrix and fibroblasts of premalignant lesions. We are in the process of determining when the blood vessels become detectable with our probes in breast cancer development. Screens for the vasculature of metastases have been initiated.

1c. Screen aptamer libraries for aptamers that bind to a receptor in tumor vessels where the binding leads to a stable change in conformation that eliminates receptor binding and can be monitored in the blood.

Since their initial description (Gold et al., 2012; Keefe et al, 2010), aptamers have shown considerable promise as a synthetic alternative to monoclonal antibodies. Importantly, aptamers, more than any other type of probes, have the capability of altering conformation upon binding of a ligand. In this project, we initially sought to use aptamer screening *in vivo* to identify tumor-homing aptamers that could then be used to develop a cancer test based on conformation-changing aptamers.

As reported previously, we have worked on strategies that would allow us to target angiogenic vasculature. The Soh laboratory used $\alpha v \beta 3$ integrin as a target to develop a selection strategy for isolating aptamer pairs that bind to distinct epitopes of a target protein (Gong et al., 2012). They have identified two families of aptamers that specifically recognize the αv and $\beta 3$ subunits. The isolated aptamers from these families (αv -1 and $\beta 3$ - 1) exhibit low nanomolar affinities for their respective targets, with minimal cross-reactivity to other, closely related integrin homologues. These nuclease-resistant, 2'-F-modified aptamer pairs did not interfere with each other's binding and could be effectively used as reagents for assays in buffer as well as complex mixtures such as undiluted serum. These aptamers will now be used to determine whether *in vivo* targeting with aptamers is possible.

With an eye toward being able to use aptamer screening *in vivo* akin to what the Ruoslahti laboratory is doing with phage. Our first attempts with conventional aptamer libraries were a failure; no specific binding was detected. We have now devised a new method of generating aptamers that is fundamentally different from the conventional SELEX-based strategies. In our screening method, the affinity of every candidate molecule is individually measured and sorted in a high-throughput fashion. To achieve this, we employ a particle display system that utilizes emulsion PCR (Diehl et al. 2006; Dressman et al., 2003) to transform an aptamer library into a pool of aptamer particles (APs), each displaying multiple copies of a unique aptamer sequence on its surface. We then incubate these APs with fluorescently labeled target protein and use fluorescence-activated cell sorting (FACS) to quantitatively screen each AP based on its mean fluorescence intensity, which is directly proportional to the binding affinity of the aptamer. As previously demonstrated in protein engineering methods based on yeast or bacterial display, the use of FACS to screen the binding properties of individual ligands in a high-throughput manner offers tremendous advantages over conventional selection methods. Through theoretical analysis, we have identified key experimental parameters that enable optimal enrichment of the highest-affinity aptamers, and show that the performance of our particle display system exceeds the theoretical maximum of existing selection methods by many orders of magnitude.

In order to experimentally validate the clear theoretical advantage of our system in isolating high-affinity aptamers, we performed particle display screens against four target proteins—thrombin, ApoE, PAI-1 and 4-1BB—using the optimal conditions identified in our theoretical analysis. It is possible to begin the particle display screen with a large random library, but due to the practical limits of FACS throughput ($\sim 10^7$ particles per hour), we first performed one round of magnetic bead-based enrichment

with a random library of $\sim 10^{14}$ single-stranded DNA molecules and used this enriched pool to synthesize our initial AP library. Prior to the screen, we performed FACS with APs displaying only the forward primer (FP) to define the reference gate. APs residing in this reference gate exhibited negligible binding to target proteins, and were not collected during the screen.

We performed three rounds (R1–3) of particle display screen for all four targets. Due to the limited initial copy number of each AP, it is important to avoid loss of potentially high-affinity APs in R1; thus, we applied lower screening stringency by setting the sort gate close to the reference gate, such that at least 0.1% of the APs were collected. Aptamers isolated in R1 were PCR amplified and used to synthesize a new set of APs; in this way, ~ 1000 copies of each AP isolated from R1 were available for R2. In R2 and R3, we used the theoretical optimal screening stringency, setting the sort gate at $F_{max}/3$ and decreasing $[T]$ such that we collected ~ 0.1 – 0.2% of the APs. Aptamers isolated in R3 exhibited high affinities for their targets (Fig 8). To estimate average k_d , we considered all APs outside of the reference gate (Fig. 1, blue), and experimentally measured the $[T]$ at which the mean fluorescence of this population is $(F_{max} + F_{bg})/2$. We found the average k_d to be 20 pM, 3 nM, 1 nM and 4 nM for thrombin, ApoE, PAI-1 and 4-1BB, respectively.

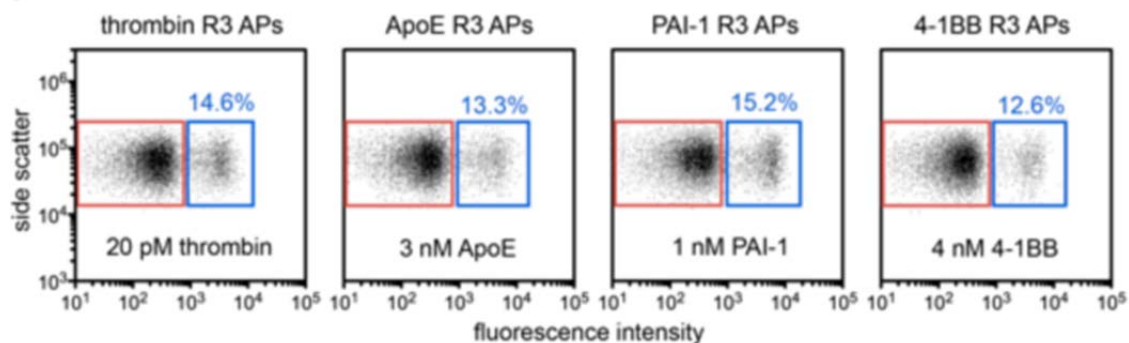


Fig. 8. Particle display screening progress and outcome. Aptamers isolated in R3 exhibited high target affinities. The average k_d of the R3 pools were 20 pM (thrombin), 3 nM (ApoE), 1 nM (PAI-1) and 4 nM (4-1BB), as measured by the mean fluorescence of the APs outside of the reference gate (blue).

Characterization of high-affinity aptamers. To obtain individual aptamer sequences, we cloned the R3 pools into competent bacterial cells and randomly picked and sequenced 20 clones from each. For the best sequences, we present the binding curve and secondary structures as predicted by mfold in Figure 9. The affinities of our aptamers against thrombin and ApoE are significantly higher than any previously reported aptamers. For example, thrombin aptamer Thrombin 03 exhibits a k_d of 7.04 pM (Fig. 9a), which surpasses the values obtained with the same binding assay using aptamers previously reported by approximately two to three orders of magnitude. Similarly, our ApoE aptamer ApoE-06 exhibits a k_d of 938 pM (Fig. 9b), a 4-fold improvement over the aptamer recently isolated by our group using high-stringency microfluidic SELEX20. Importantly, previously reported selections against PAI-1 and 4-1BB have repeatedly failed without the use of modified bases. However, we successfully generated high affinity aptamers for these proteins based entirely on natural DNA; our PAI-1-01 sequence exhibits a k_d of 339 pM (Fig. 9c) and 4-1BB-07 shows a k_d of 2.32 nM (Fig. 9d), both comparable to the performance of aptamers generated using modified bases¹².

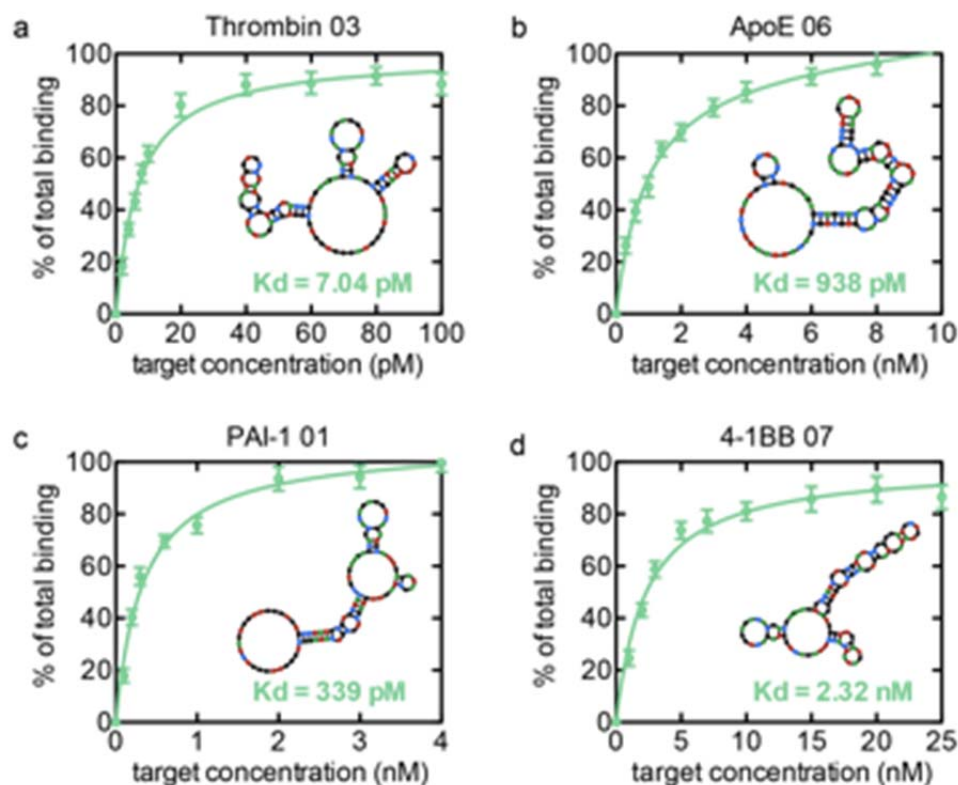


Fig. 9. Affinity measurements of individual aptamers. We used a beadbased fluorescence assay to measure the binding affinity of the top aptamers against (a) thrombin, (b) ApoE, (c) PAI-1 and (d) 4-1BB. We calculated k_d using a Langmuir 1:1 binding model and predicted aptamer secondary structure using mfold.

In conclusion, we report a quantitative screening method for generating high affinity aptamers that offers significant advantages over all previous selection methods. After synthesizing pools of aptamer particles that display $\sim 10^5$ copies of a single aptamer sequence, we used FACS to individually measure the affinity of $\sim 10^8$ aptamer sequences, enabling isolation of those with highest affinity with unprecedented resolution. Our method offers a critical advantage over conventional SELEX-based methods. Using selection, it is challenging to discard aptamer sequences that proliferate due to factors such as library synthesis bias, non-specific background binding and PCR bias. These effects often lead to the isolation of inferior aptamers or failed selection (Gold et al., 2012). In contrast, our method eliminates the confounding effects of such biases by quantitatively measuring the actual affinity of each individual aptamer for its target at every round, such that aptamers with low affinities are effectively discarded regardless of their copy number.

Through theoretical analysis, we show that these improvements translate to an extraordinary difference in performance, and our particle display method exceeds the theoretical enrichment limit of any selection-based method by orders of magnitude. By performing screens against four different protein targets, we have demonstrated that these significant theoretical advantages can be realized experimentally, and the affinities of our aptamers against ApoE and thrombin are 4- to 160-fold higher than previously reported sequences. More importantly, we successfully performed particle display screens against two recalcitrant proteins for which selections were reported to repeatedly fail without the

use of modified bases¹², and generated DNA aptamers with high affinities (PAI-1, $k_d = 339$ pM and 4-1BB, $k_d = 2.32$ nM). We believe our particle display method should also be compatible with other natural and modified nucleic acid systems, such as natural RNA, 2'-fluoro-modified RNA, 2'-O-methyl-modified RNA and chemically modified DNA. Given that particle display does not require the immobilization of target molecules to a solid support, it is interesting to consider the extension of our method to other molecules in addition to conventional protein targets, including post-translational modifications, lipids, glycans and other classes of biomolecules. Success in doing so may unlock the true potential of nucleic acids as affinity reagents. These capabilities could be particularly relevant in screening for aptamer binders of tumor markers. Even *in vivo* screening for such markers may become possible.

Task 2. Engineer chimeric nanoparticles that deploy signal transduction inhibitors and cytotoxic chemotherapies for synergistic antitumor outcome.

The Sengupta laboratory has demonstrated that rational design of active molecules can facilitate supramolecular assembly in the nanoscale dimension. Using cisplatin as a template, we synthesized a unique platinum (II) tethered to a cholesterol backbone via a unique monocarboxylato and O→Pt coordination environment that facilitates nanoparticle assembly with a fixed ratio of phosphatidylcholine and 1,2-distearoyl-sn-glycero-3-phosphoethanolamine- N-[amino (polyethylene glycol)-2000]. Briefly, cholesterol-tethered cisplatinum (II) amphiphile was engineered, the design of which was inspired by the process of “aquation,” wherein

the chloride leaving groups of cisplatin are rapidly displaced to form $\text{cis-Pt}[(\text{NH}_3)_2(\text{OH}_2)\text{Cl}]^+$ and $\text{cis-Pt}[(\text{NH}_3)_2(\text{OH}_2)_2]^{2+}$. Indeed, we had demonstrated that Pt chelated to a polyisobutylene maleic acid glucosamine copolymer via a monocarboxylato and an O→Pt coordinate bond release of Pt in a pH-dependent manner, and more efficiently than when the Pt was chelated using dicarboxylato bonds or via a monocarboxylato and an N→Pt coordinate bond. As a result, we rationalized that the introduction of a coordination environment where the Pt was chelated via a monocarboxylato and an O→Pt coordinate bond is critical to the design of an efficacious platinate. As outlined in the given scheme (Fig. 10), we first synthesized cholesterol-ethylenediamine conjugate in near quantitative yield (99.1%) by reacting cholesteryl chloroformate with excess ethylene diamine. Next, we introduced monocarboxylato and amide chelating moiety by reacting cholesterol-ethylenediamine conjugate with succinic anhydride (at 95% yield). Finally, the conjugate was reacted with aquated $\text{cis-Pt}[(\text{NH}_3)_2(\text{OH}_2)_2]^{2+}$ in 1:1 molar ratio in acidic pH (pH = 6.4) to obtain cholesterol-cisplatin conjugate, characterized by monocarboxylato and an O→Pt coordinate bond of an amide, as indicated by a unique single ^{195}Pt NMR peak at $-1,621.497$ ppm. We engineered the SACNs from the cholesterol-succinic acid-platinum (II) molecule, phosphatidylcholine (PC) and 1,2-distearoyl-sn-glycero-3-phosphoethanolamine-N [amino(polyethylene glycol)-2000] (DSPEPEG) in 1:2:0.2 weight ratio using a lipid-film hydration self assembly method (20)

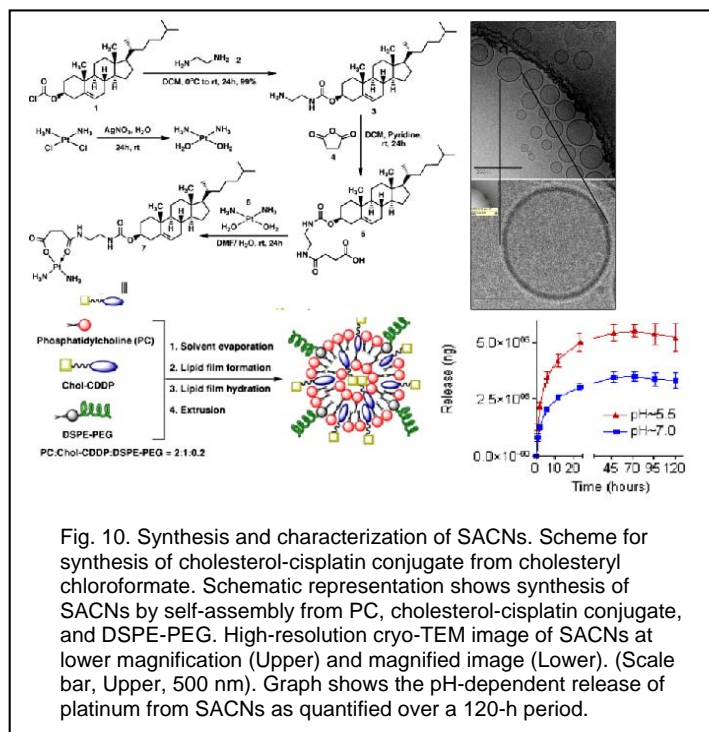
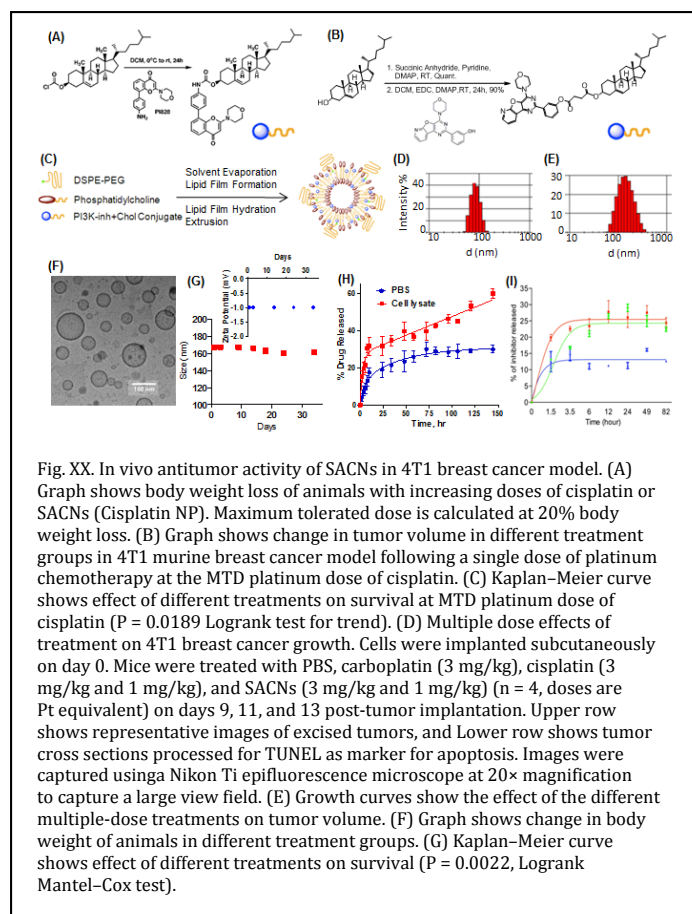


Fig. 10. Synthesis and characterization of SACNs. Scheme for synthesis of cholesterol-cisplatin conjugate from cholesteryl chloroformate. Schematic representation shows synthesis of SACNs by self-assembly from PC, cholesterol-cisplatin conjugate, and DSPE-PEG. High-resolution cryo-TEM image of SACNs at lower magnification (Upper) and magnified image (Lower). (Scale bar, Upper, 500 nm). Graph shows the pH-dependent release of platinum from SACNs as quantified over a 120-h period.

(Fig. 10). The ultrastructure analysis using cryo-transmission electron microscopy (cryo-TEM) (Fig. 10) revealed the formation of predominantly uni- and rare multilamellar structures less than 200 nm in diameter, with a membrane thickness ~ 5 nm. Dynamic light scattering further confirmed the size distribution of SACNs with a mean hydrodynamic diameter of 141.4 ± 1.2 nm ($n = 9$) (Fig. 11C). To validate the kinetics of cisplatin release, SACNs were incubated at acidic pH 5.5 over 120 h, with pH 7 as a reference. As shown in Fig. 11D, SACNs exhibited a pH-dependent sustained release of cisplatin. Interestingly, the rate of release was slower than observed earlier using a polymeric system, indicating that the cholesterol can incorporate into the lipid layer in a manner where the Pt moiety is present both on the outer as well as inner part of the membrane.

Self-assembling cholesterol-succinic acid-cisplatinum II-based nanoparticles (SACNs) exhibited

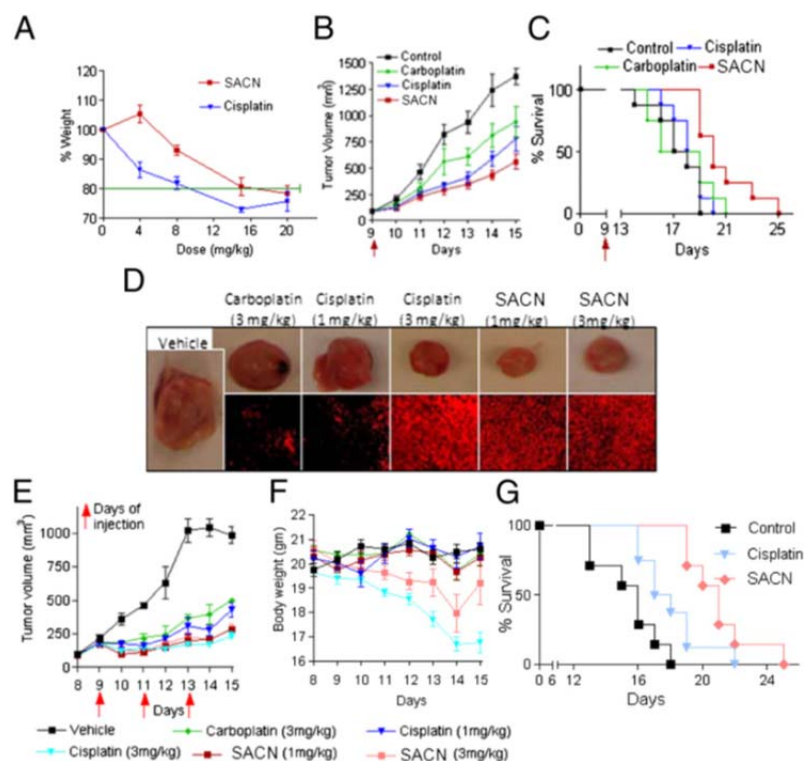


increased potency and efficacy in vitro and in vivo, respectively. The maximum tolerated dose (MTD) for the SACNs in BALB/c mice to be 16 mg/kg compared with 9 mg/kg of cisplatin (Fig. 11). We next dosed syngeneic BALB/c mice bearing 4T1 breast tumors (mean tumor volume ~ 100 mm³) with a single dose of cisplatin (8 mg/kg). Other groups of animals received vehicle, carboplatin, or SACNs, (the latter two received a Pt dose equivalent to 8 mg/kg dose of cisplatin). As shown in Fig. 11, although all of the platinates resulted in significant tumor inhibition compared with the vehicle-treatment, the SACNs exerted the maximal tumor inhibition ($P < 0.01$ vs. control) followed by cisplatin and carboplatin. Furthermore, although treatment with carboplatin or cisplatin exerted only minor increase in survival over vehicle-treated controls, the SACNs significantly increased overall survival trend (Fig. 11). We next tested the effects of multiple low-dose treatment with cisplatin, carboplatin, or the SACNs, with the highest platinum dose in each case adding up to the levels of Pt delivered at the MTD of cisplatin. Two additional groups were included that were treated with a lower dose of cisplatin or SACNs

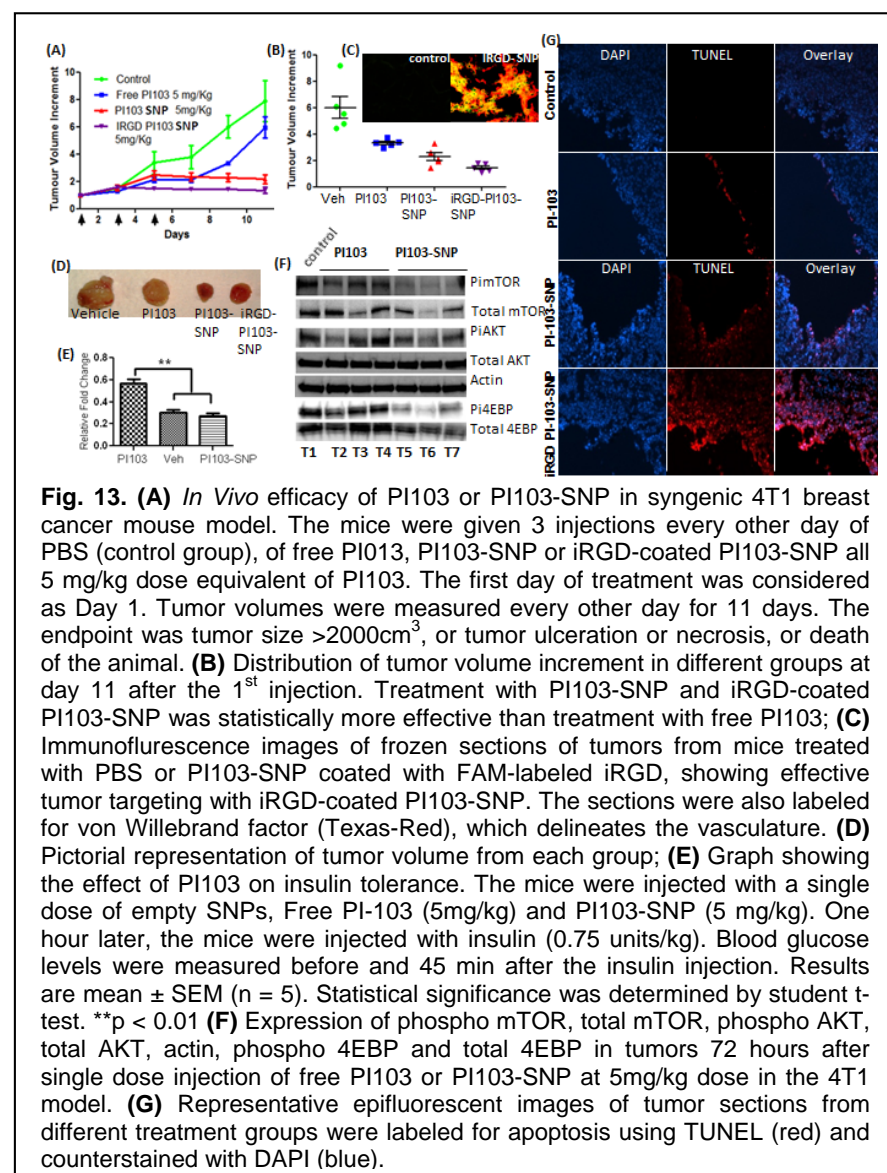
(equivalent of 1 mg/kg dose of platinum). As shown in Fig. 11 treatment with cisplatin resulted in a dose-dependent inhibition of tumor growth. Interestingly, although at the highest doses the tumor inhibition with the SACNs or cisplatin were identical, at the lower doses the SACNs exerted a superior antitumor effect compared with free cisplatin ($P < 0.05$, ANOVA). Furthermore, cisplatin resulted in a significant reduction in mean body weight ($P < 0.05$, ANOVA) compared with the SACN-treated groups (Fig. 11), indicating that the latter can reduce the systemic toxicity associated with cisplatin chemotherapy. Interestingly, even at the lower dose both the SACNs and cisplatin exerted greater tumor inhibition as opposed to the higher dose of carboplatin (Fig. 11). At the higher dose, both cisplatin and SACNs were found to increase survival, although the latter was superior (Fig. 11). These results have recently been published in the PNAS.

We had proposed that we will engineer nanoparticles in which we will entrap PI3K inhibitors. Interestingly, the supramolecular nanoparticle platform can be extended to engineering nanoparticles from PI3K inhibitors. In a recent study, we have engineered such a nanoparticle using PI828 and PI103, potent inhibitors of PI3K. As shown in Fig. 12, we engineered the SNPs from the cholesterol-PI828 or cholesterol-PI103 conjugates, phosphatidylcholine (PC) and 1,2-distearoyl-*sn*-glycero-3-phosphoethanolamine-N-[amino(polyethylene glycol)-2000] (DSPE-PEG2000) at optimized weight ratios using a lipid-film hydration self assembly method. The incorporation efficiency for the cholesterol-PI828 SNPs was 43%, and $60 \pm 5\%$ for PI103-cholesterol conjugate SNPs. As shown in Fig. 11D, cholesterol-PI828 conjugates resulted in the formation of SNPs with hydrodynamic diameter of 108 ± 8.9 nm as determined by dynamic light scattering. PI103-SNPs showed a mean particle diameter of 172 ± 1.8 nm. Ultrastructure analysis using cryo-transmission electron microscopy (cryo-TEM) revealed the formation of predominantly unilamellar structures 100 nm or less in diameter. The size difference between TEM and DLS measurements can be attributed to the hydration sphere arising from the PEG coating, which can facilitate the masking from the reticuloendothelial system. Additionally, aliquots of the PI103-SNPs were stored for a period of over a month, and the size and zeta potential was measured periodically as a measure of stability of the nanostructure. As shown in Fig. 12, no significant temporal variation was observed in either size or zeta potential during this period, indicating that the formulations were stable. To study the temporal kinetics of PI3K inhibitor release, the SNPs were incubated either in phosphate buffer saline or in cell lysate. While the amount of drug released in PBS was saturated at $\sim 20\%$, a sustained release of drug was observed in cell lysate, consistent with the cleavage of the linkers in acidic and enzymatic (esterase) conditions. Interestingly, while a sustained and increasing drug release was observed with PI103-SNP, the rate of release of PI828 was significantly lower. This is consistent with the carbamate linker between the drug and cholesterol, which is more stable than the ester linkage in the PI103-SNPs.

Fig. 12: Synthetic scheme showing conjugation of (A) PI-828 and (B) PI103 to cholesterol via carbamate and ester linkages respectively; (C) Schematic representation shows assembly of supramolecular nanoparticles (SNPs) from phosphatidylcholine (PC), PI103/PI828-cholesterol conjugate and DSPE-PEG; Distribution of hydrodynamic diameter of (D) PI828-SNPs and (E) PI103-SNPs measured using dynamic light scattering; (F) High resolution cryo-transmission electron microscopy image of PI103-SNPs (Scale Bar = 100 nm); (G) Physical stability of PI103-SNPs during storage condition at 4°C as measured by changes in size. Inset shows changes in Zeta potential of nanoparticles at 4°C ; (H) Release kinetics of PI103 from SNPs in PBS, pH 7.4, and in 4T1 breast cancer cell lysate. (I) Release kinetics of PI828 from SNPs in PBS, pH 7.4 (blue line), and in lysates from 4T1 cells (red line) and PI3K-overexpressing 4306 ovarian cancer cells (green line). Data shown are mean \pm SEM (at least triplicates at each condition).



We next investigated the anti-tumor efficacy of PI103-SNPs in 4T1 breast cancer, which is negative for



both the free drug and PI103-SNP compared to the vehicle-treated group. PI103-SNP seemed more efficient, but the difference was not statistically significant. Interestingly, the phosphorylated forms of downstream signaling molecules, mTOR and 4EBP, were more strongly inhibited in the PI103-SNP-treated group than in the PI103-treated tumors ($P < 0.05$, t test).

To test whether targeting the nanoparticles to the tumor using ‘homing’ peptides increases antitumor efficacy, a separate group of tumor mice were treated with PI103-SNPs that were surface-decorated with iRGD peptide. As shown in Fig. 13, such a treatment resulted in greater tumor inhibition than what was obtained with SNPs that accumulate via passive uptake. Indeed, previous observations have shown that iRGD-coated nanostructures exhibit increased extravasation and tissue penetration in a tumor-specific and neuropilin-1-dependent manner. As shown in **Fig. 13**, epifluorescence imaging of tumor cross-sections revealed significant intra-tumoral localization of FAM-labeled iRGD coated PI103-SNPs. To elucidate the mechanism underlying the increased *in vivo* efficacy, the tumors were excised post-

ER and PR, and expresses a low level of the mouse Her2/neu equivalent. Transplanted into syngeneic mice, the 4T1 form aggressive, highly metastatic breast cancers. Mutations in genes that constitute the PI3K pathway occur in $>70\%$ of breast cancers. We have previously demonstrated that the 4T1 cells mount a survival response to standard chemotherapy via an upregulation of PI3K signaling. We treated mice with 4T1 tumors with a dose equivalent to 5 mg/kg of PI103 as free drug or as PI103-SNP. The treatment was started when the mean tumor volume had reached 100mm^3 . As shown in **Fig. 13**, treatment with PI103 resulted in tumor growth inhibition relative to PBS-treated controls, but tumor rebound was observed after the treatment was stopped. In contrast, treatment with PI103-SNP resulted in sustained tumor growth inhibition over the study period. This was consistent with the sustained level of the drug in the SNP group. After a single injection, intratumoral Akt phosphorylation was inhibited by

treatment, and processed for terminal deoxynucleotidyl transferase dUTP nick end labeling (TUNEL) as a marker for apoptosis. As shown in **Fig. 13**, treatment with PI103-SNPs resulted in greater apoptosis than treatment with free PI103. iRGD-coated PI103-SNPs induced highest level of apoptosis, followed by PI103-SNPs and free PI103, consistent with the tumor inhibition result.

Task 3. Assay for tumor detection (hit-and-run assay)

3a. Test a prototype assay in which a mixture of nanoparticles coated with either a tumor-homing peptide or a control peptide is injected into a tumor-bearing mouse and a change in the ratio of the particles in the circulation is monitored.

3a.1. Functionalization of magnetic nanoparticles with cleavable homing-CendR peptide chimera and physicochemical characterization.

The Ruoslahti laboratory, in collaboration with the Reich laboratory, has provided the first reduction to practice of the hit-and-run assay. This novel multiplexed nanoparticle platform utilizes iron oxide nanoparticles doped with gadolinium isotopes for in vivo tracking. Blood samples and tissue samples were analyzed using ultra-high sensitivity inductively coupled plasma-mass spectrometry (ICP-MS).

The principle is outlined in **Fig. 14**. The detection and barcoding are based on measurement of radiostable gadolinium isotopes by ICP-MS. Each type of nanoparticle is labeled with a unique isotope and functionalized with a distinct peptide sequence. The mixture of nanoparticles is injected into tumor-bearing and non-tumor bearing (normal) mice. Blood analysis detects the binding of receptors within vascularized, diseased tissue, by monitoring the selective clearance of targeted nanoparticles relative to control nanoparticles.

We have developed materials and methods with reliable multiplexing results across at least four logs of injected dose, validated over several combinations of nanoparticle coatings. In principle the technique may eventually allow multiplexing 10-100 isotopes in a blood or biopsy assay. High atomic mass, stable isotopes, with low biological abundance are ideal. We chose gadolinium since it has been shown to be easy to dope into iron oxide nanoparticles. The main challenges to ICP-MS hit-and-run are 1) the reproducible synthesis of a pair of labeled materials that differ only in the prescribed manner, i.e. outer ligand region. The clearance of materials is the major source of interference in this assay and the dependence on surface chemistry is not well understood. 2) A procedure for digesting and analyzing small volumes of blood. 3) Instrument calibration and stability in multiplexed mode of operation.

We set out to use ratios to monitor selective clearance since that quantity best captures subtle changes in the blood. Ratios correct for certain difficult to control parameters in dosing and collection. The internal standard corrects for differences in injected volume and the blood sampled, dilution/digestion pipetting errors, and instrument sensitivity variation. ICP-MS is very accurate in isotopic ratio analysis, and extremely sensitive in detection. We have explored in depth both ratio and absolute quantities and find the ratio analysis reliable for analyzing large sample sets.

In the experiments described below we detect the presence of a tumor using circulating iRGD peptide carried on nanoparticles and PEG controls. The iRGD pool is depleted in the tumor mouse in a rate and degree related to the particle accumulation in the tumor. This is validated by end-point tissue analysis by ICP-MS and tissue section microscopy.

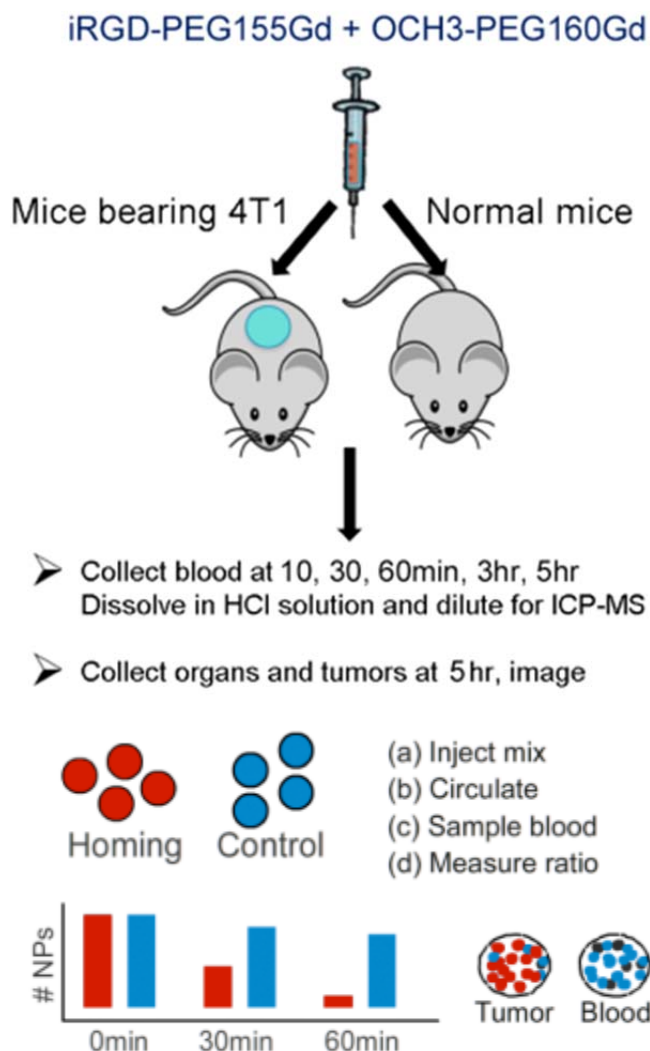


Fig. 14. Targeting with iRGD peptide, versus high molecular weight PEG control particle. Isotope-labeled iron oxide nanoparticles (metals: 5% Gd, 95% Fe) coated with dextran and PEG are functionalized with either a tumor homing peptide (iRGD) or having the inert methoxy group (OCH₃), and contain either 155Gd or 160Gd. The two barcoded particles are then mixed at ~1:1 and injected into the tail vein of a mouse. Over the course of a few hours blood is taken and measured for relative nanoparticle content. A sample of the injected solution is analyzed for the 160Gd/155Gd isotopic concentration. Blood values reveal the consumption of homing particles by the tumor.

3a.2. In vivo evaluation of the prototype nanoparticle

The homing properties of the Gd-doped nanoparticles are shown in Figure 15 using the tumor penetrating peptide, iRGD. We could detect the iRGD-Gd-Iron oxide (GDI) across different injection doses (5, 0.5, 0.05 mg/kg) and find that with reduction in the injection dose less nanoparticles accumulate in the tumor and liver. We attribute this to saturation of the sites at the high dosage.

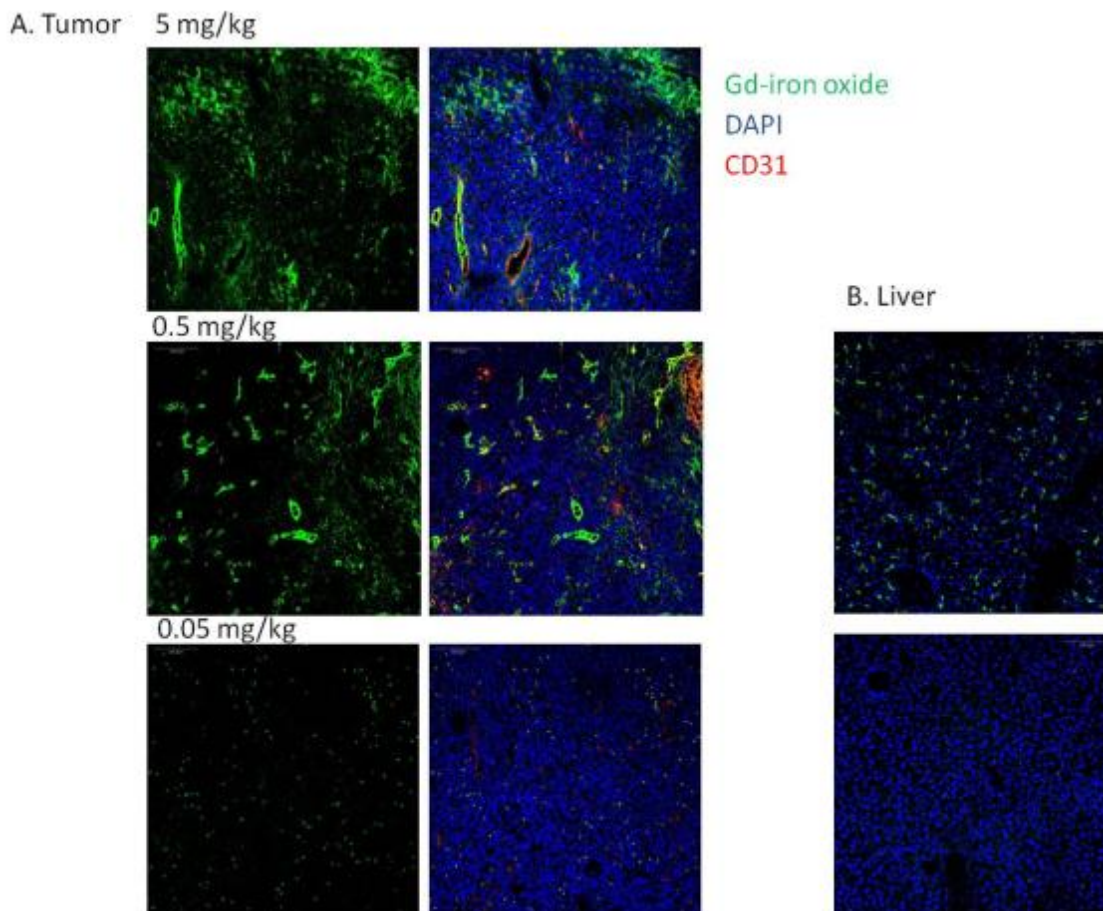


Figure 15. Gd-doped iron oxide (GDI) nanoparticles were conjugated to iRGD through a 5K-PEG linker. After injection the organs were collected and analyzed by confocal microscopy. iRGD-GDI homes and extravasates into the tumor tissue. At lower dose the homing property is retained. Green, FAM-iRGD-GDI; red CD31 staining indicates blood vessels; DAPI shows cell nuclei.

Blood analysis monitors the ratio of the two particles as given by their isotope labels (^{160}Gd and ^{155}Gd). We show here that the rapid phase of clearance of PEGylated and iRGD (targeted) nanoparticles happens during the first 30 min (Figure 16). A difference between the PEG and iRGD non-targeted nanoparticles is detected at ~ 10 min (Figure 16B). We found this behavior consistent across a range of injected dosage.

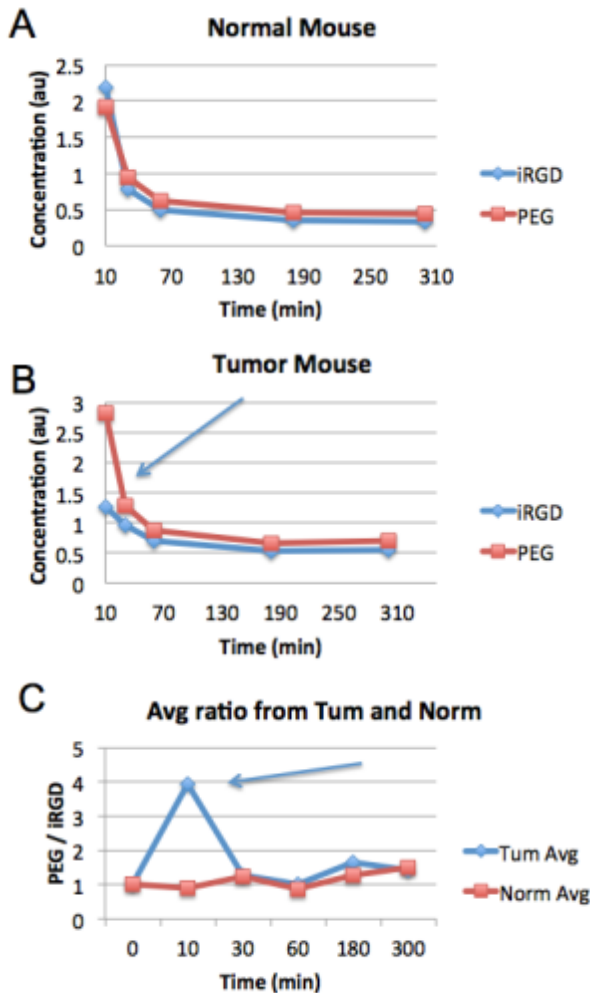


Figure 16. An example experiment using 0.0005 mg/kg Gd-doped iron oxide, coated with either PEG or PEG-iRGD coatings. These are termed PEG and iRGD nanoparticles, respectively. They were mixed and injected into mice with blood samples of 10 μ L taken at 10, 30, 60, 180, and 300 min. Multiplexed ICP-MS blood analysis for the concentration of Gd isotopes shows clearance of iRGD nanoparticles is quite similar to PEG nanoparticles in the normal mouse (A), whereas in the tumor-bearing mouse the iRGD selectively disappears from circulation (B). (C) The ratio of PEG/iRGD may be used to capture the difference between the mice. The average of two normal and two tumor mice is plotted, showing a peak difference at \sim 10 min.

$$\begin{aligned}
 \text{A) } \frac{iRGD_{Tumor}}{OCH3_{Tumor}} &= \text{Tumor Ratio} \\
 \frac{iRGD_{Norm}}{OCH3_{Norm}} &= \text{Normal Ratio} \\
 \text{B) } OCH3_{Norm} &= OCH3_{Tumor} \quad (*\text{assumption}) \\
 \text{C) } \frac{\text{Tumor Ratio}}{\text{Control Ratio}} &= \frac{iRGD_{Tumor}}{iRGD_{Norm}} \quad \text{Specificity}
 \end{aligned}$$

Figure 17. Specificity defined by a ratio of ratios. A) Multiplexed blood ratio value for each time point is acquired. B) We assume a similar relative clearance of the non-targeted OCH3 particle. C) Dividing the tumor-mouse's ratio trace by the trace of the normal mouse gives the specific response of iRGD for the tumor.

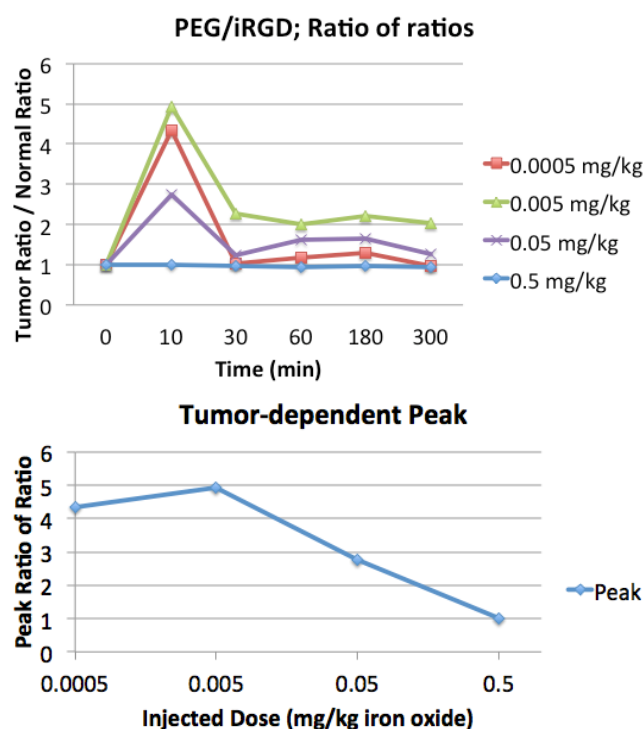


Figure 18. Difference between normal and tumor-bearing mice were quantified at each time by dividing the ratios shown for 0.0005 mg/kg in Figure 16C. Here we look at how the ‘ratio of ratios’ can give insight as we increase the dose in log units. Diagnostic contrast in our tumor mouse model appears when the dose is under 0.05 mg/kg, with iRGD delivery to the tumor showing up as a peak in the ratio of ratios ~10 min post injection. At longer time points the continual clearance of both particles by the liver and spleen (RES) counteracts the differences between the two particles, and the ratio moves back towards a value of one. The quantity of iRGD nanoparticles that bind in the tumor (disappear from blood) is a modest fraction of the total dose only until vascular receptor saturation, shown here and by microscopy in Figure 15 to occur above 0.05 mg/kg. It is considered that receptor recycling, if taking place, is not competitive with the bulk RES interference for this set of nanoparticles.

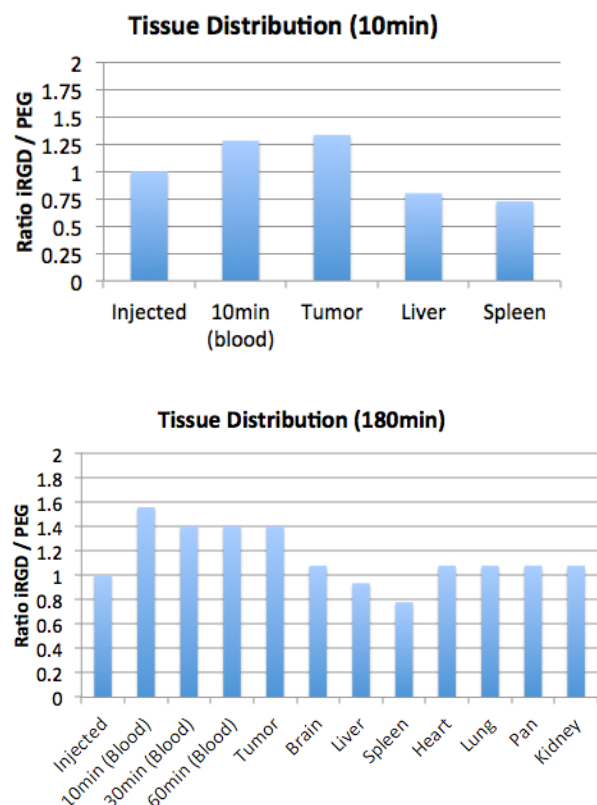


Figure 19. Correlating selective blood clearance of iRGD nanoparticles with end-point perfusion and tissue digestion ICP-MS. PEG nanoparticles serve as control, co-injected as described above. All ratios of $^{155}\text{Gd}/^{160}\text{Gd}$ (iRGD/PEG) are normalized to the injected value therefore positive deviations can be converted into preferential iRGD accumulation. At both 10 min and 180 min we detect an excess of iRGD in the tumor. Interestingly, the liver and spleen show the opposite accumulation. Other organs show a neutral value. We note that the absolute signals of brain, heart, lung, pancreas, and kidney were all significantly lower than tumor levels, an indicator of perfusion quality, and the low non-specific uptake of the nanoparticles.

$$C_p = A \cdot e^{-\alpha t} + B \cdot e^{-\beta t}$$

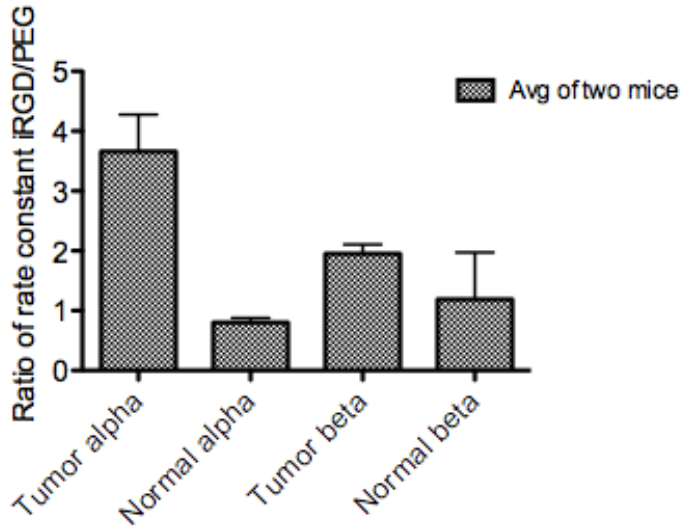


Figure 20. Rate constants were determined using a two-compartment model. C_p is concentration of the nanoparticle in question, alpha and beta are macro rate constants for double-exponential half-life pharmacokinetics as observed. A and B are proportional to initial dosage. Alpha, the faster rate constant, characterizes early clearance from the blood (central compartment), into tissue (peripheral compartment). The ratio of (alpha iRGD) / (alpha PEG) is higher for tumor-bearing mice than for normal mice, as expected for rapid binding assay (liver obscures later phase). We are currently comparing validity of other more complex models.

Using the two-compartment model we have gained insight into the key variables for the assay. For each component of the injected mixture we fitted using the double exponential decay function (Figure 20, C_p formula). When clearance of a given material has both fast and slow decay rates, component alpha defined as the faster rate constant and beta the slower. We calculate alpha and beta for each isotope, by fitting the absolute concentrations in blood over time. PEG alpha value (the faster rate constant) is significantly different from iRGD alpha only in tumor-bearing mice. Beta ratio values were similar between the two isotopes for the two groups. In Figure 20 we have plotted the $\alpha_{iRGD}/\alpha_{PEG}$ ratio values showing the significant difference in tumor-bearing mice (Figure 20). Consistent with this analysis, the early phase 0 to 30 min is where the nanoparticle concentration ratios diverged in Figure 18.

The aim of this project is to diagnose and stage a tumor by injecting a pre-mixed set of nanoparticles where some bind to vascular targets, others do not, and measuring the progressive changes in their blood ratio. Our current data demonstrates the feasibility of detecting a tumor by blood analysis alone. The difficulty in detecting low concentrations of nanoparticles from blood is largely solved by the use of ICP-MS and barcoding nanoparticles with isotopes that are not found in the body, and which are non-toxic. Synthetically the particles should be as similar as one can make them, with long half-lives and high, specific affinity. We use an iron oxide core to minimize potential toxicity of the carrier, although the doses used here are well below those typical for iron oxide or gadolinium based MRI contrast agents.

The multi-valency cyclic peptide has strong affinity (and avidity) which encourages rapid binding, on a time scale least complicated by the liver and spleen RES system. We expect that advances in nanoparticle coatings, driven by a better understanding of RES-nanoparticle interactions will free the hit-and-run assay to include more sophisticated theranostic nanoparticles that may act on longer timescales. We are now testing a peptide control that has D-amino acids in just two positions of the iRGD sequence. We hypothesize that it will behave most similarly to iRGD with respect to RES clearance rates, but the mutations completely remove the integrin binding affinity. Subtle changes such as these should be ideal for detecting the presence of a binding pocket within the complex environment of blood and vascular receptors.

3b. Examine the suitability of surface enhanced Raman spectroscopy (SERS) for *in vivo* detection of barcoded nanoparticles

We encountered problems with high background and low sensitivity of SERS detection of *in vivo* probes and developed the gadolinium-doped iron oxide nanoparticles described in 3a as an alternative.

3c. Bipartite tumor-homing peptides

Most of our effort has been exploiting the discovery reported last year of ratiometric ACPPs (RACPPs) in which cleavage not only unmask adhesive (arg)₉ but disrupts fluorescence resonance energy transfer between Cy5 and Cy7, leading to a large increase in Cy5/Cy7 emission ratios, which in turn allows more rapid and robust discrimination between tumors and surrounding normal tissues. Our optical system for real-time fluorescence-guided surgery required much modification and upgrading to produce continuous pseudocolor-encoded emission ratio images in real time. The major new findings are as follows:

1) *Extension of RACPPs to proteases other than matrix metalloproteinases-2 and -9*: We synthesized RACPPs specific for other enzymes such as elastase and thrombin and found that their FRET responses

were practically unchanged despite the necessary changes in substrate sequence. Therefore the RACPP design seems applicable to any protease (and probably any cleavage activity) for which a specific substrate can be designed.

2) *RACPPs Enable Detection of Metastases onto Liver* - Previous single fluorophore labeled ACPPs gave high uptake into normal liver, which made it unlikely that we could distinguish metastases by standard single-wavelength imaging. We have developed a syngeneic model in which GFP-labeled 8119 mammary tumor cells colonize the liver (GFP image, Fig. 21a,e). Gratifyingly, these metastases gave high ratio

Figure 21

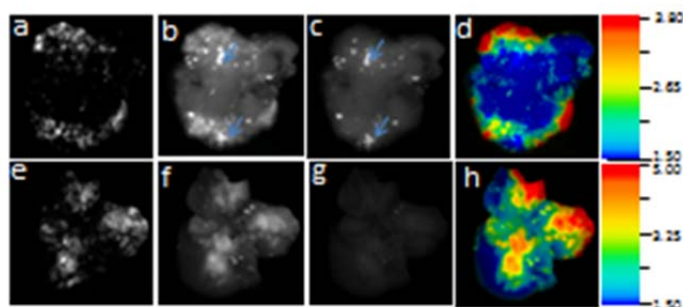


Figure 21. Livers containing PyMT 8119 GFP positive metastases, harvested from mice 2 hr after IV injection of RACPP1 (MMP2/9-selective, a-d) or RACPP3 (elastase-sensitive, e-h). a, e) GFP fluorescence images. b, f) Cy5 fluorescence images obtained by exciting Cy5 at 620 nm. c, g) Cy7 emission images obtained by exciting Cy5. d, h) Cy5/Cy7 emission ratio images. Ratio images showed better correlation with GFP reference emission images than either Cy5 or Cy7 independent images. The ratio contrast for metastases relative to normal liver was higher for RACPP3 (h) than for RACPP1 (d). Arrows exemplify two of the many nontumor regions (as judged by lack of GFP fluorescence) where both Cy5 and Cy7 fluorescence intensities were high, resulting in relatively low ratios.

metastasis was verified by independent post mortem histology. Although the ratio of ACPPD Cy5 intensities in nodes vs. adjacent normal tissue was significantly higher ($p = 0.02$) for metastatic than nonmetastatic nodes, there was considerable overlap preventing perfect discrimination at any threshold. The same measure using only Cy5 intensities for RACPP1, i.e. treating it only as a dequenching probe, gave an even more significant difference ($p = 0.0007$) and complete separation according to node status. Even more robust ($p < 10^{-4}$) discriminations of metastatic status were obtained from Cy5/Cy7 ratios of just the node or of the node further ratioed against adjacent normal tissue (Fig. 23b).

Figure 23

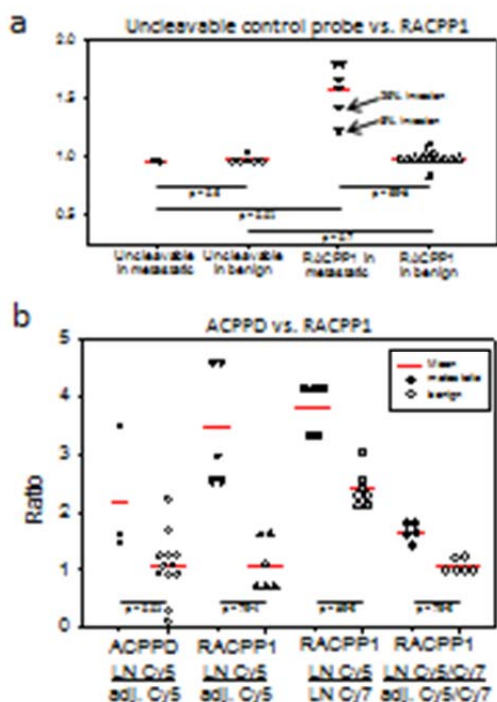


Figure 23. a) Cy3/Cy7 ratio of lymph nodes versus adjacent normal tissue in animals injected intravenously with either control uncleavable probe or RACPP1. Each symbol represents a separate lymph node whose status (solid = metastatic, hollow = non-metastatic) was independently determined by histology. In mice injected with control uncleavable probe, the presence (solid circles) or absence (hollow circles) of cancer invasion did not change the ratio of lymph node Cy3/Cy7 emission ratios relative to adjacent normal tissue, all values being near 1. In mice injected with RACPP1, lymph nodes with cancer invasion (solid triangles) had significantly higher ratios than lymph nodes without cancer invasion (hollow triangles). Interestingly, the ratio of Cy3/Cy7 emission ratios in nodes vs. adjacent normal tissue correlated with the degree of cancer invasion, where the lymph nodes with partial cancer invasion (arrows) showed less ratio increase (albeit still higher than any normal tissue) than lymph nodes with 100% cancer invasion. b) Dot density graph showing higher sensitivity/specificity of RACPP1 compared to ACPPD in the differentiation between lymph nodes bearing cancer invasion (solid symbols) versus adjacent normal tissue (hollow symbols). For ACPPD, although mean Cy5 fluorescence intensity of metastatic lymph nodes relative to adjacent normal tissue (solid circles) is significantly higher ($p = 0.02$) than for lymph nodes without metastasis (open circles), there is overlap which decreases sensitivity/specificity. Metastatic lymph nodes in mice following IV injection of RACPP1 show higher Cy5 intensity relative to adjacent normal tissue (solid triangles), Cy3/Cy7 ratio alone (solid squares) or ratios against adjacent normal tissue (solid diamonds) significantly higher ($p = 7 \times 10^{-4}$, 8×10^{-4} , 7×10^{-4} , respectively) than nonmetastatic nodes (hollow symbols). Because metastatic and benign nodes do not overlap in the RACPP1 ratios, sensitivity and specificity can be 100%.

4) *Ex vivo analysis of patient samples* – Two critical questions in translating these results to patients are

- what fraction of clinical tumors have enough protease activity to cleave our RACPPs?
- can we develop a personalized assay from biopsy material to tell whether a given patient's tumor has enough protease activity? Obviously if the patient's tumor lacks activity, we should not attempt to use RACPPs to guide surgery. Both these questions become answerable with RACPPs, because the loss of FRET over time can be measured in homogenates prepared from small amounts of frozen tissue, including banked tissues examined retrospectively. Previous nonratiometric ACPPs could not be assayed *ex vivo* because the only effect of enzyme activity was to increase pharmacokinetic retention, which can only be tested *in vivo*, not on homogenates from frozen tissue. Preliminary results indicate promising distinction between normal tissues and known tumors (Fig. 24), but we are collecting large numbers of fresh-frozen and banked clinical specimens (including mammary tumors) to achieve sufficient statistics. We are also attempting to extend this principle to a histological assay so that RACPP-cleaving (i.e.

protease) activity can be mapped with high spatial resolution on thin sections.

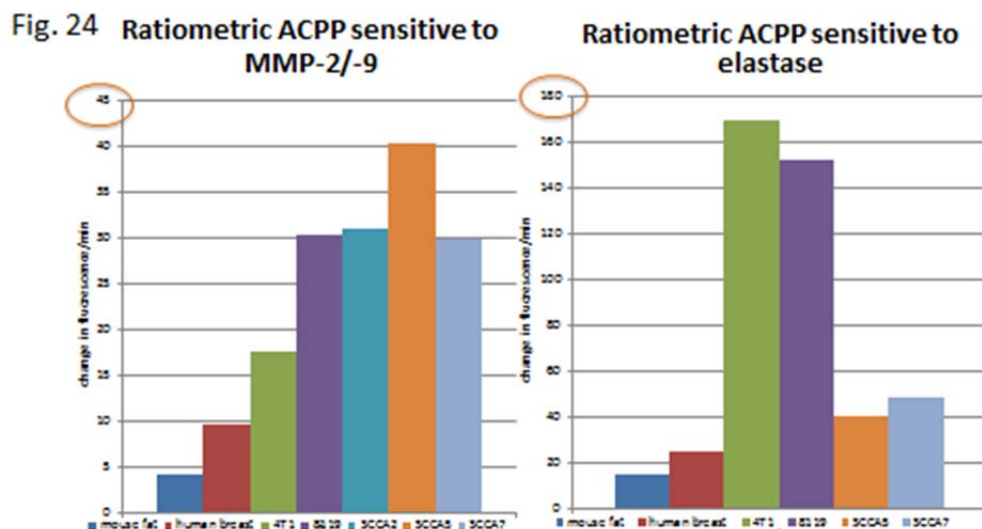


Fig. 24: Ability to cleave RACPPs can be assayed *ex vivo* on frozen tissue samples and may differentiate normal from tumor tissues. Y axis indicates rates of change of Cy5 fluorescence (arbitrary units) over time following addition of MMP- and elastase-sensitive RACPPs to 100 mg homogenized fatty tissue from mouse, normal human breast, two mouse breast cancer grafts (4T1 and 8119), and human head and neck squamous cell carcinoma lines.

Efforts to develop a “hit-and-run” assay to measure intact substrate vs. cleavage products in readily accessible body fluids like blood and urine were suspended due to inconclusive preliminary results and the recruitment by industry of the postdoc skilled in electrophoretic separations of crude samples.

Task 4. **Develop a multifunctional nanoparticle that delivers a drug to tumor vessels and tumor cells, while releasing a diagnostic component into the circulation**

4a. Adapt the barcoded diagnostic technology onto polymer-based drug-loaded multifunctional nanoparticles, and characterize for physicochemical properties

The Ruoslahti laboratory has developed two nanosystems for cancer treatment that are based on iron oxide nanoparticles and shown their efficacy in breast cancer. An intratumorally spreading local tumor treatment effective in breast cancer models has also been developed (Chen et al., *Cancer Res.* in revision). These advances have been reported in detail elsewhere ((W81XWH-08-1-0727 annual report – Oct 2012). The bar-coded detection can easily be incorporated into the nanosystems.

4b. Characterization of multifunctional nanoparticle in *in vivo* tumor models, including testing for tumor homing, penetration and uptake into tumor cells

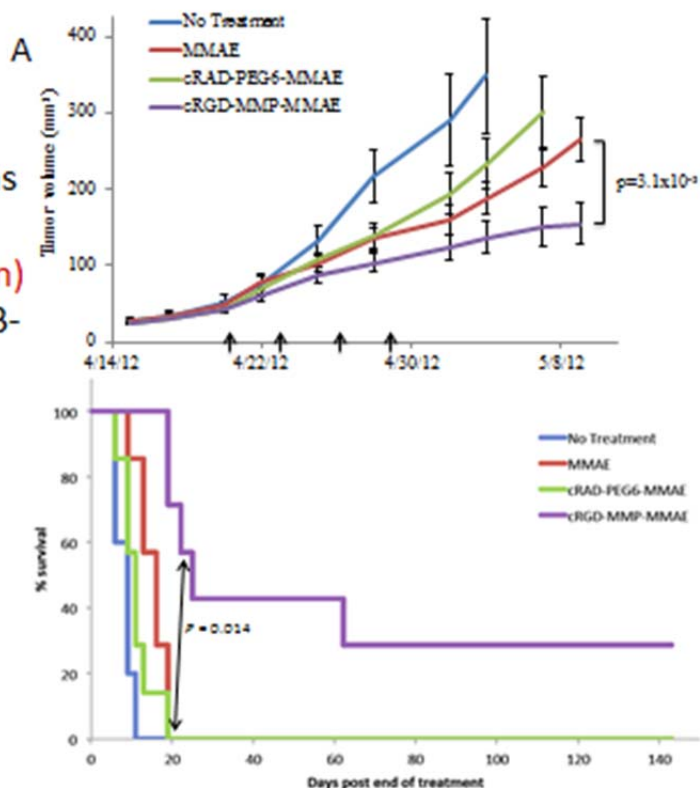
Last year the Tsien group reported that the ACPPs conjugated to ligands for integrin $\alpha\beta3$ gave considerably more tumor contrast than either targeting mechanism alone, consistent with literature reports that $\alpha\beta3$ and MMP-2 form a molecular complex. We have now applied such targeting to chemotherapeutic applications by synthesizing ACPPs with a powerful cytoskeletal inhibitor,

monomethyl auristatin E (MMAE), targeted with our best combination, cyclic(RGD) in combination with the MMP-2/-9 cleavable PLGC(Me)AG within the ACPP. The MMAE was attached to the (arg)₉ domain via the same cathepsin-sensitive linker as used in the recently FDA-approved antibody-drug conjugate brentuximab vedotin. Fig. 25 shows promising early results in regressing orthotopic MDA-MB-231 xenografts, a model for triple-negative breast cancer. The mice were dosed either with vehicle, 0.2 mg/kg free MMAE, equimolar cRGD-(MMP-sensitive ACPP)-MMAE (6.5 nanomoles peptide), or a control drug conjugate in which both the cyclic(RGD) and ACPP were crippled. Dosing was every three days for a total of four doses and tumor volumes were measured at regular intervals. The dual negative peptide drug conjugate (c(RADfC) and PEG6, green lines) performed worse than unconjugated MMAE (red lines), whereas the dual targeted peptide drug conjugate (c(RGDfC) and PLGC(Me)AG, purple lines) demonstrated a significant ($p=3.1 \times 10^{-3}$) reduction in average tumor volume and longer survival ($p=0.014$ by log rank test) compared to unconjugated MMAE (red lines). 2 out of 7 mice seem to have achieved permanent cure. When the dose was increased to 0.32 mg/kg MMAE (peptides still equimolar), the dual targeted peptide caused 4 out of 8 tumors to regress completely, compared to 2 out of 8 for equimolar free MMAE. The ACPPs caused no weight loss or gross toxicity. We are continuing to explore different doses, look more closely for any toxicities, and dissect the relative contributions of the c(RGD) and ACPP targeting mechanisms. ACPPs are much smaller than antibodies, should penetrate solid tumors more easily, and so far have shown much wider applicability across a range of tumor types than any single antibody.

Figure 25

c(RGD)-ACPP-drug
conjugate outperforms
untargeted drug
(monomethylauristatin)
in regressing MDA-MB-
231 orthotopic
xenografts

Jessica Crisp,
Elamprakash Savariar



4c. Characterize the antitumor efficacy and mechanism of action of the multifunctional bar-coded nanoparticles *in vivo* Future work will address this aim.

REPORTABLE OUTCOMES

(1) Papers published, in press, and submitted:

The Ruoslahti laboratory:

Sanchez-Martin, D., Cuesta, A.M., Fogal, V., Ruoslahti, E., and Alvarez-Vallina, L. The multi-compartmental p32/gCiqR as a new target for antibody based tumor targeting strategies. *J Biol Chem* 286:5197-5203 (2011) PMC:3037632

Roth, L., Agemy, L., Kotamraju, V.R., Braun, G., T. Teesalu, T, Sugahara, K.N., Hamzah, J., and Ruoslahti E. Transtumoral targeting enabled by a novel neuropilin-binding peptide. *Oncogene*, 31: 3754-3763(2012). PMID: 22179825

Ruoslahti, E. Peptides as targeting elements and tissue penetration devices for nanoparticles. *Adv. Mat.* (review article) 24:3747-3756. (2012). [Epub ahead of print] PMID: 22550056.

Braun G B., Friman, T., Pang H-B., Kotamraju, VR, Pallaoro, A., Reich, NO., Teesalu, T. and Ruoslahti, E. Etchable and bright silver nanoparticle probes for cell internalization assays. Submitted

Chen, R., Braun, G.B., Luo, X. Sugahara, K.N., Teesalu, T., Ruoslahti, E. Application of a proapoptotic peptide for an intratumoral-spreading cancer therapy. (2012). *Cancer Research*, Provisionally accepted.

Alberici L., Roth, L., Sugahara, K.N., Agemy, L., Kotamraju, V.R., Teesalu, T., Bordignon, C., Traversari, C., Rizzardi, G.-P., Ruoslahti, E. De Novo Design of a Tumor Penetrating Peptide (2012) *Cancer Research*, Provisionally accepted.

Erkki Ruoslahti and members of his laboratory have given numerous invited seminars and presentations at various national and international conferences.

The Tsien laboratory:

During the year covered by this report, Roger Tsien made presentations related to the above projects at many meetings. The first three sub-areas of progress with RACPPs are covered in two manuscripts, one in press in *Angewandte Chemie* (one of the highest-profile chemistry journals) and one under revision at *Cancer Research*. Provisional and full U.S. patent applications on the RACPPs have been filed. Patent disclosures have been filed with the UCSD Technology Transfer Office covering the improved surgical imaging system and the *ex vivo* personalized protease assay. Avelas Biosciences, UCSD's exclusive licensee for ACP technology, has developed its own RACPPs closely related to ours, has independently obtained discrimination between metastatic and unaffected lymph nodes similar to Fig. 3, has begun GMP production and preliminary toxicology, and is planning to file an IND and begin Phase I clinical trials in the second half of 2013. The initial indication will be to help decide intraoperatively how many lymph nodes should be removed during resection of breast cancers.

The Sengupta laboratory: Please refer to separate report filed by Dr. Sengupta.

(2) Patents filed:

Title: Truncated LYP-1 Peptides and Methods and Compositions Using Truncated LYP-1 Peptides

Inventor(s): Erkki Ruoslahti, Tambet Teesalu, Kazuki Sugahara, and Lise Roth

Date Reported to iEdison: October 19, 2012

The new peptides reported here will be patented, as well.

Please refer to separate reports filed by Drs. Tsien and Sengupta

CONCLUSION

New peptides recognizing very early changes in breast cancer development have been discovered. Interestingly, the changes detected by these peptides take place before the vasculature in the premalignant lesions is detectably altered. These peptides may be useful in imaging applications. A new aptamer screening technology has been developed under this grant that will help bring the aptamer technology to bear on cancer research and treatment. The Ruoslahti and Sengupta laboratories have developed new nanotechnologies for diagnostic and therapeutic applications in breast cancer. Ratiometric ACPPs from the Tsien laboratory improve the speed and robustness with which tumors can be discriminated from normal background tissues, particularly metastases of mammary tumor cells to liver and to lymph nodes. They enable personalized *ex vivo* assays on patient samples. ACPPs have now shown promise in delivering chemotherapeutic payloads, not just imaging agents. The technologies from all three laboratories have been licensed by the respective institutions to biotech companies that have detailed plans and realistic schedules to begin clinical trials.

References

Alberici, L., Roth, L., Sugahara, K.N., Agemy, L., Kotamraju, V.R., Teesalu, T., Bordignon, C., Traversair, C., Rizzardi, G-P, Ruoslahti, E. *De Novo* Design of a Tumor-Penetrating Peptide. Cancer Research, provisionally accepted. (2012).

Chen, R., Braun, G.B., Luo, X., Sugahara, K.N., Teesalu, T., Ruoslahti, E. Application of a proapoptotic Peptide for an Intratumoral-Spreading Cancer Therapy. Cancer Research, provisionally accepted. (2012).

Diehl, F. et al. BEAMing: single-molecule PCR on microparticles in water-in-oil emulsions. Nature methods 3, 551–9 (2006).

Dressman, D., Yan, H., Traverso, G., Kinzler, K. W. & Vogelstein, B. Transforming single DNA molecules into fluorescent magnetic particles for detection and enumeration of genetic variations. Proc. Natl. Acad. Sci. USA 100, 8817–22 (2003).

Gold, L. et al. Aptamers and the RNA world, past and present. Cold Spring Harbor perspectives in biology 4, (2012).

Gong, Q., Wang, J., Ahmad, K.M., Csordas, A.T., Zhou, J., Nie, J., Stewart, R., Thomson J.A., Rossi,

J.J., Soh, H.T. Selection Strategy to Generate Aptamer Pairs that Bind to Distinct Sites on Protein Targets. *Anal. Chem.* 84, 5365–5371 (2012).

Keefe, A. D., Pai, S. and Ellington, A. Aptamers as therapeutics. *Nature reviews. Drug discovery* 9, 537–50 (2010).

Roth, L., Agemy, L., Kotamraju, V.R., Braun, G., T. Teesalu, T, Sugahara, K.N., Hamzah, J., and Ruoslahti E. Transtumoral targeting enabled by a novel neuropilin-binding peptide. *Oncogene*, 31: 3754-3763 (2012). PMID: 22179825

Sugahara, K.N., Teesalu T., Karmali P., Kotamraju V.R., Agemy L, Girard O.M., Hanahan D., Mattrey, R.F., and Ruoslahti E. Tissue-penetrating delivery of compounds and nanoparticles into tumors. *Cancer Cell*, 16:510-520, (2009). PMCID: PMC2791543.

The Multicompartmental p32/gC1qR as a New Target for Antibody-based Tumor Targeting Strategies^{*[S]}

Received for publication, July 7, 2010, and in revised form, November 30, 2010. Published, JBC Papers in Press, December 14, 2010, DOI 10.1074/jbc.M110.161927

David Sánchez-Martín^{‡1}, Ángel M. Cuesta[‡], Valentina Fogal^{§2}, Erkki Ruoslahti^{§¶}, and Luis Álvarez-Vallina^{‡3}

From the [‡]Molecular Immunology Unit, Hospital Universitario Puerta de Hierro Majadahonda, 28222 Madrid, Spain, the [§]Cancer Research Center, Sanford-Burnham Medical Research Institute, La Jolla, California 92037, and the [¶]Vascular Mapping Center, Sanford-Burnham Medical Research Institute, University of California Santa Barbara, Santa Barbara, California 93106-9610

Tumor-associated cell surface antigens and tumor-associated vascular markers have been used as a target for cancer intervention strategies. However, both types of targets have limitations due to accessibility, low and/or heterogeneous expression, and presence of tumor-associated serum antigen. It has been previously reported that a mitochondrial/cell surface protein, p32/gC1qR, is the receptor for a tumor-homing peptide, LyP-1, which specifically recognizes an epitope in tumor cells, tumor lymphatics, and tumor-associated macrophages/myeloid cells. Using antibody phage technology, we have generated an anti-p32 human monoclonal antibody (2.15). The 2.15 antibody, expressed in single-chain fragment variable and in trimerbody format, was then characterized *in vivo* using mice grafted subcutaneously with MDA-MB-231 human breast cancers cells, revealing a highly selective tumor uptake. The intratumoral distribution of the antibody was consistent with the expression pattern of p32 in the surface of some clusters of cells. These results demonstrate the potential of p32 for antibody-based tumor targeting strategies and the utility of the 2.15 antibody as targeting moiety for the selective delivery of imaging and therapeutic agents to tumors.

The localization of tumors may be accomplished by any of several combinations including computed tomography, ultrasonography, gamma camera examination, and glucose consumption (1, 2). However, targeted localization of the tumors is preferred, mainly using specific probes that bind to tumor-associated cell surface antigens or to markers of angiogenesis expressed by endothelial cells or present in the surrounding extracellular matrix (3–6). Probes that bind to tumor-associated cell surface antigens have some drawbacks (7) such as the heterogeneous expression on the cell surface or the increased serum levels of the antigen as tumors grow, which may act as

a trap for the targeting agent. Angiogenesis related targets are readily accessible; however, the relatively low abundance of endothelial cells in tumor tissue makes the molecular imaging of tumor neovessels more challenging. Furthermore, angiogenesis may occur also in a physiological context, thus adding more complexity to the targeting.

With these limitations in mind, we hypothesized as an alternative target a marker selectively expressed in different compartments in the tumor area. One targeting agent specific for the tumor but not restricted to the tumor cells is the tumor homing peptide (LyP-1), which strongly and specifically accumulates in the tumor after systemic administration, localizing preferentially associated to lymphatic markers (8–10). LyP-1-binding protein was characterized as p32 (10), a multi-ligand and multicompartmental protein that has been independently identified in several contexts and has been named accordingly as SF2P32 (splicing factor SF2-associated protein; 11), HABP-1 (hyaluronic acid binding protein-1; 12), gC1qR (globular domain of C1q receptor; Ref. 13), or HIV TAP (Tat-associated protein; 14). Although p32 is primarily present in the mitochondria, it has been, under certain conditions (15), detected in different cellular compartments (nucleus, cellular surface, endoplasmic reticulum (13, 16–20)) and in different cell types (B lymphocyte (13)), platelets (21), neutrophils (22), eosinophils (23), endothelial cells (24), macrophages and dendritic cells (25, 26), or fibroblasts (27)). p32 has also been recently reported in the surface of tumor cells in hypoxic/nutrient-deprived areas as well as in the cell surface of a tumor-associated macrophage/myeloid cell subpopulation closely linked to tumor lymphatics (10).

In this work, we take advantage of the over-expression of the multicompartmental p32/gC1qR (hereafter referred to as p32) associated to tumors (in tumor cells, tumor lymphatics, and tumor-associated macrophages) to generate a human anti-p32 single-chain Fv (scFv)⁴ antibody (2.15). This antibody has shown to selectively target solid tumors *in vivo* both as a monovalent and trivalent antibody fragment.

EXPERIMENTAL PROCEDURES

Cells and Culture Conditions—All cells were from the ATCC. HEK-293 cells (human embryonic kidney epithelia; CRL-1573), and MDA-MB-231 (human breast adenocarcinoma; HTB-26) were grown in DMEM supplemented with

^{*} This work was supported by grants from the Ministerio de Ciencia e Innovación (BIO2008-03233), the Comunidad Autónoma de Madrid (S-BIO-0236-2006), the European Union (SUDOE-FEDER (IMMUNONET-SOE1/P1/E014; to L. A.-V.), and a grant from the U. S. Department of Defense Breast Cancer Program (to E. R.).

^[S] The on-line version of this article (available at <http://www.jbc.org>) contains supplemental Figs. 1 and 2.

¹ Supported by Comunidad Autónoma de Madrid/Fondo Social Europeo Training Grant FPI-000531.

² Supported a fellowship from the Susan Komen Foundation.

³ To whom correspondence should be addressed: Unidad de Inmunología Molecular, Hospital Universitario Puerta de Hierro, C/Manuel de Falla 1, 28222 Majadahonda, Madrid, Spain. Tel.: 34-911916764; Fax: 34-913160644; E-mail: lalvarezv.hpth@salud.madrid.org.

⁴ The abbreviations used are: scFv, single-chain fragment variable; NIP, 4-hydroxy-5-iodo-3-nitrophenyl; rhp32, recombinant human p32.

10% heat-inactivated FCS (all from Invitrogen) in humidified CO₂ (5%) incubator at 37 °C. U-937 cells (human histiocytic lymphoma; CRL-1593.2) and 4T1 cells (mouse breast tumor; CRL-2539) were maintained in RPMI supplemented with 10% FCS. Differentiation of the U-937 cells was induced for the indicated time intervals in fresh culture medium containing 5 nM phorbol myristic acid (Sigma-Aldrich).

Recombinant Proteins, Antibodies, Peptides, and Reactives—Recombinant human p32 (rhp32) was obtained from bacteria and purified by immobilized metal ion affinity chromatography. Recombinant mouse p32 was purchased from United States Biological (USBio). Purified rabbit polyclonal anti-full-length p32 was directed against the N terminus (amino acids 76–93). The mAbs used included mouse anti-p32 (60.11 and 74.5.2), anti-human c-Myc 9.E10, FITC-conjugated anti-human c-Myc 9.E10 (Abcam, Cambridge, UK); anti-human MHC class I molecules W6/32 (eBioscience, San Diego, CA); rat anti-mouse CD31 (BD Biosciences); HRP-conjugated anti-human c-Myc (Invitrogen); and HRP-conjugated anti-M13 bacteriophage (GE Healthcare). The polyclonal antibodies used included an Alexa Fluor 546-conjugated anti-rat IgG (Invitrogen); a phycoerythrin-conjugated goat anti-mouse IgG (Jackson ImmunoResearch Europe, Suffolk, UK); an HRP-conjugated donkey anti-rabbit IgG; and an HRP-conjugated sheep anti-mouse IgG (GE Healthcare). Trypsin, BSA, *o*-phenylenediamine dihydrochloride, and isopropyl-beta-D-thiogalactopyranoside were from Sigma-Aldrich. BSA was conjugated with 4-hydroxy-5-iodo-3-nitrophenyl (NIP; Sigma-Aldrich) in a molar ratio of 10:1 (NIP10-BSA) as described (28). Mouse EHS-laminin (LM111) was from (BD Biosciences).

Selection of scFv Phage Library on rhp32—Recombinant scFv phages (Griffin.1 library, Medical Research Council Cambridge; total diversity, $\sim 1.2 \times 10^9$) (29) were panned for binding on purified antigen (rhp32) as described (30) with slight modifications: immunotubes (Maxisorp, Nunc, Roskilde, Denmark) were coated overnight at 4 °C with 4 ml of rhp32 at a concentration of 10 μ g/ml in PBS. After washing twice with PBS, the tubes were blocked for 2 h at 37 °C with 4% BSA in PBS. Meanwhile, 10¹³ phages were blocked with 1 ml 4% BSA in PBS. Preblocked phages were added to the immunotube and incubated at room temperature with continuous rotation for 30 min, followed by 90 min of stationary incubation. The tubes were washed 10 times (in the first round of selection, 20 in the subsequent selections) with PBS containing 0.05% Tween 20 and then with PBS. Bound phages were eluted with 1 ml of trypsin (1 mg/ml in 50 mM Tris-HCl, pH 7.4, 1 mM CaCl₂) at room temperature with continuous rotation for 20 min. Eluted phages were recovered by infecting logarithmically growing ($A_{600} = 0.5$) *Escherichia coli* TG1 (K12, $\Delta(lac-pro)$, *supE*, *thi*, *hsdD5/F' traD36*, *proA*⁺*B*⁺, *lacI*^q, *lacZ* Δ M15 (31)) at 37 °C for 30 min. The infected cells were plated on LB agar supplemented with 100 μ g/ml ampicillin and 1% glucose and incubated overnight at 37 °C. This enriched library was grown on *E. coli* TG1 and rescued upon infection with the helper phage KM13 (32). Phages displaying scFv fragments were purified from the culture supernatant by precipitation with 20% PEG 6000 and 2.5 M NaCl and were

resuspended in sterile cold PBS with 15% glycerol for long term storage at –80 °C and for subsequent rounds of selection.

Screening of Selected Phages by ELISA—Single colonies were screened by ELISA to evaluate the frequency of phage displaying rhp32-binding scFv fragments as described (33). rhp32-binding phages were fingerprinted by amplifying the scFv using primers LMB3 and FdSeq1 (LMB3, 5'-CAG GAA ACA GCT ATG AC-3'; FdSeq1, 5'-GAA TTT TCT GTA TGA GG-3') followed by digestion with the frequent cutting enzyme BstN-I (New England Biolabs). Molecular characterization was completed by sequencing the variable regions using primers FOR_LinkSeq (V_H; 5'-GCC ACC TCC GCC TGA ACC-3') and pHEN_Seq (V_L; 5'-CTA TGC GGC CCC ATT CA-3'). Sequences were analyzed and aligned to the VBASE2 database (34) to learn the amino acids forming the loops in the complementarity-determining regions used and type of chains present.

Soluble Antibody Expression and Purification—Phage particles from selected clones were used to infect logarithmically growing ($A_{600} = 0.5$) *E. coli* HB2151 (nonsuppressor strain (K12, *ara*, $\Delta(lac-pro)$, *thi*/F' *proA*⁺*B*⁺, *lacI*^q Δ M15 (35)), and soluble scFv fragments were obtained as described (33). Purification was performed using the ÄKTAprime plus system (affinity step: HisTrap or HiTrap rProtein A FF columns (GE Healthcare) according to the manufacturer's protocol followed by gel filtration HiPrep 16/60 Sephacryl S100-HR) and checked by ELISA and SDS-PAGE. Either supernatant from isopropyl-beta-D-thiogalactopyranoside-induced HB2151 or purified scFv was used. Competition ELISA was performed as a standard ELISA but with a previous step of blockade using mAb; after blocking with 300 μ l 4% BSA in PBS at 37 °C for 1 h, wells were incubated with 100 μ l of a 20 μ g/ml solution of the appropriate reagent (mAb 60.11, mAb 74.5.2, or control mouse IgG1) for 1 h at room temperature and 30 rpm.

Flow Cytometry—To study the ability of the scFv to detect p32 on the cell surface, unstimulated mouse 4T1 cells and phorbol myristic acid-stimulated human U-937 cells (5 nM for 3, 6, or 12 h prior to the staining) were incubated with anti-p32 mAb (5 μ g/ml) or purified scFv (10 μ g/ml) and mAb 9E10 (4 μ g/ml) in 100 μ l for 45 min. After washing, the cells were treated with appropriate dilutions of phycoerythrin-conjugated goat anti-mouse IgG. The samples were analyzed with an EPICS XL (Coulter Electronics, Hialeah, FL).

Construction of Expression Vectors and Purification of Recombinant Multivalent Antibodies—The coding sequence of the scFv 2.15 was amplified using primers ClaI-2.15 (5'-TCA TCG ATG GAG GTG CAG CTG GTG GAG-3') and FdSeq1 and ligated into pCR2.1 TOPO. The ClaI/NotI-digested fragment was ligated into the ClaI/NotI pCR3.1-L36-NC1^{ES-}-digested plasmid (6) to obtain the pCR3.1–2.15-NC1^{ES-} plasmid. All constructs were verified by sequencing. The details about the plasmid pCEP4-B1.8-NC1^{ES-} containing the B1.8 (anti-NIP) trimerbody and the procedure to obtain purified trimerbodies can be found elsewhere (6).

Antibody Labeling with Cyanine 5—Purified antibodies (scFvs and trimerbodies) were labeled with the near-infrared cyanine 5 (Cy5) *N*-hydroxysuccinimide (NHS) esters (GE

Healthcare) according to the manufacturer's recommendations. One milliliter of the antibody solution (1 mg/ml) was conjugated with 0.1 ml of a 2 mg/ml Cy5 solution for 1 h in the dark at room temperature. Cy5-labeled recombinant antibodies were separated from unconjugated Cy5 dye by gel filtration on Sephadex G-25 Superfine HiTrap Desalting columns (PD-10 columns, GE Healthcare), and concentrated in 10,000 molecular weight cutoff (MWCO) Vivaspin 500 filter (Vivascience) to 1 mg/ml. The labeling ratio of Cy5 to antibody (Cy5:antibody) was calculated as described (36) and was close to 1:(1–2). The functionality of Cy5-labeled antibodies was verified by ELISA against specific antigen.

Infrared Immunophotodetection in Tumor-bearing Mice—Imaging was performed as described (6) with slight modifications. Briefly, wild-type MDA-MB-231 cells (2×10^6) were implanted into the mammary fat pad of 6-week-old female Hsd:athymic nude-*Foxn1*tm mice (Harlan Ibérica, Barcelona, Spain) maintained with a low manganese diet (ssniff Spezialdiäten GMBH, Soest, Germany). Nodule dimensions were used to calculate tumor volume using the formula: width² \times length \times 0.52. When tumors reached a volume of 0.2–0.4 cm³, mice were injected in the tail vein with 100 μ l Cy5-labeled antibody solution in PBS. Mice were imaged using the high resolution charge-coupled device cooled digital camera ORCA-2BT and Hokawo software (Hamamatsu Photonics France, Massy, France) under anesthesia. Three images were acquired for each experiment: a bright field image, a Cy5-specific image (emission, red light filter centered at 632.8 nm; optical filter, 665–680 nm), and an autofluorescence reference image (emission, blue light filtered at 470 nm; optical filter, 665–680 nm). Normalized reference autofluorescence was subtracted from the Cy5-specific image, and the resultant was tinted and merged with the bright-field image (tinted in the GFP blue-shifted spectral (448 nm) for better contrast) using the Hokawo software. Further editing included only cropping, resizing, and rotating the image for a better view of the picture. All mice were handled in accordance with the guidelines of the Hospital Universitario Puerta de Hierro Animal Care and Use Committee and performed in accordance with Spanish legislation.

Immunohistology—Tumors were removed after infrared imaging (2.5 h after i.v. injection), frozen in optimal cutting temperature (OCT) embedding medium (Sakura Tissue Tek, Alphen aan den Rijn, The Netherlands), and sectioned (4–7- μ m thickness) using the Leica CM1850 cryostat. Sections were incubated overnight with the primary antibodies (anti-Myc:FITC antibody (1:200) and rat anti-mouse CD31 (1:100)), followed by anti-rat secondary reagents (1:1000), and mounted by using VectaShield mounting media with 4',6-diamidino-2-phenylindole (Vector Laboratories, Burlingame, CA). Images were acquired using a confocal scanning inverted Leica AOBSP2-microscope (Leica Microsystems).

RESULTS

Isolation of Human Anti-rhp32 Antibodies by Panning a scFv Library—The Griffin.1 library was panned against affinity purified recombinant human p32 (rhp32) immobilized in Nunc immunotubes. The frequency of binding clones was

studied by ELISA after each round of selection. The percentage of binders was 20% after the first round and 60% after the second. BstNI fingerprinting of 24 selected clones (by rhp32/BSA ratio (in preliminary 96-well ELISA) > 3) indicated 16 different restriction patterns, which were later confirmed by DNA sequencing.

Biochemical Characterization of scFv Fragments—Ten different clones that were consistent binders were used in a phage-ELISA assay against rhp32 and other unrelated proteins (Fig. 1A). Most of the clones were highly specific for rhp32, showing almost no reactivity against other elements present in the selection process (plastic and BSA) or an unrelated protein (LM111). After expression as soluble scFv, although different from clone to clone, there was a significant reactivity of most of the scFvs against rhp32 (Fig. 1B). The binding of LyP-1 phage to p32 is inhibited by monoclonal antibody 60.11, which is directed against the C1q binding domain of p32 (10). To identify scFv sharing the epitope with mAb 60.11, four scFv fragments (1.6, 2.9, 2.15, and 2.25) were expressed using the nonsuppressor host *E. coli* HB2151 and purified from the supernatant by standard affinity chromatography procedures. The purified scFv fragments gave rise to a single protein band of expected mobility (Fig. 1C, inset); a competition ELISA was designed using either mAb 60.11 directed against p32 N-terminal amino acids 76–93 or 74.5.2 directed against amino acids 204–218 from the C terminus of p32. Preincubation with 60.11 but not 74.5.2 greatly diminished the binding of scFv 2.9 and 2.15, indicating overlapping, if not identical, epitopes (Fig. 1C). Due to the degree of cross-species conservation between rodents and humans, both in sequence and in the ability to bind C1q (37), we further investigated whether the selected scFv fragments were able to bind immobilized purified recombinant mouse p32. It was found that 2.9 gave no signal on recombinant mouse p32, whereas 2.15 gave comparable signals on both mouse and human p32 immobilized on plastic (Fig. 1D).

Reactivity of scFv Fragments to Cell Surface-expressed p32—The ability of the scFv fragments to recognize cell surface-expressed p32 was assessed by flow cytometry using freshly purified soluble scFv. Nonstimulated human U-937 cells reacted minimally with either anti-p32 mAbs (60.11 or 74.5.2) or scFv (2.9 or 2.15) (data not shown). In contrast, U-937 activation with phorbol myristic acid produced a consistently increased p32 expression as reflected by mAbs and scFv fragments. Staining with mAb 60.11 showed that ~50% of stimulated U-937 cells expressed p32 in the surface (Fig. 2A). Purified scFv fragments corresponding to 2.9 and 2.15, also stained the U-937 cells, and a slightly higher percentage of the cells were stained than with the 60.11 antibody (Fig. 2A). Surface staining of mouse 4T1 cells demonstrated the presence of p32 on the cell surface, in agreement with previous studies (10). The mAb 60.11 produced a small but consistent shift in flow cytometry analysis of live 4T1 cells (Fig. 2B). A similar staining pattern was observed in 4T1 cells incubated with the 2.15 scFv. In contrast, incubation of 4T1 cells with 2.9 scFv revealed no staining (Fig. 2B). Thus, further corroborating the ability of 2.15 to detect the mouse cell surface p32 to a extent similar to the mAb 60.11.

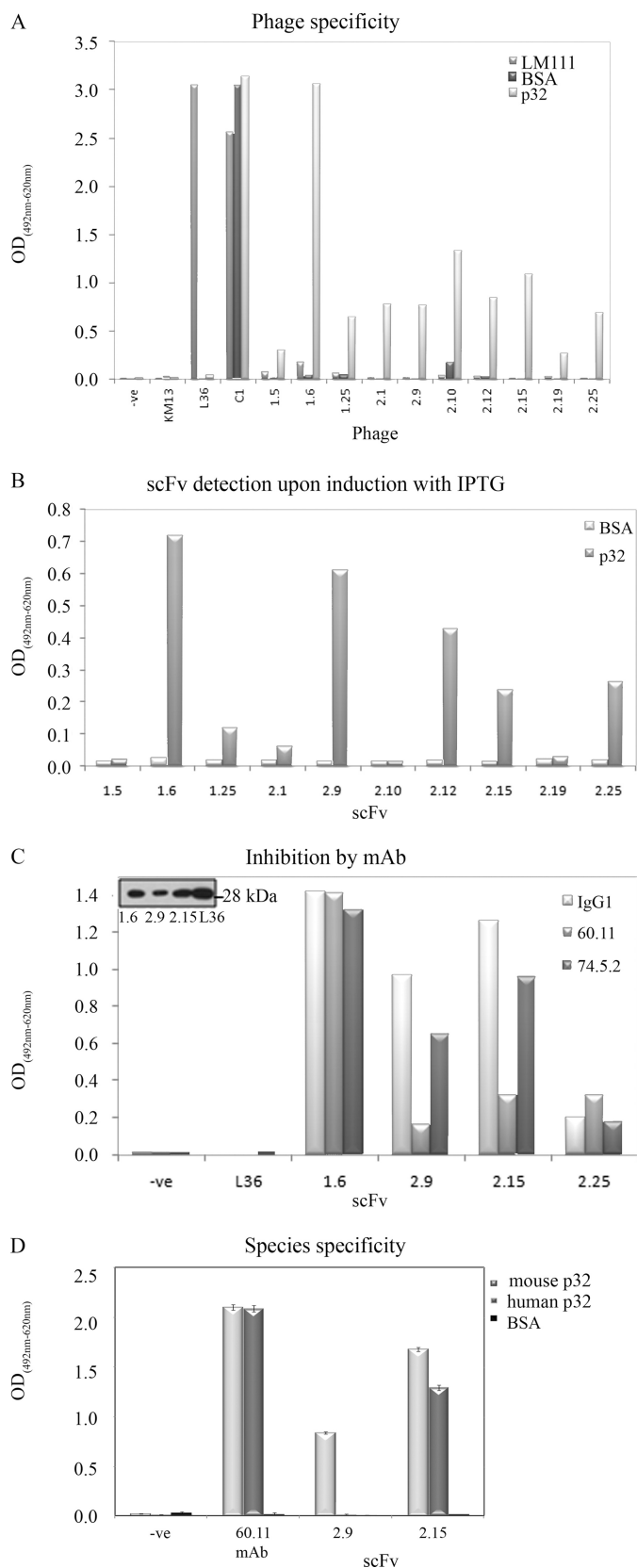


FIGURE 1. Characterization of anti-p32 phage-derived scFvs. A, specificity of phage scFv fragments from selected clones by ELISA. Reactivity was assessed against the following: elements present in the selection process (BSA); murine laminin-1 (LM111); and the target protein rhp32 (p32). Internal controls were as follows: L36 binds to LM111, but not other proteins; KM13, empty phage, does not bind any protein, whereas C1-phage binds

Tumor Targeting with Mono- and Trivalent Anti-p32

Antibodies—We selected the scFv 2.15 for *in vivo* targeting assays based on its inhibition by the 60.11 mAb as shown by ELISA on its ability to detect p32 expressed in the surface of both human and mouse cells as shown by flow cytometry. Control scFv antibodies included the following: B1.8 (anti-hapten NIP) and L36 (recognizes a conformational epitope of LM111 exposed in several solid tumor models (6)). Antibodies were labeled with the near-infrared fluorochrome Cy5 and injected in the tail vein of nude mice bearing MDA-MB-231 human xenografts. All of the antibodies showed a rapid renal clearance after i.v. injection, with peak signal intensity at 1–2 h and no detectable bladder signal at 24 h post-injection (Fig. 3B). The control scFv-B1.8 showed no detectable localization, whereas both 2.15 and L36 localized in the tumors (Fig. 3A). Maximum resolution was achieved at ~2h (Fig. 3A), when the ratio of the signal of the 2.15 and that of the B1.8 was near 7 (supplemental Fig. 1). *Ex vivo* imaging of the organs further confirms the specific accumulation of 2.15 and L36 in the tumors, while showing a similar uptake by the kidneys for all the antibodies (Fig. 3C). Staining of the tumors from mice that received the scFvs with FITC-conjugated anti-Myc mAb (to detect the injected scFv) and anti-CD31 mAb showed that most of the endothelial cells were negative for the scFv, and most of the scFv staining was dispersed in clusters of cells (Fig. 4, white arrow). However, some of the main vessels showed a distinct co-staining in the basal side of the cells (Fig. 4, arrowhead).

We have previously reported that the trimerbody format offers advantages over scFv molecules for tumor-targeting applications *in vivo* against a cell surface antigen or an extracellular matrix antigen (LM111) (6). We hypothesized that an anti-p32 trimerbody would also surpass its scFv counterpart for *in vivo* imaging. For this reason, the 2.15 scFv was assembled in the trimerbody format and expressed as a soluble secreted protein in human HEK-293 cells and purified from conditioned medium. The purification scheme yielded antibodies that were >95% pure by SDS-PAGE. The functionality of purified 2.15 trimerbody was demonstrated by ELISA against rhp32 (supplemental Fig. 2). Trimerbodies (2.15 and B1.8) were labeled with Cy5 and injected in the tail vein of nude mice bearing MDA-MB-231 human xenografts. Trimerbodies showed slower clearance than the corresponding scFvs (Fig. 5B). The control B1.8 trimerbody showed no detectable localization in the tumor, whereas a strong and selective accumulation was observed in the case of the 2.15 trimerbody. Maximum tumor uptake was detected at 2.5 and 5 h; the signal intensity decreased at 24 h although remained detectable for at least 48 h (Fig. 5A), whereas most of the systemic protein was eliminated at 24h (Fig. 5B).

BSA). Phage input was essentially the same for each clone and each ELISA as assessed by phage-ELISA. The y axis represents $A_{492\text{ nm}}$ corrected with $A_{620\text{ nm}}$ except otherwise stated. B, soluble scFv fragments retained their specificity after cloning in HB2151 and expression after induction with isopropyl- β -D-thiogalactopyranoside (IPTG). C, monoclonal antibody competition analyses for p32 binding. Binding of 2.9 and 2.15 to rhp32 was diminished after incubation with mAb 60.11, suggesting a common epitope for the scFv and mAb. Inset, Western blotting of the purified scFv. D, 2.15, but not 2.9, was able to bind to human and mouse p32. Error bars represent the standard error of the mean of three different experiments.

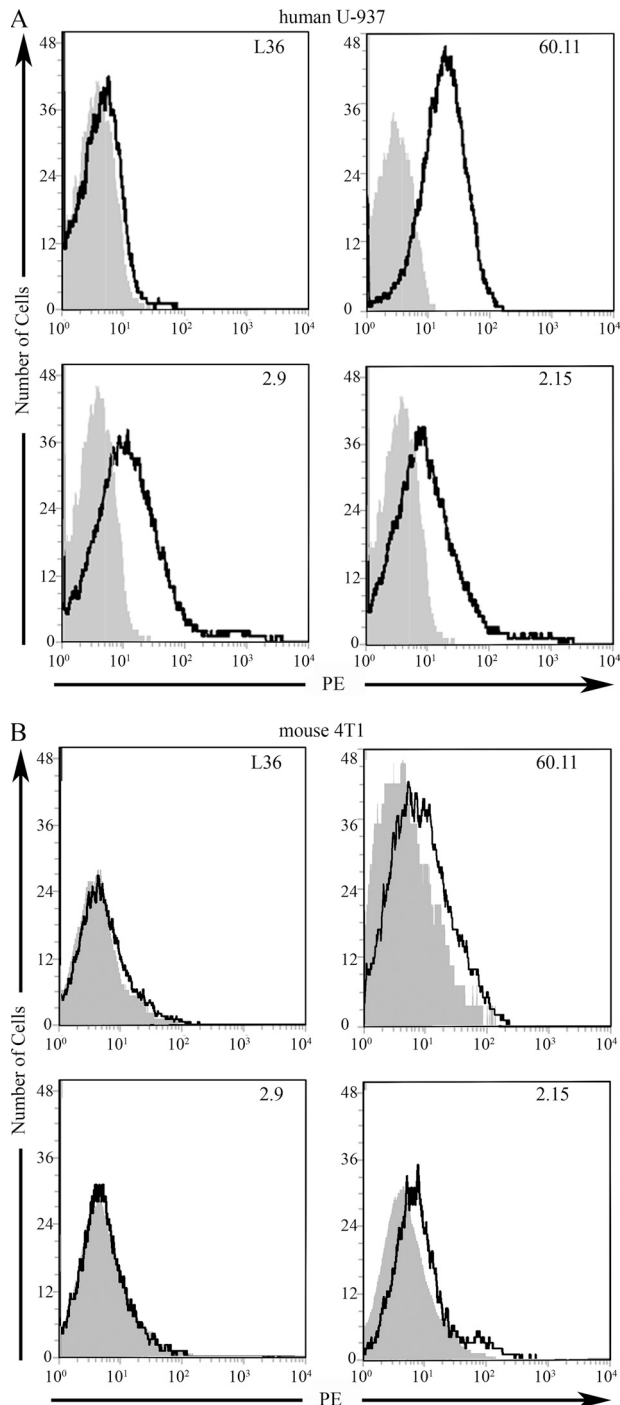


FIGURE 2. Reactivity of scFv fragments to cell surface expressed p32. A, binding of anti-p32 mAb and purified scFv fragments to phorbol myristic acid-stimulated human U-937 cells by flow cytometry. B, binding of anti-p32 mAb and purified scFv fragments to mouse 4T1 cells by flow cytometry. For purified scFv fragments, the bound scFv was detected with sequential incubations with 9E10 anti-Myc mAb and phycoerythrin (PE)-labeled goat anti-mouse IgG. FACScan histograms show the binding of each scFv clone (bold line) and the backgrounds of phycoerythrin-conjugated secondary antibodies (gray).

DISCUSSION

We have generated a human recombinant antibody against the multicompartmental protein p32/gClqR. We have demonstrated the ability of different formats of this antibody (scFv and trimerbody) to target solid tumors *in vivo*. These results

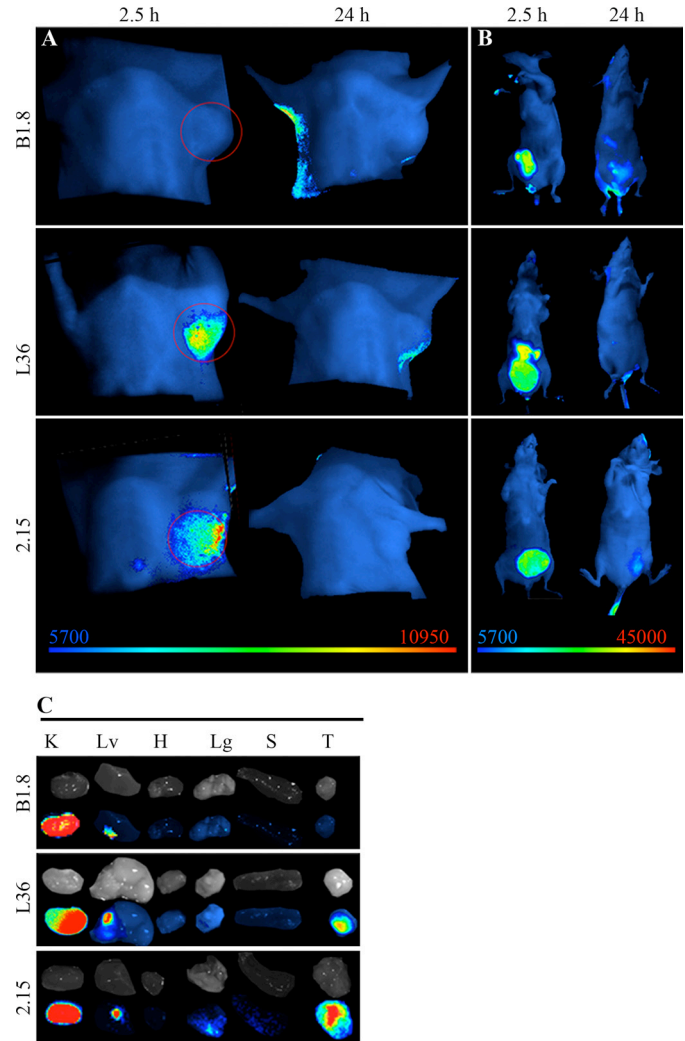


FIGURE 3. Targeting of fluorescently labeled anti-p32 scFv to human tumors. Near-infrared fluorescence imaging of nude mice bearing MDA-MB-231 human breast tumor xenografts. A, anti-hapten B1.8 did not localize in the tumor, whereas L36 and 2.15 showed a specific signal. A representative image of four mice is shown (2.15 scFv) and three mice (B1.8 and L36). B, ventral view shows similar accumulation of the scFv in the bladder. C, ex vivo imaging of the organs (kidney (K), liver (Lv), heart (H), lung (Lg), spleen (S), and tumor (T)) shows similar uptake of the Cy5-labeled reagents in the kidneys.

represent a new concept in tumor targeting. So far, antibody-based tumor targeting strategies have been based on tumor-associated cell surface antigens or tumor-associated vascular markers. Antibodies specific to tumor surface antigens, such as HER2-neu (38), carcinoembryonic antigen (39), or prostate-specific antigen (40), among others, have proven useful for *in vivo* localization of solid tumors. However, tumor surface antigens exhibit a high shedding profile and are dependent on tumor dedifferentiation or clonal proliferation. Antigens that are preferentially expressed in the tumor extracellular matrix may be better suited for tumor-targeting applications. In fact, several groups have demonstrated that antibodies specific to components of the extracellular matrix (EDB domain of fibronectin (41), domain C of tenascin C (42), and laminin (6, 33)) were capable of selective targeting of neo-vascular structures in solid tumors. However, it has been shown that antibodies against tumor-associated vascular

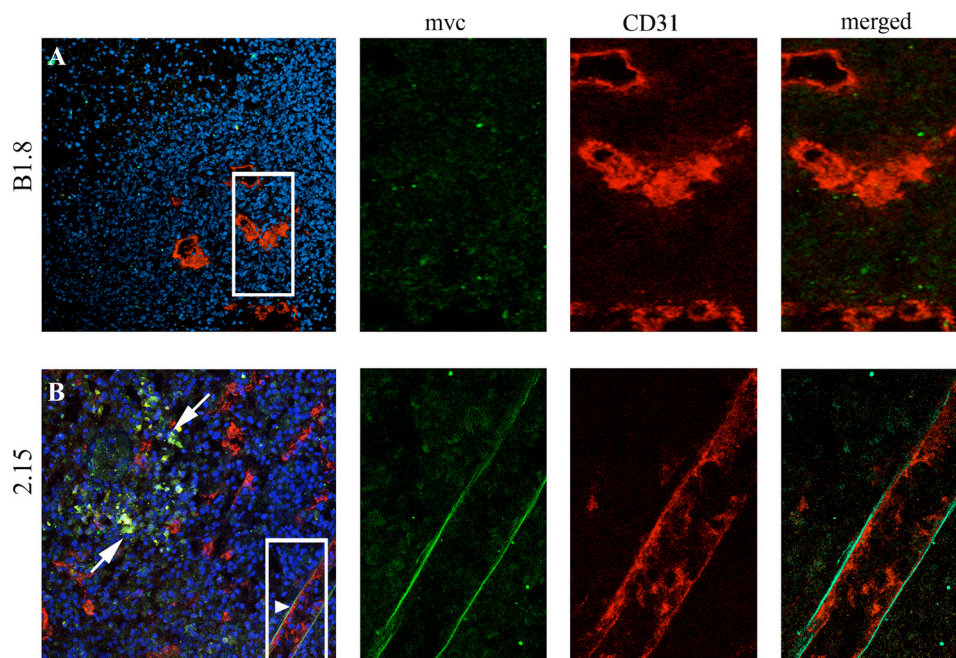


FIGURE 4. 2.15 scFv recognizes dispersed clusters of cells and the basal side of endothelial cells. After i.v. administration of the scFv, tumors were removed, embedded in OCT, and stained for myc (green) or for an endothelial marker (CD31, red). *A*, B1.8 does not localize in the tumor stroma. It does not localize either associated with vessels (right panel). *B*, 2.15 localizes in the tumor in dispersed clusters of cells (white arrow). A distinct co-staining occurred in the basal side of endothelial cells (arrowhead and right panel).

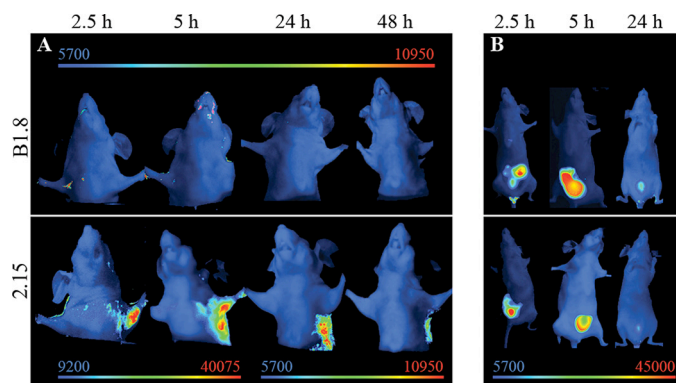


FIGURE 5. Targeting of fluorescently labeled anti-p32 trimerbody to human tumors. Near-infrared fluorescence imaging of nude mice bearing MDA-MB-231 human breast tumor xenografts. *A*, an anti-hapten B1.8 trimerbody did not localize in the tumor, whereas the 2.15 trimerbody showed a rapid (2.5 h) and sustained (up to 48 h) localization. Note the different scale bar for the early images. *B*, ventral view shows similar trimerbody accumulation in the bladder, as well as some elimination through the liver.

markers fail to accumulate in nonproliferating tumors (43). It is tempting to speculate that this can be a major problem in a proportion of patients as well as certain types of tumors with a very low growth rate.

Although p32 has been reported in the surface of several other cell types under certain circumstances (fibroblasts, neutrophils, endothelial cells, platelets, etc. (15)), the majority of the protein is cytoplasmic and is detectable after permeabilization of the cell membrane (44). Nonetheless, certain cells are able to translocate and release the protein, which can result in the modification of a number of cellular and vascular protein responses (15). The role of cell surface p32 in the tumor remains unclear; however, the unique expression pattern of p32 in tumor cells, tumor lymphatics, and tumor-associ-

ated macrophages/myeloid cells makes p32 an ideal target for the diagnosis and therapy of cancer. In fact, it has been reported that p32/gC1qR is the receptor for a tumor-homing peptide, LyP-1. The LyP-1 peptide has been shown to localize in the tumor lymphatics (9), and to effectively target nanoparticles to the tumor (45). In this work, we confirmed that systemically administered 2.15 scFv penetrates the tumor covering a broad population of cells but in a pattern distinct from that of the LyP-1 peptide (8, 9). Although LyP-1 is probably processed as a CendR peptide upon binding to p32 and thus can actively penetrate the tissue (46, 47), the antibody may remain partially bound to the p32 readily accessible from the lumen of the blood vessels and also reach some clusters of cells (probably macrophages) in the stroma nearby.

Multimerization of scFv constructs has important advantages for tumor-targeting applications. Trimerbodies are intermediate-sized molecules that exhibit high stability under physiological conditions and enhanced avidity for the target owing to the trivalent structure (6, 48). In fact, we report that the 2.15 antibody in a trimerbody format stained the tumor more brightly than the 2.15 scFv at all time points. Anti-p32 trimerbody localized rapidly and specifically in the tumors. The tumor uptake reached a maximum at 2.5–5 h post injection and slowly washed out over time. Fluorescence was still detectable in the tumor 48 h after the trimerbody inoculation.

In summary, we have demonstrated that the human anti-p32 antibody 2.15 can selectively localize tumors *in vivo*. These results illustrate the potential of this new antibody for imaging and therapeutic applications and suggest that p32 might be universal target for cancer targeting.

Acknowledgments—We thank Drs. Paloma Sánchez-Mateos and Rafael Samaniego for help with the confocal microscope.

REFERENCES

- Jacobsson, H., Wallin, G., Werner, S., and Larsson, S. A. (1994) *Eur. J. Nucl. Med.* **21**, 582–586
- Nguyen, B. D., Roarke, M. C., Karstaedt, P. J., Ingui, C. J., and Ram, P. C. (2009) *Curr. Probl. Diagn. Radiol.* **38**, 68–83
- Vogel, C. A., Bischof-Delaloye, A., Mach, J. P., Pèlerin, A., Hardman, N., Delaloye, B., and Buchegger, F. (1993) *Br. J. Cancer* **68**, 684–690
- Sanz, L., Kristensen, P., Blanco, B., Facticeau, S., Russell, S. J., Winter, G., and Alvarez-Vallina, L. (2002) *Gene Ther.* **9**, 1049–1053
- Steffen, A. C., Orlova, A., Wikman, M., Nilsson, F. Y., Ståhl, S., Adams, G. P., Tolmachev, V., and Carlsson, J. (2006) *Eur. J. Nucl. Med. Mol. Imaging* **33**, 631–638
- Cuesta, A. M., Sánchez-Martín, D., Sanz, L., Bonet, J., Compte, M., Kremer, L., Blanco, F. J., Oliva, B., and Alvarez-Vallina, L. (2009) *PLoS ONE* **4**, e5381
- Buchsbaum, G. M., Moll, C., and Duecy, E. E. (2004) *Int. Urogynecol. J. Pelvic. Floor Dysfunct.* **15**, 432–433
- Laakkonen, P., Akerman, M. E., Biliran, H., Yang, M., Ferrer, F., Karpanen, T., Hoffman, R. M., and Ruoslahti, E. (2004) *Proc. Natl. Acad. Sci. U.S.A.* **101**, 9381–9386
- Laakkonen, P., Porkka, K., Hoffman, J. A., and Ruoslahti, E. (2002) *Nat. Med.* **8**, 751–755
- Fogal, V., Zhang, L., Krajewski, S., and Ruoslahti, E. (2008) *Cancer Res.* **68**, 7210–7218
- Krainer, A. R., Mayeda, A., Kozak, D., and Binns, G. (1991) *Cell* **66**, 383–394
- Gupta, S., Batchu, R. B., and Datta, K. (1991) *Eur. J. Cell Biol.* **56**, 58–67
- Ghebrehewet, B., Lim, B. L., Peerschke, E. I., Willis, A. C., and Reid, K. B. (1994) *J. Exp. Med.* **179**, 1809–1821
- Yu, L., Loewenstein, P. M., Zhang, Z., and Green, M. (1995) *J. Virol.* **69**, 3017–3023
- Eggleton, P., Tenner, A. J., and Reid, K. B. (2000) *Clin. Exp. Immunol.* **120**, 406–412
- Dedio, J., and Müller-Esterl, W. (1996) *FEBS Lett.* **399**, 255–258
- Braun, L., Ghebrehewet, B., and Cossart, P. (2000) *EMBO J.* **19**, 1458–1466
- Kittleson, D. J., Chianese-Bullock, K. A., Yao, Z. Q., Braciale, T. J., and Hahn, Y. S. (2000) *J. Clin. Invest.* **106**, 1239–1249
- Mahdi, F., Shariat-Madar, Z., Todd, R. F., 3rd, Figueroa, C. D., and Schmaier, A. H. (2001) *Blood* **97**, 2342–2350
- Mahdi, F., Madar, Z. S., Figueroa, C. D., and Schmaier, A. H. (2002) *Blood* **99**, 3585–3596
- Peerschke, E. I., Reid, K. B., and Ghebrehewet, B. (1994) *J. Immunol.* **152**, 5896–5901
- Eggleton, P., Ghebrehewet, B., Sastry, K. N., Coburn, J. P., Zaner, K. S., Reid, K. B., and Tauber, A. I. (1995) *J. Clin. Invest.* **95**, 1569–1578
- Kuna, P., Iyer, M., Peerschke, E. I., Kaplan, A. P., Reid, K. B., and Ghebrehewet, B. (1996) *Clin. Immunol. Immunopathol.* **81**, 48–54
- Peerschke, E. I., Smyth, S. S., Teng, E. I., Dalzell, M., and Ghebrehewet, B. (1996) *J. Immunol.* **157**, 4154–4158
- Steinberger, P., Szekeres, A., Wille, S., Stöckl, J., Selenko, N., Prager, E., Staffler, G., Madic, O., Stockinger, H., and Knapp, W. (2002) *J. Leukocyte Biol.* **71**, 133–140
- Vegh, Z., Goyarts, E. C., Rozengarten, K., Mazumder, A., and Ghebrehewet, B. (2003) *International Immunopharmacol.* **3**, 345–357
- Oiki, S., and Okada, Y. (1988) *J. Immunol.* **141**, 3177–3185
- Hawkins, R. E., Russell, S. J., and Winter, G. (1992) *J. Mol. Biol.* **226**, 889–896
- Griffiths, A. D., Williams, S. C., Hartley, O., Tomlinson, I. M., Waterhouse, P., Crosby, W. L., Kontermann, R. E., Jones, P. T., Low, N. M., and Allison, T. J. (1994) *EMBO J.* **13**, 3245–3260
- Nissim, A., Hoogenboom, H. R., Tomlinson, I. M., Flynn, G., Midgley, C., Lane, D., and Winter, G. (1994) *EMBO J.* **13**, 692–698
- Gibson, T. (1984) *Studies in the Epstein-Barr Virus Genome*, Ph.D. thesis, MRC Laboratory of Molecular Biology, University of Cambridge, Cambridge, UK
- Kristensen, P., and Winter, G. (1998) *Folding Des.* **3**, 321–328
- Sanz, L., Kristensen, P., Russell, S. J., Ramirez García, J. R., and Alvarez-Vallina, L. (2001) *Cancer Immunol. Immunother.* **50**, 557–565
- Retter, I., Althaus, H. H., Münch, R., and Müller, W. (2005) *Nucleic Acids Res.* **33**, D671–674
- Carter, P., Bedouelle, H., and Winter, G. (1985) *Nucleic Acids Res.* **13**, 4431–4443
- Birchler, M., Neri, G., Tarli, L., Halin, C., Viti, F., and Neri, D. (1999) *J. Immunol. Methods* **231**, 239–248
- Lynch, N. J., Reid, K. B., van den Berg, R. H., Daha, M. R., Leigh, L. A., Ghebrehewet, B., Lim, W. B., and Schwaebler, W. J. (1997) *FEBS Lett.* **418**, 111–114
- Harries, M., and Smith, I. (2002) *Endocr. Relat. Cancer* **9**, 75–85
- Begent, R. H., Verhaar, M. J., Chester, K. A., Casey, J. L., Green, A. J., Napier, M. P., Hope-Stone, L. D., Cushen, N., Keep, P. A., Johnson, C. J., Hawkins, R. E., Hilson, A. J., and Robson, L. (1996) *Nat. Med.* **2**, 979–984
- McDevitt, M. R., Barendswaard, E., Ma, D., Lai, L., Curcio, M. J., Sgouros, G., Ballangrud, A. M., Yang, W. H., Finn, R. D., Pellegrini, V., Geerlings, M. W., Jr., Lee, M., Brechbiel, M. W., Bander, N. H., Cordon-Cardo, C., and Scheinberg, D. A. (2000) *Cancer Res.* **60**, 6095–6100
- Neri, D., Carnemolla, B., Nissim, A., Leprini, A., Querzè, G., Balza, E., Pini, A., Tarli, L., Halin, C., Neri, P., Zardi, L., and Winter, G. (1997) *Nat. Biotechnol.* **15**, 1271–1275
- Silacci, M., Brack, S. S., Späth, N., Buck, A., Hillinger, S., Arni, S., Weder, W., Zardi, L., and Neri, D. (2006) *Protein Eng. Des. Sel.* **19**, 471–478
- Birchler, M. T., Thuerl, C., Schmid, D., Neri, D., Waibel, R., Schubiger, A., Stoeckli, S. J., Schmid, S., and Goerres, G. W. (2007) *Otolaryngol. Head Neck Surg.* **136**, 543–548
- van den Berg, R. H., Prins, F., Faber-Krol, M. C., Lynch, N. J., Schwaebler, W., van Es, L. A., and Daha, M. R. (1997) *J. Immunol.* **158**, 3909–3916
- Karmali, P. P., Kotamraju, V. R., Kastantin, M., Black, M., Missirlis, D., Tirrell, M., and Ruoslahti, E. (2009) *Nanomedicine* **5**, 73–82
- Ruoslahti, E., Bhatia, S. N., and Sailor, M. J. (2010) *J. Cell Biol.* **188**, 759–768
- Teesalu, T., Sugahara, K. N., Kotamraju, V. R., and Ruoslahti, E. (2009) *Proc. Natl. Acad. Sci. U.S.A.* **106**, 16157–16162
- Cuesta, A. M., Sainz-Pastor, N., Bonet, J., Oliva, B., and Alvarez-Vallina, L. (2010) *Trends Biotechnol.* **28**, 355–362

ORIGINAL ARTICLE

Transtumoral targeting enabled by a novel neuropilin-binding peptide

L Roth^{1,2}, L Agemy^{1,2}, VR Kotamraju^{1,2}, G Braun³, T Teesalu^{1,2}, KN Sugahara², J Hamzah^{1,2} and E Ruoslahti^{1,2}¹Sanford-Burnham Medical Research Institute, Vascular Mapping Laboratory, Center for Nanomedicine, University of California, Santa Barbara, CA, USA; ²Sanford-Burnham Medical Research Institute, Cancer Research Center, La Jolla, CA, USA and ³Institute for Collaborative Biotechnologies, University of California, Santa Barbara, CA, USA

We have recently described a class of peptides that improve drug delivery by increasing penetration of drugs into solid tumors. These peptides contain a C-terminal C-end Rule (CendR) sequence motif (R/K)XX(R/K), which is responsible for cell internalization and tissue-penetration activity. Tumor-specific CendR peptides contain both a tumor-homing motif and a cryptic CendR motif that is proteolytically unmasked in tumor tissue. A previously described cyclic tumor-homing peptide, LyP-1 (sequence: CGNKRTRGC), contains a CendR element and is capable of tissue penetration. We use here the truncated form of LyP-1, in which the CendR motif is exposed (CGNKRTR; tLyP-1), and show that both LyP-1 and tLyP-1 internalize into cells through the neuropilin-1-dependent CendR internalization pathway. Moreover, we show that neuropilin-2 also binds tLyP-1 and that this binding equally activates the CendR pathway. Fluorescein-labeled tLyP-1 peptide and tLyP-1-conjugated nanoparticles show robust and selective homing to tumors, penetrating from the blood vessels into the tumor parenchyma. The truncated peptide is more potent in this regard than the parent peptide LyP-1. tLyP-1 furthermore improves extravasation of a co-injected nanoparticle into the tumor tissue. These properties make tLyP-1 a promising tool for targeted delivery of therapeutic and diagnostic agents to breast cancers and perhaps other types of tumors.

Oncogene advance online publication, 19 December 2011; doi:10.1038/nc.2011.537

Keywords: tumor homing; tumor penetration; breast cancer; nanoparticles

Introduction

Targeted delivery of therapeutic or diagnostic agents to tumors constitutes a major goal in cancer treatment. By increasing the amount of a drug reaching the tumor, the efficacy is improved while side effects are reduced. This strategy relies on the identification of the molecular

signature of tumor vessels, and development of specific affinity ligands to carry payloads to the tumor (Ruoslahti, 2002a,b). Nanoparticles can be used to further improve drug delivery and efficacy by incorporating multiple functions and increasing the payload (Ruoslahti *et al.*, 2010). However, dysfunctional tumor blood vessels and high interstitial pressure tend to prevent penetration of drugs and nanoparticles into the tumor tissue, limiting the efficacy of the treatments (Jain, 1999; Heldin *et al.*, 2004).

We have recently described a technology that provides a way to overcome the limited tissue penetration. C-end Rule (CendR) peptides induce extravasation and tissue penetration via a mechanism that involves cell internalization (Sugahara *et al.*, 2009, 2010; Teesalu *et al.*, 2009). CendR peptides are defined by the presence of the motif (R/K)XX(R/K) (X represents any amino acid), which has to be at the C-terminus for the cell- and tissue-penetration activity. The receptor for the CendR motif was shown to be neuropilin-1 (NRP1) (Teesalu *et al.*, 2009).

NRP1 is a modular transmembrane protein previously identified as a receptor for various forms and isoforms of VEGF (vascular endothelial growth factor) and members of the class 3 semaphorin family (Takagi *et al.*, 1987; He and Tessier-Lavigne, 1997; Kolodkin *et al.*, 1997; Soker *et al.*, 1998). Neuropilin-2 (NRP2), the second member of the neuropilin family, exhibits sequence and structure homology with NRP1, and shares common ligands, among them VEGFA₁₆₅ (Chen *et al.*, 1997; Kolodkin *et al.*, 1997; Gluzman-Poltorak *et al.*, 2000). However, there are also ligands that show selective affinity for one or the other NRP (Chen *et al.*, 1997; Gluzman-Poltorak *et al.*, 2000). Moreover, NRP1 and NRP2 display different expression patterns, with NRP2 (but not NRP1) overexpressed in tumor lymphatics (Caunt *et al.*, 2008). In the CendR pathway, NRP1 appears to be essential for cell internalization and tissue penetration (Teesalu *et al.*, 2009), whereas the role of NRP2 has not been investigated.

Binding to NRP1 requires an exposed C-terminal CendR motif, and peptides with an embedded binding motif in their sequence depend on proteolytic cleavage to activate the CendR internalization pathway. The recently described tumor-penetrating peptide iRGD follows this two-step mechanism. Indeed, iRGD contains an RGD motif for recruitment to angiogenic

Correspondence: Professor E Ruoslahti, Sanford-Burnham Medical Research Institute, UCSB Campus, Biology II Building, Room #3119, University of California, Santa Barbara, CA 93106-9610, USA.

E-mail: ruoslahti@sanfordburnham.org

Received 3 September 2011; revised and accepted 18 October 2011

blood vessels and a cryptic CendR motif that is proteolytically unmasked in tumor to trigger extravasation and tissue penetration (Sugahara *et al.*, 2009, 2010). As a result of the proteolytic cleavage, iRGD loses its affinity for the integrins, acquires NRP1-binding capacity and induces extravasation (Sugahara *et al.*, 2009). Importantly, co-injected drugs or particles penetrate inside the tumor parenchyma along with iRGD, allowing an increase of treatment efficacy in a number of different cancer models (Sugahara *et al.*, 2010).

Similar to iRGD, LyP-1 is a tumor-homing cyclic nonapeptide, which contains a cryptic CendR motif (sequence: CGNKRTRGC), and was identified in our laboratory by phage display (Laakkonen *et al.*, 2002). LyP-1 homes to tumor lymphatics, tumor cells and tumor macrophages by specifically binding to its receptor p32, a mitochondrial protein expressed on the surface of these cells (Laakkonen *et al.*, 2002; Fogal *et al.*, 2008). LyP-1 also homes to atherosclerotic plaques and penetrates into their interior (Hamzah *et al.*, 2011; Uchida *et al.*, 2011). The presence of the cryptic CendR motif suggests the possibility of secondary binding to NRP1 (and perhaps to NRP2 in the lymphatics) and involvement of the CendR pathway. This hypothesis is supported by previous studies showing that LyP-1 is able to extravasate and penetrate the tumor parenchyma (Laakkonen *et al.*, 2002; von Maltzahn *et al.*, 2008; Karmali *et al.*, 2009).

Here, we investigate LyP-1 internalization pathway, and characterize a new peptide derived from LyP-1, with an active CendR element for tumor targeting.

Results

LyP-1 is a cryptic CendR peptide

In order to investigate the role of the CendR motif in LyP-1 peptide, we tested the binding of phage displaying the predicted active CendR fragment CGNKRTR (tLyP-1, for truncated LyP-1) and other truncated forms of LyP-1 to cultured tumor cells. We used DU145 prostate carcinoma cells, because they express only NRP1, and not NRP2 (Supplementary Figures S1A and S2A). As these peptides could have other receptors on the DU145 cells, we used inhibition of cell binding by a function-blocking anti-NRP1 antibody as an indicator of NRP1 dependence of phage binding. The antibody inhibited the cell binding of the phage expressing RPAPAR, the prototypic CendR peptide, by about 70% (Figure 1a). A similar degree of inhibition was obtained for the phage tLyP-1. The NRP1 antibody did not significantly inhibit the binding of the other truncated forms of LyP-1 (Figure 1b). Thus, a single or double basic residue at the C-terminus, as in CGNK or CGNKR, was not enough to confer significant ability to bind to NRP1. CGNKRTRG showed a mild reproducible decrease in DU145 cell binding upon anti-NRP1 treatment, suggesting that the presence of the glycine residue C-terminal of the CendR motif may be compatible with NRP1 binding. This is supported by recent modeling studies showing that glycine-containing peptides (G₇, G₃RG₃ and G₄RG₂) were able to dock in NRP1-binding pocket without major deformation of the receptor structure (Haspel *et al.*, 2011). In contrast, the

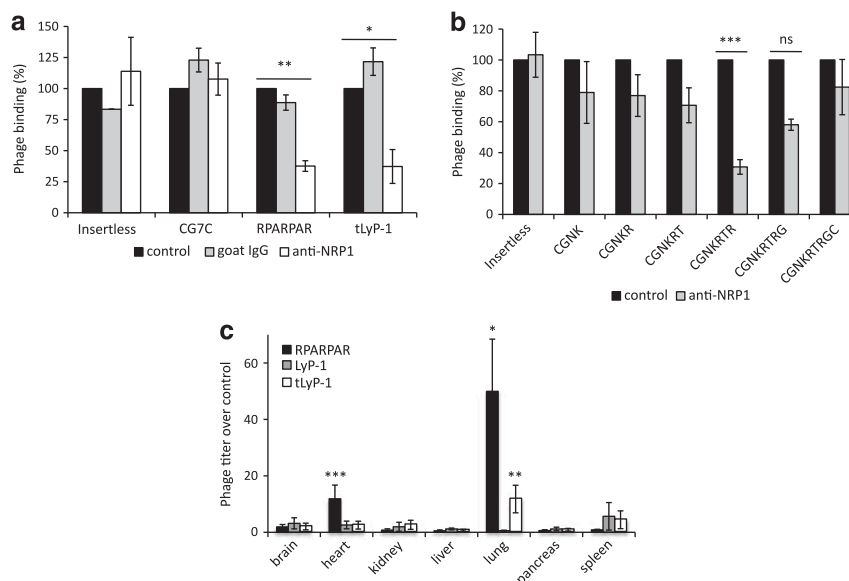


Figure 1 CGNKRTR is the active CendR element of LyP-1. (a) DU145 cells were incubated with phage at 4 °C to assess NRP1 binding. Ligand-blocking anti-NRP1 inhibited binding of both CGNKRTR and RPAPAR phage, whereas goat IgG had no effect. Insertless and CG7C control phage binding was not inhibited. Binding is expressed as percentage of binding in control conditions (mean \pm s.e.m.; $n = 4$ /group; * $P < 0.05$; ** $P < 0.01$). (b) DU145 cells were incubated with various truncated versions of LyP-1 phage at 4 °C to determine the minimum essential element for NRP1 binding. Ligand-blocking anti-NRP1 inhibited binding of CGNKRTR but not of the other phage. Insertless phage binding was not inhibited. Binding is expressed as percentage of binding in control conditions (mean \pm s.e.m.; $n = 5$ /group; *** $P < 0.001$; ns, not significant). (c) Tissue distribution of intravenously injected phage after 15 min circulation in normal mice. tLyP-1 phage significantly accumulated in the lungs. The titer of phage is expressed as fold over control insertless phage (mean \pm s.e.m.; $n = 3$ /group; * $P < 0.05$; ** $P < 0.01$; *** $P < 0.001$).

binding of full-length LyP-1 to the cells was not inhibited by the anti-NRP1, suggesting that the peptide has to be processed into its CendR form to be able to bind to NRP1.

We next analyzed the distribution of intravenously administered tLyP-1 phage in normal mice after 15 min circulation, and observed that it showed significant accumulation in the lungs (Figure 1c). This finding agrees with previously described accumulation of CendR phage in the lungs, presumably because it is the first vascular bed encountered by intravenously injected substances (Teesalu *et al.*, 2009). Taken together, the binding and inhibition results, and the *in-vivo* phage distribution strongly suggest that tLyP-1 is an active CendR peptide.

NRP1 binds tLyP-1 phage and mediates its internalization

We next tested the binding of tLyP-1 to purified NRP1. The tLyP-1 phage bound to immobilized NRP1 about 120 times more than insertless control phage,

whereas phage expressing intact LyP-1 showed no binding (Figure 2a). RPARPAR phage exhibited a 280-fold binding ratio over the control phage, suggesting a higher affinity for NRP1 than tLyP-1.

RPARPAR-displaying phage was originally shown to strongly bind to and internalize into cultured PPC1 prostate carcinoma cells (Teesalu *et al.*, 2009), which express high levels of NRP1 (Supplementary Figure S1A). We found that tLyP-1 phage had a similar activity, whereas LyP-1 phage did not interact with the PPC1 cells (Figure 2b).

As observed with RPARPAR phage, all or almost all the PPC1 cells were positive for tLyP-1 phage uptake. Moreover, tLyP-1 phage co-localized with NRP1 in vesicular structures inside the cells, suggesting that the two proteins co-internalized upon interaction (Figure 2c, arrows). tLyP-1 internalization into the PPC1 cells was inhibited in a dose-dependent manner by oligomeric RPARPAR peptide (Figure 2d), further showing that tLyP-1 internalization follows the CendR pathway.

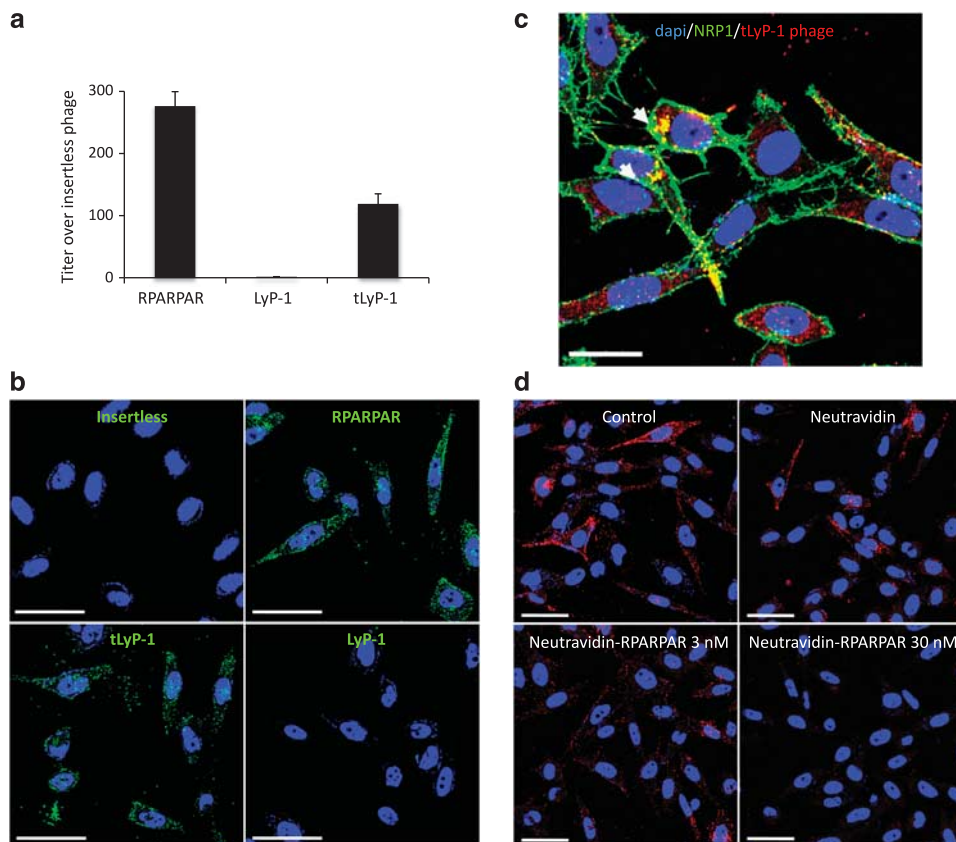


Figure 2 NRP1 binds tLyP-1 and mediates its internalization. (a) Purified NRP1 was coated on microtiter wells and the binding of insertless, RPARPAR, LyP-1 and tLyP-1 phage was tested. Binding is expressed as fold over control phage (RPARPAR/insertless = 276, LyP-1/insertless = 1.6, tLyP-1/insertless = $119 \pm \text{s.e.m.}$, $n = 3/\text{group}$). (b) Confocal microscope images of PPC1 cells incubated in the presence of 10^9 p.f.u. of insertless, RPARPAR, LyP-1 or tLyP-1 phage. Phage clones were detected by staining with anti-T7 phage polyclonal antibody (green). Nuclei were stained with DAPI (blue) (original magnification, $\times 40$; scale bars, $50 \mu\text{m}$). (c) Confocal microscope image of PPC1 cells incubated with tLyP-1 phage (red). Cells were co-stained for NRP1 (green) and nuclei were stained with DAPI (blue). Arrowheads indicate co-localization between tLyP-1 phage and NRP1 (original magnification, $\times 40$; scale bar, $25 \mu\text{m}$). (d) After 30 min pre-incubation with increasing concentrations of NA-RPARPAR peptide, PPC1 cells were incubated with tLyP-1 phage (red) for 2 h. Nonconjugated NA was used as a control. Nuclei were stained with DAPI (blue). Cells were analyzed by confocal microscopy (original magnification, $\times 40$; scale bars, $50 \mu\text{m}$).

NRP2 binds CendR peptides and mediates their internalization

NRP2 involvement in the CendR pathway has not been addressed. Given the homology between NRP1 and NRP2, and the similarities in LyP-1 homing and NRP2 tissue and cell distribution, we hypothesized that NRP2 could also be a CendR receptor. Indeed, tLyP-1 phage bound to purified NRP2 about eight times more than insertless phage (Figure 3a). As observed for NRP1 binding, RPAPAR phage exhibited higher level of binding to NRP2 than tLyP-1 phage (binding ratios over control = 29 versus 8). The binding of both peptides was higher to NRP1 than to NRP2, suggesting that CendR peptides preferentially bind to NRP1. LyP-1 phage did not bind to NRP2 (binding ratio over control = 0.6). We next studied binding and internalization of phage clones into MDA-MB-435 breast carcinoma cells that express only NRP2, and not NRP1 (Supplementary Figure S1A). tLyP-1 phage bound and internalized into these cells, where it co-localized with NRP2 (Supplementary Figure S2B; Figure 3b, arrows). tLyP-1 phage internalization into MDA-MB-435 cells was lower than into PPC1 cells, possibly due to the weaker affinity for NRP2 than for NRP1, or/and to

lower total NRP expression in the MDA-MB-435 cells. Using a function-blocking antibody against NRP2, we confirmed that tLyP-1 phage directly bound to NRP2 in MDA-MB-435 cells (Figure 3c). The anti-NRP2 antibody also inhibited RPAPAR phage binding, and oligomeric RPAPAR peptide blocked the binding and internalization of phage tLyP-1 in the cells, further demonstrating the role of NRP2 in the CendR pathway (Figure 3d).

LyP-1 internalization uses the CendR pathway

The MDA-MB-435 cells express the cell surface LyP-1 primary receptor p32, and LyP-1 internalizes into these cells (Fogal *et al.*, 2008). To test whether internalization of tLyP-1 and LyP-1 could occur through p32, we explored tLyP-1 capacity to bind to this receptor. A saturation assay performed with fluorescein-labeled peptides (FAM-peptides) showed low binding of tLyP-1 to purified p32, whereas robust binding was seen with FAM-LyP-1 (Supplementary Figure S3). Moreover, affinity chromatography of 4T1 breast tumor extracts on tLyP-1 revealed no binding of p32 to the tLyP-1 affinity matrix (data not shown). Thus, only the intact LyP-1 peptide binds to p32.

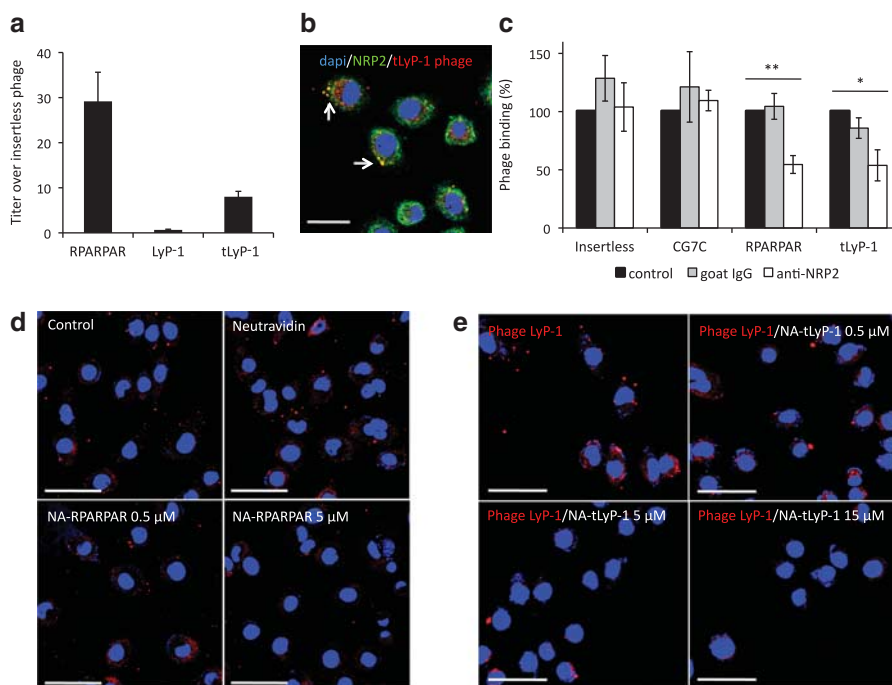


Figure 3 NRP2 binds tLyP-1 and mediates its internalization. **(a)** Purified NRP2 was coated on microtiter wells and the binding of insertless, RPAPAR, LyP-1 and tLyP-1 phage was tested. Binding is expressed as fold over control phage (RPAPAR/insertless = 29, LyP-1/insertless = 0.6, tLyP-1/insertless = 8 \pm s.e.m., $n = 3$ /group). **(b)** Confocal microscope image of MDA-MB-435 cells cultured for 2 h in presence of tLyP-1 phage (red). Cells were co-stained for NRP2 (green) and nuclei were stained with DAPI (blue). Arrowheads indicate co-localization between tLyP-1 phage and NRP2 (original magnification, $\times 40$, scale bar, 25 μ m). **(c)** MDA-MB-435 cells were incubated with phage at 4 $^{\circ}$ C to assess NRP2 binding. Ligand-blocking anti-NRP2 inhibited binding of both CGNKRT and RPAPAR phage, whereas goat IgG had no effect. Insertless and CG7C control phage binding was not inhibited. Binding is expressed as percentage of binding in control conditions (mean \pm s.e.m.; $n = 4$ /group; * $P < 0.05$; ** $P < 0.01$). **(d)** After 30 min pre-incubation with increasing concentrations of NA-RPAPAR peptide, MDA-MB-435 cells were incubated with tLyP-1 phage (red) for 2 h. Nonconjugated NA was used as a control. Nuclei were stained with DAPI (blue) (original magnification, $\times 40$; scale bars, 50 μ m). **(e)** After 30 min pre-incubation with increasing concentrations of NA-tLyP-1 peptide, MDA-MB-435 cells were incubated with LyP-1 phage for 2 h. Phage was stained with anti-T7 antibody (red). Nuclei were stained with DAPI (blue) (original magnification, $\times 40$; scale bars, 50 μ m).

Having established that (i) tLyP-1 but not LyP-1 binds to NRP1 and NRP2, (ii) LyP-1 but not tLyP-1 binds to p32 and (iii) both LyP-1 and tLyP-1 internalize into MDA-MB-435 cells, we tested the effect of tLyP-1 on LyP-1 cell internalization. Oligomeric tLyP-1 peptide concentration dependently and fully inhibited LyP-1 phage internalization (Figure 3e). This result supports our hypothesis of a common internalization pathway for LyP-1 and tLyP-1, and the likely cleavage of LyP-1 into the CendR form tLyP-1.

We thus hypothesize that LyP-1 internalization mechanism is very similar to what has been documented for the iRGD peptide (Sugahara *et al.*, 2009): LyP-1 first binds to cell surface p32 in tumors, which triggers a protease cleavage into the tLyP-1 form, and a shift from p32 to NRP1/2 binding, made possible by the loss of affinity for p32 and newly acquired affinity for the NRPs. The NRP binding then activates the CendR cell internalization pathway (Figure 4).

tLyP-1 specifically homes to breast tumors

Given the high NRP expression in the majority of tumors (Ellis, 2006; Guttman-Raviv *et al.*, 2006; Bagri *et al.*, 2009), we set out to study tissue distribution of intravenously injected tLyP-1 in mice bearing orthotopic breast cancers. The mouse 4T1 cells overexpress both NRP1 and NRP2 (Supplementary Figure S1B) and NRP1 and NRP2 exhibit a high sequence homology between mice and humans (93 and 95%, respectively; Chen *et al.*, 1997; He and Tessier-Lavigne, 1997). Phage tLyP-1 bound and internalized into 4T1 cells *in vitro* (Supplementary Figure S4). Tumors examined 1 h after the injection of FAM-tLyP-1 were strongly fluorescent under blue light (Figure 5a). Normal tissues, which

express NRP1 at lower levels than tumors (Ellis, 2006; Guttman-Raviv *et al.*, 2006; Bagri *et al.*, 2009), were negative, with the exception of the kidneys, which reflects the clearance of the peptide through this organ. A control peptide, FAM-ARALPSQSR (Laakkonen *et al.*, 2002), did not accumulate in the 4T1 tumors. Similar results were obtained in human MDA-MB-435 breast cancer xenografts (Figure 5b). Further confocal microscopy analyses confirmed the selective accumulation of FAM-tLyP-1 in 4T1 tumor tissue, and revealed extensive spreading of the label within the tumor (Figure 5c).

To evaluate the capability of tLyP-1 to deliver nanoparticles into tumors and penetrate into tumor tissue, we conjugated FAM-tLyP-1 to elongated iron oxide nanoparticles dubbed nanoworms (tLyP-1-NWs; dimensions: 30 × 80–100 nm) (Park *et al.*, 2009; Agemy *et al.*, 2010). Iron oxide nanoparticles have the advantage that they can serve as a contrast agent in magnetic resonance imaging. Examination of tLyP-1-NW biodistribution showed specific homing of tLyP-1-NWs to 4T1 tumors (Figure 6a). As reported previously for various nanoparticles, the NWs nonspecifically accumulated in the liver and spleen to a small extent (Thorek *et al.*, 2006), and some were also found in the kidney, presumably reflecting the release of the labeled peptide from the NWs (Supplementary Figure S5). The accumulation of the NWs in the tumor was observed at all time points studied (from 30 min to overnight circulation) (Figure 6a; Supplementary Figure S5). The tLyP-1-NWs also specifically homed to the tumors in a third breast cancer model, human MDA-MB-231 xenografts, which express both NRP1 and NRP2 (Supplementary Figure S6A).

Comparison of tLyP-1-NWs with LyP-1-NWs and RPARPAR-NWs

The tissue distribution profile of tLyP-1-NW was comparable to that of the parental LyP-1-NW with respect to tumor-specific homing, but their spreading patterns were different (Figure 6a). After 4 h of circulation, tLyP-1-NWs showed a significantly wider distribution in the tumor tissue than LyP-1-NWs; the fluorescent surface area in the tumor sections was about four times larger in the tLyP-1 tumors (Figure 6b). The enhanced penetration properties of tLyP-1-NW may be attributable to the exposed CendR motif.

The distribution of the tLyP-1-NWs was strikingly different from NWs coated with the prototypic CendR, RPARPAR. Indeed, besides extensive tumor accumulation, RPARPAR-NWs were also present in each of the other tissues we examined (Figure 6c). The accumulation of the RPARPAR-NWs in the liver, spleen and kidney was higher than that of tLyP-1-NWs or LyP-1-NWs. In addition, the RPARPAR-NWs were present in the heart, lungs and pancreas, which were negative for tLyP-1-NWs. Thus, tLyP-1, even though it is an active CendR peptide, is a specific tumor-homing peptide, possibly because of its lower affinity for NRP receptors compared with RPARPAR.

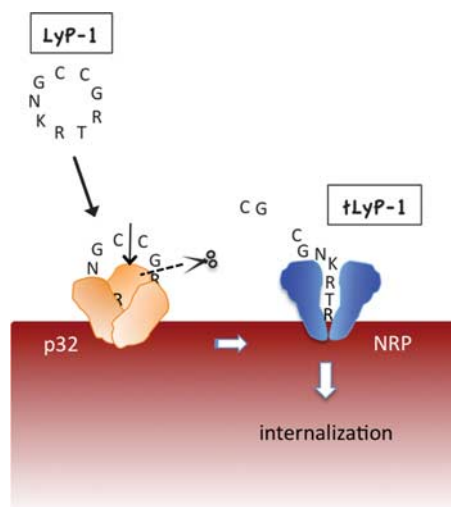


Figure 4 LyP-1 is a cryptic CendR peptide. Cyclic LyP-1 concentrates at the surface of tumor cells by binding to its primary receptor p32. LyP-1 is then proteolytically cleaved into the linear truncated form, tLyP-1, which diminishes its affinity for p32. The exposed C-terminal CendR motif becomes active and triggers binding to NRP1 and/or NRP2, and subsequent cell internalization.

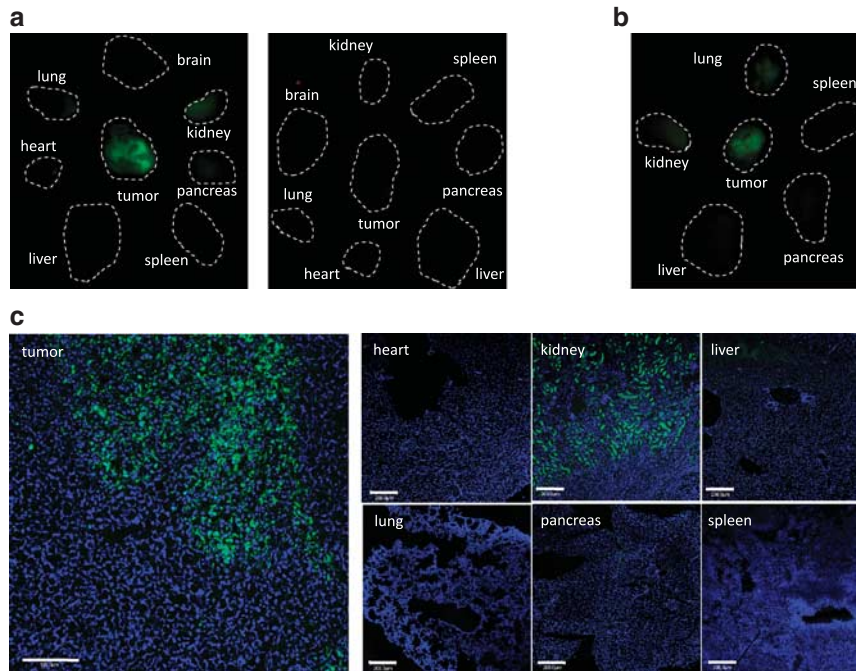


Figure 5 FAM-tLyP-1 homes specifically to breast tumors. (a) FAM-tLyP-1 (left panel) or control FAM-ARALPSQSR (right panel) was intravenously injected into 4T1 tumor-bearing mice. The peptides were allowed to circulate for 1 h and tumors and organs were collected and viewed under blue light. Dotted lines delineate the organs. Representative images of three independent experiments are shown. Note the strong fluorescence in the tumor from the FAM-tLyP-1 injected mouse compared with the other organs, and the absence of fluorescence in the control panel. (b) FAM-tLyP-1 was intravenously injected into MDA-MB-435 tumor-bearing mice. The peptide was allowed to circulate for 45 min, and tumor and organs were collected and viewed under blue light. Dotted lines delineate the organs. Representative image of three independent experiments are shown. Note that the fluorescence is only found in the tumor. (c) Confocal microscope images of the tumor and of normal organs after 1 h of FAM-tLyP-1 circulation in 4T1 tumor-bearing mice. FAM-tLyP-1: green, nuclei: blue (original magnification, $\times 20$; scale bars, 100 μm (tumor); 10 \times ; scale bars, 200 μm (other organs)).

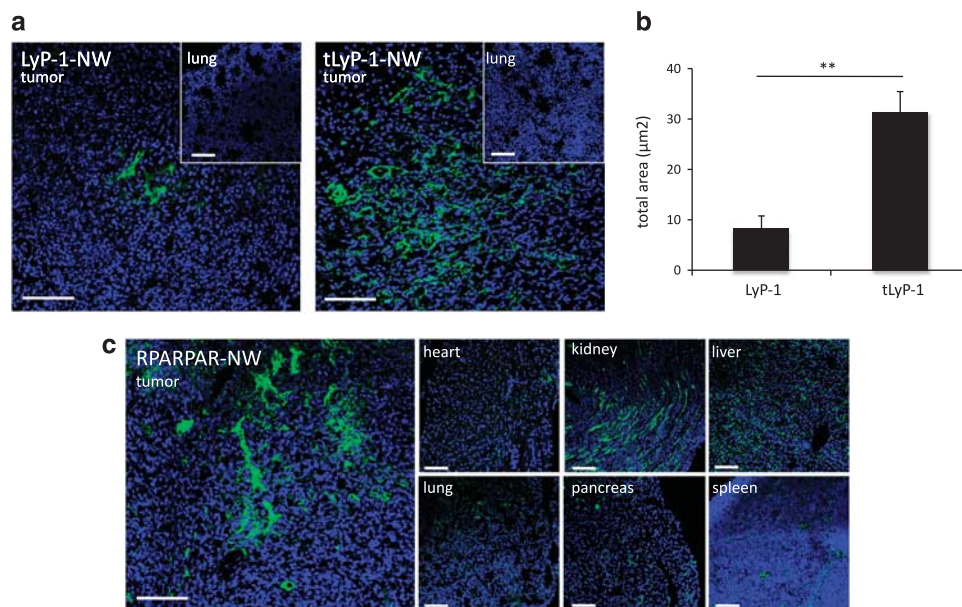


Figure 6 Comparison of tLyP-1-NW homing with LyP-1-NW and RPARPAR-NW homing. (a) NWs conjugated to FAM-LyP-1 (left panel) and FAM-tLyP-1 (right panel) peptides were intravenously injected into 4T1 tumor-bearing mice (5 mg iron/kg mouse) and allowed to circulate for 4 h. FAM-peptides: green, nuclei: blue (original magnification, $\times 20$; scale bars, 100 μm). Note the absence of fluorescence in the lungs. (b) Fluorescence of 10 fields/tumor was quantified with Image J (mean \pm s.e.m.; $n = 3$ /group; ** $P < 0.01$). (c) NWs conjugated to FAM-RPARPAR peptide were intravenously injected into 4T1 tumor-bearing mice (5 mg iron/kg mouse) and allowed to circulate for 4 h. FAM-RPARPAR: green, nuclei: blue. Note the presence of fluorescence in all the organs (original magnification, $\times 20$; scale bars, 100 μm).

tLyP-1-NWs extravasate into regions positive for NRP1 and NRP2 and tLyP-1 peptide increases tumor penetration of a co-injected compound

To assess tLyP-1-NWs tumor penetration over time, tumor sections were analyzed after different circulation times, and blood vessels were stained with an anti-CD31 antibody (Figure 7a). After 30 min of circulation, tLyP-1-NWs fluorescence co-localized to a high extent with the CD31 staining, showing that the NWs were mainly inside the blood vessels or associated with the blood vessel walls. After 4 h, most of the NWs had extravasated and penetrated the tumor tissue, with only a small fraction still associated with the blood vessels. Similar extravasation pattern was also observed in MDA-MB-231 breast cancer xenografts (Supplementary Figure S6B). tLyP-1-NWs were present in tumor regions where NRP1 and NRP2 were abundantly expressed, and co-localization with anti-NRP1 and anti-NRP2 immunostaining was observed (Figure 7b, arrows). tLyP-1-NWs were still seen in the tumor after overnight circulation, whereas the nonspecific accumulation in the liver, spleen and kidney was no longer detectable (Supplementary Figure S5). For this time point, the tLyP-1-NW signal no longer co-localized with

tumor blood vessels and had spread deeper through the tumor tissue.

We also tested the ability of tLyP-1 to trigger tumor penetration of a co-administered compound by activating the CendR pathway (Teesalu *et al.*, 2009; Sugahara *et al.*, 2010). We injected tLyP-1 peptide together with NWs coated with a tumor-homing peptide (sequence: CGKRRK) that is unable to get out of the blood vessels by itself (Hoffman *et al.*, 2003; Agemy *et al.*, 2011). Confocal microscopy analyses revealed enhanced tumor penetration of CGKRRK when injected with tLyP-1 (Figure 7c). Thus, tLyP-1 can also induce penetration of a co-administered compound.

Discussion

Our results show that the tumor-homing peptide LyP-1 (Laakkonen *et al.*, 2002) uses the CendR mechanism for cell internalization. More importantly, we document a novel tumor-homing peptide, tLyP-1, which exhibits enhanced penetration capacity within tumor tissue compared with full-length LyP-1, even when tethered

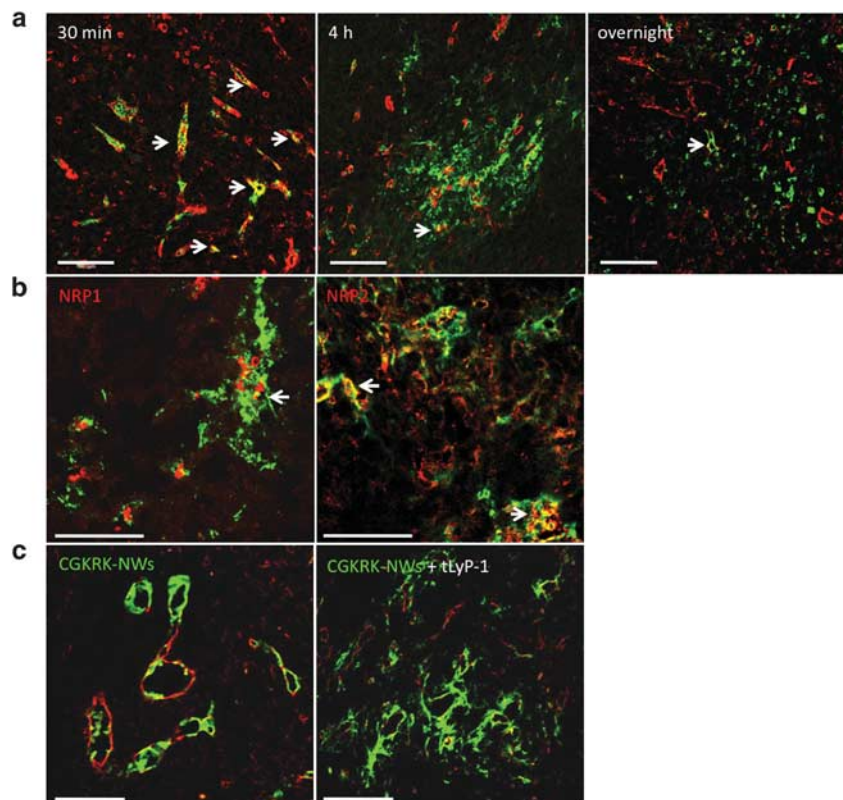


Figure 7 tLyP-1-NWs extravasate into regions positive for NRP1/2 and increase penetration of a co-injected compound. **(a, b)** Confocal microscope images of tLyP-1-NWs (green) in comparison with blood vessels and NRPs. **(a)** Blood vessels were stained with anti-CD31 antibody (red). Arrowheads indicate co-localization between the NWs and the blood vessels. Note the spreading of the label in the tumor tissue over time (original magnification, $\times 20$; scale bars, 100 μm). **(b)** tLyP-1-NWs after 4 h of circulation. (Left panel) Tumor sections were stained with anti-NRP1 (red). (Right panel) Tumor sections were stained with anti-NRP2 (red). Arrowheads indicate co-localization between the NWs and the NRP (original magnification, $\times 40$; scale bars, 50 μm). **(c)** CGKRRK-NWs (green) were injected alone (left panel) or together with tLyP-1 peptide (right panel) and allowed to circulate for 4 h. Tumor sections were stained with anti-CD31 (red). Note the extravasation in the tumor parenchyma in the presence of tLyP-1 (original magnification, $\times 20$; scale bars, 100 μm).

on nanoparticles. This peptide is furthermore able to induce penetration of a co-injected substance.

A strong body of evidence links LyP-1 to the CendR pathway (Sugahara *et al.*, 2009; Teesalu *et al.*, 2009). First, we show that exposure of the CendR motif in LyP-1 triggers binding to the established CendR receptor, NRP1. Second, we show that this binding is specific, and follows the CendR rule—the CendR motif ‘KRTR’ must possess a free C-terminus for the binding to occur. Third, we show that when the CendR motif is exposed, the phage is internalized into cells, where it co-localizes with NRP1. Inhibition of the internalization by the prototypic CendR RPARPAR confirmed the involvement of the CendR pathway. These results strongly suggest that the tumor-penetrating properties of LyP-1 depend on the exposure of the cryptic CendR motif.

The previously identified cryptic CendR peptide, iRGD, loses its affinity for the primary tumor receptor α_v integrin after proteolytic cleavage and acquires affinity for NRP1 (Sugahara *et al.*, 2009). Similarly, the LyP-1 CendR fragment, tLyP-1, exhibited a weak affinity for the primary receptor p32, suggesting that cryptic CendR peptides follow a general pattern involving loss of affinity for the primary receptor after cleavage, and acquisition of an affinity for NRP1. Hence, the full inhibition of LyP-1 internalization by the CendR fragment tLyP-1 likely indicates that internalization occurs through NRP, and not through p32, even though we cannot entirely rule out the participation of other binding molecules.

VEGFA₁₆₅, which induces vascular permeability through its interaction with NRP1 (Becker *et al.*, 2005; Mamluk *et al.*, 2005; Acevedo *et al.*, 2008), binds to NRP2 as well (Soker *et al.*, 1998; Gluzman-Poltorak *et al.*, 2000). Interestingly, using cancer cell lines that express selectively one or the other NRP, we were able to show that NRP2 is also a receptor for CendR peptides, although with a lower binding capacity compared with NRP1. NRP2 is expressed in tissues and cells where NRP1 is absent. Thus, ability to bind NRP2 might be crucial for penetration of CendR peptides in these specific tissues, an example of which may be tumor lymphatics, which express high levels of NRP2 and are a specific target of LyP-1 (Laakkonen *et al.*, 2002, 2004). The distinct properties of various CendR peptides therefore increase the targeting possibilities offered by this technology.

The most significant and surprising finding in this study was the specific homing of the CendR fragment tLyP-1 to tumors, and its high penetration characteristics. The poor quality and leakiness of tumor vessels can cause extravasation and retention of materials in tumors (Greish, 2007). However, our results show that the accumulation of FAM-tLyP-1 in the tumors is specific. The tLyP-1 peptide alone or conjugated to nanoparticles specifically homed to three different types of breast tumors, and spread widely within the tumor tissue. This significantly enhanced penetration compared with LyP-1 nanoparticles is likely due to the direct exposure of the CendR motif and the absence of proteolytic activity require-

ment. tLyP-1 was also able to induce co-penetration of CGKRK-NWs, which do not extravasate when injected alone, further demonstrating that it exhibits CendR characteristics *in vivo*.

tLyP-1 showed more specific homing properties than the prototypic CendR peptide RPARPAR. RPARPAR nanoparticles accumulated in all organs analyzed, which is related to its capacity to induce extravasation and tissue penetration through NRP1 binding (Teesalu *et al.*, 2009). In contrast, tLyP-1 only accumulated in tumors, both as a free peptide and on nanoparticles. Possible reasons for this difference include the lower affinity of tLyP-1 for NRPs, which should favor binding to tissues with the highest local concentration of NRPs, the tumors (Bagri *et al.*, 2009). It is also possible that NRPs are at a higher state of activation in tumors than in normal tissues; regulation of receptor activation is a well-documented phenomenon with other receptors (for example, integrins; Hynes, 2002). Enhanced neuropilin activation could accentuate the effects of the affinity difference between RPARPAR and tLyP-1.

The high expression of both NRP1 and NRP2 in tumors allows one to envision applications for tLyP-1 in tumor targeting. In this study, we show homing and penetration of tLyP-1 to tumors in three different breast cancer models with different patterns of cancer cell NRP expression. Moreover, NRP1 and NRP2 are also present in tumor vessels, where NRP1 is involved in angiogenesis, and NRP2 in lymphangiogenesis (Liang *et al.*, 2007; Pan *et al.*, 2007; Caunt *et al.*, 2008; Dallas *et al.*, 2008). Thus, tLyP-1 may be useful in targeting a variety of solid tumors and to deliver therapeutic or diagnostic agents deep inside the tumor tissue. As a proof of principle, we have shown here that tLyP-1 was able to carry fluorescein and superparamagnetic iron oxide nanoparticles to the tumor interior. Moreover, tLyP-1 induced co-penetration of NWs conjugated with a tumor-homing peptide from tumor blood vessels to the tumor parenchyma. Previous studies with another tumor-penetrating peptide, iRGD, have demonstrated the efficacy of these strategies in tumor treatment and imaging (Sugahara *et al.*, 2009, 2010). Thus, the strong tumor-homing and penetrating properties of tLyP-1 make it a potentially important addition to the arsenal of targeting agents for drug delivery.

Materials and methods

Antibodies and purified proteins

Purified proteins were used for phage binding assays: recombinant human NRP1 (R&D, Minneapolis, MN, USA) and recombinant human NRP2 Fc chimera (R&D). The ligand-blocking polyclonal antibodies, goat anti-rat NRP1 and goat anti-human NRP2, were purchased from R&D. Goat IgG (AbCam, Cambridge, MA, USA) was used as control. For immunofluorescence, the primary antibodies were (i) monoclonal rat anti-mouse CD31 (BD Biosciences, San Diego, CA, USA), (ii) polyclonal rabbit anti-human NRP1 (Chemicon, Temecula, CA, USA), (iii) polyclonal rabbit anti-human NRP2 (Novus Biologicals, Littleton, CO, USA) and (iv)

polyclonal rabbit anti-T7 phage (Teesalu *et al.*, 2009). The following secondary antibodies were used: donkey anti-goat 488/546, goat anti-rat 546 and goat anti-rabbit 488/546 (Invitrogen, Carlsbad, CA, USA).

Cell lines and tumors

MDA-MB-435 (Fogal *et al.*, 2008), DU145 (purchased from ATCC, Manassas, VA, USA) and PPC1 (Teesalu *et al.*, 2009) cells were cultured in Dulbecco's modified eagle medium (Gibco) and 4T1 cells (purchased from ATCC) in IMDM (Gibco). Media were supplemented with 10% fetal bovine serum and 1% penicillin-streptomycin (Gibco, Grand Island, NY, USA). Cells were maintained at 37 °C/5% CO₂.

To produce 4T1 tumors, BALB/c mice were orthotopically injected into the mammary fat pad with 10⁶ cells suspended in 100 µl of phosphate-buffered saline (PBS). Experiments were performed 10 days after the tumor cell injection, before the tumors get highly necrotic and hemorrhagic (average tumor size: 300–500 mm³). To produce MDA-MB-435 tumors, BALB/C athymic nude mice were injected into the mammary fat pad with 2 × 10⁶ cells in 100 µl of PBS, and the mice were used for experiments 4–6 weeks later (average tumor size: 500 mm³). Before any surgical procedure, mice were anesthetized with intraperitoneal injections of xylazine (10 mg/kg) and ketamine (50 mg/kg). Animal experimentation was performed according to the procedures approved by the Animal Research Committees at the University of California, Santa Barbara.

Peptides and peptide-conjugated NWs

The peptides were synthesized as described (Teesalu *et al.*, 2009).

Tetrameric peptides were obtained by conjugation with neutravidin (NA; Pierce, Rockford, IL, USA). NA was dissolved at 5 mg/ml in ultrapure water with 5% glycerol, heated to 37 °C for 1 h, sonicated and filtered. Biotinylated peptide stocks were prepared in water shortly before use, sonicated and added at equal volume to the NA for a final concentration of 250 µM peptide and 40 µM NA. Conjugates were used after 30 min with no additional purification.

NWs coated with peptides were prepared as previously described (Park *et al.*, 2009; Agemy *et al.*, 2010).

In vitro phage binding and internalization

Microtiter wells (Costar, Bloomington, MN, USA) were coated with 5 µg/ml of purified NRP1 or NRP2, blocked with PBS/0.5%. Bovine serum albumin and incubated with 10⁸ plaque-forming units (p.f.u.) of phage in 100 µl of PBS/0.05% Tween 20 for 20 h at 37 °C. After six washes in PBS/0.05% Tween 20, bound phage was eluted with 200 µl of 1 M Tris-HCl (pH 7.5)/0.5% sodium dodecyl sulfate for 30 min and quantified by a plaque assay (titration).

To measure phage binding on cells, 2 × 10⁵ suspended cells were incubated with 7 × 10⁸ p.f.u./ml of T7 phage in Dulbecco's modified eagle medium/bovine serum albumin 1% for 1 h at 4 °C. Ligand-blocking antibodies or control goat IgG isotype (10 µg/sample) were added 30 min before phage incubation. The cells were washed four times with Dulbecco's modified eagle medium/bovine serum albumin 1%, and lysed with lysis broth/1% Nonidet P-40 (LB/NP40) before phage titration.

Phage, NW and peptide homing in vivo

Normal BALB/c mice were intravenously injected with 10¹⁰ p.f.u. of phage, which were allowed to circulate for 15 min. The mice were then perfused through the heart with

PBS containing 1% Bovine Serum Albumin and tissues were collected and homogenized in 1 ml of LB/NP40 for titration.

4T1 tumor-bearing BALB/c mice and MDA-MB-435 tumor-bearing nude mice were intravenously injected with, respectively, 150 and 100 µl of 1 mM FAM-labeled synthetic peptides. After 1 h circulation, mice were perfused and tissues were collected, observed under blue light (Illumatool Bright Light System LT-9900, Lighttools Research, Encinitas, CA, USA) and processed for immunofluorescence analysis.

Peptide-NWs (5 mg iron/kg mouse) were intravenously injected in 4T1 tumor-bearing mice and allowed to circulate for 30 min to 16 h. For co-injection experiments, a mixture of CGKRK-NWs (5 mg iron/kg mouse) and tLyP-1 peptide (1 mM) (peptide:peptide-NWs, 50:50) was intravenously injected in 4T1 tumor-bearing mice. After perfusion, organs were harvested and processed for immunofluorescence analysis.

Immunofluorescence

Tissues were fixed with 4% paraformaldehyde and cryoprotected in 30% sucrose before OCT (optimal cutting temperature, Sakura, Torrance, CA, USA) embedding and freezing. Tissues were sectioned at 7 µm and stained with primary antibodies at 4 °C overnight. Secondary antibodies were incubated for 1 h at 37 °C. Stained tissue sections were mounted in Vectashield DAPI (4',6-diamidino-2-phenylindole)-containing mounting media (Vector Laboratories, Burlingame, CA, USA) and examined on a Fluoview 500 confocal microscope (Olympus America, Center Valley, PA, USA). To quantify the homing area of peptide-NWs, 10 fields/tumor cryosection were analyzed.

Cells were grown on collagen I-coated coverslips (BD Biosciences) for 24–72 h. After 4% paraformaldehyde fixation, cells were stained with antibodies following the same procedure as for tumor sections, and mounted in DAPI-containing mounting media. For phage binding assay, 10⁹ p.f.u. of phage in cell culture medium were incubated for 1–2 h. When NA-peptide inhibitors were used, they were added to the cell medium 30 min before phage incubation. NA alone, at the maximum concentration used in the assay, was used as a control. Cells were examined on a Fluoview 500 confocal microscope.

Statistical analysis

Data were analyzed by two-tailed Student's *t*-test.

Conflict of interest

The authors declare no conflict of interest.

Acknowledgements

We thank Dr Eva Engvall for comments on the manuscript. This work was supported by grant number W81XWH-09-1-0698 and W81XWH-08-1-0727 from the USAMRAA for the Department of Defense (ER). LR was supported by Susan G Komen for the Cure post-doctoral fellowship (KG091411) and GB by a fellowship from the Santa Barbara Cancer Center. ER was supported in part by CA30199 the Cancer Center Support Grant from the NCI.

Author contributions: ER and LR designed the research; LR, LA, TT, KNS and JH performed the research; LA, GB and VRK contributed reagents; LR and ER analyzed the data and wrote the paper. All authors discussed the results and commented on the manuscript.

References

- Acedo LM, Barillas S, Weis SM, Gothert JR, Cheresch DA. (2008). Semaphorin 3A suppresses VEGF-mediated angiogenesis yet acts as a vascular permeability factor. *Blood* **111**: 2674–2680.
- Agemy L, Friedmann-Morvinski D, Kotamraju VR, Roth L, Sugahara KN, Girard OM *et al.* (2011). Targeted nanoparticle enhanced proapoptotic peptide as potential therapy for glioblastoma. *Proc Natl Acad Sci USA* **108**: 17450–17455.
- Agemy L, Sugahara KN, Kotamraju VR, Gujraty K, Girard OM, Kono Y *et al.* (2010). Nanoparticle-induced vascular blockade in human prostate cancer. *Blood* **116**: 2847–2856.
- Bagri A, Tessier-Lavigne M, Watts RJ. (2009). Neuropilins in tumor biology. *Clin Cancer Res* **15**: 1860–1864.
- Becker PM, Waltenberger J, Yachechko R, Mirzapoiazova T, Sham JS, Lee CG *et al.* (2005). Neuropilin-1 regulates vascular endothelial growth factor-mediated endothelial permeability. *Circ Res* **96**: 1257–1265.
- Caunt M, Mak J, Liang WC, Stawicki S, Pan Q, Tong RK *et al.* (2008). Blocking neuropilin-2 function inhibits tumor cell metastasis. *Cancer Cell* **13**: 331–342.
- Chen H, Chedotal A, He Z, Goodman CS, Tessier-Lavigne M. (1997). Neuropilin-2, a novel member of the neuropilin family, is a high affinity receptor for the semaphorins Sema E and Sema IV but not Sema III. *Neuron* **19**: 547–559.
- Dallas NA, Gray MJ, Xia L, Fan F, van Buren 2nd G, Gaur P *et al.* (2008). Neuropilin-2-mediated tumor growth and angiogenesis in pancreatic adenocarcinoma. *Clin Cancer Res* **14**: 8052–8060.
- Ellis LM. (2006). The role of neuropilins in cancer. *Mol Cancer Ther* **5**: 1099–1107.
- Fogal V, Zhang L, Krajewski S, Ruoslahti E. (2008). Mitochondrial/cell-surface protein p32/gC1qR as a molecular target in tumor cells and tumor stroma. *Cancer Res* **68**: 7210–7218.
- Gluzman-Poltorak Z, Cohen T, Herzog Y, Neufeld G. (2000). Neuropilin-2 is a receptor for the vascular endothelial growth factor (VEGF) forms VEGF-145 and VEGF-165 [corrected]. *J Biol Chem* **275**: 18040–18045.
- Greish K. (2007). Enhanced permeability and retention of macromolecular drugs in solid tumors: a royal gate for targeted anticancer nanomedicines. *J Drug Target* **15**: 457–464.
- Guttmann-Raviv N, Kessler O, Shraga-Heled N, Lange T, Herzog Y, Neufeld G. (2006). The neuropilins and their role in tumorigenesis and tumor progression. *Cancer Lett* **231**: 1–11.
- Hamzah J, Kotamraju VR, Seo JW, Agemy L, Fogal V, Mahakian LM *et al.* (2011). Specific penetration and accumulation of a homing peptide within atherosclerotic plaques of apolipoprotein E-deficient mice. *Proc Natl Acad Sci USA* **108**: 7154–7159.
- Haspel N, Zanuy D, Nussinov R, Teesalu T, Ruoslahti E, Aleman C. (2011). Binding of a C-end rule peptide to the neuropilin-1 receptor: a molecular modeling approach. *Biochemistry* **50**: 1755–1762.
- He Z, Tessier-Lavigne M. (1997). Neuropilin is a receptor for the axonal chemorepellent Semaphorin III. *Cell* **90**: 739–751.
- Heldin CH, Rubin K, Pietras K, Ostman A. (2004). High interstitial fluid pressure – an obstacle in cancer therapy. *Nat Rev Cancer* **4**: 806–813.
- Hoffman JA, Giraudo E, Singh M, Zhang L, Inoue M, Porkka K *et al.* (2003). Progressive vascular changes in a transgenic mouse model of squamous cell carcinoma. *Cancer Cell* **4**: 383–391.
- Hynes RO. (2002). Integrins: bidirectional, allosteric signaling machines. *Cell* **110**: 673–687.
- Jain RK. (1999). Transport of molecules, particles, and cells in solid tumors. *Annu Rev Biomed Eng* **1**: 241–263.
- Karmali PP, Kotamraju VR, Kastantin M, Black M, Missirlis D, Tirrell M *et al.* (2009). Targeting of albumin-embedded paclitaxel nanoparticles to tumors. *Nanomedicine* **5**: 73–82.
- Kolodkin AL, Levengood DV, Rowe EG, Tai YT, Giger RJ, Ginty DD. (1997). Neuropilin is a semaphorin III receptor. *Cell* **90**: 753–762.
- Laakkonen P, Akerman ME, Biliran H, Yang M, Ferrer F, Karpanen T *et al.* (2004). Antitumor activity of a homing peptide that targets tumor lymphatics and tumor cells. *Proc Natl Acad Sci USA* **101**: 9381–9386.
- Laakkonen P, Porkka K, Hoffman JA, Ruoslahti E. (2002). A tumor-homing peptide with a targeting specificity related to lymphatic vessels. *Nat Med* **8**: 751–755.
- Liang WC, Dennis MS, Stawicki S, Chanthery Y, Pan Q, Chen Y *et al.* (2007). Function blocking antibodies to neuropilin-1 generated from a designed human synthetic antibody phage library. *J Mol Biol* **366**: 815–829.
- Mamluk R, Klagsbrun M, Detmar M, Bielenberg DR. (2005). Soluble neuropilin targeted to the skin inhibits vascular permeability. *Angiogenesis* **8**: 217–227.
- Pan Q, Chanthery Y, Liang WC, Stawicki S, Mak J, Rathore N *et al.* (2007). Blocking neuropilin-1 function has an additive effect with anti-VEGF to inhibit tumor growth. *Cancer Cell* **11**: 53–67.
- Park JH, von Maltzahn G, Zhang L, Derfus AM, Simberg D, Harris TJ *et al.* (2009). Systematic surface engineering of magnetic nanoworms for *in vivo* tumor targeting. *Small* **5**: 694–700.
- Ruoslahti E. (2002a). Specialization of tumour vasculature. *Nat Rev Cancer* **2**: 83–90.
- Ruoslahti E. (2002b). Drug targeting to specific vascular sites. *Drug Discov Today* **7**: 1138–1143.
- Ruoslahti E, Bhatia SN, Sailor MJ. (2010). Targeting of drugs and nanoparticles to tumors. *J Cell Biol* **188**: 759–768.
- Soker S, Takashima S, Miao HQ, Neufeld G, Klagsbrun M. (1998). Neuropilin-1 is expressed by endothelial and tumor cells as an isoform-specific receptor for vascular endothelial growth factor. *Cell* **92**: 735–745.
- Sugahara KN, Teesalu T, Karmali PP, Kotamraju VR, Agemy L, Girard OM *et al.* (2009). Tissue-penetrating delivery of compounds and nanoparticles into tumors. *Cancer Cell* **16**: 510–520.
- Sugahara KN, Teesalu T, Karmali PP, Kotamraju VR, Agemy L, Greenwald DR *et al.* (2010). Coadministration of a tumor-penetrating peptide enhances the efficacy of cancer drugs. *Science* **328**: 1031–1035.
- Takagi S, Tsuji T, Amagai T, Takamatsu T, Fujisawa H. (1987). Specific cell surface labels in the visual centers of *Xenopus laevis* tadpole identified using monoclonal antibodies. *Dev Biol* **122**: 90–100.
- Teesalu T, Sugahara KN, Kotamraju VR, Ruoslahti E. (2009). C-end rule peptides mediate neuropilin-1-dependent cell, vascular, and tissue penetration. *Proc Natl Acad Sci USA* **106**: 16157–16162.
- Thorek DL, Chen AK, Czupryna J, Tsourkas A. (2006). Superparamagnetic iron oxide nanoparticle probes for molecular imaging. *Ann Biomed Eng* **34**: 23–38.
- Uchida M, Kosuge H, Terashima M, Willits DA, Liepold LO, Young MJ *et al.* (2011). Protein cage nanoparticles bearing the LyP-1 peptide for enhanced imaging of macrophage-rich vascular lesions. *ACS Nano* **5**: 2493–2502.
- von Maltzahn G, Ren Y, Park JH, Min DH, Kotamraju VR, Jayakumar J *et al.* (2008). *In vivo* tumor cell targeting with ‘click’ nanoparticles. *Bioconjug Chem* **19**: 1570–1578.

Supplementary Information accompanies the paper on the Oncogene website (<http://www.nature.com/onc>)

Peptides as Targeting Elements and Tissue Penetration Devices for Nanoparticles

Erkki Ruoslahti*

The use of nanoparticles in medicine (nanomedicine) has recently become an intensely studied field. Nanoparticles carrying drugs and imaging agents have already reached the clinic, but they are essentially passive delivery vehicles, not what are referred to as “smart” nanoparticles. An important function to add to make nanoparticles smarter is active homing to the target tissue. It makes nanoparticles accumulate in the target tissue at higher concentrations than would be the case without this feature, increasing therapeutic efficacy and reducing side effects. This review discusses the recent developments in the nanoparticle targeting field with emphasis on peptides that home to vascular “zip codes” in target tissues and provide a tissue- and cell-penetrating function.

1. Introduction

Nanoparticles (NPs) are thought to have great potential as drug delivery vehicles in medicine. The first NP drugs are already in the clinic. Examples include a NP composed of albumin-paclitaxel complexes (Abraxane) and liposomes loaded with doxorubicin (Doxil), which are both cancer therapeutics. However, these NPs are essentially passive drug delivery vehicles that do not fully exploit the potential of NPs. By virtue of being particles, NPs can accommodate multiple functions, such as being able to zero in on their target in the body. The targeting can be accomplished by coupling onto the NP a homing element, such as an antibody or peptide that specifically binds to the target tissue. The concept of targeted drug delivery is an old one. The idea is appealing because this approach has some of the advantages of topical application of drugs: high local concentration at the site of the disease process and low systemic exposure. Some of the reasons for the modest success of the approach so far include the early focus on targeting the parenchymal (tumor) cells, which has been largely stymied by poor penetration of the probes into extravascular tissue. The realization that the vasculature is more accessible to molecular probes has been a significant advance. Moreover, the recent

emergence of NPs as delivery vehicles and the identification of specific targets in the vasculature have rekindled interest in the targeting approach. We call this mode of drug delivery “synaptic” (Gr. syn, together; aphic, affinity) targeting; it is also referred to as ‘active’ or ‘pathotropic’ targeting.

Peptides are particularly well suited for NP targeting because they are small, easy to synthesize and typically non-immunogenic, and because the multivalent presentation of a peptide on a NP provides high avidity for the target. We screen phage libraries in live mice to identify peptides that direct phage homing to a specific target, such as a tumor or

the vascular bed of a certain tissue. As the phage is a NP, it is essentially confined to the vessels, and the screening primarily targets differentially expressed endothelial cell markers (vascular “zip codes”;^[1]). Endothelial marker molecules are readily available for NP binding, and quite frequently the parenchymal cells express the same marker as the endothelium. However, NP access to the extravascular tissue is limited. Recently discovered tumor-penetrating and tissue-penetrating peptides provide a solution to this problem, as they are capable of taking a payload deep into extravascular tissue. Remarkably the NP or drug does not even have to be coupled to the peptide; the peptide activates a bulk transport system that sweeps along any compound that is present in the blood.^[2,3] Treatment studies in mice show improved anti-tumor efficacy and less damage to normal tissues. In this review, I discuss the recent advances in NP delivery focusing on the use of molecular markers in the vasculature as the primary target, NP exit from the blood vessels, and their transport through the target tissue.

2. Molecular Specialization of the Vasculature

2.1. Peptides Detecting Vascular Zip Codes

Studies designed to examine the possibility that tissue-specific metastasis of tumors depended on a specific affinity of circulating tumor cells for the vessels of the preferred host tissue suggested molecular heterogeneity of the endothelium.^[4] In the early 1990s, I decided to explore the proposed molecular heterogeneity and its role in metastasis by using phage display *in vivo*. A library of peptides expressed as fusions to a phage surface protein and typically containing about 1 billion different peptides is intravenously injected into live mice under

Prof. E. Ruoslahti
Center for Nanomedicine
UCSB, Biology II Bldg., University of California
Santa Barbara, CA 93106-9610, USA
E-mail: ruoslahti@sanfordburnham.org

Prof. E. Ruoslahti
Cancer Center, Sanford-Burnham Medical Research Institute
10901 N. Torrey Pines Rd., La Jolla, CA 92037, USA



DOI: 10.1002/adma.201200454

anesthesia, and 5–10 minutes later, the tissue of interest is collected for phage isolation. By repeating the process a number of times, one obtains a pool of phage enriched in phage clones displaying peptides that selectively home to the target tissue. Sequencing the part of the phage genome that encodes the peptide insert in a sample of phage clones from the enriched pool typically reveals repeated peptide sequences; those are the candidate homing peptides. We initially showed that it was possible to identify homing peptides for brain and kidney vessels.^[5] Phage screening has since been used to identify homing peptides for many additional tissues, so many that it seems reasonable to conclude that every tissue puts a specific signature on its vasculature (reviewed in ref. [6]). We also used *in vivo* phage display to identify a breast cancer cell surface protein that recognizes a lung vascular zip code, promoting metastasis to the lungs.^[7] These results support the metastasis hypothesis that inspired the initial *in vivo* phage display studies.

Various diseases put disease-specific signatures on the vasculature of the diseased tissue, and *in vivo* phage display has also proven useful in the identification of these disease-specific vascular markers. Cancer, inflammation, atherosclerotic plaques, arthritis, and regenerating tissue are known to induce the expression of new molecular markers in the blood vessels. A major advantage of the *in vivo* phage screening is that it is unbiased in revealing what works *in vivo*. Other unbiased methods, such as antibody-based screens,^[8] cloning strategies,^[9] and *in vivo* biotinylation^[10] have also been used successfully in analyzing tumor vasculature. A major advantage of phage screening is that it recognizes proteins that are expressed at the cell surface in tumors but are entirely intracellular in normal tissues. This expression pattern is quite common in tumors and other activated tissues (see the section on receptors).

Vascular specificities are often shared among cancer, atherosclerosis, inflammation and tissue regeneration. The apparent reason is that they all involve angiogenesis, the sprouting of new blood vessels from existing ones.^[11] However, that does not mean that the specificity profiles in different diseases are identical. A striking example of the dependence of vascular marker expression on the nature of the lesion is what happens during tumorigenesis: the vessels of premalignant lesions differ from those of fully malignant lesions (while both differ from normal vessels). *In vivo* phage display in two *de novo* transgenic mouse tumor models yielded peptides that recognized the vessels of premalignant lesions, but no longer bound to the vessels in lesions that had turned into fully malignant tumors in the same tumor model. Other peptides displayed the opposite binding pattern, and a third set recognized the vessels in both pre-malignant and fully malignant lesions.^[12,13] In addition to the interesting biology, being able to specifically target pre-malignant lesions has potentially important diagnostic and therapeutic implications. It may be possible to image very early incipient malignancies and target them for destruction. Also, when a target receptor and targeting probe are chosen for tumor imaging and therapy, it will be important to know whether the system also recognizes pre-malignant conditions. Comparison of tumor vessels and vessels from regenerating liver by gene expression analysis revealed distinct differences.^[14] Similarly, *in vivo* phage display with tumors as a target has produced different sets of peptides than when wounds^[15] or arthritic



the U.S. National Academy of Sciences.

Dr. Erkki Ruoslahti is Distinguished Professor and former president of Sanford-Burnham Medical Research Institute and a founder of the Center for Nanomedicine at UCSB. Dr. Ruoslahti is a pioneer in the field of cell adhesion. He now studies specific vascular addresses in directing drugs to sites of disease. He is a member of

joints^[16] were targeted. One of the wound-homing peptides, a cyclic peptide with the sequence CARSKNKDC, also recognizes tumor vessels, but is much more potent as a homing peptide for wounds and inflamed tissues.^[15,17]

2.2. Target Molecules (Receptors) for Homing Peptides

A homing peptide identified by phage screening can be used to identify the corresponding receptor. The most commonly used method for receptor identification is affinity chromatography or “pull-down” on the peptide, followed by mass spectrometry analysis of the bound proteins. Some receptors for tissue-specific vascular homing peptides have been identified.^[18–20] More is known about the receptors in tumors. An early phage screening study^[21] yielded a tumor-homing peptide with an RGD sequence motif. As RGD is an integrin-binding motif,^[22] and RGD-binding integrins such as $\alpha v \beta 3$ and $\alpha v \beta 5$ are specifically expressed in tumor endothelia,^[23] this result confirmed the validity of *in vivo* screening.

New targets identified with homing peptides in tumor vasculature include a form of aminopeptidase N (CD13), which binds peptides containing the NGR motif.^[24,25] A peptide representing a 31-amino acid fragment of human high mobility group protein 2, termed F3, is an example of a novel tumor-homing peptide identified by *in vivo* phage screening of protein fragments encoded by cDNAs.^[26] The receptor for F3 is nucleolin expressed at the cell surface. Nucleolin is ubiquitous as an intracellular protein, but is specifically expressed at the cell surface of endothelial cells and tumor cells *in vivo*.^[27,28] Nucleolin was the first example of what appears to be a common phenomenon, expression of intracellular proteins at the cell surface of tumor cells and tumor endothelial cells. Phage display is particularly well suited for the discovery of markers, the accessibility of which at the cell surface makes them tumor specific, rather than high overall expression. Other examples of such markers in tumor vasculature include the cytoplasmic proteins annexin1^[29,30] and plectin-1,^[31] and the mitochondrial protein p32 (also known as gC1q receptor, and hyaluronic acid binding protein). This protein is the receptor for the tumor homing peptide LyP-1, also originally discovered using *in vivo* phage display.^[32] LyP-1 targets p32 on the cell surface of lymphatic,

myeloid, and cancer cells in tumors, whereas normal tissues only express p32 inside the cells, where it is not available for peptide binding.^[33]

The fibrin-fibronectin complex in blood clots is a well-recognized target in vascular thrombosis. Less appreciated, but perhaps even more important, is the presence of such complexes in tumors and atherosclerotic plaques. The walls of tumor vessels and the interstitial spaces in tumors contain products of blood clotting, presumably as a result of plasma protein seepage from leaky tumor vessels. Fibrinogen leaked from blood vessels is converted to a fibrin meshwork by tissue procoagulant proteins such as tissue factor.^[34–36] Other plasma proteins, plasma fibronectin in particular, become covalently linked or otherwise bound to the fibrin meshwork. These fibrin-fibronectin complexes can be accessed with peptides such as the 9-amino acid cyclic peptide CLT-1^[36,37] and the pentapeptide CREKA.^[38] Subtle clotting also takes place on the surface of atherosclerotic plaques, and has been made use of in delivering cargo to plaques.^[39]

Homing peptides in the clinic. Remarkable success in delivering the cytokine tumor necrosis factor α (TNF α) into tumors has been reported with RGD and NGR peptides; the targeted cytokine was effective in doses as much as 1,000-fold lower than the usual dose, mitigating side effects of this highly toxic cytokine.^[40] A TNF α -NGR fusion protein is currently in phase 3 clinical trials.^[41] The reasons for this success are likely to be two-fold: TNF α is a trimer and the NGR peptide is attached to each subunit, enhancing binding through an avidity effect. In addition, the chimeric protein has two receptors potentially acting in concert: the receptors for TNF α and the NGR peptide. The same RGD and NGR peptides have also been used to deliver tissue factor in human patients to induce blood clotting specifically in tumor blood vessels, with resulting occlusion of the vessels and tumor infarct.^[42]

2.3. Tissue-Penetrating Peptides

We have recently described a tissue-penetrating transport pathway that can be activated with peptides and can be made disease-specific. The key element in the tissue-penetration is the sequence motif R/KXXR/K, which binds to neuropilin-1 (NRP-1), a co-receptor for VEGF. We have named R/KXXR/K the C-end Rule (CendR) motif, because the second arginine or lysine residue has to be C-terminal for the motif to bind to NRP-1.^[43] When the CendR peptide binds to NRP-1, a cell internalization and trans-tissue transport pathway is activated. This pathway can transport payloads ranging from small molecules to NPs. Most importantly, it can be activated in a tissue-specific manner by making the CendR motif cryptic and delivering it to the target tissue. The tissue specificity (in this case tumor-specificity) was accomplished with the prototypic peptide of this class, iRGD.^[2,3] The sequence of iRGD is CRGDKGPD (the lysine residue can also be an arginine, and the aspartic acid a glutamic acid) and it is cyclized through a disulfide bond between the cysteine residues. This peptide homes to tumors because it contains the integrin-binding RGD motif. What makes it special, however, is the basic residue after the RGD, which creates an internal, cryptic CendR motif (RGDR

or RGDK). The multiple steps that make a cryptic CendR peptide a tissue-specific activator of the NRP-1-dependent pathway are as follows:^[2] (1) a peptide containing an internal R/KXR/K motif binds to a vascular receptor specific for a target tissue (RGD binding to $\alpha\beta 3$ and $\alpha\beta 5$ in the case of iRGD); (2) as a result of this initial binding at the target, the peptide is proteolytically processed to convert the internal R/KXR/K motif into a C-terminal one; (3) the C-terminal R/KXXR/K motif binds to NRP-1, inducing the transport pathway out of the blood vessels and through the extracellular tissue (Figure 1). The peptide can carry a payload that is either covalently coupled to the peptide, or the payload can simply be administered together with the peptide because the endocytic bulk transport pathway triggered through neuropilin-1 sweeps along by-stander molecules.^[3]

The cell surface binding mediated by the integrin binding is needed for the proteolytic step to occur in cell culture,^[2] explaining why the CendR motif of iRGD is only activated in tumors in vivo. The protease that activates iRGD and other cryptic CendR peptides has not been identified. In fact, more than one protease capable of cleaving after a basic residue may be involved, as these peptides can be activated in vitro by trypsin.^[43] However, furins are likely candidates because the CendR motif conforms to their consensus substrate. Interestingly, furin expression has been shown to be elevated in tumors and has been used for tumor targeting.^[44] NRP-1 is often also highly expressed in tumors.^[45] Thus, high furin and NRP-1 may add to the tumor specificity created by the RGD-integrin interaction.

A number of homing peptides described earlier may be tumor-penetrating peptides similar to iRGD. That this is the case with LyP-1 (CGNKRTRGC;^[32]) has been shown.^[46] Surprisingly, the truncated version of LyP-1 with an active CendR motif exhibited a degree of tumor selectivity.^[46] Although RGD peptides with a basic residue following the RGD motif bind poorly to integrins,^[2] a peptide resembling the CendR fragment of iRGD (RGDK) has been reported to selectively home to tumors.^[47] It may be that a combination of over-expression of neuropilin-1, which is common in tumors, with even a weak binding to a tumor-specific component can render a peptide partially selective for tumor homing. Two other tumor-homing peptides, F3 (KDEPQRRSARLSAKPAPPKPEPKPKAPAKK^[1]) and CRGRRST^[13] also contain potential CendR sequences (underlined). We used quantum dots coated with the LyP-1 and F3 peptides in our early NP studies to show the feasibility of in vivo targeting.^[48]

Many of the well-known cell-penetrating peptides (CPPs), such as the Tat peptide, contain CendR motifs. However, the CPPs are not cell-type specific,^[49] they enter into all types of cells. Likely reasons for the lack of cell type-specificity include the following: First, The CendR motif of a CCP may be irrelevant, because the CPP uses a ubiquitous pathway different from the CendR pathway. Second, The CendR motif may be active (C-terminal) in the CPP causing internalization to all cells expressing NRP-1 (or NRP-2). Third, a CPP may bind to a ubiquitous primary receptor causing activation of its cryptic CendR motif at the surface of all cells. Tumor-homing variations of CPPs have been engineered. In one peptide, the cell-binding activity of the positively charged Tat peptide is neutralized by tethered negatively charged amino acids, until a tumor protease

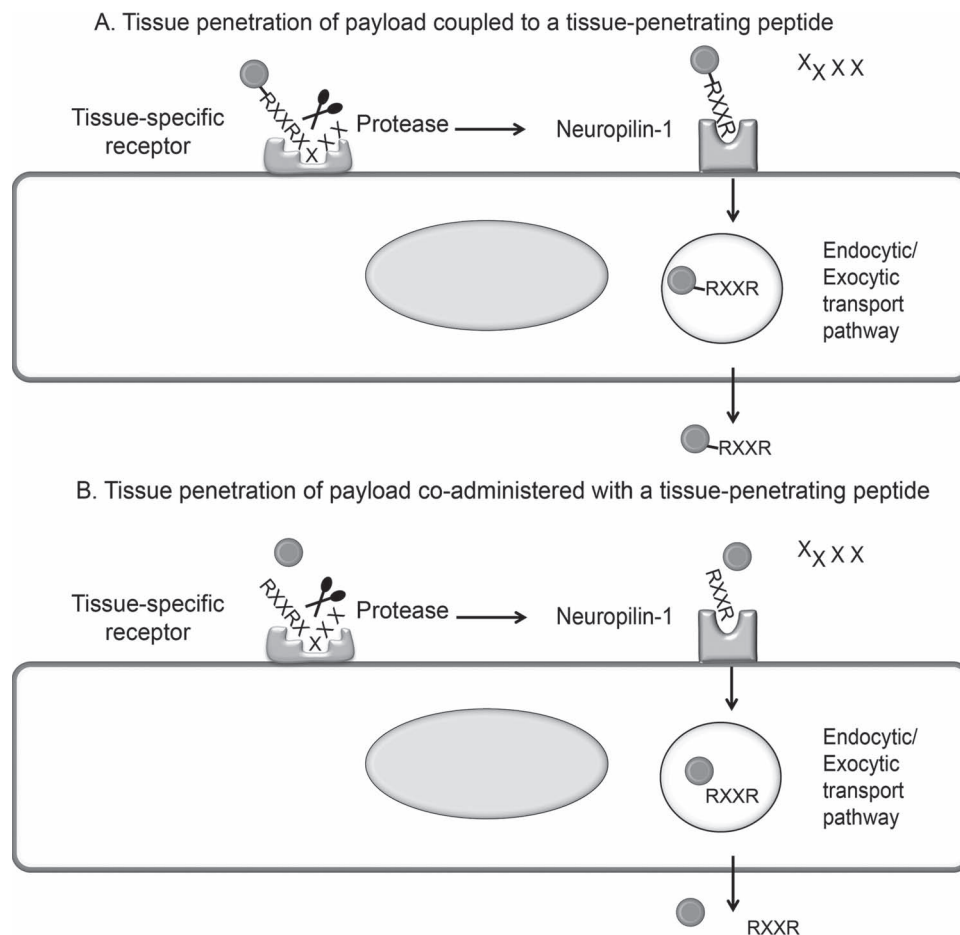


Figure 1. Schematic representation of the trans-tissue transport pathway induced by tissue-penetrating peptides of coupled and co-administrated payloads.^[43,2,3] Note that the exosome aspect of the pathway shown in the figure is an inference from the properties of the pathway and has not been directly observed. See the text for detail.

cleaves the tether, reversing the blockade.^[50] Others have combined a CPP with a tumor-homing peptide, and somewhat surprisingly, the homing peptide activity overrides the universal internalizing properties if the CPP and the chimeric peptides become selective for tumors.^[51,52]

We have shown, particularly for the prototype cryptic CendR peptide iRGD, that the delivery of therapeutic and diagnostic agents specifically into tumors can be greatly enhanced with these peptides.^[2,3,53,46] This difference is particularly striking when the vascular homing peptide also binds to the cells in tumor parenchyma, as this helps retain the peptide and drive its further spreading within the extravascular tumor tissue. For example, the receptors for iRGD, integrins and NRP-1, are expressed in tumor vessels, as well as on the various other cell types present in the tumor mass, including usually the tumor cells.^[2] The studies described above focused on tumor-homing CendR peptides. However, homing peptides for other diseases and tissues exist,^[54] and the neuropilin CendR receptors are ubiquitously expressed, albeit that the expression tends to be higher in tumors.^[45,46] Thus, there seems to be no reason why disease- and tissue-specific CendR peptides could not be obtained for purposes other than cancer targeting. For example,

in addition to tumors, LyP-1 specifically homes to atherosclerotic plaques and penetrates into them, but does not recognize normal vessels.^[55]

A major advantage of the CendR system is that by allowing effective extravasation and tissue penetration, a CendR peptide makes more of the target tissue (such as a tumor) available for a therapeutic agent than would be the case with targeting elements that lack the CendR properties. The ability of CendR peptides to promote tissue entry and accumulation of compounds that are not conjugated with the peptide (by-stander effect) provides additional unique advantages: First, it is not necessary to create a new chemical entity to target a drug by CendR peptide co-administration, as is the case when a drug is coupled to a targeting element. This greatly simplifies the path to clinical application. Second, the amount of any given receptor in a target tissue is likely to be quite low, and this is a major limitation of synaptic targeting of drug conjugates.^[56] For example, if one assumes that a gram of tumor tissue contains 10^9 cells, and they express an average of 100,000 receptors per cell, there would be roughly 170 pmoles of the receptor in that tumor mass. Only a fraction of the total receptor is likely to be available for the binding of a targeting probe. For many

drugs, the required tissue concentration is much higher than a few picomoles per gram of tissue, which means that only a limited amount of a covalently coupled conjugate can be specifically targeted. The by-stander effect does not have this limitation, as the targeted receptor is only used to activate the CendR transport pathway.

The CendR pathway has only been partially characterized so far. It is an endocytic pathway, and marker studies suggest that the CendR endosomes are not related to any of the well-known endosomal vesicles.^[43] The fact that this pathway, once activated, sweeps along by-stander molecules and even NPs, suggests a relationship to pinocytosis. Although this has not been directly observed, the CendR vesicles may also be exocytic because it would be difficult to explain the tissue penetration if the payload would only enter cells and not come out of them. The pathway is an active transport pathway; it requires energy and is much faster than what could be explained on the basis of diffusion.^[3]

3. Nanoparticle Targeting

3.1. Homing Peptide-Targeted Nanoparticles

NPs can incorporate unique functions that cannot readily be engineered into simple drugs. One such function is selective homing to a target. Coating the surface of NPs with a targeting element, such as a homing peptide, confers the NPs specific affinity to the intended target tissue. NPs with a surface studded with binding elements have been dubbed nanoburrs,^[57] a term that conveys the idea of binding, but does not quite cover the specificity of the binding.

Vascular targeting is particularly advantageous with NPs, which have limited ability to exit the vasculature. There is a vast literature on passive NP targeting to tumors through the so-called enhanced permeability and retention (EPR) effect, but EPR is not very effective, and its size-dependency, slow time frame, and variability from tumor to tumor limit its usefulness.^[58,59] High interstitial pressure and fibrosis constitute additional barriers to the access of NPs to the interior of tumors.^[60–62] Furthermore, EPR is unlikely to operate in non-tumor vascular beds. For these reasons, it is important to design systems that initially target the vasculature, rather than the parenchymal cells.

The luminal side of vessels is fully accessible to NPs circulating in the blood and the vessels can serve as a gateway to the interior of the targeted tissue. NPs are an ideal payload for homing peptides because the presentation of multiple copies of the peptide on the NP surface makes possible multivalent binding. The high avidity resulting from the multivalency compensates the generally moderate affinity of peptides. In addition, elongated shape, such as that of iron oxide nanoworms can enhance homing peptide-mediated binding of NPs to the surface of cells, presumably because more interactions between the two surfaces are possible than when the NP is spherical.^[63] Since we use phage display to find homing peptides, and the phage is a NP and the display is multivalent,^[6] the peptides identified in this manner are already selected for NP homing.

The “dark” side of NP multivalency is that all surface features in them are presented in a multivalent fashion, providing potential recognition signals for the reticuloendothelial system (RES). RES is also known as the mononuclear phagocyte system (MPS). RES eliminates foreign materials, such as NPs from the circulation by capturing them into the liver and spleen. Minimizing NP uptake by RES is critical to ensure effective drug delivery. Various ‘stealth’ coatings, and modifying the shape and size of the particles can mitigate this problem (e.g. ref. [64]), but only delay the inevitable; NPs eventually end up in the RES. However, any delay in the RES uptake of NPs is important because it gives them more time to reach the intended target. The RES remains a major problem in nanomedicine (reviewed in ref. [56,65]) and better solutions for this problem are likely to come from more complete understanding of the RES phagocytosis process at the molecular level.

3.2. Amplified Tumor Homing of Nanoparticles

While both drugs and NPs can be targeted, NP targeting can be enhanced by engineered more complex, cooperative targeting functions into them. We have described NPs that self-amplify their own homing to tumors. Superparamagnetic iron oxide NPs (SPIO) are coated with a pentapeptide (sequence: CREKA) that binds to fibrin-fibronectin complexes deposited in tumor blood vessels (and tumor stroma) as a result of subtle clotting.^[38] These deposits are not present in normal vessels, making the homing tumor specific. The initial accumulation of the CREKA-SPIO in tumor vessels causes additional clotting in these vessels, which creates new binding sites for additional NPs, which causes more clotting, and so on. This self-amplifying homing system occludes about 20% of tumor vessels, and the enhancement factor from the amplification is about six-fold.^[38] The amplified NP homing greatly enhanced tumor imaging, but the level of vessel occlusion was not sufficient for significant inhibition of tumor growth. Recent improvements to the system have made it possible to occlude 60–70% of tumor vessels, resulting in tumor necrosis and growth inhibition.^[66] A clotting activator (tissue factor) that is targeted to tumors with a homing peptide has been introduced into clinical trials.^[42] The CREKA system has the advantage that the NPs could be loaded with a drug to further enhance its anti-tumor potency.

Integrating multiple functions into a single NP can reduce the efficacy of the individual functions. For example, we have found that a two-fold reduction of homing peptide density on an NP can drastically reduce the efficacy of tumor homing.^[66] Dividing the functions between two NPs that then cooperate in their functions can circumvent these problems. In one study, we coated two different tumor homing peptides with partially non-overlapping selectivity for tumor vessels onto separate SPIO NPs. Surprisingly, when the two NPs were injected together into the circulation of tumor mice, they completely colocalized producing a wider distribution of each NPs than was obtained with either one alone. This phenomenon, which presumably depends on an attractive force between the NPs, allowed us to greatly increase the number of tumor vessels occluded by the CREKA-SPIO.^[66] The clotting promoting activity of CREKA-SPIO in tumors requires three elements: (1) The NP has to be

slightly thrombogenic, as is the case with SPIO. Micelles coated with CREKA home to tumors, but do not cause additional clotting. (2) The CREKA peptide is necessary; SPIO coated with another tumor-homing peptide also home to tumors, but have no clotting activity in tumor vessels. (3) The pro-coagulant tumor environment is needed. CREKA-SPIO NPs accumulate in the liver RES, but no occlusion of liver vessels has been observed. CREKA-SPIO also bind to the endothelium over atherosclerotic plaques, where subtle clotting produces fibrin-fibronectin complexes, but cause no additional clotting.^[39,66] Thus, this approach to occlude tumor vessel occlusion seems to be safe.

In another strategy, photothermal heating mediated by tumor-targeted gold nanorods increased the expression of the receptor for a homing peptide coated onto a second, drug-carrying NP.^[67,68] The clotting cascade also lends itself to cooperating NP designs.^[69] A combination therapy with NPs that carry different drugs would be another possible application of cooperating NPs. Designing NPs that aggregate under the influence of a feature of the target tissue, such as the expression of an enzyme, is another way of constructing an amplified targeting system, as aggregated NPs are not likely to wash out from a target tissue. Interestingly, one such system utilizes furin cleavage as the triggering mechanism for NP aggregation,^[70,71] which may benefit both from the aggregation and a CendR effect.

In some cases, it will be possible to replace nanosystems that use multiple NPs with multi-compartment NPs, which enable co-presentation of dissimilar properties on the same particle. For example, the requirement of high homing peptide concentration on a NP for optimal homing could be satisfied by coating a compartment of a NP with the peptide, leaving the rest of the surface available for other function.^[72]

3.3. Nanoparticle Biocompatibility

In vivo use of NPs for medical purposes places strict requirements on biocompatibility and lack of toxicity. Iron oxide NPs are clinically approved for imaging applications and for the treatment of anemia caused by iron deficiency. Organic NPs (Abraxane and Doxil) are being used in cancer therapy. However, many of the inorganic NPs now studied in animals, such as various types of quantum dots and carbon nanotubes are likely to face high regulatory hurdles. Porous silicon NPs exhibit a favorable toxicity profile as they degrade in vivo producing silicic acid, which is a physiological compound eliminated through the urine.^[73] The non-toxicity, high capacity for cargo, and quantum dot-like optical properties make porous silicon NPs a promising material for the design of next generation NPs.

3.4. Tissue-Penetrating Nanoparticles

As discussed above, tissue-penetrating peptides can induce exit from the blood vessels in the target tissue and transport through that tissue, particularly when the receptor for the peptide is shared between the vascular and parenchymal cells. The tumor-homing iRGD peptide is an example of a probe that fulfills these criteria. The results with NP targeting have been particularly

striking because NPs are much larger than peptides or proteins, and that hinders their diffusion out of the blood vessels.

Coating of Abraxane with the iRGD or LyP-1 peptide resulted in enhanced accumulation and several-fold higher activity than seen with the original drug.^[53,2] It was also shown that the iRGD effect on Abraxane, and on doxorubicin liposomes, could be achieved by simple co-administration of the peptide with the NPs, without having to couple the two together.^[3]

Recently, we have used iRGD in the co-administration mode to construct a nanopatform for the delivery of a drug into glioblastomas.^[74] The system consists of elongated iron oxide NPs (nanoworms; NWs;^[63] which are coated with a bifunctional peptide through a PEG linker. One branch of the peptide, CGKRK is a tumor-specific vascular homing element,^[13] and the other branch is $D[KLAKLAK]_2$, a membrane perturbing pro-apoptotic D-amino acid peptide, which serves as a drug. We have previously shown that the $D[KLAKLAK]_2$ peptide can be targeted to tumors and other disease sites by directly conjugating it to a homing peptide.^[75,76] The conjugates were effective, but also highly toxic. Unexpectedly, we found that the NP-bound $D[KLAKLAK]_2$ was hundreds of times more potent in killing cells in culture than the soluble form. Standley et al.^[77] have also reported high efficacy of multivalent $D[KLAKLAK]_2$. The greatly increased specific activity of the NP-bound pro-apoptotic peptide was important in that it made it possible to reduce the dose of the peptide. The lower dose in turn brought the dose needed into the range that would not be expected to overwhelm the CGKRK receptors. The resulting improvement in targeting reduced the side effects to a moderate increase in enzyme markers of liver damage, which was reversible upon termination of the treatment. Another significant feature of the CGKRK- $D[KLAKLAK]_2$ system that the homing peptide directs the pro-apoptotic $D[KLAKLAK]_2$ peptide to the subcellular organelle this pro-apoptotic peptide acts on, the mitochondria. CGKRK binds to mitochondria, and it apparently also has cell penetrating properties, because the NWs were seen in association with the mitochondria of the target cells.^[74]

The CGKRK- $D[KLAKLAK]_2$ nanosystem eradicated the tumors in one glioblastoma model and significantly extended the life span of the mice in another, more aggressive model;^[74] (Figure 2). When the nanosystem was combined with iRGD injections, there was a further, highly significant extension of survival of the tumor mice with the aggressive tumors. CGKRK is an internalizing peptide, but it lacks tissue-penetrating properties. Accordingly, the NWs, when injected alone, stayed in the blood vessels. However, when co-injected with iRGD they extravasated (Figure 3). Thus, the likely reason for the improvement of the therapy results is that by using iRGD, we had made the tumor cells a secondary target in addition to the vasculature. Importantly, these results also suggest that iRGD can help a therapeutic agent penetrate the blood-brain barrier in glioblastomas, albeit that the barrier may be somewhat compromised in the tumors. A somewhat analogous nanosystem consisting of the membrane-disrupting toxin melittin targeted to tumors with perfluorocarbon NPs coated with an RGD-mimic compound has been described.^[78] Interestingly, melittin contains a cryptic CendR motif. It would be interesting to know whether activation of the CendR system contributed to the anti-tumor activity of these NPs.

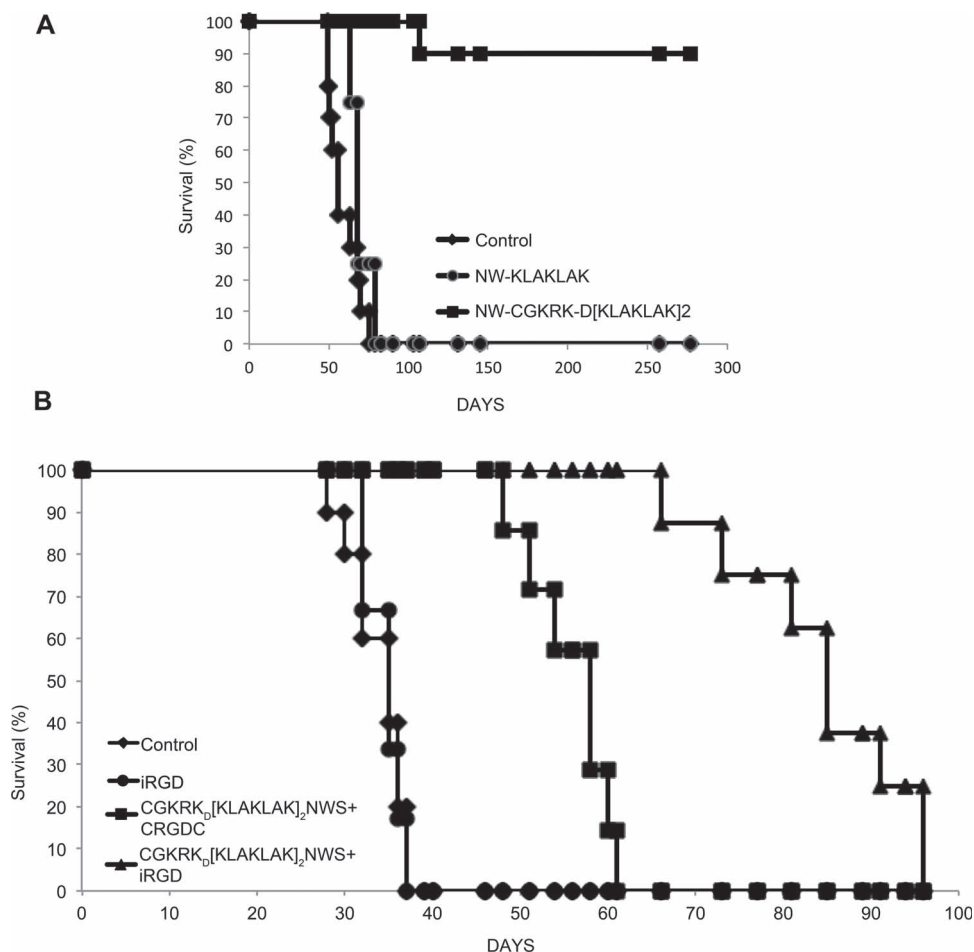


Figure 2. Glioblastoma treatment with CGKRK_D[KLAKLAK]₂-nanoworms (NWs) in mice. A. Mice bearing lentiviral (H-RasV12-shp53) induced brain tumors^[86,87] in the right hippocampus were intravenously injected with iron oxide NWs coated with peptides (5 mg of iron per kg). The particles were administered every other day for 18 days, starting 3 weeks post-viral injection. Survival curves ($n = 8$ –10 mice per group) shows rapid demise of the mice in the control groups and long-term survival of the group treated with CGKRK_D[KLAKLAK]₂NWs. B. Mice bearing orthotopic 005 tumors implanted 10 days earlier ($n = 8$ –10 mice per group) received every other day for 3 weeks intravenous injections of either CGKRK_D[KLAKLAK]₂-NWs (5 mg of iron/kg), or CGKRK_D[KLAKLAK]₂-NWs (5 mg/kg) mixed with 4 mmol/kg of iRGD or PBS. CGKRK_D[KLAKLAK]₂-NWs have a strong anti-tumor effect, which is further enhanced when the NWs are co-injected with iRGD. In contrast to the CGKRK_D[KLAKLAK]₂ nanosystem, a number of other treatments, such as various anti-angiogenic agents have shown no activity in these models.^[87] Modified with permission.^[74] Copyright 2011, The National Academy of Sciences.

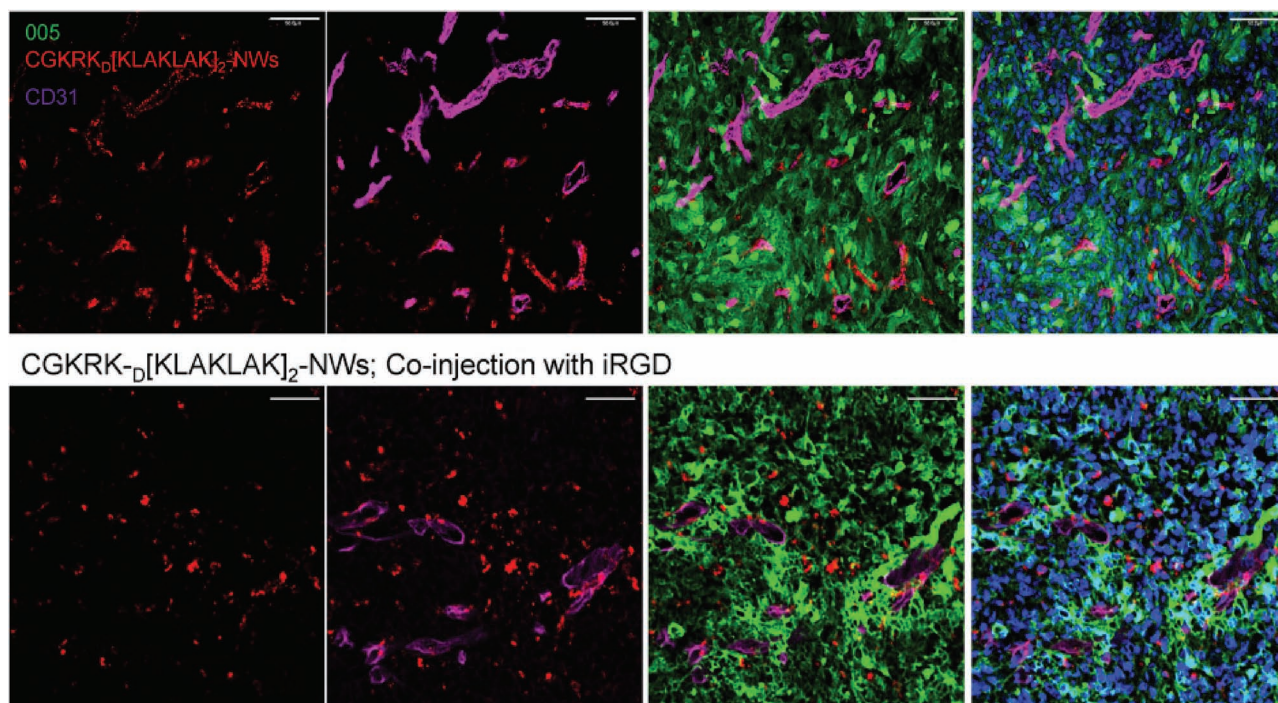
3.5. Subcellular Targeting of Nanoparticles

The CGKRK_D[KLAKLAK]₂ described above is an example of combined targeting that encompasses systemic delivery of a NP payload to a target tissue (tumor vessels), internalization into cells, and further delivery to a specific subcellular organelle. The entire process was accomplished with one peptide.^[74] Similar targeting has been accomplished in cell cultures by coating NPs with cell-penetrating peptides fused with organelle localization signals for the nucleus (e.g. KKKRK^[79]) and mitochondria.^[80] An important question concerns the delivery of NP payloads into the cytoplasm. Therapies that rely on nucleic acids, such as siRNA, have tremendous potential in making previously “undruggable” molecules accessible as treatment targets. Unfortunately, the application of this technology has been hampered by the unsolved problem of delivering the compounds to the target. The main problem is the instability of these compounds in vivo. A likely solution will come

from nanotechnology. NPs can protect the compounds, carry them to the target cells and deliver the intact compound into the cytoplasm. An encouraging advance has been the recent report of successful delivery of siRNA to the tumor of a human patient.^[81]

4. Beyond Tumor Penetration

Tissue penetration by peptides has also been observed in tissues other than tumors. LyP-1, which has been shown to be a tumor-penetrating peptide that depends on the CendR mechanism,^[46] also homes to atherosclerotic plaques, penetrating into the plaque interior.^[55] Iron oxide NPs and protein cage NPs have been shown to enter plaques when coated with LyP-1.^[55,82] Moreover, peptides in a panel of heart-homing peptides, which were also found to penetrate into extravascular heart tissue, contain CendR sequences,^[20] and likely also use the CendR



CGKRRD[KLAKLAK]₂-NWs; Co-injection with iRGD

Figure 3. Enhanced penetration of CGKRRD[KLAKLAK]₂-NWs co-injected with iRGD into extravascular glioblastoma tissue. Mice bearing orthotopic 005 glioblastomas^[87] were intravenously injected with CGKRRD[KLAKLAK]₂-NWs (5 mg of iron/kg) in combination with 4 mmol/kg of either non-labeled CRGDC (upper row) or iRGD (lower row) peptide. The tumors and tissues were collected 5–6 hours later, and analyzed by confocal microscopy. CGKRRD[KLAKLAK]₂-NWs (red) are found outside the blood vessels (magenta), associated with tumor cells (green) when co-injected with iRGD, but remained associated with blood vessels when co-injected with the conventional RGD peptide, CRGDC, which lacks tumor-penetrating properties. Nuclei were stained with DAPI (blue). Scale bars, 50 mm. Modified with permission.^[74] Copyright 2011, The National Academy of Sciences.

Table 1. Nanoparticle delivery with tumor-penetrating peptides.

Nanoparticle	Target	Peptide	Reference
Quantum dots	Tumors, lungs	LyP-1, F3 ^{a)}	[48]
Micelles	Tumors	LyP-1	[53]
Iron oxide NPs	Tumors, athero-sclerotic plaques	iRGD, LyP-1, F3	[2,3,55,88]
Protein cage NPs	Atherosclerotic plaques	LyP-1	[82]
Albumin-paclitaxel NPs (Abraxane)	Tumors	iRGD	[2,3]
Doxorubicin lipo-somes	Tumors	iRGD, LyP-1	[73,3]
Bismuth sulfide NPs	Tumors	LyP-1	[89]
Hydrogel NPs	Tumors	F3	[90]

^{a)}F3 contains a CendR motif and internalizes into cells, but the involvement of the CendR pathway in F3 activities has not been formally proven.

pathway. Finally, it is striking that a number of peptides reported to cross the blood-brain barrier also contain cryptic CendR sequences.^[83–85] Taken together with the results on glioblastoma discussed above this suggests that CendR sequences activated at the brain endothelium may be able to cross the blood-brain barrier and take a payload, even NPs, with them. **Table 1** lists the many types of NPs and tumor-penetrating peptides that have been used to deliver compounds to various targets.

5. Conclusion and Future Prospects

Poor tissue penetration of NPs limits the application of NPs to the treatment of disease. The capacity of the receptors at the target tissue poses a further limitation to the number of NPs that can be specifically targeted to a target tissue. The tumor-penetrating peptides we have recently described can solve these problems. These peptides activate a bulk tissue-specific transport pathway in that once activated is not limited by the availability of specific receptors for the targeted NPs. The specificity of the peptide determines the tissue the pathway is activated in, resulting in target specific delivery of compounds that are

co-administered with the peptide. A current challenge that is likely to only be resolved by nanomedical approaches is the delivery of nucleic acid-based therapeutics. Substantial progress has already been made in this area, but efficacious subcellular delivery still remains to be resolved. Finally, a major future advance in nanomedicine would be engineering NPs in which binding to a target would elicit an activity, such as release of a drug.

Acknowledgements

I thank Dr. Eva Engvall for comment on the manuscript. Research in the author's laboratory is supported by Innovator Awards W81XWH-08-1-0727, W81XWH-09-0698 from the Department of Defense, and grant CA CA152327 from the National Cancer Institute.

Received: February 1, 2012

Revised: February 29, 2012

Published online: May 2, 2012

- [1] E. Ruoslahti, *Biochem. Soc. Trans.* **2004**, 32, 397.
- [2] K. N. Sugahara, T. Teesalu, P. P. Karmali, V. R. Kotamraju, L. Agemy, O. M. Girard, D. Hanahan, R. F. Mattrey, E. Ruoslahti, *Cancer Cell* **2009**, 16, 510.
- [3] K. N. Sugahara, T. Teesalu, P. P. Karmali, V. R. Kotamraju, L. Agemy, D. R. Greenwald, E. Ruoslahti, *Science* **2010**, 328, 1031.
- [4] R. Auerbach, W. C. Lu, E. Pardon, F. Gumkowski, G. Kaminska, M. Kaminski, *Cancer Res.* **1987**, 47, 1492.
- [5] R. Pasqualini, E. Ruoslahti, *Nature* **1996**, 380, 364.
- [6] T. Teesalu, K. N. Sugahara, E. Ruoslahti, *Methods Enzymol.* **2012**, 503, 35.
- [7] D. M. Brown, E. Ruoslahti, *Cancer Cell* **2004**, 5, 365.
- [8] B. S. Jacobson, D. B. Stolz, J. E. Schnitzer, *Nat. Med.* **1996**, 2, 482.
- [9] E. B. Carson-Walter, D. N. Watkins, A. Nanda, B. Vogelstein, K. W. Kinzler, B. St Croix, *Cancer Res.* **2001**, 61, 6649.
- [10] B. Borgia, C. Roesli, T. Fugmann, C. Schliemann, M. Cesca, D. Neri, R. Giavazzi, *Cancer Res.* **2010**, 70, 309.
- [11] K. Alitalo, P. Carmeliet, *Cancer Cell* **2002**, 1, 219.
- [12] J. A. Hoffman, E. Giraudo, M. Singh, L. Zhang, M. Inoue, K. Porkka, D. Hanahan, E. Ruoslahti, *Cancer Cell* **2003**, 4, 383.
- [13] J. A. Joyce, P. Laakkonen, M. Bernasconi, G. Bergers, E. Ruoslahti, D. Hanahan, *Cancer Cell* **2003**, 4, 393.
- [14] S. Seaman, J. Stevens, M. Y. Yang, D. Logsdon, C. Graff-Cherry, B. St Croix, *Cancer Cell* **2007**, 11, 539.
- [15] T. A. Jarvinen, E. Ruoslahti, *Am. J. Pathol.* **2007**, 171, 702.
- [16] Y. H. Yang, R. Rajaiah, E. Ruoslahti, K. D. Moudgil, *Proc. Natl. Acad. Sci. USA* **2011**, 108, 12857.
- [17] T. Urakami, T. A. Jarvinen, M. Toba, J. Sawada, N. Ambalavanan, D. Mann, I. McMurtry, M. Oka, E. Ruoslahti, M. Komatsu, *Am. J. Pathol.* **2011**, 178, 2489.
- [18] D. Rajotte, E. Ruoslahti, *J. Biol. Chem.* **1999**, 274, 11593.
- [19] M. G. Kolonin, P. K. Saha, L. Chan, R. Pasqualini, W. Arap, *Nat. Med.* **2004**, 10, 625.
- [20] L. Zhang, J. A. Hoffman, E. Ruoslahti, *Circulation* **2005**, 112, 1601.
- [21] W. Arap, R. Pasqualini, E. Ruoslahti, *Science* **1998**, 279, 377.
- [22] E. Ruoslahti, *Matrix Biol.* **2003**, 22, 459.
- [23] S. M. Weis, D. A. Cheresh, *Nat. Med.* **2011**, 17, 1359.
- [24] R. Pasqualini, E. Koivunen, R. Kain, J. Lahdenranta, M. Sakamoto, A. Stryhn, R. A. Ashmun, L. H. Shapiro, W. Arap, E. Ruoslahti, *Cancer Res.* **2000**, 60, 722.
- [25] A. Corti, F. Curnis, *Curr. Pharm. Biotechnol.* **2011**, 12, 1128.
- [26] K. Porkka, P. Laakkonen, J. A. Hoffman, M. Bernasconi, E. Ruoslahti, *Proc. Natl. Acad. Sci. USA* **2002**, 99, 7444.
- [27] S. Christian, J. Pilch, M. E. Akerman, K. Porkka, P. Laakkonen, E. Ruoslahti, *J. Cell. Biol.* **2003**, 163, 871.
- [28] E. A. Said, B. Krust, S. Nisole, J. Svab, J. P. Briand, A. G. Hovanesian, *J. Biol. Chem.* **2002**, 277, 37492.
- [29] P. Oh, Y. Li, J. Yu, E. Durr, K. M. Krasinska, L. A. Carver, J. E. Testa, J. E. Schnitzer, *Nature* **2004**, 429, 629.
- [30] S. Hatakeyama, K. Sugihara, T. K. Shibata, J. Nakayama, T. O. Akama, N. Tamura, S. M. Wong, A. A. Bobkov, Y. Takano, C. Ohyama, M. Fukuda, M. N. Fukuda, *Proc. Natl. Acad. Sci. USA* **2011**, 108, 19587.
- [31] K. A. Kelly, N. Bardeesy, R. Anbazhagan, S. Gurumurthy, J. Berger, H. Alencar, R. A. Depinho, U. Mahmood, R. Weissleder, *PLoS Med* **2008**, 5, e85.
- [32] P. Laakkonen, K. Porkka, J. A. Hoffman, E. Ruoslahti, *Nat. Med.* **2002**, 8, 751.
- [33] V. Fogal, L. Zhang, S. Krajewski, E. Ruoslahti, *Cancer Res.* **2008**, 68, 7210.
- [34] H. F. Dvorak, D. R. Senger, A. M. Dvorak, V. S. Harvey, J. McDonagh, *Science* **1985**, 227, 1059.
- [35] K. Abe, M. Shoji, J. Chen, A. Bierhaus, I. Danave, C. Micko, K. Casper, D. L. Dillehay, P. P. Nawroth, F. R. Rickles, *Proc. Natl. Acad. Sci. USA* **1999**, 96, 8663.
- [36] J. Pilch, D. M. Brown, M. Komatsu, T. A. Jarvinen, M. Yang, D. Peters, R. M. Hoffman, E. Ruoslahti, *Proc. Natl. Acad. Sci. USA* **2006**, 103, 2800.
- [37] F. Ye, X. Wu, E. K. Jeong, Z. Jia, T. Yang, D. Parker, Z. R. Lu, *Bioconjug. Chem.* **2008**, 19, 2300.
- [38] D. Simberg, T. Duza, J. H. Park, M. Essler, J. Pilch, L. Zhang, A. M. Derfus, M. Yang, R. M. Hoffman, S. Bhatia, M. J. Sailor, E. Ruoslahti, *Proc. Natl. Acad. Sci. USA* **2007**, 104, 932.
- [39] D. Peters, M. Kastantin, V. R. Kotamraju, P. P. Karmali, K. Gujrati, M. Tirrell, E. Ruoslahti, *Proc. Natl. Acad. Sci. USA* **2009**, 106, 9815.
- [40] F. Curnis, A. Gasparri, A. Sacchi, R. Longhi, A. Corti, *Cancer Res.* **2004**, 64, 565.
- [41] V. Gregorc, G. Citterio, G. Vitali, A. Spreafico, P. Scifo, A. Borri, G. Donadoni, G. Rossoni, A. Corti, F. Caligaris-Cappio, A. Del Maschio, A. Esposito, F. De Cobelli, F. Dell'Acqua, A. Troysi, P. Bruzzi, A. Lambiasi, C. Bordignon, *Eur. J. Cancer* **2010**, 46, 198.
- [42] R. Bieker, T. Kessler, C. Schwoppe, T. Padro, T. Persigehl, C. Bremer, J. Dreischaluck, A. Kolkmeier, W. Heindel, R. M. Mesters, W. E. Berdel, *Blood* **2009**, 113, 5019.
- [43] T. Teesalu, K. N. Sugahara, V. R. Kotamraju, E. Ruoslahti, *Proc. Natl. Acad. Sci. USA* **2009**, 106, 16157.
- [44] K. Hajdin, V. D'Alessandro, F. K. Niggli, B. W. Schafer, M. Bernasconi, *PLoS One* **2010**, 5, e10445.
- [45] A. Bagri, M. Tessier-Lavigne, R. J. Watts, *Clin. Cancer Res.* **2009**, 15, 1860.
- [46] L. Roth, L. Agemy, V. R. Kotamraju, G. Braun, T. Teesalu, K. N. Sugahara, J. Hamzah, E. Ruoslahti, *Oncogene* **2011**.
- [47] D. Pramanik, B. K. Majeti, G. Mondal, P. P. Karmali, R. Sistla, O. G. Ramprasad, G. Srinivas, G. Pande, A. Chaudhuri, *J. Med. Chem.* **2008**, 51, 7298.
- [48] M. E. Akerman, W. C. Chan, P. Laakkonen, S. N. Bhatia, E. Ruoslahti, *Proc. Natl. Acad. Sci. USA* **2002**, 99, 12617.
- [49] J. M. Gump, S. F. Dowdy, *Trends Mol. Med.* **2007**, 13, 443.
- [50] T. Jiang, E. S. Olson, Q. T. Nguyen, M. Roy, P. A. Jennings, R. Y. Tsien, *Proc. Natl. Acad. Sci. USA* **2004**, 101, 17867.
- [51] M. Tan, K. H. Lan, J. Yao, C. H. Lu, M. Sun, C. L. Neal, J. Lu, D. Yu, *Cancer Res.* **2006**, 66, 3764.
- [52] H. Myrberg, L. Zhang, M. Mae, U. Langel, *Bioconjug. Chem.* **2008**, 19, 70.
- [53] P. P. Karmali, V. R. Kotamraju, M. Kastantin, M. Black, D. Missirlis, M. Tirrell, E. Ruoslahti, *Nanomedicine* **2009**, 5, 73.
- [54] E. Ruoslahti, *Nat. Rev. Cancer* **2002**, 2, 83.
- [55] J. Hamzah, V. R. Kotamraju, J. W. Seo, L. Agemy, V. Fogal, L. M. Mahakian, D. Peters, L. Roth, M. K. Gagnon, K. W. Ferrara, E. Ruoslahti, *Proc. Natl. Acad. Sci. USA* **2011**, 108, 7154.
- [56] E. Ruoslahti, S. N. Bhatia, M. J. Sailor, *J. Cell Biol.* **2010**, 188, 759.

- [57] J. M. Chan, J. W. Rhee, C. L. Drum, R. T. Bronson, G. Golomb, R. Langer, O. C. Farokhzad, *Proc. Natl. Acad. Sci. USA* **2011**, *108*, 19347.
- [58] H. Maeda, J. Wu, T. Sawa, Y. Matsumura, K. Hori, *J. Control Release* **2000**, *65*, 271.
- [59] A. K. Iyer, G. Khaled, J. Fang, H. Maeda, *Drug Discov. Today* **2006**, *11*, 812.
- [60] R. K. Jain, *Annu. Rev. Biomed. Eng.* **1999**, *1*, 241.
- [61] C. H. Heldin, K. Rubin, K. Pietras, A. Ostman, *Nat. Rev. Cancer* **2004**, *4*, 806.
- [62] K. P. Olive, M. A. Jacobetz, C. J. Davidson, A. Gopinathan, D. McIntyre, D. Honess, B. Madhu, M. A. Goldgraben, M. E. Caldwell, D. Allard, K. K. Frese, G. Denicola, C. Feig, C. Combs, S. P. Winter, H. Ireland-Zecchini, S. Reichelt, W. J. Howat, A. Chang, M. Dhara, L. Wang, F. Ruckert, R. Grutzmann, C. Pilarsky, K. Izeradjene, S. R. Hingorani, P. Huang, S. E. Davies, W. Plunkett, M. Egorin, R. H. Hruban, N. Whitebread, K. McGovern, J. Adams, C. Iacobuzio-Donahue, J. Griffiths, D. A. Tuveson, *Science* **2009**, *324*, 1457.
- [63] J. H. Park, G. von Maltzahn, L. Zhang, A. M. Derfus, D. Simberg, T. J. Harris, E. Ruoslahti, S. N. Bhatia, M. J. Sailor, *Small* **2009**, *5*, 694.
- [64] N. Doshi, S. Mitragotri, *PLoS One* **2010**, *5*, e10051.
- [65] S. M. Moghimi, A. C. Hunter, J. C. Murray, *Pharmacol. Rev.* **2001**, *53*, 283.
- [66] L. Agemy, K. N. Sugahara, V. R. Kotamraju, K. Gujraty, O. M. Girard, Y. Kono, R. F. Mattrey, J. H. Park, M. J. Sailor, A. I. Jimenez, C. Cativiela, D. Zanuy, F. J. Sayago, C. Aleman, R. Nussinov, E. Ruoslahti, *Blood* **2010**, *116*, 2847.
- [67] J. H. Park, G. von Maltzahn, M. J. Xu, V. Fogal, V. R. Kotamraju, E. Ruoslahti, S. N. Bhatia, M. J. Sailor, *Proc. Natl. Acad. Sci. USA* **2010**, *107*, 981.
- [68] G. von Maltzahn, A. Centrone, J. H. Park, R. Ramanathan, M. J. Sailor, T. A. Hatton, S. N. Bhatia, *Adv. Mater.* **2009**, *21*, 3175.
- [69] G. von Maltzahn, J. H. Park, K. Y. Lin, N. Singh, C. Schwoppe, R. Mesters, W. E. Berdel, E. Ruoslahti, M. J. Sailor, S. N. Bhatia, *Nat. Mater.* **2011**, *10*, 545.
- [70] G. Liang, H. Ren, J. Rao, *Nat. Chem.* **2010**, *2*, 54.
- [71] D. Ye, G. Liang, M. L. Ma, J. Rao, *Angew. Chem. Int. Ed.* **2011**, *50*, 2275.
- [72] J. Lahann, *Small* **2011**, *7*, 1149.
- [73] J. H. Park, L. Gu, G. von Maltzahn, E. Ruoslahti, S. N. Bhatia, M. J. Sailor, *Nat. Mater.* **2009**, *8*, 331.
- [74] L. Agemy, D. Friedmann-Morvinski, V. R. Kotamraju, L. Roth, K. N. Sugahara, O. M. Girard, R. F. Mattrey, I. M. Verma, E. Ruoslahti, *Proc. Natl. Acad. Sci. USA* **2011**, *108*, 17450.
- [75] H. M. Ellerby, W. Arap, L. M. Ellerby, R. Kain, R. Andrusiak, G. D. Rio, S. Krajewski, C. R. Lombardo, R. Rao, E. Ruoslahti, D. E. Bredesen, R. Pasqualini, *Nat. Med.* **1999**, *5*, 1032.
- [76] W. Arap, W. Haedicke, M. Bernasconi, R. Kain, D. Rajotte, S. Krajewski, H. M. Ellerby, D. E. Bredesen, R. Pasqualini, E. Ruoslahti, *Proc. Natl. Acad. Sci. USA* **2002**, *99*, 1527.
- [77] S. M. Standley, D. J. Toft, H. Cheng, S. Soukasene, J. Chen, S. M. Raja, V. Band, H. Band, V. L. Cryns, S. I. Stupp, *Cancer Res.* **2010**, *70*, 3020.
- [78] N. R. Soman, S. L. Baldwin, G. Hu, J. N. Marsh, G. M. Lanza, J. E. Heuser, J. M. Arbeit, S. A. Wickline, P. H. Schlesinger, *J. Clin. Invest.* **2009**, *119*, 2830.
- [79] B. Kang, M. A. Mackey, M. A. El-Sayed, *J. Am. Chem. Soc.* **2010**, *132*, 1517.
- [80] A. M. Derfus, W. Chan, S. N. Bhatia, *Adv. Mater.* **2004**, *16*, 961.
- [81] M. E. Davis, J. E. Zuckerman, C. H. Choi, D. Seligson, A. Tolcher, C. A. Alabi, Y. Yen, J. D. Heidel, A. Ribas, *Nature* **2010**, *464*, 1067.
- [82] M. Uchida, H. Kosuge, M. Terashima, D. A. Willits, L. O. Liepold, M. J. Young, M. V. McConnell, T. Douglas, *ACS Nano* **2011**, *5*, 2493.
- [83] C. Che, G. Yang, C. Thiot, M. C. Lacoste, J. C. Currie, M. Demeule, A. Regina, R. Beliveau, J. P. Castaigne, *J. Med. Chem.* **2010**, *53*, 2814.
- [84] P. Kumar, H. Wu, J. L. McBride, K. E. Jung, M. H. Kim, B. L. Davidson, S. K. Lee, P. Shankar, N. Manjunath, *Nature* **2007**, *448*, 39.
- [85] C. Rousselle, P. Clair, J. Temsamani, J. M. Scherrmann, *J. Drug Target.* **2002**, *10*, 309.
- [86] T. Marumoto, A. Tashiro, D. Friedmann-Morvinski, M. Scadeng, Y. Soda, F. H. Gage, I. M. Verma, *Nat. Med.* **2009**, *15*, 110.
- [87] Y. Soda, T. Marumoto, D. Friedmann-Morvinski, M. Soda, F. Liu, H. Michiue, S. Pastorino, M. Yang, R. M. Hoffman, S. Kesari, I. M. Verma, *Proc. Natl. Acad. Sci. USA* **2011**, *108*, 4274.
- [88] G. R. Reddy, M. S. Bhojani, P. McConville, J. Moody, B. A. Moffat, D. E. Hall, G. Kim, Y. E. Koo, M. J. Woolliscroft, J. V. Sugai, T. D. Johnson, M. A. Philbert, R. Kopelman, A. Rehemtulla, B. D. Ross, *Clin. Cancer Res.* **2006**, *12*, 6677.
- [89] J. M. Kinsella, R. E. Jimenez, P. P. Karmali, A. M. Rush, V. R. Kotamraju, N. C. Gianneschi, E. Ruoslahti, D. Stupack, M. J. Sailor, *Angew. Chem. Int. Ed.* **2011**, *50*, 12308.
- [90] I. Winer, S. Wang, Y. E. Lee, W. Fan, Y. Gong, D. Burgos-Ojeda, G. Spahlinger, R. Kopelman, R. J. Buckanovich, *Cancer Res.* **2010**, *70*, 8674.

Science Manuscript Template

Title: Etchable and Bright Silver Nanoparticle Probes for Cell Internalization Assays

Authors: Gary B. Braun^{a,b}, Tomas Friman^{a,b}, Hong-Bo Pang^b, Venkata Ramana Kotamraju^{a,b}, Alessia Pallaoro^c, Norbert O. Reich^c, Tambet Teesalu^{a,b,d}, Erkki Ruoslahti^{a,b}

Affiliations:

a: Sanford-Burnham Medical Research Institute at University of California, Santa Barbara, CA 93106, Center for Nanomedicine, University of California, Santa Barbara, CA 93106

b: Cancer Research Center, Sanford-Burnham Medical Research Institute, La Jolla, CA 92037, USA

c: Department of Chemistry and Biochemistry, University of California, Santa Barbara, CA 93106

d: Laboratory of Cancer Biology, Institute of General and Molecular Pathology, University of Tartu, Estonia

*Correspondence to: ruoslahti@sanfordburnham.org

Abstract: Nanoparticles are often used to deliver drugs and other bioactive compounds to cells *in vitro* and *in vivo*. Fluorescent imaging used to study internalization and subcellular localization of nanoparticles, does not allow unequivocal distinction between cell surface-bound and internalized particles. We have developed a simple technique to rapidly remove silver nanoparticles outside living cells leaving only the internalized pool. Etching is based on the sensitivity of silver to a redox-based destain solution. This strategy, based on dye-labeled silver, can be used to study internalization of nanoparticles by techniques such fluorescence and darkfield microscopy, flow cytometry, and inductively coupled plasma–mass spectrometry (ICP-MS).

One Sentence Summary: We describe a rapid and selective technique to remove bright silver nanoparticles outside living cells leaving only the internalized pool.

Main Text:

Designing nanoparticles for therapeutic, diagnostic and theranostic applications is of pivotal importance in advancing nanomedicine[1, 2]. Nanoparticles (NPs) enter cultured cells at rates determined by their surface coating, size and shape [3-5]. Most of the clinically relevant nanoparticle targets are intracellular and NPs are typically coated with an effector layer to engage cellular receptors and trigger internalization. Cell culture assays are used to gauge the particle internalization by fluorescent, chemical, radioactive, or enzymatic tracers. Distinguishing internalized NPs from cell surface-bound particles typically involves disrupting ligand-protein interactions by exposing cells to low pH or using a competitive ligand, which may have unwanted effects on cells and be challenging for high-avidity nanoparticles. Here we demonstrate a cell-impermeable silver etchant that rapidly dissolves extracellular silver NPs (AgNPs) while leaving internalized AgNPs visible for imaging or quantification.

Silver is increasingly used for biomedical imaging applications because of its unique optical properties including fluorescence and Raman enhancement of near-surface molecules and intense darkfield scattering from the core, each of which arise from size- and shape-dependent plasmonic effects[6-11]. In contrast, gold NPs typically quench fluorescence and are not as well suited for microscopy, and dye-labeled polymer NPs require harsh solvents or etchants to dissolve (e.g. dimethylformamide)[12-14]. Commercial silver etch or 'destain' solutions widely used in photography, and to dissolve silver associated with protein bands in polyacrylamide gels, are well suited for dissolving AgNPs. A typical etchant solution uses the redox agent ferricyanide (Fe(III)CN_6^{3-}), which oxidizes Ag^0 to Ag^+ , and thiosulfate anion to solubilize the ions[15, 16]. The etchant removes AgNPs in seconds due to their small size (Fig. 1A,B), and the process can be performed in cell culture medium and is well tolerated by mammalian cells (Fig. S1-4)[17]. The Fe(III) complex is reduced to Fe(II) , ferrocyanide, but remains ligand-stabilized and thus all reagents are removed upon washing. Notably, gold NPs are resistant to this etchant if hydroxide is absent[18] and ascorbate, known to reduce ferricyanide blocks the etch activity towards Ag (Fig. S5)[17].

C-end rule (CendR) peptides trigger neuropilin-dependent cell and tissue penetration when exposed at the C-terminus of a polypeptide chain[19]. The design of fluorescent dye-labeled AgNPs coated with the prototypic CendR peptide RPARPAR, and their distribution before and after etch in neuropilin-1-expressing PPC-1 prostate cancer cells are shown in Figure 1. Darkfield and fluorescence microscopy (Fig. 1C-D, S1) demonstrate the removal of extracellular particles (those bound to the cell surface and the culture plate surface between cells). Internalized particles protected from etchant by the plasma membrane remain unaltered in intensity. The resonant scattering wavelength in darkfield imaging red-shifts when AgNPs are within one diameter length from each other[8]. This effect is clearly visible in the perinuclear region, presumably due to endosome fusion. Quantification by flow cytometry showed that under these incubation conditions ~60% of the signal from RPARPAR AgNPs could not be etched due to their internalization (Fig. 1D-F). As expected, AgNPs functionalized with RPARPARA (an inactive control peptide with an alanine residue added to the C-terminus of RPARPAR[20, 21]) showed weak surface binding to cells with complete etchability (Fig 1E). Removal of elemental silver from outside the cells was verified using inductively coupled plasma mass spectrometry (Fig. S3). The etch strategy was also used for facile analysis of AgNP coatings. The brightness and photostability of dyes positioned near metal surfaces can increase through a decreased excited state lifetime caused by coupling to surface plasmons, with significant enhancement from AgNPs larger than ~40 nm[8, 9]. The enhancement factor for the dye-labeled coating on the 80 nm AgNPs was 9-fold (Fig. 1F), determined by etching the core at constant volume. Smaller AgNP (~25 nm) showed negligible enhancement with a similar coating [9]. Together, these results illustrate how etchable silver nanoparticle cores with tailored coatings can be a powerful tool in studies of uptake and endosomal trafficking.

References and Notes:

Acknowledgments:

We thank K. N. Sugahara, L. Agemy, R. Chen, and M. Moskovits for helpful discussions, A. Kylander-Clark for assistance and technical support with ICP-MS, J. Wang for flow cytometry assistance, and the NRI-MCDB Microscopy Facility at UCSB. This work was supported by US

DoD awards W81XWH-10-1-0199 and W81XWH-09-0698. G.B.B. was supported by the Cancer Center of Santa Barbara.

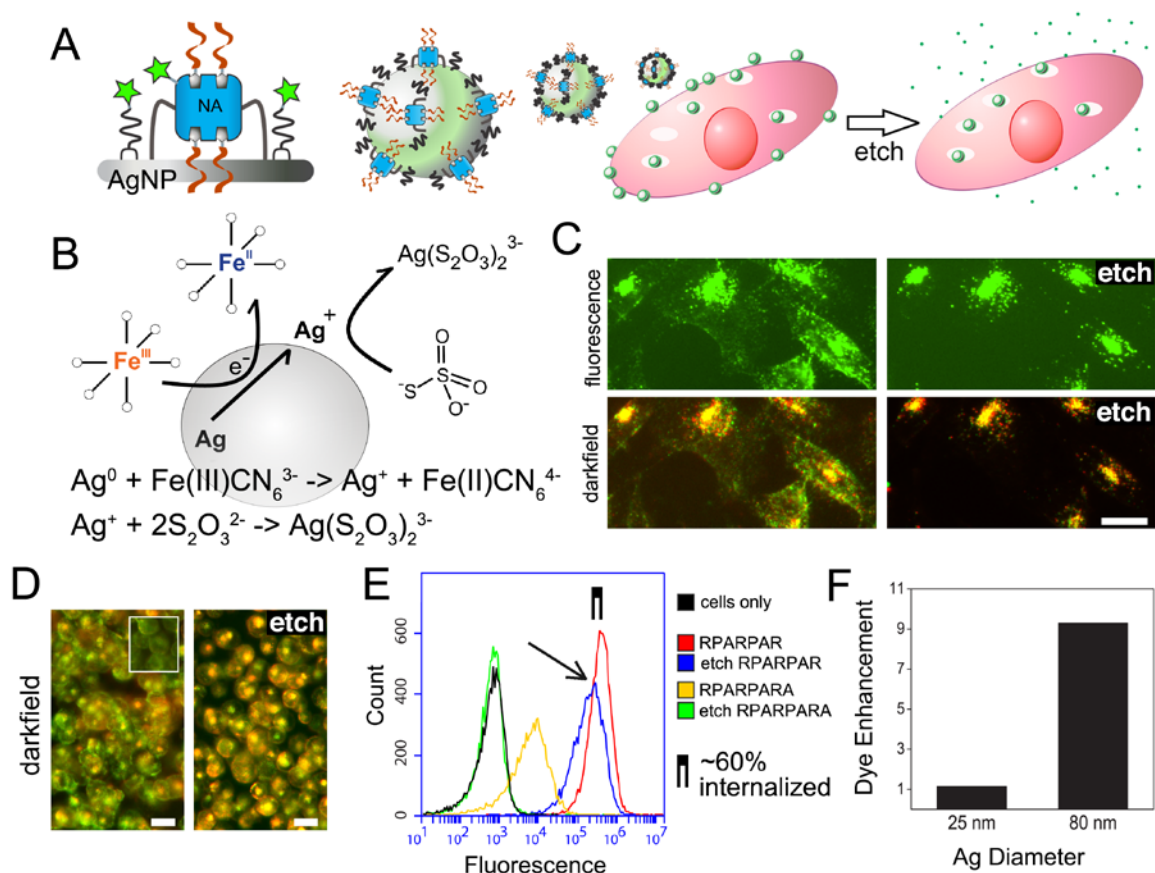


Figure 1. (A) Scheme of silver nanoparticles AgNP with neutravidin (NA) coating, fluorescent dyes (green stars), and internalizing peptide biotin-x-RPARPAR, x is aminohexanoic linker. AgNP-RPARPAR bind to and are taken up by cells, which are treated with brief exposure to etching solution to remove extracellular particles. (B) Etch reagents ferricyanide (10 mM) and thiosulfate (10 mM) oxidize and stabilize silver ions, respectively, releasing components into solution. (C) Fluorescence and darkfield microscopy of cells incubated with dye-labeled AgNP-RPARPAR. Post-etch images show internalized (etch-protected) nanoparticles. Collections of AgNPs in endosomes have the expected red-shifted darkfield scattering. (D) Darkfield images of cell suspensions with AgNP-RPARPAR. Etched cells retain red-shifted signals. Inset shows cells without AgNPs. (E) Flow cytometry fluorescence histograms of cells with AgNP-RPARPAR before (red), and after etching (blue), versus cells without AgNPs (black), and non-internalizing control, biotin-x-RPARPAR AgNPs (yellow, unetched and green, etched). Percent internalization is defined as the ratio of net mean fluorescence signal of etched and unetched populations. (F) AgNP fluorescence enhancement was determined for two Ag diameters by the ratio of solution fluorescence of etched and unetched samples. Strong enhancement is found for the larger Ag.

Supplementary Materials:

Materials and Methods

Figures

Etch solution.

20X Etchant. *Reagent A*: Potassium ferricyanide ($\text{K}_3\text{Fe}(\text{CN})_6$, Sigma, CAS# 13746-66-2) was dissolved in PBS (Hyclone) at 0.20 M. *Reagent B*: Sodium thiosulfate pentahydrate ($\text{Na}_2\text{S}_2\text{O}_3 \cdot 5\text{H}_2\text{O}$, Sigma, CAS# 10102-17-7) was also dissolved in PBS at 0.2 M. These were stored at room temperature in 50 mL polypropylene tubes.

Typically the two solutions were combined with PBS or media to form a 2X solution, used within several hours. E.g. 800 μL PBS, 100 μL Reagent A, 100 μL Reagent B. Equal volume was added to the media containing the cells and AgNPs. Etching power was verified using a stock of concentrated silver particles with observation of color change culminating at that given by the ferricyanide solution itself (yellow). See Fig. S5 for typical colors.

Preparation of silver neutravidin nanoparticles.

Neutravidin (NA, Thermo Scientific) for silver nanoparticle coupling was prepared by modification of NA with NHS-PEG5k-OPSS (Jenken), where OPSS is ortho-pyridyl disulfide. The NA-OPSS was dialyzed against 0.1X PBS ~ pH 6 with 2 mM NaN_3 and assayed for OPSS using reduction by TCEP (tris(2-carboxyethyl)phosphine, 0.5M solution pH 7.0, Sigma). On average 2.2 OPSS were bound per NA, using extinction from pyridyl leaving group of $8.08 \times 10^3 \text{ M}^{-1} \text{ cm}^{-1}$ and $99.6 \times 10^3 \text{ M}^{-1} \text{ cm}^{-1}$ NA (60 kDa).

80 nm silver nanoparticles were prepared using a modification of a method reported by Xia et al. (Sun, Y. G. and Xia, Y. N. J. Am. Chem. Soc. 2004, 126, 3892-3901). First, 0.375 g of AgNO_3 and 1.5 g PVP (polyvinylpyrrolidone, $M_w = 55000$) were dissolved in 150 mL ethylene glycol. This mixture was then heated to 160 °C and the reaction proceeded for 1 h. The silver was cooled and precipitated in a large amount of acetone followed by centrifugation at 1000 RCF for 10 min. The precipitates were redispersed in water. Extinction coefficient used was $1.1 \times 10^{11} \text{ M}^{-1} \text{ cm}^{-1}$, for 80 nm diameter solid spherical silver nanoparticles.

Neutravidin-OPSS was added to the silver PVP in water (~ pH 6) and incubated overnight, then washed by centrifugation at 3300 RCF, sonicating into PBST, made from PBS (Hyclone) with 0.005% Tween 20 (Sigma). Lipoic PEG amine (3400 g/mol, Nanocs Inc.) was dissolved in 70% ethanol and added to the silver NA at a final concentration of 20 μM and incubated overnight at room temperature and 4 °C for 3 days. After centrifuge washing the particles in PBST at 3300 \times g and sonicating, NHS-dyes were added at 50 μM and incubated overnight at 4 °C followed by extensive washing. Particles were washed with PBST and biotin peptides were added at 40 μM for >1 h, then washed with PBST. Dye used for Fig. 1C was CF488A-NHS (Biotium, Cat# 92120), Fig 1D-F Alexa Fluor 647-NHS (Invitrogen, Cat# A20106), and in 1S was CF555-NHS (Biotium, Cat# 92130). Biotin peptides were biotin-x-RPARPAR-OH and biotin-x-RPARPARA-OH (the C-terminal alanine abolishes neuropilin-1 binding), synthesized in house as described previously (19), where x indicates aminohexanoic linker.

25 nm AgNP were synthesized similarly as above but using 10 kDa PVP instead of 55 kDa as given for the 20 nm AgNP procedure (9). 20 g PVP 10kDa (Sigma) was first dissolved in 150 mL ethylene glycol at room temperature, and to this solution the 400 mg AgNO_3 was added with continuous stirring. The suspension was then stirred at room temperature until complete dissolution of the AgNO_3 was achieved. Then, the system was heated up to 120 °C using an oil bath, and the reaction was allowed to proceed for 1 h at this temperature. At the end of the reaction period the colloidal dispersion was cooled until the system reached room temperature. Acetone precipitation was performed as for the larger AgNPs.

Darkfield and epifluorescence microscopy.

For Fig. 1C, PPC-1 cells were plated in 96-well plates, incubated overnight in DMEM with 10% FBS and penicillin/streptomycin. Silver NA with peptide were added and incubated at 37 °C for 1 h, washed, and imaged before and after etching. For darkfield imaging in Fig. 1C a Leica DM-IRE2 inverted microscope, 20X objective, with darkfield condenser S2 was used. Inserting the DAPI filter set passes blue scattering components ~450 nm to

the CCD detector, while the rhodamine filter passes ~570 nm scattered light. Capturing each separately and overlaying identifies monomer silver particles in blue and aggregates in both blue and red. For fluorescence the lamp was used with fluorescein filter set inserted. For visual clarity the darkfield blue channel was pseudocolored green in Figure 1C, such that red-shifted scattering appears yellow in the overlay.

Flow cytometry.

PPC-1 cells were released using enzyme-free dissociation buffer, washed with Hanks buffered saline solution (HBSS, Hyclone) and resuspended in DMEM with 10 μ M t-RNA to limit non-specific binding, and aliquoted into tubes. Silver NA, with either biotin-X-RPAPAR or biotin-X-RPAPARA, was added and the tubes were rotated for 1 h. For etched samples an equal volume of 2X etchant in PBS was added followed by centrifuging and resuspension in media. Analysis was performed on an Accuri C6 Flow Cytometer with blue and red (640 nm) laser, where the red was used to detect Alexa Fluor 647 dye on the silver coating, channel FL-4, and the blue was used for forward and side scatter (FSC, SSC).

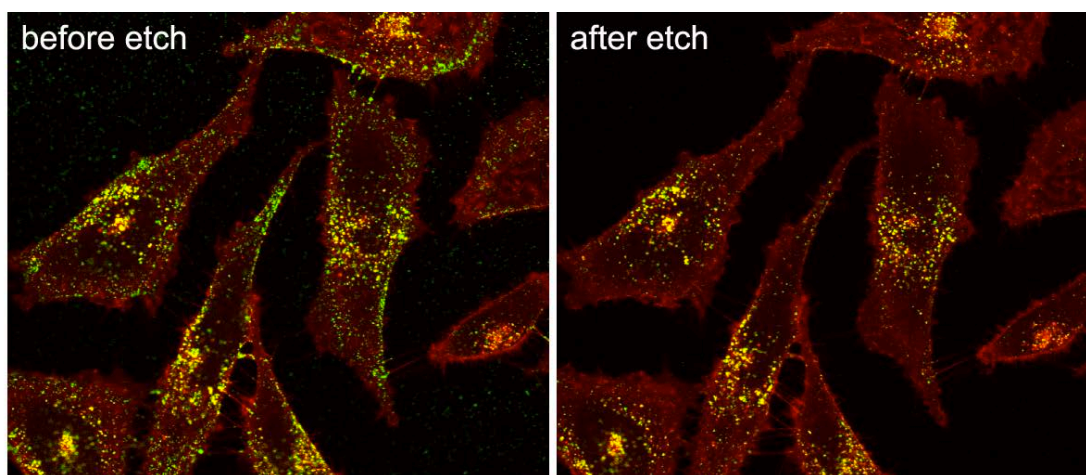
Fluorescence enhancement test.

Fig. 1F experimental info. AgNP-NA was reacted with Biotium 555-NHS dye as described above, and washed extensively by centrifugation in PBST. 100 μ L was aliquoted into wells in a 96 well plate. To control wells, 100 μ L PBS was added. Etched samples received 100 μ L of 2X etch in PBS. In separate experiments the dye was found to not be affected by the etch solution. Small AgNP had minimal difference between etched and unetched wells, supporting the robustness of the dye and the use of this simple method to compare coatings during synthesis.

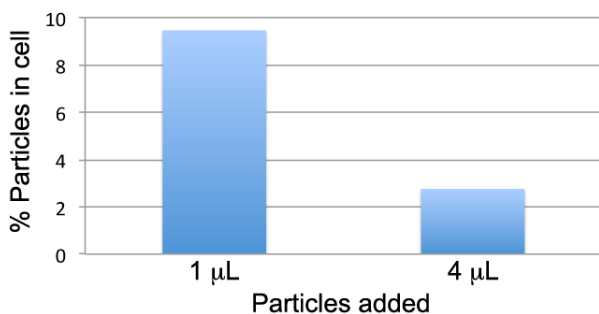
Supplemental Figures, methods and legends.

Figure S1. Live imaging of NP internalization using CF488A-dye.

PPC-1 cells were grown on collagen I (BD) coated coverslips (eight chambers, Bioexpress) for two days. The cells were then incubated with cell mask orange (Invitrogen) for 5 min in cell culture media, to visualize the membrane as well as endosomes formed after staining. The cells were washed three times in HBSS and ~10 pM 80 nm CF488 AgNPs was added in cell culture media and incubated for 45 min. Unbound particles were washed off with HBSS. An equal volume of etching solution was then injected into the culture chamber while on the microscope stage (Fluoview 500, Olympus). Time-lapse series of images were collected and movies were produced with Fluoview software (Olympus). Frames were cropped and presented here before and after etch. Cell mask stain in red traces the plasma membrane and endosomal structures, and green for the AgNPs, overlaid. Yellow indicates colocalization.



Samples were analyzed using a Nu Atom high-resolution ICP-MS in static peak-jumping mode. Cells were incubated with high dose silver NA RPARPAR in 6 well plates, washed with HBSS to saturate uptake and verify removal of silver. Wells were lysed then etch was added to give ‘total’ silver. ‘Internalized’ samples were etched and washed prior to cell lysis, then etched again to recover internalized silver. ICP-MS signals from ‘internalized’ divided by ‘total’ was used to quantify cell uptake. Notably, with this assay format any particles that non-specifically bind the plate will decrease uptake value.



Concentration of the two reagents was optimized in a plate format. Complete etching of a high concentration of silver nanoparticles was judged by visual inspection of the color and reduced scattering, and darkfield microscopy. Ag particles with PVP coating (80 nm diam, 200 optical density at 450 nm) were diluted by 10 in PBS with 0.005% Tween-20 (Sigma). 100 μ L was added per well. A variable amount of sodium thiosulfate solution (100 mM in water) and potassium ferricyanide (30mM, or (*)100mM for rows G and H, in water). Boxed wells show the clarified solution at minimum of 8 mM ferricyanide and 8 mM thiosulfate. The lack of particles was verified by depositing solution onto a glass slide for darkfield analysis. A fraction of particles were observed to survive the well for 6.5 mM ferricyanide and 4 mM thiosulfate. Working concentration of 10 mM of each component was chosen for each component.

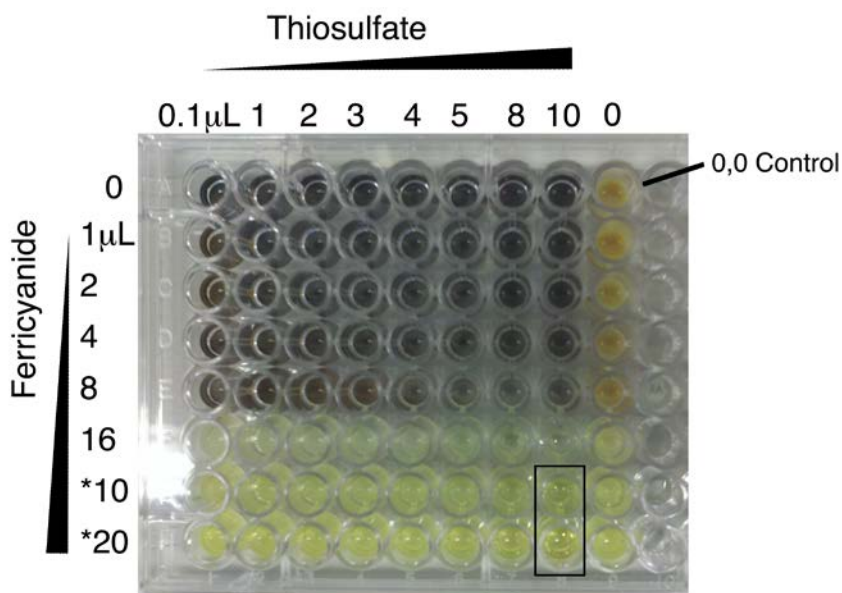


Figure S4. Cell viability after etching. (A) PPC-1 cells were exposed to AgNP with NA and biot-x-RPARPAR-OH for one hour. The etch solution was added, incubated for 1 h, followed by washing and replacing with new media. After overnight culture at 37°C the cell morphology by brightfield analysis was compared to (B) control cells having nothing added.

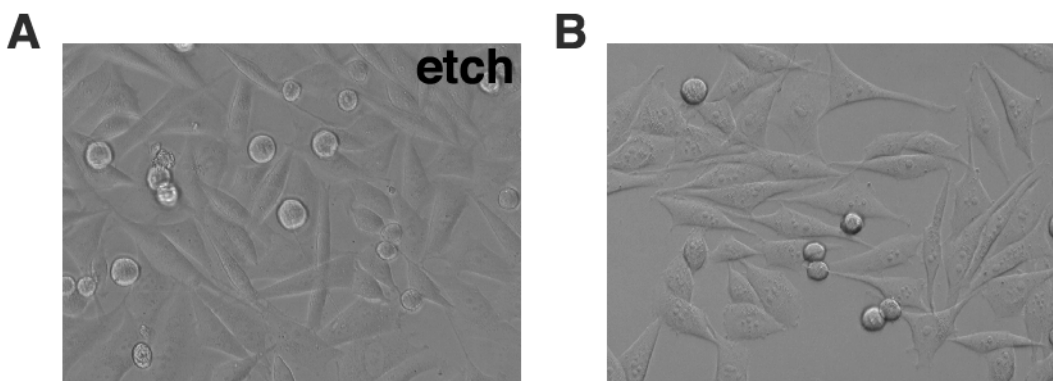


Figure S5. Ascorbate effect on etching. Sodium ascorbate, known for its ability to reduce the ferricyanide, was found to block the etching of AgNPs. The yellow ferricyanide/thiosulfate solution turns clear upon adding ascorbate at a 2:1 molar ratio over the ferricyanide. AgNPs survive the ascorbate blocked etch. This supports the importance of the redox state of ferricyanide, and indicates the use of ascorbate as a quenching agent.

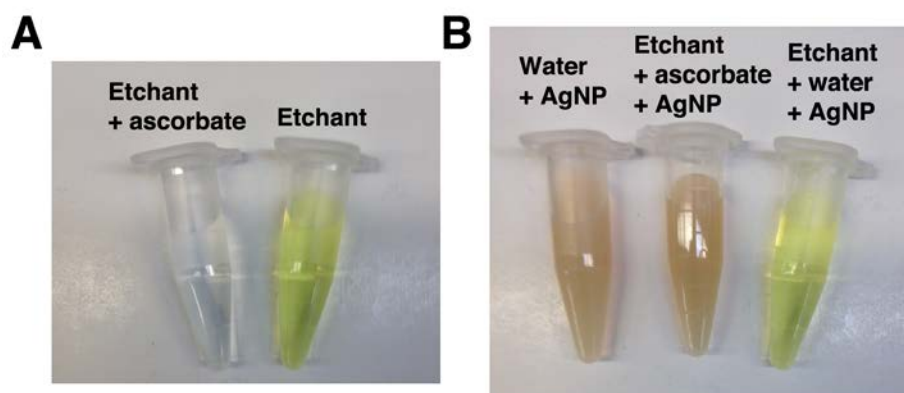
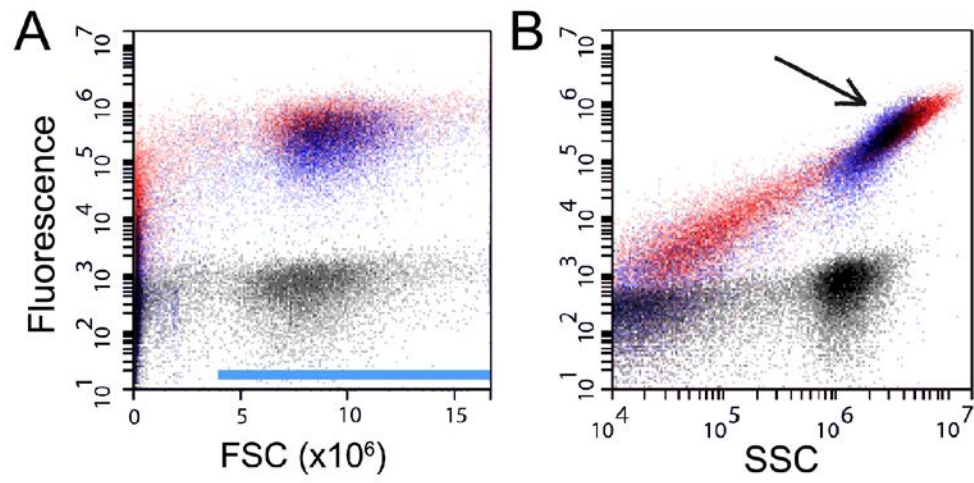


Figure S6. Additional flow cytometry. Dot plots of fluorescence versus forward scatter (FSC) and side scatter (SSC) show all events collected for the data set in Fig. 1D. (A) FSC detects cells but not AgNPs and is used for gating. Cells were identified for Fig. 1D by the FSC window indicated by the blue bar. The color code is the same as for Fig. 1D, where red is AgNP-RPARPAR and blue is with etch. Black is for control cells without AgNP. (B) SSC shows some sensitivity to AgNP, likely due to the overlap of plasmon resonance with the laser (450 nm resonance, 488 nm laser). Fluorescence is found to be linearly proportional to SSC (red streak), for AgNP which are free or bound to debris, or in cells (which have a characteristic SSC given in black). Etch sample in blue shows loss of

events below the cell-minimum SCC, consistent with these being cell associated, and a slight loss of the upper-rightmost population, attributed to the loss of membrane bound AgNP.



1. Tassa, C., S.Y. Shaw, and R. Weissleder, *Dextran-coated iron oxide nanoparticles: a versatile platform for targeted molecular imaging, molecular diagnostics, and therapy*. *Acc Chem Res*, 2011. 44(10): p. 842-52.
2. Ruoslahti, E., *Peptides as Targeting Elements and Tissue Penetration Devices for Nanoparticles*. *Adv Mater*, 2012.
3. Jiang, W., et al., *Nanoparticle-mediated cellular response is size-dependent*. *Nat Nanotechnol*, 2008. 3(3): p. 145-150.
4. Chithrani, B.D. and W.C. Chan, *Elucidating the mechanism of cellular uptake and removal of protein-coated gold nanoparticles of different sizes and shapes*. *Nano Lett*, 2007. 7(6): p. 1542-50.
5. Chithrani, B.D., A.A. Ghazani, and W.C.W. Chan, *Determining the size and shape dependence of gold nanoparticle uptake into mammalian cells*. *Nano Lett*, 2006. 6(4): p. 662-668.
6. Sun, Y. and Y. Xia, *Gold and silver nanoparticles: a class of chromophores with colors tunable in the range from 400 to 750 nm*. *Analyst*, 2003. 128(6): p. 686-91.
7. Wiley, B., Y. Sun, and Y. Xia, *Synthesis of silver nanostructures with controlled shapes and properties*. *Acc Chem Res*, 2007. 40(10): p. 1067-76.
8. Lakowicz, J.R., *Radiative decay engineering 5: metal-enhanced fluorescence and plasmon emission*. *Anal Biochem*, 2005. 337(2): p. 171-94.
9. Zhang, F., et al., *Fabrication of Ag@SiO₂@Y(2)O(3):Er nanostructures for bioimaging: tuning of the upconversion fluorescence with silver nanoparticles*. *J Am Chem Soc*, 2010. 132(9): p. 2850-1.
10. Mulvihill, M.J., et al., *Anisotropic etching of silver nanoparticles for plasmonic structures capable of single-particle SERS*. *J Am Chem Soc*, 2010. 132(1): p. 268-74.
11. Braun, G.B., et al., *Generalized Approach to SERS-Active Nanomaterials via Controlled Nanoparticle Linking, Polymer Encapsulation, and Small-Molecule Infusion*. *Journal of Physical Chemistry C*, 2009. 113(31): p. 13622-13629.
12. Kim, J.H., et al., *Specific and sensitive detection of nucleic acids and RNases using gold nanoparticle-RNA-fluorescent dye conjugates*. *Chem Commun (Camb)*, 2007(42): p. 4342-4.
13. Goulet, P.J., G.R. Bourret, and R.B. Lennox, *Facile phase transfer of large, water-soluble metal nanoparticles to nonpolar solvents*. *Langmuir*, 2012. 28(5): p. 2909-13.
14. Cho, E.C., et al., *Understanding the role of surface charges in cellular adsorption versus internalization by selectively removing gold nanoparticles on the cell surface with a I₂/KI etchant*. *Nano Lett*, 2009. 9(3): p. 1080-4.
15. Meywald, T., H. Scherthan, and W. Nagl, *Increased specificity of colloidal silver staining by means of chemical attenuation*. *Hereditas*, 1996. 124(1): p. 63-70.
16. Scheler, C., et al., *Peptide mass fingerprint sequence coverage from differently stained proteins on two-dimensional electrophoresis patterns by matrix assisted laser desorption/ionization-mass spectrometry (MALDI-MS)*. *Electrophoresis*, 1998. 19(6): p. 918-27.

17. Van Duijn, M.M., *Ascorbate Stimulates Ferricyanide Reduction in HL-60 Cells through a Mechanism Distinct from the NADH-dependent Plasma Membrane Reductase*. *Journal of Biological Chemistry*, 1998. 273(22): p. 13415-13420.
18. Burdinski, D. and M.H. Bles, *Thiosulfate- and thiosulfonate-based etchants for the patterning of gold using microcontact printing*. *Chemistry of Materials*, 2007. 19(16): p. 3933-3944.
19. Teesalu, T., et al., *C-end rule peptides mediate neuropilin-1-dependent cell, vascular, and tissue penetration*. *Proc Natl Acad Sci U S A*, 2009. 106(38): p. 16157-62.
20. Sugahara, K.N., et al., *Tissue-penetrating delivery of compounds and nanoparticles into tumors*. *Cancer Cell*, 2009. 16(6): p. 510-20.
21. Teesalu, T., K.N. Sugahara, and E. Ruoslahti, *Mapping of vascular ZIP codes by phage display*. *Methods Enzymol*, 2012. 503: p. 35-56.

**Application of a Proapoptotic Peptide for an Intratumoral-Spreading
Cancer Therapy**

Renwei Chen, Gary B Braun, Xiuquan Luo, Kazuki N. Sugahara, Tambet Teesalu,
Erkki Ruoslahti

Center for Nanomedicine, Sanford-Burnham Medical Research Institute at University
of California, Santa Barbara, CA 93106 and Cancer Research Center, Sanford-
Burnham Medical Research Institute, La Jolla, CA 92037, USA

Correspondence to: Erkki Ruoslahti, M.D., Ph.D. Tel: 1(805)893-5327, Fax:
1(805)893-5805, E-mail: ruoslahti@sanfordburnham.org

Running title: Intratumorally spreading tumor therapy

Key words: Bit1 cell death domain, protein transduction, cell internalization, tissue
penetration, tumor therapy

The abbreviations used are: Bit1, Bcl-2 inhibitor of transcription; CDD, cell death
domain; Pth2, peptidyl-tRNA hydrolase 2; AES, amino enhancer of split; TLE,
transducing-like enhancer of split; CendR, C-end Rule; NRP-1, neuropilin-1; SPDP,
N-succinimidyl 3-(2-pyridyldithio)-propionate.

Footnotes: Xiuquan Luo, present address: University of Texas Southwestern Medical
Center, Simmons Comprehensive Cancer Center, xiuquan.luo@utsouthwestern.edu

1 Word count: 4995

2 Total number of Figures: 6

3

4 Grant support: This work was supported by grants W81XWH-10-1-0199 and

5 W81XWH-08-1-0727 from the DOD (E.R.) and Cancer Center Support Grant

6 CA30199 from the NCI.

7

8 Competing Interest: KNS, TT and ER are shareholders of CendR Therapeutics Inc,

9 that has rights to some of the technology described in this paper. RC, GB, and XL

10 declare no conflict of interest.

11

1 **Abstract**

2

3 Bit1 is a pro-apoptotic mitochondrial protein associated with anoikis. Upon cell
4 detachment, Bit1 is released into the cytoplasm and triggers caspase-independent
5 cell death. Bit1 consists of 179 amino acids; the C-terminal two thirds of the molecule
6 functions as a peptidyl-tRNA hydrolase, while the N-terminus contains a
7 mitochondrial localization signal. Here, we localize the cell death domain (CDD) to
8 the N-terminal 62 amino acids of Bit1 by transfecting cells with truncated Bit1 cDNA
9 constructs. CDD was more potent in killing cells than the full-length Bit1 protein when
10 equivalent amounts of cDNA were transfected. To develop Bit1 CDD into a cancer
11 therapeutic we engineered a recombinant protein consisting of the CDD fused to
12 iRGD, which is a tumor-specific peptide with unique tumor-penetrating and cell-
13 internalizing properties. iRGD-CDD internalized into cultured tumor cells through a
14 neuropilin-1-activated pathway and triggered cell death. Importantly, iRGD-CDD
15 spread extensively within the tumor when injected intratumorally into orthotopically
16 implanted breast tumors in mice. Repeated treatment with iRGD-CDD strongly
17 inhibited tumor growth, resulting in an average reduction of 77% in tumor volume
18 and eradication of some tumors. The caspase independence of Bit1-induced cell
19 death makes CDD a potentially attractive anti-cancer agent because tumor
20 resistance to the main mechanisms of apoptosis is circumvented. Using iRGD to
21 facilitate the spreading of a therapeutic agent throughout the tumor mass may be a
22 useful adjunct to local therapy of tumors that are surgically inoperable or difficult to
23 treat systemically.

24

25

1 **Introduction**

2

3 Cell-matrix interactions are important for cell survival, and failure of cells to
4 adhere to the extracellular matrix results in anoikis (1). Bit1 is a mitochondrial
5 peptidyl-tRNA hydrolase that causes cell death when released into the cytoplasm or
6 experimentally expressed there (2). Bit1 release occurs upon loss of cell attachment,
7 resulting in cell death (2). Bit1 negatively regulates Erk activation, revealing a
8 possible molecular pathway for the anoikis regulation (3, 4). Cytosolic Bit1 interacts
9 with the Groucho family transcriptional co-regulator Amino-terminal Enhancer of Split
10 (AES) to induce caspase-independent cell death (2). These activities and the ability
11 of Bit1 to counteract transducin-like enhancer of split 1 (TLE1), which is an anti-
12 apoptotic oncoprotein, suggest a tumor suppressor role for Bit1 (2, 5, 6). A unique
13 property of Bit1 is that cell attachment through certain integrins can prevent cell
14 death induced by cytoplasmic Bit1, whereas various anti-apoptotic signaling
15 molecules, such as Bcl-2, Bcl-xL, PI-3K, and Akt, can prevent the release of Bit1
16 from mitochondria, but are unable to rescue the cell death caused by cytoplasmic
17 Bit1 (2).

18 Bit1 is a 179-amino acid protein in which amino acids 63-179 at the C-terminus
19 of the molecule constitute the catalytic, peptidyl-tRNA hydrolase 2 (Pth2) domain and
20 the N-terminus serves as a mitochondrial localization signal (2, 7). It is also known
21 that the N-terminal domain is needed for the apoptotic activity (2, 7), but the active
22 site has not been mapped in detail and the mechanism whereby Bit1 causes cell
23 death is not fully understood. We undertook this study to define the cell death
24 domain (CDD) of Bit1, delineate its mechanism of action, and explore its use as an
25 anti-tumor drug. To deliver Bit1 CDD protein into tumor cells and deal with the

1 problem of poor penetration of anticancer drugs in solid tumors (8, 9), we employed
2 so-called C-end Rule or CendR peptides. These peptides contain a CendR motif
3 (R/KXXR/K), which binds to neuropilin-1 (NRP-1) triggering a cell internalization and
4 tissue penetration pathway (10, 11). The CendR motif has to be at the C-terminus of
5 the peptide to be active. The iRGD peptide contains a cryptic CendR motif
6 (sequence: CRGDKGPDC; CendR motif underlined). This peptide activates the
7 CendR pathway specifically in tumors because it first binds to $\alpha v \beta 3$ and $\alpha v \beta 5$
8 integrins, which are expressed in tumor vessels and various types of other cells
9 within tumors, but not in normal tissues. Having bound to the integrins in a tumor,
10 iRGD is proteolytically cleaved to generate a fragment with a C-terminal CendR motif
11 that binds to NRP-1 and activates the CendR pathway (10).

12

13 **Materials and Methods**

14

15 *Reagents, cell lines, and tumors*

16 Mouse anti-human NRP-1 monoclonal antibody was purchased from Miltenyi
17 Biotec Inc; rabbit anti-Ki67 polyclonal antibody was from Abcam; mouse anti- β -actin
18 monoclonal antibody was from Sigma-Aldrich; The secondary antibodies used were
19 Alexa Fluor® 488-conjugated goat IgG (Invitrogen Life Technologies) Full-length
20 cDNA for Bit1 in the mammalian expression vector pCMV-myc were generated
21 previously in the lab (2). QuikChange Mutagenesis Kit for Bit1 mutagenesis was
22 purchased from Agilent Technologies. In situ cell death detection kit for terminal
23 deoxynucleotidyl transferase-mediated deoxyuridine triphosphate nick end labeling
24 (TUNEL) and FuGENE®6 Transfection Reagent for overexpression was purchased

1 from Roche Applied Science. MTT for cell viability assay was from Invitrogen Life
2 Technologies.

3 Human cell lines from Embryonic Kidney (HEK) 293T, PPC1 prostate cancer,
4 M21 melanoma, and MCF-10CA1a breast cancer were maintained in Dulbecco's
5 modified Eagle's medium with glutamine containing 10% FBS, penicillin and
6 streptomycin at 37°C and 5% CO₂. Mouse breast cancer cell line 4T1 was
7 maintained in Iscove's modified Dulbecco's medium with glutamine containing 10%
8 FBS, penicillin and streptomycin.

9 To produce orthotopic tumors, one million of tumor cells in 100 µl of PBS were
10 injected into the mammary fat pad of mice. Athymic nude mice (Harlan Laboratories)
11 were used for MCF-10CA1a cells and normal Balb/C mice (Charles River) for 4T1
12 cells. All animal procedures were performed in compliance with the guidelines
13 approved by the Animal Research Committee at the University of California, Santa
14 Barbara.

16 *Construction and production of recombinant CDD proteins*

17 Recombinant CDD proteins were prepared as follows: The CDD sequence was
18 cloned into the bacterial expression vector pRSET containing a hexahistidine tag
19 (Invitrogen Life Technologies). Because CDD harbors a mitochondrial signal peptide,
20 a myc-tag was placed at the N-terminus of CDD to prevent the fusion protein from
21 localizing to mitochondria. To generate cell and tissue-penetrating CDD proteins,
22 oligonucleotides encoding the CendR peptides, RPARPAR (11) or iRGD (sequence:
23 CRGDKGPDC) (10) were synthesized and ligated to the downstream of
24 oligonucleotides encoding the CDD, with a glycine-serine linker placed in between
25 (Supplementary Fig. S1A). All construct sequences were confirmed by DNA

1 sequencing. Proteins were expressed in *E. coli* BL21 (DE3) plysS strain (Novagen)
2 after induction at 30°C for 24 h using MagicMedia™ *E. coli* Expression Medium
3 (Invitrogen Life Technologies) according to the manufacturer's instructions. The
4 recombinant proteins were purified using Ni-NTA affinity chromatography under
5 native conditions by using ÄKTA™ FPLC system. The bound proteins were eluted
6 with 20 mM sodium phosphate buffer containing 300 mM imidazole, pH 8.0. The
7 eluates were dialyzed against PBS pH 7.4 containing an additional 360 mM NaCl. In
8 some experiments, the his-tag was removed using enterokinase (Invitrogen Life
9 Technologies) according to the manufacturer's instructions. Bit1 CDD proteins
10 migrated as major bands at 13 kDa (CDD) and 16 kDa (RPARPAR-CDD and iRGD-
11 CDD) in Coomassie Blue-stained 4-20 % SDS-PAGE. The protein identities were
12 confirmed by immunoblotting using antibodies against his-tag or myc-tag
13 (Supplementary Fig. S1B). Labeled recombinant proteins were prepared by
14 conjugating with a Dylight 550 NHS ester dye (Dy550) (Pierce Biotechnology) at
15 amine groups. The labeled protein was dialyzed and filtered (0.22 µm). Absorbance
16 measurement was used to determine the dye concentration and degree of labeling,
17 which was somewhat less than an average of one dye group per protein molecule.

18

19 *Cell internalization of the recombinant proteins*

20 Sub-confluent tumor cells on chamber slides (Nalge Nunc International) were
21 incubated with 3 µM Dy550-labeled protein between 30 min and 24 h. The cells were
22 then washed 3 times with PBS and fixed with ice-cold methanol for 10 min. The
23 specimens were mounted with DAPI-containing Vectashield® media (Vector
24 Laboratories) and analyzed under a confocal microscope, Olympus Fluoview 500.

1 Peptide-conjugated dextran was used to inhibit peptide-CDD protein for cell
2 internalization. A thiol-reactive dextran conjugate was prepared by modifying amino-
3 dextran 10 kDa (5.1 amines per strand, Invitrogen Life Technologies) with N-
4 succinimidyl 3-(2-pyridyldithio)-propionate (SPDP), and dialyzed using Slide-A-Lyzer
5 Dialysis Cassettes 3,500 MWCO (Pierce Biotechnology). To the SPDP-dextran, an
6 excess Cys-peptide was added, followed by extensive dialysis. Each dextran
7 molecule contained, on average, 5 copies of peptide. Inhibition assays were carried
8 out by incubating 3 μ M dextran conjugated peptide and 3 μ M Dy550-labeled CDD
9 protein with PPC1 cells for 1 h at 37°C. The cells were then washed, fixed, and
10 analyzed by confocal microscopy as described above.

11 *Tumor tissue penetration ex vivo and in vivo*

12 Protein penetration in tumors was studied *ex vivo* using fresh explants of MCF-
13 10CA1a tumors. Excised tumors were cut into pieces and incubated at 37°C with 20
14 μ M Dy550-labeled proteins in DMEM containing 1% BSA. Binding and entry of
15 proteins to the cut surface were examined by confocal microscopy (Olympus
16 Fluoview 500). *In vivo* protein penetration was analyzed using orthotopic MCF-
17 10CA1a tumor xenografts in mice. Dy550-labeled protein (20 μ l of 35 μ M solution;
18 approximately 10 μ g protein per tumor) was injected into the center of tumor (60-
19 80mm³) with spheroidal shape using 31-gauge needle, and 4 hours later, entire tumors
20 were dissected and fixed in 4% PFA. Five- μ m serial sections from entire tumors
21 were stained with DAPI and scanned using ScanScope FL 6114 (Aperio
22 Technologies, Inc).

23 *Tumor treatment*

1 Tumor-bearing mice were assigned to three treatment groups approximately 4
2 weeks after the inoculation of MCF-10CA1a cells and 9 days after the inoculation of
3 4T1 cells. The assignment was based on tumor size to ensure there was no
4 statistically significant difference in tumor volume among the groups at the time the
5 treatment began. Tumor volume was calculated from two diameter measurements
6 using a digital vernier caliper and the formula: tumor volume = (length × width²) / 2.
7 Proteins were diluted in PBS at 0.3 µg/µl and injected intratumorally. The injected
8 volume was one third of the tumor volume (0.33 µl of solution per mm³ of the tumor)
9 (12). The tip of the needle was advanced to the center of the tumor and the protein
10 solution was injected over the course of 30 seconds. The injections were given every
11 3 days (a total of 4 injections in the MCF-10CA1a and 3 in the 4T1 model).

12

13 *Statistical analysis*

14 Data were analyzed by Student t-test, one-way ANOVA, and two-way ANOVA
15 followed by a suitable post hoc test using GraphPad Prism 5 software (Graphy Pad
16 Software, San Diego, CA).

17

18 **Results**

19

20 *Localization of Bit 1 cell death domain*

21 Forced expression in the cytoplasm of full-length Bit1 has been shown to induce
22 caspase-independent cell death, whereas the C-terminal catalytic domain lacks this
23 activity (2). Hence we focused our analysis on the N-terminal domain. To identify the
24 cell death domain, we expressed a panel of N-terminally myc-tagged Bit1 fragments
25 in HEK 293T cells because the N-terminal tag prevents mitochondrial localization of

1 Bit1 (2). Transient transfection of full-length Bit1 and the N-terminal 1-62 amino
2 acids (F1-62) caused significant cell death, whereas various shorter fragments from
3 the N-terminal domain showed lesser or no activity (Fig. 1; Supplementary Fig. S2A).
4 The catalytic Pth2 domain did not induce cell death, but instead caused a modest
5 increase in cell viability, providing a possible explanation for the higher activity of F1-
6 62 than full-length Bit1 (Fig. 1). The vector control had no effect on cell viability.
7 Based on these results, we defined the F1-62 fragment as a Bit1 cell death domain
8 (CDD).

9 The Bit1 CDD includes a conserved transmembrane segment at residues 14-33
10 (PSTLGLAVGVACGMCLGWSL) in the human Bit1 sequence (Supplementary Fig.
11 S2B). Deleting these residues (Δ 14-33) resulted in cytosolic and nuclear expression,
12 whereas the first 13 residues were not required for the mitochondrial localization
13 (Supplementary Fig. S2C). These findings are consistent with the enzymatic Pth2
14 domain exposed to the cytoplasm (Supplementary Fig. S2D and S2E).

15

16 *Internalization of CendR-modified Bit1 CDD protein into cells*

17 To deliver Bit1 CDD into cells and potentially into their cytoplasm, we fused CDD
18 to a tumor-penetrating peptide iRGD. For comparison, we also used RPARPAR, a
19 peptide in which the CendR motif is constitutively active. Bit1 CDD with no CendR
20 peptide showed negligible binding to PPC1 cells, a cell line that expresses high
21 levels of NRP-1 (Fig. 2A, panel a). In contrast, both RPARPAR-CDD and iRGD-CDD
22 effectively bound to and were taken up into these cells (Fig. 2A, panels b and c).
23 CDD and RPARPAR-CDD did not bind to or internalize into the NRP-1-deficient
24 melanoma cell line M21 (11) (Fig 2A, panels d and e). iRGD-CDD bound to the
25 surface of the M21 cells but was only weakly internalized (Fig. 2A, panel e),

1 consistent with M21 cells expressing high levels of the relevant integrins (13). Cell
2 entry of RPARPAR-CDD was rapid; after 30-min incubation, the protein was
3 detectable in PPC1 cells, colocalizing with NRP-1 (Fig. 2B). The amount of
4 internalized RPARPAR-CDD peaked around 3 h and much of the protein was found
5 in perinuclear vesicles. Consistent with the 3-step cell entry process, internalization
6 of iRGD-CDD was slower than that of RPARPAR-CDD (Fig. 2C). Twenty-four hours
7 after these proteins were introduced into the cultures, the cells rounded up, shrank,
8 and partially detached, indicating cell death (Fig. 2B and 2C). Dextran-conjugated
9 RPARPAR and iRGD inhibited the internalization of RPARPAR-CDD and iRGD-CDD
10 protein, respectively, whereas dextran alone or dextran conjugated with iRGE
11 (CRGEKGPDC), which does not bind to integrins showed no inhibition of the iRGD-
12 CDD interaction with cells (Fig. 2D). These controls clearly establish the specificity of
13 the CendR peptide-modified CDDs.

14

15 *Reduction of cell viability by CendR-modified CDD proteins*

16 Treatment of cultured breast cancer cells MCF-10CA1a and 4T1 with iRGD-CDD
17 or RPARPAR-CDD significantly reduced cell viability, whereas non-modified CDD
18 protein had a modest effect at the highest concentrations or no effect at all (Fig. 3A).
19 RPARPAR-CDD was no more cytotoxic to NRP-1-deficient M21 cells than
20 unmodified CDD protein at the highest concentration used (3 μ M), indicating that the
21 marginal toxicity at this concentration was not related to the CendR targeting. iRGD-
22 CDD decreased M21 cell viability more than the other two CDD proteins, possibly
23 because of integrin-mediated internalization, but the difference to RPARPAR-CDD
24 and CDD was not statistically significant (Fig. 3A).

1 Histidine has been shown to enhance endosomal escape, explained in part by a
2 cationic transition at low pH (14-17). Enterokinase cleaves fusion proteins containing
3 the (Asp)₄-Lys recognition sequence (18), which is positioned in our construct
4 between the his-tag and the CDD domain. The his-tag in iRGD-CDD was cleaved
5 and removed using enterokinase and Ni-NTA affinity chromatography purification.
6 The removal of the his-tag in the resulting iRGD-CDD was confirmed by SDS-PAGE
7 (Fig. 3B). Cytotoxicity tests in MCF-10CA1a cells showed that the his-tag effect on
8 construct toxicity was not significant (Fig. 3C). Thus, the his-tag plays only a minor
9 role, if any, in the endosomal escape of the iRGD-CDD protein.

11 *Penetration of iRGD-CDD into tumor tissue*

12 The iRGD peptide extravasates and penetrates into extravascular tumor tissue
13 when intravenously injected into tumor-bearing mice (10). We analyzed the
14 penetration ability of the CDD proteins by using fresh MCF-10CA1a tumor explants.
15 CDD showed modest binding to the cut surface of tumor tissue. iRGD-CDD, however,
16 bound strongly and even penetrated several cell layers into the tumor tissue (Fig.
17 4A).

18 The tumor penetration activity was also apparent when fluorescently labeled
19 iRGD-CDD was intratumorally injected into MCF-10CA1a tumors in mice. The strong
20 iRGD-CDD signal was detectable in all sections from an entire tumor (Fig. 4B). It
21 exhibited a web-like pattern resembling fibrotic stromal morphology (Fig. 4B, panel 5
22 inset a). Fibrosis is one of the major barriers that prevent drug distribution within
23 tumor tissue. The ability of iRGD to penetrate fibrotic areas in tumors should help
24 overcome this issue and improve local chemotherapy. The wide positive areas along
25 the tumor periphery were presumably caused by outside-in penetration of iRGD-

CDD that overflowed during the injection and the signals were not detectable outside of tumor rim (Fig. 4B, panel 5 inset *b*). Sporadic localized iRGD-CDD signals were detectable throughout the tumor suggesting protein penetration by active transport (Fig. 4B, panel 7 inset). When CDD was injected, significant intratumoral signals were only present near the injection site (Fig. 4C, panels 3 and 4). The CDD protein that overflowed during the injection remained outside the tumor rim (Fig. 4C, panels 1 through 6, and inset), and showed minimal penetration into the tumor tissue (Fig. 4C). The total signal of the CDD protein was lower than that of the iRGD-CDD, possibly because there is no ligand for CDD protein on tumor cells, allowing the protein to be exported from the tumor. These data support the notion that iRGD mediates active tumor penetration of the CDD protein utilizing the NRP-1-dependent CendR pathway.

Inhibitory effect of iRGD-CDD on tumor growth in mice

Two aggressive breast tumor models MCFA-10CA1a and 4T1 were used for evaluation of antitumor effect by the iRGD-CDD protein. Etoposide, a topoisomerase inhibitor that induces caspase-dependent apoptosis in cancer cells (19), was capable of activating caspase 3 in 4T1 cells, but failed in MCF-10CA1a cells, suggesting an impaired caspase cascade signaling in the MCF-10CA1a cells (Supplementary Fig. S3). This lack of correlation between CDD activity and caspase independence agrees with the previously documented caspase independence of cell death induced by the full length of Bit1 protein.

We next sought to determine whether tumor-targeted Bit1 CDD could be used as a therapeutic agent. We initially administered iRGD-CDD or CDD intravenously at 10 mg per kilogram of mouse body weight every other day. The initial results suggested

1 an anti-tumor effect by iRGD-CDD that was not seen with CDD, but symptom of the
2 severe toxicity required euthanasia intervention (Fig. S4). Thus, we turned our
3 attention to local treatment. The MCF-10CA1a tumors grew rapidly in mice treated
4 with intratumoral injections of the PBS or CDD. In the iRGD-CDD treated mice,
5 inhibition of tumor growth was evident as early as 3 days after the treatment began.
6 At the end of treatment on day 12, the tumor volume was reduced by about 77%
7 compared to the PBS and CDD controls (Fig. 5A). Tumor weights at the end of the
8 experiments were in agreement with the size measurements; the mean weight of the
9 tumors in the iRGD-CDD group was 30% of that in the control groups (Fig. 5B).
10 Notably, 2 out of 8 mice (25%) in the iRGD-CDD treated group had too small tumors
11 to be excised after 12 days of treatment. The small nodules at the tumor inoculation
12 site in these two mice disappeared during the following several weeks without any
13 further treatment. No skin abnormalities were observed around the injection sites,
14 suggesting the tumor specific penetration of iRGD-CDD (Fig. 5C). The mice were
15 healthy and had no signs of tumor metastasis during 6 months of observation.

16 The treatment results in the 4T1 tumor model were also positive, but reflected
17 the greater aggressiveness of these tumors than the MCF-10CA1a tumors. Tumor
18 volume in iRGD-CDD group was about 40% and tumor weight about 50% smaller
19 than in the PBS and CDD control groups (Fig. 5D and 5E).

20 Hematoxylin and eosin (H&E) stained tumor sections did not show differences
21 among tumors treated with iRGD-CDD, CDD, or PBS (Fig. 6A). Tumors from the
22 iRGD-CDD groups, however, showed significantly stronger TUNEL staining than
23 tumors treated with PBS or CDD, indicating substantial cell death in the iRGD-CDD-
24 treated tumors (Fig. 6B). In agreement with the TUNEL result, staining for the Ki-67

1 marker of cell proliferation was significantly lower in the iRGD-CDD-treated tumors
2 than in the PBS or CDD controls (Fig. 6C).

3 4 **Discussion**

5 In this work, we define the Bit1 cell death domain, localize it to the presumed
6 membrane-embedded domain of the protein and show that CDD is more potent than
7 full length Bit1 in causing cell death when tested by cDNA transfection. We also
8 show that the CDD protein is highly active when introduced into tumor cells using
9 protein transduction mediated by the tumor-penetrating and cell-internalizing peptide
10 iRGD, and that the fusion protein is a promising anti-tumor agent capable of
11 spreading within tumor tissue from an intratumoral injection.

12 Our results place the CDD of Bit1 in the N-terminal domain, which contains the
13 20-amino acid hydrophobic sequence thought to anchor Bit1 to the mitochondrial
14 outer membrane. Targeting of polypeptides encoded in the nucleus to mitochondria
15 requires the presence of a signal sequence for mitochondrial localization. Most of
16 these sequences contain positively charged amphipathic alpha helical stretch at the
17 N-terminus, followed by a stretch of hydrophobic residues (20). The Bit1 N-terminus
18 fulfills these criteria (Supplementary Fig. S2A). The mitochondrial signal sequences
19 can direct a protein through both of the mitochondrial membranes to the interior of
20 mitochondria, to the space between the outer and inner membranes, or anchor a
21 protein to the outer membrane (21-23). Our results show that Bit1 is available for
22 protease digestion at the surface of intact mitochondria (Supplementary Fig. S2D).
23 Thus, Bit1 membrane-embedded domain likely attaches the protein to the outer
24 mitochondrial membrane without mediating transfer through the membrane.

1 Recent results provide clues to the mechanisms underlying Bit1 and Bit1 CDD-
2 mediated cell death. Bit 1, when translocated to the cytoplasm from the mitochondria,
3 interacts with the Groucho/TLE family member AES, suggesting that Bit1 may
4 regulate the activities of the anti-apoptotic and oncogenic TLE proteins (2, 6, 24).
5 Other results show that disrupting Bit1 expression with shRNA confers weakly
6 malignant MCF7 cells enhanced anoikis resistance and increased migratory potential.
7 These changes correlated with an increase in active extracellular kinase regulated
8 (Erk) levels and a decrease in Erk-directed phosphatase activity (25), providing
9 another possible mechanism for the reduced viability of cells with increased Bit1
10 activity.

11 We demonstrated the CDD activity and specificity using two methods, cDNA
12 transfection and protein transduction. As CDD is thought to act in the cytoplasm and
13 the effects of the protein transduction and cDNA transfection were similar, we infer
14 that the CendR peptides delivered CDD into the cytoplasm. This is the first
15 demonstration that peptides using the CendR pathway can be active in protein
16 transduction.

17 Traditional cell-penetrating peptides have been used to deliver recombinant
18 proteins to mammalian cells (26, 27), but these peptides are non-selective; they
19 promote entry into all cells. The prototype of these peptides, Tat, resembles our
20 peptides in that it contains several CendR (R/KXXR/K) motifs (11). However, Tat is
21 active whether fused to the N- or C-terminus of a protein, whereas the activity of
22 CendR peptides is position-dependent in that the CendR motif must be exposed at
23 the C-terminus to be active (11). Hence, activation of peptides with cryptic CendR
24 motifs in a target tissue can be used in tissue-specific delivery of payloads. Indeed,
25 our tumor-homing CendR peptides, such as iRGD and LyP-1 are specific for tumors,

1 whereas the Tat-type peptides are not specific of any cell type or tissue (10, 28).
2 Thus, the tumor-specific CendR peptides offer new opportunities for cell type-specific
3 and tissue-specific protein transduction.

4 The iRGD peptide selectively activates the CendR trans-tissue transport
5 pathway in tumor, taking payloads as large as nanoparticles with it (10, 29-31). Here
6 we show that these peptides can provide a protein with an anti-cancer activity and
7 the ability to penetrate into tumor tissue from a local site without affecting the
8 surrounding normal tissue.

9 We made use of the tumor penetration activity of iRGD-CDD in a new anti-
10 cancer treatment. Treating-tumor bearing mice with iRGD-CDD effectively inhibited
11 tumor growth *in vivo*, causing nearly 80% reduction in tumor volume of the MCF-
12 10CA1a tumors and 40% reduction in 4T1 tumors. Importantly, 25% of the MCF-
13 10CA1a tumors were eradicated by the iRGD-CDD treatment. Targeting caspase-
14 independency for tumor therapeutics is a promising strategy to eliminate cancer cells
15 because tumor cells often develop resistance to anti-tumor agents by developing
16 defects in caspase activation. Activating a caspase-independent cell death pathway
17 with Bit1 CDD may be an effective way of attacking tumor cells resistant to
18 apoptosis. Caspase activation is blocked in the MCF-10CA1a cells, whereas this
19 pathway is intact in the 4T1 cells. The greater inhibitory effect of Bit1 CDD in the
20 MCF-10CA1a tumor than in the 4T1 tumor suggests an inverse correlation between
21 the activity of the caspase-dependent cell death pathways (32).

22 Intratumoral treatment may be particularly useful for tumors that are difficult to
23 remove surgically or treated systemically. Advanced tumors in vital organs can be
24 unresectable, and some tumors are protected from systemic chemotherapy by the
25 blood-brain barrier and fibrotic stroma. Indeed, adjuvant local chemotherapy has

1 been applied to malignant glioma and tested in advanced tumors localizing in the
2 lungs, pancreas, and esophagus (33-37). However, poor drug spreading within the
3 tumor tissue has been a limiting factor for successful local tumor therapies (35, 38,
4 39). iRGD-CDD, the novel tumor-penetrating cell death protein, may significantly
5 advance local tumor therapies and offer new treatment options to cancer patients
6 with locally advanced tumors.

8 **Acknowledgements**

9 We thank Dr. Eva Engvall for comments on the manuscript, Christopher
10 Brunquell for scientific discussions, and Paul Kirsch for editorial assistance. This
11 work was supported by grants W81XWH-10-1-0199 and W81XWH-08-1-0727 from
12 the DOD (E.R.) and Cancer Center Support Grant CA30199 from the NCI.

14 **References**

- 15 1. Frisch SM, Vuori K, Ruoslahti E, Chan-Hui PY. Control of adhesion-dependent
16 cell survival by focal adhesion kinase. *J Cell Biol.* 1996;134:793-9.
- 17 2. Jan Y, Matter M, Pai JT, Chen YL, Pilch J, Komatsu M, et al. A mitochondrial
18 protein, Bit1, mediates apoptosis regulated by integrins and Groucho/TLE
19 corepressors. *Cell.* 2004;116:751-62.
- 20 3. Biliran H, Jan Y, Chen R, Pasquale EB, Ruoslahti E. Protein kinase D is a
21 positive regulator of Bit1 apoptotic function. *J Biol Chem.* 2008;283:28029-37.
- 22 4. Kairouz-Wahbe R, Biliran H, Luo X, Khor I, Wankell M, Besch-Williford C, et al.
23 Anoikis effector Bit1 negatively regulates Erk activity. *Proc Natl Acad Sci U S A.*
24 2008;105:1528-32.

- 1 5. Matsuyama A, Hisaoka M, Iwasaki M, Iwashita M, Hisanaga S, Hashimoto H.
2 TLE1 expression in malignant mesothelioma. *Virchows Arch.* 2010.
- 3 6. Sonderegger CK, Vogt PK. Binding of the corepressor TLE1 to Qin enhances
4 Qin-mediated transformation of chicken embryo fibroblasts. *Oncogene.*
5 2003;22:1749-57.
- 6 7. De Pereda JM, Waas WF, Jan Y, Ruoslahti E, Schimmel P, Pascual J. Crystal
7 structure of a human peptidyl-tRNA hydrolase reveals a new fold and suggests
8 basis for a bifunctional activity. *J Biol Chem.* 2004;279:8111-5.
- 9 8. Hambley TW, Hait WN. Is anticancer drug development heading in the right
10 direction? *Cancer Res.* 2009;69:1259-62.
- 11 9. Minchinton AI, Tannock IF. Drug penetration in solid tumours. *Nat Rev Cancer.*
12 2006;6:583-92.
- 13 10. Sugahara KN, Teesalu T, Karmali PP, Kotamraju VR, Agemy L, Girard OM, et al.
14 Tissue-penetrating delivery of compounds and nanoparticles into tumors. *Cancer*
15 *Cell.* 2009;16:510-20.
- 16 11. Teesalu T, Sugahara KN, Kotamraju VR, Ruoslahti E. C-end rule peptides
17 mediate neuropilin-1-dependent cell, vascular, and tissue penetration. *Proc Natl*
18 *Acad Sci U S A.* 2009;106:16157-62.
- 19 12. Giustini AJ, Ivkov R, Hoopes PJ. Magnetic nanoparticle biodistribution following
20 intratumoral administration. *Nanotechnology.* 2011;22:345101.
- 21 13. Cheresh DA, Spiro RC. Biosynthetic and functional properties of an Arg-Gly-Asp-
22 directed receptor involved in human melanoma cell attachment to vitronectin,
23 fibrinogen, and von Willebrand factor. *J Biol Chem.* 1987;262:17703-11.

- 1 14. Chang KL, Higuchi Y, Kawakami S, Yamashita F, Hashida M. Efficient gene
2 transfection by histidine-modified chitosan through enhancement of endosomal
3 escape. *Bioconjug Chem.* 2010;21:1087-95.
- 4 15. Hatefi A, Megeed Z, Ghandehari H. Recombinant polymer-protein fusion: a
5 promising approach towards efficient and targeted gene delivery. *J Gene Med.*
6 2006;8:468-76.
- 7 16. Lo SL, Wang S. An endosomolytic Tat peptide produced by incorporation of
8 histidine and cysteine residues as a nonviral vector for DNA transfection.
9 *Biomaterials.* 2008;29:2408-14.
- 10 17. Stevenson M, Ramos-Perez V, Singh S, Soliman M, Preece JA, Briggs SS, et al.
11 Delivery of siRNA mediated by histidine-containing reducible polycations. *J*
12 *Control Release.* 2008;130:46-56.
- 13 18. Collins-Racie LA, McColgan JM, Grant KL, DiBlasio-Smith EA, McCoy JM,
14 LaVallie ER. Production of recombinant bovine enterokinase catalytic subunit in
15 *Escherichia coli* using the novel secretory fusion partner DsbA. *Biotechnology (N*
16 *Y).* 1995;13:982-7.
- 17 19. Kaufmann SH. Induction of endonucleolytic DNA cleavage in human acute
18 myelogenous leukemia cells by etoposide, camptothecin, and other cytotoxic
19 anticancer drugs: a cautionary note. *Cancer Res.* 1989;49:5870-8.
- 20 20. Schmidt O, Pfanner N, Meisinger C. Mitochondrial protein import: from
21 proteomics to functional mechanisms. *Nat Rev Mol Cell Biol.* 2010;11:655-67.
- 22 21. Rapaport D. Finding the right organelle. Targeting signals in mitochondrial outer-
23 membrane proteins. *EMBO Rep.* 2003;4:948-52.

- 1 22. van der Laan M, Hutu DP, Rehling P. On the mechanism of preprotein import by
2 the mitochondrial presequence translocase. *Biochim Biophys Acta*.
3 2010;1803:732-9.
- 4 23. Waizenegger T, Stan T, Neupert W, Rapaport D. Signal-anchor domains of
5 proteins of the outer membrane of mitochondria: structural and functional
6 characteristics. *J Biol Chem*. 2003;278:42064-71.
- 7 24. Zhang X, Chen HM, Jaramillo E, Wang L, D'Mello SR. Histone deacetylase-
8 related protein inhibits AES-mediated neuronal cell death by direct interaction. *J*
9 *Neurosci Res*. 2008;86:2423-31.
- 10 25. Karmali PP, Brunquell C, Tram H, Ireland SK, Ruoslahti E, Biliran H. Metastasis
11 of tumor cells is enhanced by downregulation of Bit1. *PLoS One*. 2011;6:e23840.
- 12 26. Wadia JS, Dowdy SF. Modulation of cellular function by TAT mediated
13 transduction of full length proteins. *Curr Protein Pept Sci*. 2003;4:97-104.
- 14 27. Zhou H, Wu S, Joo JY, Zhu S, Han DW, Lin T, et al. Generation of induced
15 pluripotent stem cells using recombinant proteins. *Cell Stem Cell*. 2009;4:381-4.
- 16 28. Roth L, Agemy L, Kotamraju VR, Braun G, Teesalu T, Sugahara KN, et al.
17 Transtumoral targeting enabled by a novel neuropilin-binding peptide. *Oncogene*.
18 2011.
- 19 29. Ruoslahti E. Peptides as Targeting Elements and Tissue Penetration Devices for
20 Nanoparticles. *Adv Mater*. 2012.
- 21 30. Ruoslahti E, Bhatia SN, Sailor MJ. Targeting of drugs and nanoparticles to
22 tumors. *J Cell Biol*. 2010;188:759-68.
- 23 31. Sugahara KN, Teesalu T, Karmali PP, Kotamraju VR, Agemy L, Greenwald DR,
24 et al. Coadministration of a tumor-penetrating peptide enhances the efficacy of
25 cancer drugs. *Science*. 2010;328:1031-5.

1 to the manufacturer's instruction. The vector without Bit1 fragment served as a
2 control. The percentage of cell viability was determined 24 h post-transfection by
3 MTT assay and normalized to vector control. Error bars denote mean \pm SEM of 3
4 separate experiments performed in triplicate of each Bit1 fragment indicated. One-
5 way ANOVA and student t-test were used for statistical analysis. The comparison
6 shown is to the vector control, or between Bit1 and F1-62. **, $p < 0.01$; ***, $p <$
7 0.001 , ns, not significant.

8
9 **Figure 2. Internalization of CDD fusion proteins into cells.** A, human prostate
10 tumor cells PPC1 and human melanoma cells M21 were incubated with 3 μ M fusion
11 proteins that had been labeled with the red fluorophor Dy550. The cells were washed
12 3 times with PBS and fixed with cold methanol for 10 min. Cell nuclei were stained
13 with DAPI (blue). The proteins were visualized by confocal microscopy (red). B and
14 C, comparison of the localization of RPARPAR-CDD (B), and iRGD-CDD (C) with
15 NRP-1 in PPC1 cells at various points of time. After incubation with the Dy550-
16 labeled proteins, the cells were immunostained with an anti-NRP-1 antibody (green).
17 Arrows indicate co-localization of the red CDD proteins and green NRP-1. The
18 arrowheads point at cells with dying cell morphology at the 24-hour time point. D,
19 specific inhibition of peptide-CDD fusion protein uptake into PPC1 cells by dextran
20 (Dex) conjugated peptides. The fusion proteins were incubated with the cells for 1 h
21 at 37°C in the presence of the cognate peptide inhibitors and controls. Unmodified
22 dextran (Dex; upper left panel) and dextran coated with iRGE (Dex-iRGE; lower left
23 panel) served as controls. Arrows point at bound and internalized RPARPAR-CDD or
24 iRGD-CDD (red). Scale bar: 20 μ m for all images.

1 **Figure 3. Cytotoxicity of CDD proteins in tumor cell lines.** A, breast tumor cell
2 lines from human MCF-10CA1a, mouse 4T1, and human melanoma M21 cells were
3 incubated for 48 h with the recombinant CDD proteins at various concentrations and
4 cell viability was measured by MTT assay. B, iRGD-CDD proteins with or without
5 hexahistidine tag were separated on a gradient SDS-PAGE gel and visualized using
6 Coomassie Blue staining. C, MCF-10CA1a cells were incubated for 48 h with the
7 iRGD-CDD protein with or without a his-tag. Error bars denote mean \pm SEM of 3
8 separate experiments performed in quadruplicate at each concentration of the
9 proteins. Two-way ANOVA was applied for statistical analysis. **, $p < 0.01$; ***, $p <$
10 0.001 ; ns, not significant.

11
12 **Figure 4. Tumor penetration of iRGD-CDD protein.** A, penetration into tumor
13 explants. Confocal microscopic view of MCF-10CA1a tumor explants incubated with
14 Dy550-labeled proteins (red). Cell nuclei were stained with DAPI (blue). Scale bar,
15 $100\ \mu\text{m}$. B and C, penetration through tumor tissue *in vivo*. Scanscopic images of
16 serial sections from MCF-10CA1a tumors injected intratumorally with iRGD-CDD (B)
17 or CDD (C) for 4 hours before harvesting of the tumor. The space between adjacent
18 sections is $400\ \mu\text{m}$. Thus, the thickness from section 1 through 8 is approximately 3
19 mm. Tumor rims are surrounded by dotted lines. B, iRGD-CDD is abundant within
20 the tumor, particularly in areas that appear rich in fibrotic stromal tissue (panel 5
21 insets *a* and *b*), as well as localized signal in parenchymal area (panel 7 inset). No
22 signal was seen outside of tumor rim (panel 5 inset *b*). Arrowhead points to injection
23 site; arrows point to the areas that presumably caused by outside-in penetration of
24 overflowed iRGD-CDD during the injection. C, the only significant signal of CDD
25 within the tumor tissue is around the injection site (panels 3 and 4, arrowheads).

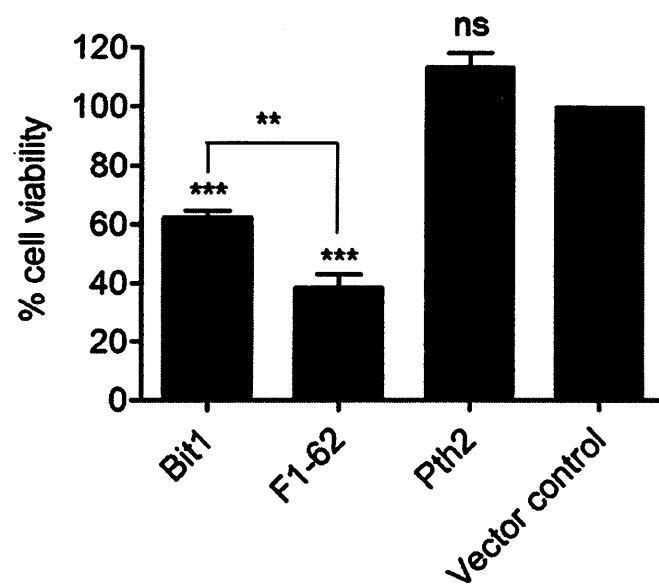
Primarily CDD is located in the tumor rim (panels 3 through 8). Scale bar in panels 1-8, 2 mm and in the insets, 50 μ m.

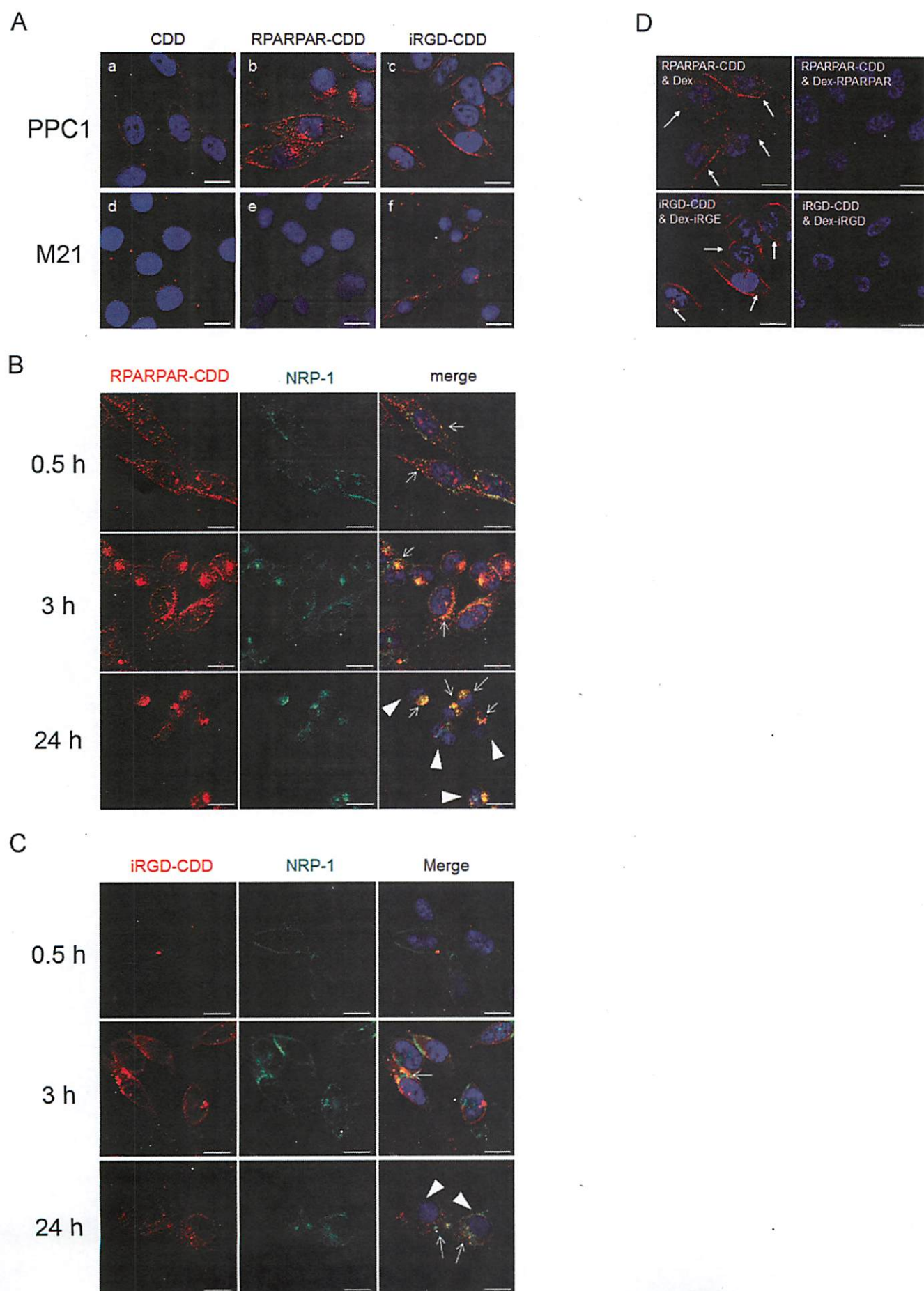
Figure 5. iRGD-CDD inhibits tumor growth in mice. Mice bearing orthotopic MCF-10CA1a (A and B) (n = 8 mice per treatment group) or 4T1 tumors (D and E) (n = 12 per group) were treated by intratumoral injections of PBS, CDD, or iRGD-CDD every 3rd day. The mean tumor volume \pm SEM and mean tumor weight \pm SEM were plotted. Two-way ANOVA was used for the analysis of tumor volume and one-way ANOVA for the tumor weight. * $p \leq 0.05$, ** $p \leq 0.01$, *** $p \leq 0.001$, ns, not significant. C, eradication of tumor by intratumoral injection of iRGD-CDD. MCF-10CA1a tumor xenograft at 63 mm³ was injected locally with iRGD-CDD every 3 days for 4 times. By the end of the treatment on day 12 tumor volume reduced to 3 mm³. The nodule disappeared in the following several weeks with no more treatment. Skin appeared normal around injection site during and after the treatment.

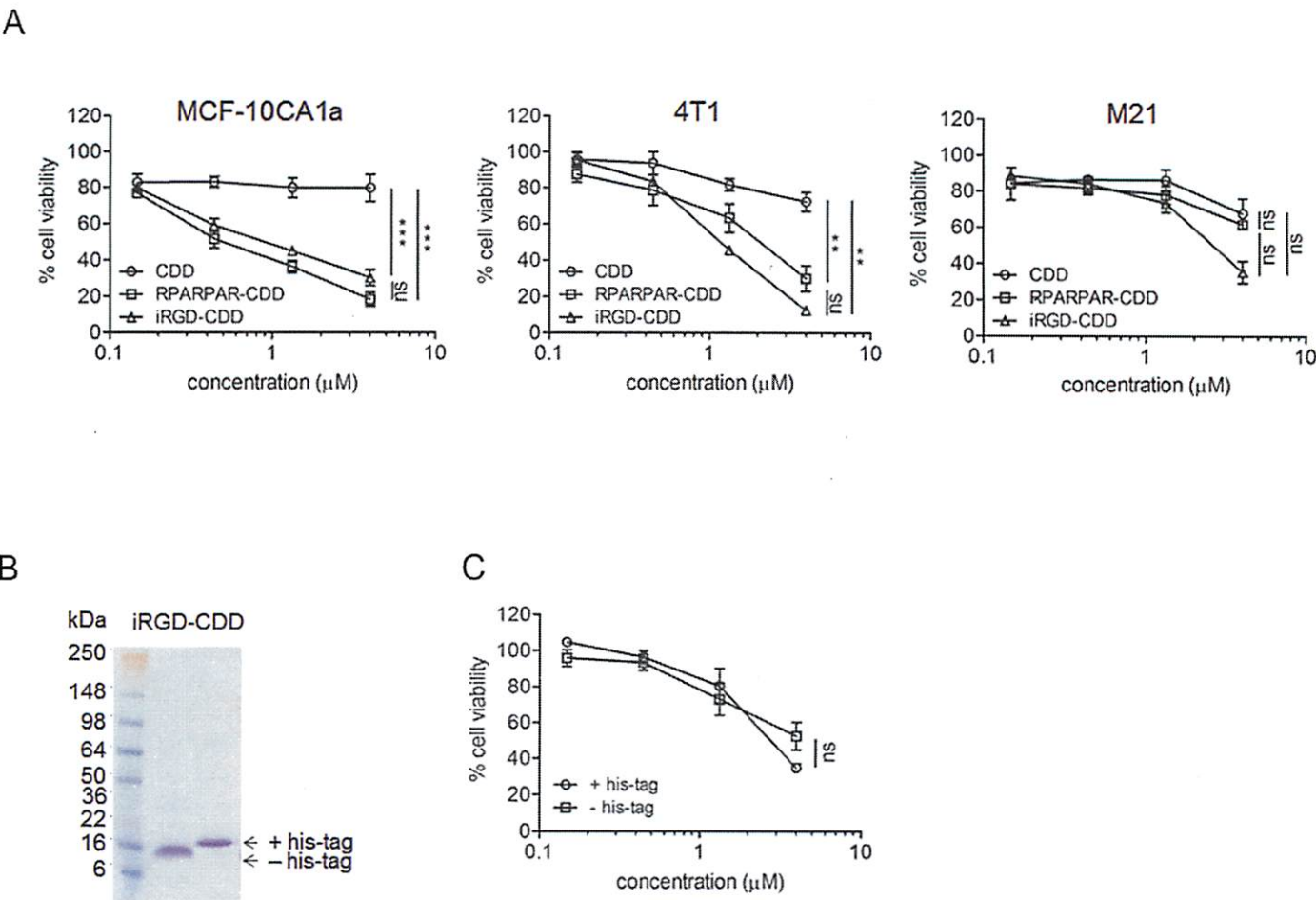
Figure 6. Analysis for cell death and anti-proliferative effect of iRGD-CDD in tumors. A, H&E staining of tumor sections from mice treated with intratumoral injections of PBS, CDD, or iRGD-CDD. B, cell death was analyzed by terminal deoxynucleotidyl transferase-mediated deoxyuridine triphosphate nick end labeling (TUNEL) staining (green). Nuclei were stained with DAPI (blue). TUNEL positivity was quantified by normalizing TUNEL signal to DAPI (right panel). C, cell proliferation was analyzed by immunostaining of tumor sections using a rabbit anti-Ki-67 polyclonal antibody, followed by Alex Fluor®-488 conjugated anti-rabbit IgG (green). Nuclei were stained with DAPI (blue). Ki-67 expression was quantified by

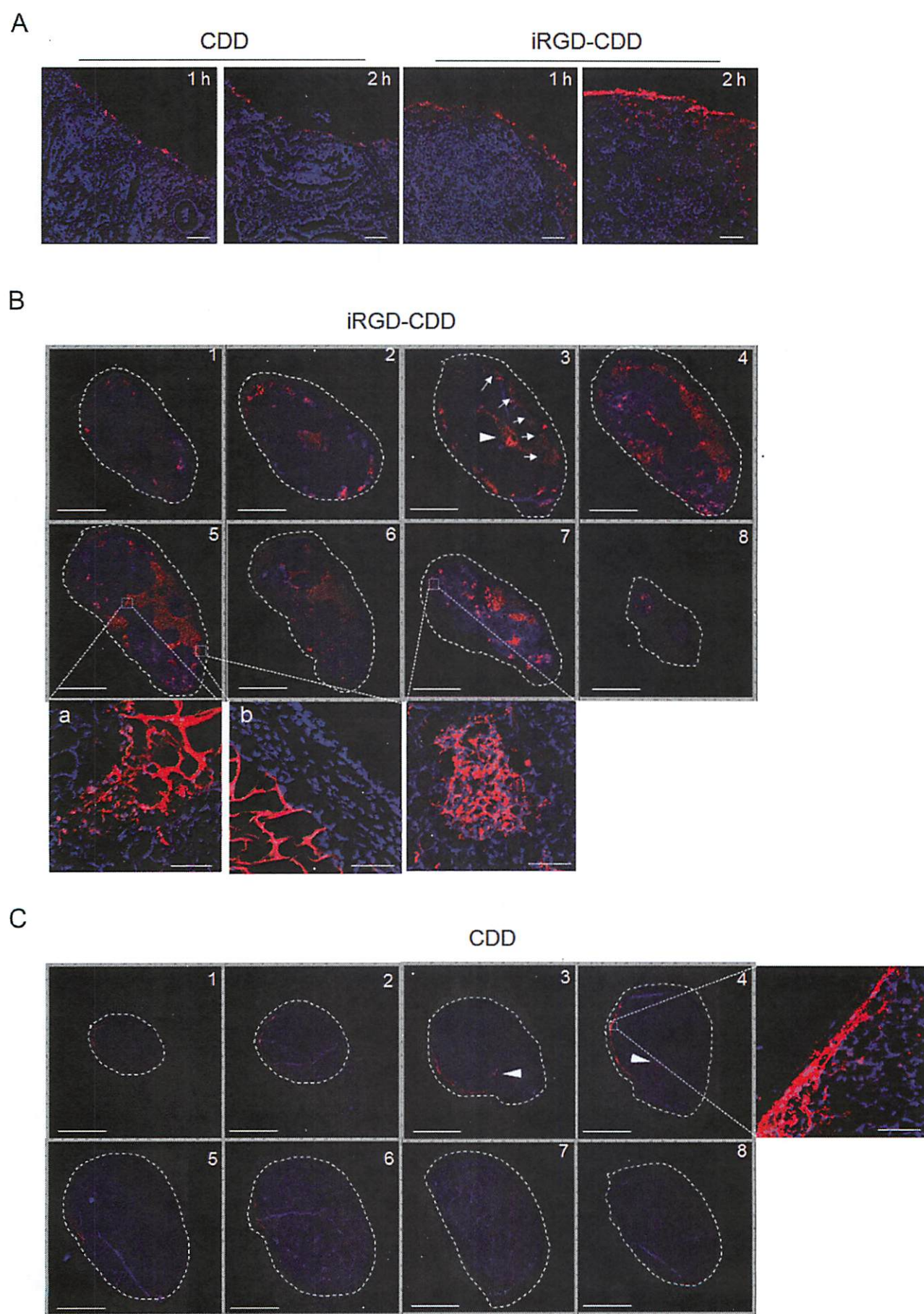
- 1 normalizing the Ki-67 signal to DAPI signal (right panel). Error bars denote mean \pm
- 2 SEM. * $p \leq 0.05$; ** $p \leq 0.01$; ns, not significant. Scale bar, 100 μm for all images.

Chen et al, Figure 1

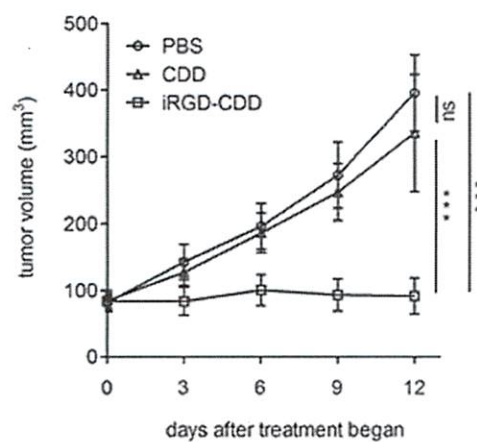




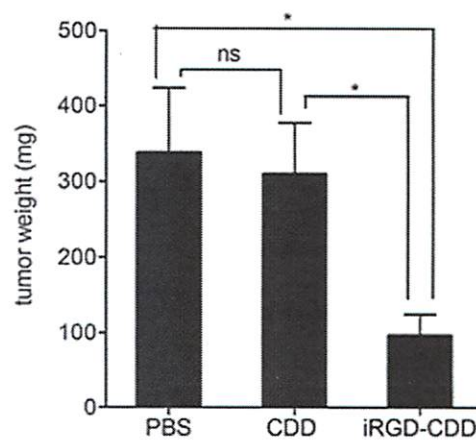




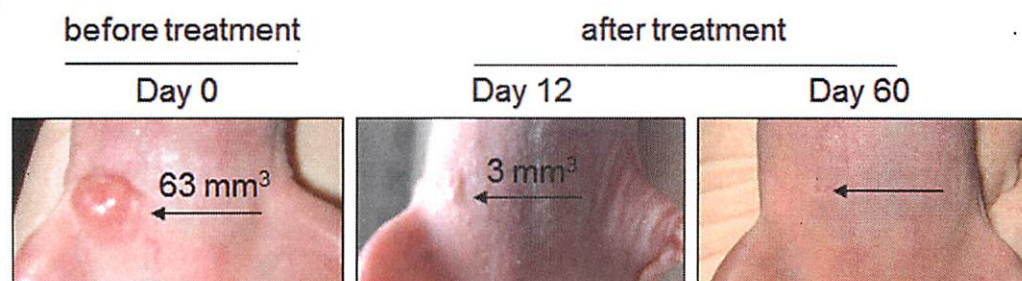
A



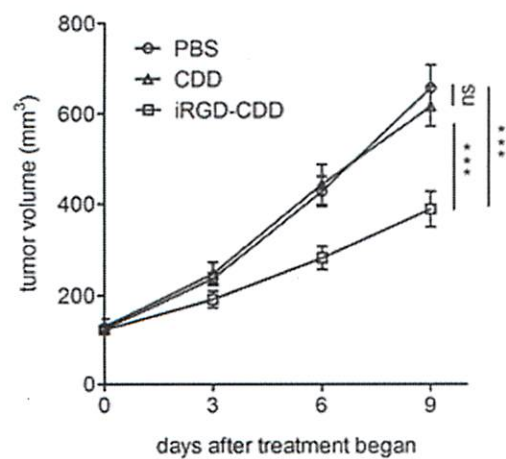
B



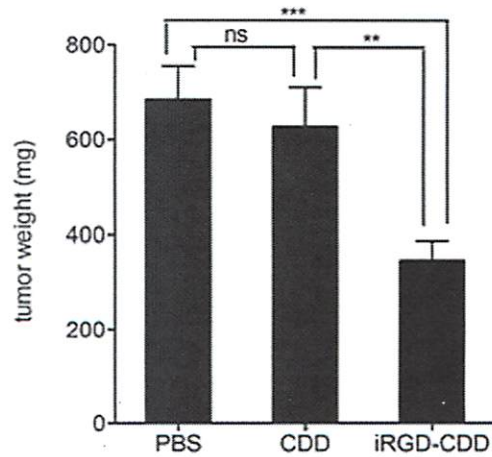
C



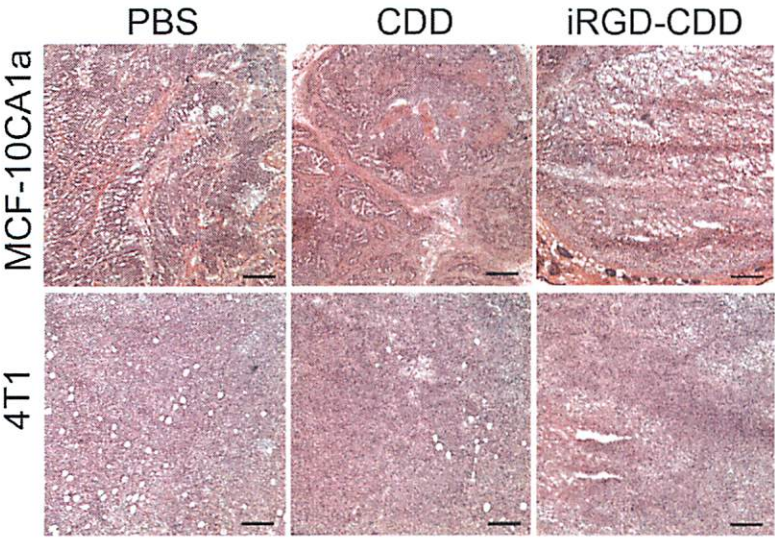
D



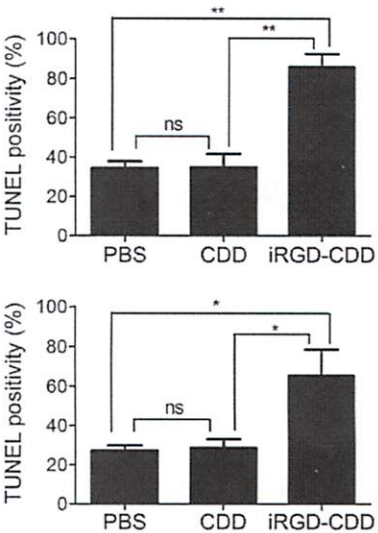
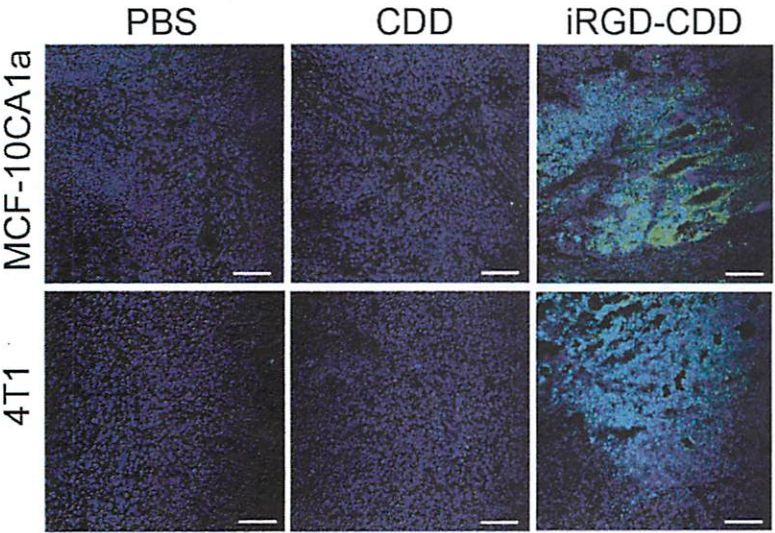
E



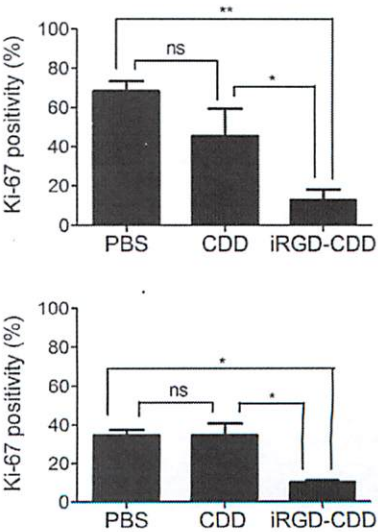
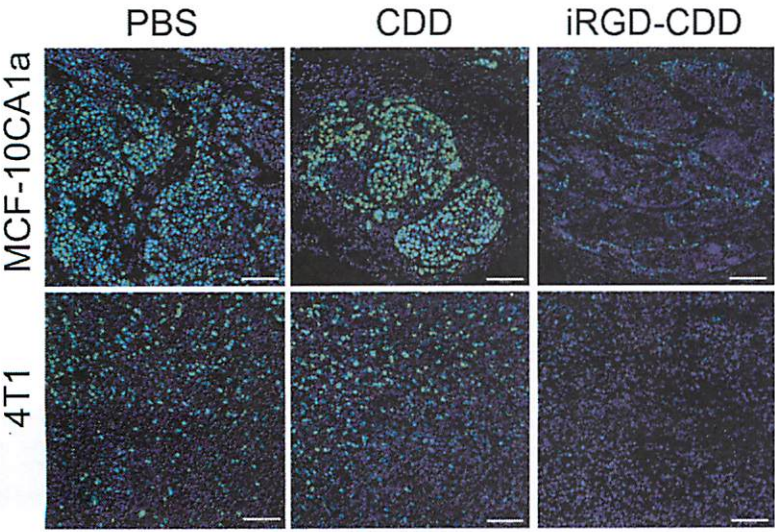
A



B



C



Supplementary data

Application of a Proapoptotic Peptide for an Intratumoral-Spreading Cancer Therapy

Renwei Chen, Gary B Braun, Xiuquan Luo, Kazuki N. Sugahara, Tambet Teesalu,
Erkki Ruoslahti

Material and methods

HeLa cervical carcinoma cell line was maintained in Dulbecco's modified Eagle's medium with glutamine containing 10% FBS, penicillin and streptomycin at 37°C and 5% CO₂. Rabbit anti-his-tag polyclonal antibody and rabbit anti-cleaved caspase 3 polyclonal antibody were from Cell Signalling; mouse anti-PARP clone2-10 monoclonal antibody was from BD Pharmingen; rabbit anti-myc-tag polyclonal antibody was from MBL Medical & Biological Laboratories Co., Ltd (Naka-ku Nagoya, Japan); mouse anti-cytochrome c monoclonal antibody was from Santa Cruz Biotech; anti-human Bit1 polyclonal antibody was prepared by immunizing a rabbit with human recombinant Bit1 protein; mouse anti-β-actin monoclonal antibody was from Sigma-Aldrich. The secondary antibodies used were Alexa Fluro® 680-conjugated goat IgG (Invitrogen Life Technologies) and IRDye 800CW-conjugated goat IgG (Li-Cor Biosciences).

To determine the orientation of Bit1 in the mitochondrial membrane, HeLa cells were permeabilized with digitonin which permeabilizes the cholesterol rich plasma membrane but leaves the low cholesterol mitochondrial membrane intact.

1 Subsequently, cells were treated with trypsin for 15 min to degrade cytosolic proteins
2 and the cytosolic part of membrane proteins on organelles (1). Degradation of Bit1
3 and cytochrome C was analyzed by immunoblot.

4 5 **Figure legends**

6
7 **Figure S1.** Construction and identification of Bit1 CDD recombinant proteins. A, a
8 schematic diagram of recombinant Bit1 CDD proteins. A hexahistidine tag, an
9 enterokinase cleavable sequence (DDDDK), and a myc-tag were placed at the N-
10 terminus of Bit1 CDD. A tissue-penetrating peptide, RPARPAR or iRGD
11 (CRGDKGPDC), was fused to the CDD C-terminus. B, purified CDD fusion proteins
12 were separated on a gradient SDS-PAGE gel and visualized by staining with
13 Coomassie blue, or immunoblotting with anti-his-tag (red) and anti-myc-tag (green)
14 antibodies.

15
16 **Figure S2.** N-terminal fragments of Bit1 cause cell death. A, HEK 293T cells were
17 transiently transfected with N-terminally myc-tagged truncated Bit1 fragments. The
18 vector without a Bit1 fragment served as a control. The percentage of cell viability
19 was determined 24 h post-transfection by MTT assay and normalized to vector
20 control. Error bars denote mean \pm SEM of 3 separate experiments performed in
21 triplicate. One-way ANOVA was used for statistical analysis. The comparisons
22 shown are to the vector control. **, $p < 0.01$; ***, $p < 0.001$; ns, not significant. B,
23 sequence alignment of the N-terminus of Bit1 is from multiple species. The numbers
24 correspond to the human Bit1 sequence (AF151905). Consensus sequences among
25 the indicated species are marked with * at the bottom. A conserved transmembrane

1 domain was identified at amino acids 14-33 in the human Bit1 sequence. C, confocal
2 micrographs of HeLa cells transiently over-expressed with Bit1 or its deletion
3 variants. Red, Bit1 or truncated Bit1; blue, nuclei. Deletion of the N-terminal 13
4 residues (Δ AAAs 1-13) did not alter the mitochondrial localization pattern of Bit1 (2).
5 Deletion of the N-terminal 33 residues (Δ AAAs 1-33) or the putative transmembrane
6 domain (Δ AAAs 14-33) resulted in cytosolic and nuclear expression. D,
7 immunoblotting of mitochondrial Bit1 and cytochrome C after digitonin and trypsin
8 treatment of the cells. Bit1 was degraded by the treatment of digitonin and trypsin
9 suggesting its localization at mitochondrial outer membrane. Cytochrome C, a
10 protein that localizes to the intermembrane space of mitochondria was not degraded
11 under the same treatment, indicating that the mitochondria had remained intact.
12 Scale bar, 10 μ m. E, a schematic diagram showing the proposed localization of Bit1
13 on the outer membrane of mitochondrion facing the cytosol.

14

15 **Figure S3.** Caspase cascade signaling is impaired in MCF-10CA1a human breast
16 cancer cells. MCF-10CA1a and 4T1 cells were treated with 0.1 μ M of etoposide or 1
17 μ M of iRGD-CDD protein for 48 h. Cell lysates were immunoblotted with a rabbit anti-
18 cleaved caspase 3 monoclonal antibody (Cell Signaling) and a mouse anti-PARP
19 monoclonal antibody (clone c2-10, BD Pharmingen). Both antibodies react with
20 human and mouse samples. β -actin was used as a loading control.

21

22 **Figure S4.** Tumor volume and body weight. Mice bearing orthotopic 4T1 tumors (n =
23 5 per group) were treated by intravenously injected of PBS, CDD, or iRGD-CDD at
24 10 mg/kg of mouse body weight every other day. A, the mean tumor volume \pm SEM
25 was plotted and analyzed by two-way ANOVA. * $p \leq 0.05$; ** $p \leq 0.01$; ns, not

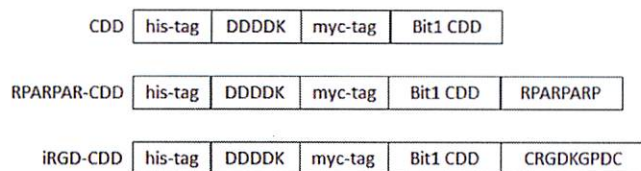
1 significant. B, the body weight before the treatment was used to calculate the mean
2 body weight variation (%). The CDD compounds caused severe toxicity and loss of
3 body weight made it necessary to euthanize these mice on day 6 of the treatment.

4 5 **References**

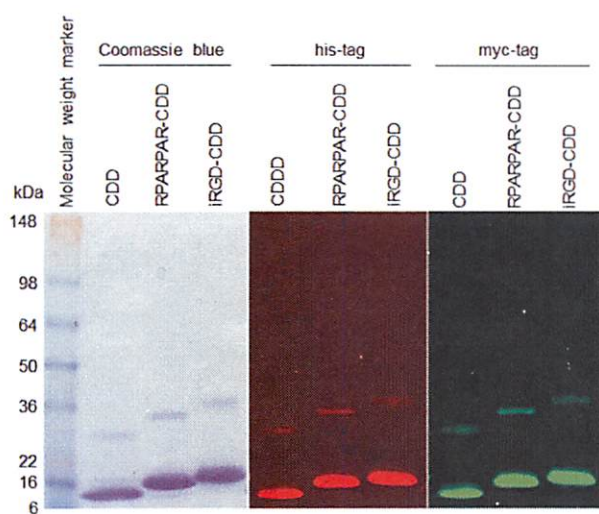
- 6 1. Nguyen M, Millar DG, Yong VW, Korsmeyer SJ, Shore GC. Targeting of Bcl-2 to
7 the mitochondrial outer membrane by a COOH-terminal signal anchor sequence.
8 J Biol Chem. 1993;268:25265-8.
- 9 2. Jan Y, Matter M, Pai JT, Chen YL, Pilch J, Komatsu M, et al. A mitochondrial
10 protein, Bit1, mediates apoptosis regulated by integrins and Groucho/TLE
11 corepressors. Cell. 2004;116:751-62.

Chen et al, Supplementary Figure S1

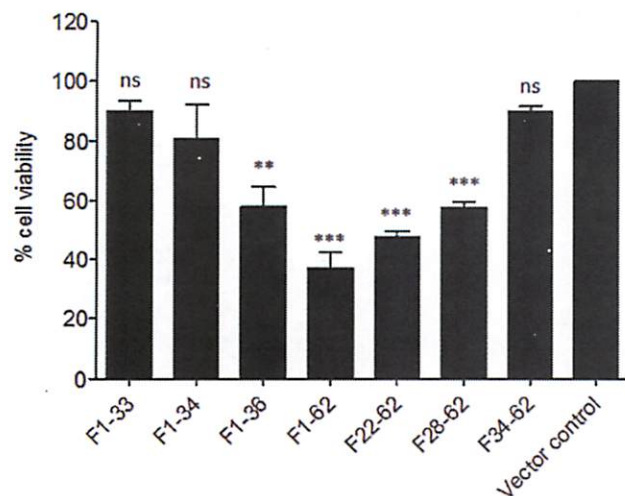
A



B



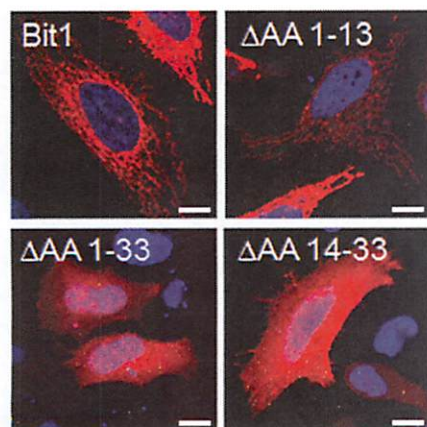
A



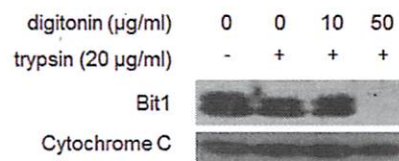
B

Amino acids	1	11	21	31	41	51	61
Homo sapiens	MPSKSLVMEYLAHPSTLGLAVGVACGMCLGWSLRVCFGMPLPKSKTSKTHTDTESEASILGDS						
Macaca mulatta	MPSKSLVMEYLAHPSALGLAIGVACGVCLGWSLRVRFGMPLPKSKTSKTHTDTESEASILGES						
Mus musculus	MMLSKFLTMEYLVHPGTLSLAAGVACGMCLGWGIRSHLGMFPQNSTSEANRDTETGTEASILGE						
Rattus norvegicus	MLSKLLTMEYLVHPGTLSLAAGVACGMCLGWGIRSHLGIFFQNSTSETNRDTEMGTEASILG						
Xenopus tropicalis	MDYFTYPGALPLTAGLACGLFLGWSLRGRFGYFRSFSTLATNEVGTEASTMGETGE						
Gallus gallus	MDYLSKPGFLSILAGVACGVCLGWGIRGRFLRQHRAMAASAGSCGTEANVMGESGE						
Bos taurus	MISRSVLMEYLTNPGLSILVAGVACGVCLGWGIRMRFGMLPKSSVRETNPDTEASEASILGES						
Consensus		* *	* *	* * * *	* * * *		

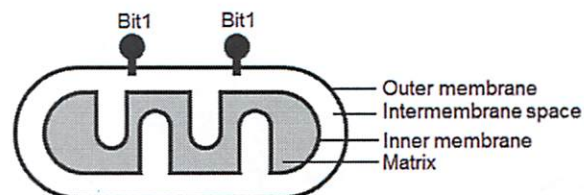
C



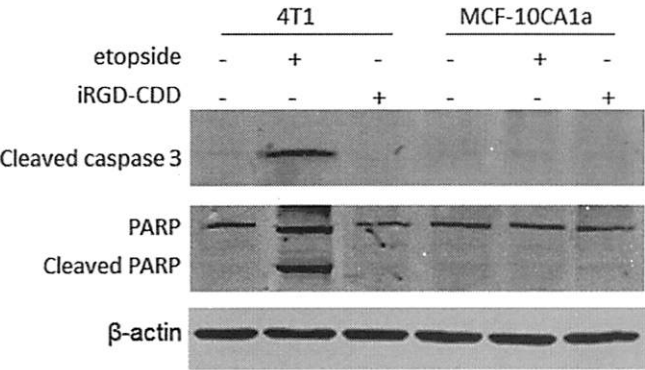
D



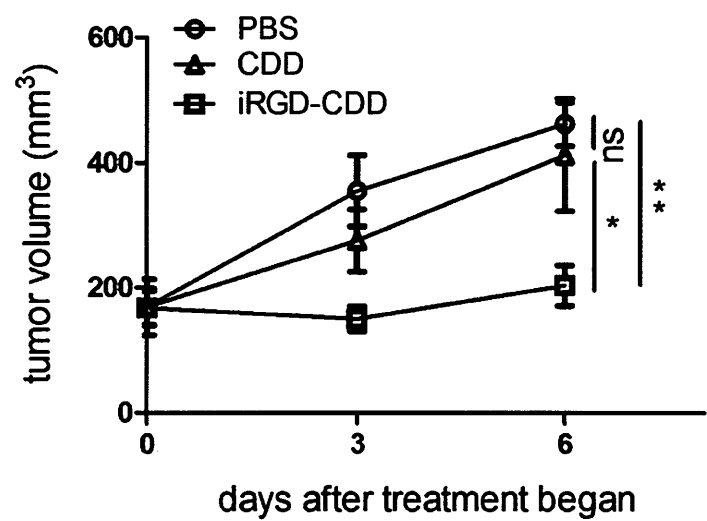
E



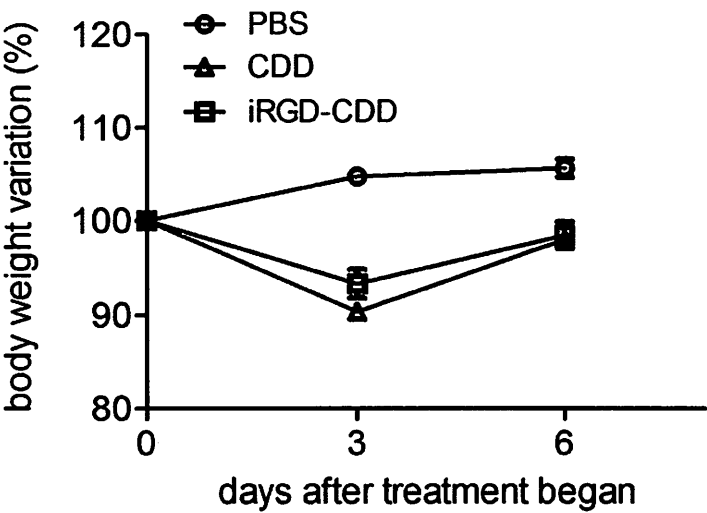
Chen et al, Supplementary Figure S3



A



B



De Novo Design of a Tumor-Penetrating Peptide

Luca Alberici^{1,2,3}, Lise Roth⁴, Kazuki N. Sugahara¹, Lilach Agemy¹, Venkata R. Kotamraju¹, Tambet Teesalu¹, Claudio Bordignon^{2,3}, Catia Traversari², Gian-Paolo Rizzardi², Erkki Ruoslahti¹

¹ Cancer Center, Sanford-Burnham Medical Research Institute, 10901 N. Torrey Pines Rd., La Jolla, CA 92037 U.S.A. and Center for Nanomedicine, Sanford-Burnham Medical Research Institute at University of California, Santa Barbara, CA 93106-9610

² MolMed S.p.A., Via Olgettina 58, 20132 Milano, Italy

³ Università Vita-Salute San Raffaele, Via Olgettina 58, 20132 Milano, Italy

⁴ Division of Vascular Oncology and Metastasis, German Cancer Research Center (DKFZ), Im Neuenheimer Feld 280, 69120 Heidelberg, Germany

Running Title: *De Novo Design of a Tumor-Penetrating Peptide*

Keywords: Tissue-penetrating peptide, C-end Rule, NGR, Tumor targeting, Drug delivery

Word count: 4921

Total number of figures: 5

Corresponding Author:

Erkki Ruoslahti, Distinguished Professor

Cancer Center, Sanford-Burnham Medical Research Institute, 10901 N. Torrey Pines Rd., La Jolla, CA 92037 U.S.A.

Phone: 858 795-5023

E-mail: ruoslahti@sanfordburnham.org

Grant Support

This work was partially supported by MolMed S.p.A. (www.molmed.com), and by grants W81XWH-09-1-0698 and W81XWH-08-1-0727 from the USAMRAA of the DoD (ER) and by grant R01 CA 152327 from the National Cancer Institute of the National Institutes of Health. ER is supported in part by CA30199 the Cancer Center Support Grant from the National Cancer Institute of the National Institutes of Health.

Competing Interest

LA, CT, GPR and CB are employees of MolMed S.p.A. KNS, VRK, TT and ER are shareholders of CendR Therapeutics Inc, which has rights to some of the technology described in this paper. LR and LAg declare no conflict of interest.

Abstract

Poor penetration of anti-tumor drugs into the extravascular tumor tissue is often a major factor limiting the efficacy of cancer treatments. Our group has recently described a strategy to enhance tumor penetration of chemotherapeutic drugs through use of iRGD peptide (CRGDK/RGPDC). This peptide comprises two sequence motifs: RGD, which binds to $\alpha\beta 3/5$ integrins on tumor endothelia and tumor cells and a cryptic CendR motif (R/KXXR/K-OH). Once integrin binding has brought iRGD to the tumor, the peptide is proteolytically cleaved to expose the cryptic CendR motif. The truncated peptide loses affinity for its primary receptor and binds to neuropilin-1, activating a tissue-penetration pathway that delivers the peptide along with attached or co-administered payload into the tumor mass. Here we describe the design of a new tumor-penetrating peptide based on the current knowledge of homing sequences and internalizing receptors. The tumor-homing motif in the new peptide is the NGR sequence, which binds to endothelial CD13. The NGR sequence was placed in the context of a CendR motif (RNGR), and this sequence was embedded in the iRGD framework. The resulting peptide (CRNGRGPDC, iNGR) homed to tumor vessels and penetrated into tumor tissue more effectively than the standard NGR peptide. iNGR induced greater tumor penetration of coupled nanoparticles and co-administered compounds than NGR. Doxorubicin given together with iNGR was significantly more efficacious than the drug alone. These results show that a tumor-specific, tissue-penetrating peptide can be constructed from known sequence elements. This principle may be useful in designing tissue-penetrating peptides for other diseases.

Introduction

The vasculature of each tissue is unique in terms of protein expression and these molecular differences are referred to as “vascular zip codes” (1). The selectively expressed proteins provide targets for specific delivery of diagnostic and therapeutic compounds to the vasculature of desired tissues. Currently, a variety of tumor-targeting peptides are in preclinical and clinical development. However, vascular abnormalities, fibrosis and contraction of extracellular matrix contribute to an increased interstitial fluid pressure inside the tumor, which impedes drug delivery into the extravascular tumor tissue (2).

Our group has recently reported the identification of the CendR motif (R/KXXR/K) that is capable of increasing the penetration of peptides, chemicals, and synthetic and biological nanoparticles into tissues through the engagement of neuropilin-1 (NRP-1) (3). Specific penetration into tumors was achieved through the use of an iRGD peptide (CRGDK/RGPDC) (4). iRGD, identified by *in vivo* phage display for tumor homing peptides, combines targeting to tumor vessels and tumor parenchyma through an RGD motif with the cell-internalizing and tissue penetrating properties of a CendR motif RGDK/R in the peptide (4). iRGD mechanism of action involves three steps. First, the RGD sequence binds to $\alpha v\beta 3/5$ integrins. Then, a proteolytic cleavage by a yet-to-be-identified host protease(s) exposes the CendR motif, which is now able to interact with NRP-1 to trigger the internalization process. This strategy allows the activation of the CendR motif only in a targeted tissue, avoiding NRP-1 activation in normal vasculature. Interestingly, iRGD triggers a specific tumor penetration of, not only iRGD-coupled compounds, but also of drugs co-administered with free iRGD peptide (5). The CendR motif also activates the penetration pathway through binding to NRP-2 (6).

Potentially, the addition of a cryptic CendR motif could increase the penetration of other tumor targeting peptides, providing more tools to overcome the poor delivery of drugs to tumors. We set out to test this hypothesis using the NGR tumor-homing motif. The NGR sequence was identified by *in vivo* phage display in tumor bearing mice (7). Initially it was thought to bind one or more of the integrins selectively expressed in angiogenic vessels (7, 8). This idea was further supported by the discovery that the asparagine in the NGR motif undergoes a spontaneous deamidation reaction that yields iso-aspartic acid (isoDGR), generating an RGD mimetic (9, 10). However, the unaltered NGR motif also specifically homes to tumor vessels, where it binds to an isoform of aminopeptidase N (CD13) (11, 12). NGR peptides have been used to target a variety of agents into tumors; an NGR conjugate of human tumor necrosis factor α is in advanced clinical trials for cancer therapy (13-16). Here we combined the NGR motif with a CendR motif to create a new tumor-homing peptide with tissue-penetrating properties.

Materials and Methods

Animal use. All procedures on the animals, including those to ensure minimizing discomfort, have been carried out according to the protocol approved at the Sanford-Burnham Medical Research Institute.

Preparation of compounds. Synthetic peptides (4), peptide-coated NWs (17) and peptide-expressing T7 phage (18) were prepared as described elsewhere. DOX was purchased from Sigma-Aldrich (St. Louis, MO). Evan's Blue was purchased from MP Biomedicals (Irvine, CA)

Cell lines and tumor models. HUVECs (Lonza, Allendale, NJ) were cultured in complete EGM-2 medium from Lonza. 4T1 cells were cultured in Dulbecco's Modified Eagle Medium (Thermo Scientific, Rockford, IL) supplemented with 10% fetal bovine serum (FBS) and penicillin/streptomycin (Gibco, Grand Island, NY). All tumor cell lines were bought and authenticated by ATCC (Teddington, UK). Orthotopic 4T1 breast tumors were generated by injecting 10^5 cells into the mammary fat pad of female BALB/c mice at the age of 4-6 weeks (Harlan Sprague-Dawley, Indianapolis, IN).

***In vitro* phage binding and internalization assays:** Phage amplification, purification, titration, sequencing, and UV inactivation were performed as reviewed (18). One million cells were incubated with 10^{10} plaque forming unit (pfu) of purified phage in DMEM-1% BSA at 4°C for binding or 37°C for internalization. The cells were washed with cold DMEM-BSA four times, lysed in lysogeny broth (LB) containing 1% Nonidet P-40 (LB-NP40) and titrated. In internalization assays, the second wash was replaced with an acid wash (500 mM NaCl, 0.1 M glycine, 1% BSA, pH 2.5) to remove and inactivate phage bound to the cell surface. In

inhibition assays, the cells were incubated with 1 µg/ml of neutralizing anti-NRP-1 antibody (R&D Systems), control IgG (Santa Cruz Biotechnology), or 10-fold excess of UV-inactivated phage 15 min prior to adding the phage of interest.

Ex vivo tumor dipping assays: The assays were performed as described elsewhere (5, 6). Briefly, 4T1 tumor bearing mice were anesthetized and perfused through the heart with PBS containing 1% BSA. The tumors were excised and incubated with 10^9 pfu of phage in DMEM-1% BSA for 1 hour at 37°C. After extensive washes with PBS, the tumors were lysed in 1 ml of LB-NP40 for phage titration. In some cases, the tumors were fixed in PBS containing 4% paraformaldehyde (PFA) and processed for immunostaining.

Biodistribution of peptides, phage and NWs. *In vivo* tumor homing experiments with peptides, phage, and NWs were performed as described (4, 17). Briefly, 10^9 pfu of phage particles were injected into the tail vein of tumor bearing mice, and allowed to circulate for 40 minutes. The mice were perfused through the heart with PBS containing 1% BSA under deep anesthesia. The tumors and tissues were excised and mechanically homogenized for phage titration or fixed in 4% PFA for immunostaining. In some cases, 50 µg of anti-NRP-1 antibody or control IgG was intravenously injected 15 minutes prior to the phage injection. For the peptide homing studies, 100 µl of 1 mM FAM-labeled peptides were intravenously injected into tumor mice and allowed to circulate for 1 hour. In case of the NWs, particles at a dose of 5 mg/kg of iron were injected into the tail vein of tumor mice and allowed to circulate for 5 hours. After perfusion of the mice, tissues were collected, macroscopically observed under UV light (Illuminatool Bright Light System LT-9900), and processed for immunostaining. Intratumoral accumulation of NWs was quantified with ImageJ.

Immunofluorescence: Immunofluorescence on cells was performed using 10 μ M FAM-peptides and following the protocol previously described (19). Immunofluorescence on frozen sections was performed as described earlier (4) using the following antibodies at 1:200 dilution: rat anti-mouse CD31 Alexa-594 (Invitrogen), rabbit anti-T7 phage (3) and donkey anti-rabbit Alexa 488 (Invitrogen). Images were taken using a Fluoview confocal microscope (Olympus, Center Valley, PA).

***In vivo* systemic permeability assay.** Tumor bearing mice were injected intravenously with 4 μ mol/kg of peptide combined with 1 mg of Evans Blue, 10 mg/kg of free DOX or 5 mg iron/kg of CGKRK-coated NWs (20). After indicated time of circulation, the mice were perfused through the heart with PBS supplemented with 1% BSA, and tissues were collected. Evans Blue was extracted by incubating the tissues in 1 ml of 2,2 N-methylformamide overnight at 37°C with mild shaking. After centrifugation, the OD₆₀₀ of the supernatant was measured. To assess the extravasation of CGKRK-NWs, tissues were fixed in 4% PFA overnight at 4°C and subjected to immunostaining for CD31-positive blood vessels. For DOX quantification (21), excised tissues were mechanically homogenized in 1 ml of 1% Sodium Dodecyl Sulphate (SDS) containing 1 μ M H₂SO₄, and frozen overnight in 2 ml of chloroform/isopropyl alcohol (1:1, v/v). The samples were melted, vortexed and centrifugated at 16,000 g for 15 min, and OD₄₉₀ of the organic (lower) phase was measured.

Tumor treatment studies. Mice bearing orthotopic 4T1 breast tumors at 50 mm³ received intravenous injections of free DOX (3 mg/kg) or PBS, combined with 4 μ mol/kg of peptide every other day. Tumor growth and body weight were monitored every other day. The tumor

volume was calculated using the following formula: $\text{volume (mm}^3\text{)} = (d^2 \times D)/2$, where d is the smallest and D is the largest tumor diameters.

Statistical analysis: All data were analyzed with one-way ANOVA. Tumor treatment studies were analyzed with two-way ANOVA for repeated measurements.

Results

Design of iNGR peptide. We used 3 elements to create the iNGR peptide (CRNGRGPDC): the NGR motif, a CendR motif (RNGR) overlapping with the NGR motif, and a cleavable consensus (GPD) from the iRGD peptide. The cyclic conformation required for high affinity binding of NGR to CD13 (22) was obtained through the addition of cysteines at the N- and C-terminus of the peptide. We also prepared the truncated version of iNGR that is expected to result from proteolytic activation of iNGR (CRNGR), which we refer to as iNGRt. The conventional NGR (CNGRC), RGD (CRGDC), iRGD (CRGDKGDPC) and activated iRGD (CRGDK) peptides were used as controls. The peptides used in this study are summarized in Table S1.

iNGR and NGR bind to the same primary receptor. Human umbilical vein endothelial cells (HUVECs) express on their surface both the NGR receptor CD13 and the CendR receptor NRP-1 (Fig S1). iNGR bound to HUVECs as efficiently as CNGRC, whether tested as FAM-labeled peptide (Fig. 1A) or displayed on phage (Fig. 1B, black columns). As expected, the iNGR phage did not bind CD13⁺ U937 monocytes (Fig. S2A-C), as previously reported for the CNGRC peptide (11). UV-inactivated phage displaying CNGRC inhibited the HUVEC binding of the iNGR phage in a dose-dependent fashion, whereas inactivated CRGDC did not differ from insertless control phage in this regard (Fig. 1C). CNGRC phage did not inhibit the binding of iRGD phage to HUVECs (Fig. S3A). Moreover, only *in vitro* deamidated CNGRC and iNGR phage showed binding to immobilized $\alpha\beta 3$ integrin (Fig. S3B). These results suggest that CNGRC and iNGR bind to the same primary receptor through the NGR motif and that the conversion of asparagine to aspartate does not take place during phage production,

purification, storage, or during the incubations. Therefore the binding of CNGRC and iNGR to cells is not due to isoDGR interacting with $\alpha\beta 3/5$ integrins.

The iNGR CendR motif interacts with NRPs and promotes cell internalization. We constructed phage displaying a truncated version of iNGR in which the CRNGR CendR motif occupies a C-terminal position (iNGRt). This phage bound avidly to HUVECs, likely due to an interaction with NRP-1 (Figs. 1A and 1B). Indeed, iNGRt phage binding to HUVECs was reduced by pre-incubation with a UV-inactivated phage expressing a prototypic CendR motif peptide (RPARPAR) or a neutralizing NRP-1 antibody (Fig. 1B), indicating involvement of the CendR/NRP-1 pathway. Pre-incubation with a phage displaying a peptide with a blocked CendR motif (RPARPARA), and a control antibody, had no effect on iNGRt binding to HUVECs. The binding of intact iNGR was not affected by the UV-inactivated RPARPAR phage or NRP-1 antibody showing that NRP-1 is not involved in the initial binding of the peptide. Measuring phage internalization by incubating phage with HUVECs at 37°C, followed by a wash with a low pH buffer to inactivate extracellular phage, showed stronger internalization of iNGR and iNGRt than CNGRC (Fig. 1D). Inhibition experiments showed that the internalization was mediated by the interaction of the CendR motif with NRP-1. These results suggest that HUVECs express a protease capable of activating the cryptic CendR motif embedded in the iNGR peptide. Indeed, mass spectrometry showed that upon incubation of HUVECs with FAM-iNGR peptide, only the cleaved FAM-CRNGR fragment (m/z : 1076.527), but not the full-length peptide (m/z : 1445.065), was present inside the cells (Fig S4). FAM-CNGRC peptide (m/z : 1020.020) did not penetrate into the cells. Direct proof that the CendR motif within the iNGR peptide is capable of binding to NRPs was provided by

CRNGR phage binding to immobilized NRP-1 (Fig. 1E). This phage also bound to NRP-2 (Fig. 1F). In agreement with the finding that the motif R/KXXR/K has to be in a C-terminal position to bind to NRPs (the Cend-Rule)(3), only phage expressing the iNGRt, and the analogous iRGDt, bound to the NRPs, whereas the corresponding full-length peptides showed only background binding. Interestingly, iNGRt showed higher affinity for NRP-1 and NRP-2 than iRGDt, suggesting that a C-terminal arginine residue (CRNGR) provides higher affinity than lysine (CRGDK).

iNGR penetrates deeper into tumors than NGR. We have previously shown in *ex vivo* tumor penetration assays that iRGD utilizes a CendR-mediated active transport system to cross tumor barriers (5). To investigate the iNGR-mediated penetration pathway, we performed an *ex vivo* tumor penetration assay of phage using explants of orthotopic 4T1 murine breast tumors (positive for expression of CD13 and NRP1/2; Fig 2A). To evaluate the extent of tumor penetration, we titrated the phage recovered from tumors (Fig 2B) and determined the distribution of phage immunoreactivity (Fig 2C). The CendR-containing phage (iNGR and iRGD) penetrated into the explants with resembling patterns, whereas non-CendR phage (CNGRC and control) remained at the outer rim of the explants. These results suggest that iNGR and iRGD share a similar CendR-mediated transport mechanism to penetrate tumor tissue.

Systemic iNGR selectively accumulates and penetrates into tumors. Having determined that the CendR motif within the iNGR peptide can be proteolytically activated to trigger interaction with NRPs and penetration into cells and tissues, we assessed the homing of iNGR *in vivo*. Intravenously administered iNGR phage accumulated within the tumor and

penetrated into the tumor stroma more than CNGRC phage (Fig 3A and B upper panels). The iNGRt phage also showed high tumor penetration, presumably because of the high expression of NRP-1 on tumor vasculature and tumor cells, but this phage also accumulated in lungs and heart of the tumor mice. iNGR penetration could be blocked by concomitantly administering a neutralizing anti-NRP-1 antibody, but not a control antibody (Fig 3B lower panels). Vascular targeting of iNGR was not inhibited by the anti-NRP-1 treatment (arrows, Fig 3B left lower panel), supporting the notion that the CendR activation occurs after iNGR accomplishes NGR-dependent vascular targeting. Intravenously injected FAM-iNGR peptide also accumulated in 4T1 breast tumors (Fig. 3C) and BxPC-3 pancreatic tumors (Fig. S5A) more strongly than FAM-CNGRC. FAM-iNGR extravasation within tumor tissue was greater than that of FAM-CNGRC (Fig 3D). FAM-iNGR selectively penetrated into tumors and not in control organs (Fig 3E). Elongated iron oxide nanoparticles (nanoworms; NWs) coated with iNGR also showed higher extravasation than CNGRC-NWs (Fig 3F and S5B). The NWs were less efficient than phage in penetrating the tissue, likely because they are larger in size (NWs, 30 x 70/200 nm; phage, 55nm).

iNGR triggers tumor-specific penetration of co-administered compounds. The engagement of NRP-1 increases vascular permeability (23), and iRGD triggers this phenomenon specifically in tumors (5). We found that iNGR significantly increased extravasation and accumulation of the albumin-binding dye Evans blue in 4T1 tumors, but not in non-tumor tissues. CNGRC or vehicle alone had no effect on the biodistribution of the dye (Fig. 4A, 4B, and S6). iNGR facilitated tumor-specific accumulation of Evans blue in CT26 colon and LLC lung tumor models as well (Fig. S7). We also co-administered iNGR with NWs

coated with a tumor homing peptide, CGKRK (20) that brings the NWs to tumor vessels, but does not trigger extravasation. iNGR allowed the NWs to extravasate into the tumor parenchyma (Fig. 4C). Finally, iNGR triggered more penetration of doxorubicin (DOX) into the tumors than DOX alone or DOX combined with CNGRC (Fig. 4D).

iNGR enhances anticancer drug efficacy. Having found that iNGR co-administration increased the local accumulation of DOX within tumors, we investigated the effect of iNGR on the activity of DOX. We treated orthotopic 4T1 breast tumor mice with a combination of DOX (3 mg/kg) and 4 μ mol/kg of iNGR, a control peptide, or PBS every other day. As shown in Figure 5A, iNGR, but not CNGRC, enhanced the antitumor effect of DOX. iNGR alone had no effect on the progression of tumor growth. Loss of body weight as an indicator of DOX toxicity was not affected by the peptide co-administration (Fig. 5B). These results demonstrate the potential of iNGR as an adjuvant to increase the efficacy of co-administered anticancer drugs.

Discussion

We report here the design of a new tumor-penetrating peptide, iNGR. The peptide was constructed by combining the tumor-targeting motif NGR and tissue-penetrating CendR motif into a 9-amino acid cyclic peptide. The iNGR peptide, homed to tumor vessels, exited the vessels, and penetrated into the tumor mass. It was able to take both coupled and co-administered payloads with it. When the co-administered payload was a drug (DOX), the efficacy of the drug increased. These results show that it is possible to use the existing knowledge to construct a new tumor-specific, tissue-penetrating peptide.

The mechanisms underlying iNGR activity are similar to those described for iRGD (4, 5). The receptor for the tumor-targeting motif NGR is a variant form of aminopeptidase N (12). The binding of iNGR to cultured cells was specifically inhibited by CNGRC, indicating that iNGR binds to the same receptor. NGR peptides are known to spontaneously undergo slow deamidation of the asparagine residue into isoaspartic acid. The resulting isoDGR peptides, like RGD peptides, bind to α_v integrins. Our results exclude integrin involvement in the binding of iNGR peptide and phage to cultured cells. It is also unlikely that isoDGR formation affects the *in vivo* tumor targeting of iNGR because the deamidation process takes several hours (24), whereas the half-life of intravenously injected peptides of the size of iNGR is only minutes (25). Thus iNGR and iRGD bind to different primary receptors on cells.

Upon engagement of the iRGD peptide at the plasma membrane of target cells, a proteolytic cleavage by a yet-to-be-identified enzyme(s) exposes the CendR sequence, which subsequently binds to NRP-1 (4). Our evidence indicates that the same mechanism operates

with iNGR. First, phage displaying the predicted CendR product of iNGR, CRNGR (iNGRt) bound to NRP-1 and NRP-2, and did so with a higher affinity than CRGDK fragment of iRGD. The reason for the difference may be that a peptide with a C-terminal arginine binds more efficiently to NRPs than a peptide with a lysine C-terminus (26). Comparison of the tumor-homing efficacy of iRGD with an arginine or a lysine (CRGDK/RGPDC) showed that the lysine-containing form was more effective *in vivo* (4). It may be that other effects of the lysine residue, such as stronger integrin binding or higher susceptibility to protease cleavage, overcome the effect of lower affinity for NRPs. Second, iNGR, both as a synthetic peptide and on phage was taken up by cells in a NRP-dependent manner. Third, we isolated the iNGRt CendR fragment from inside cells treated with the intact iNGR peptide, as has been previously done with iRGD (4). Fourth, the co-injection of iNGR phage with neutralizing anti-NRP-1 antibody resulted in a reduced extravasation of iNGR. These results show that iNGRt, the active form of iNGR, is generated through proteolysis and that the tumor-penetrating properties of iNGR are based on its ability to activate the CendR pathway.

The activation of iNGR into iNGRt appears to take place only in tumors because iNGR only accumulated in tumors. In contrast, the truncated iNGRt form, while showing preferential homing to tumors, also accumulated in the lungs and heart. This homing pattern reflects the expression of NRP-1, which is universal in the blood vessels but particularly high in tumor vessels (27). The reason for the selective activation of the cryptic CendR motif in tumors is likely to be that binding to the primary receptor is needed for activating proteolytic cleavage. Previous work from our laboratory has shown that an iRGD variant that does not bind to integrins, but contains a CendR motif, does not penetrate into cultured cells, whereas iRGD

does (4). The nature of the primary receptor does not seem to matter, as long as the receptor is tumor specific. iRGD and iNGR bind to different primary receptors, but both become activated in cell cultures and in tumors. Moreover, we have recently shown that a previously identified tumor-homing peptide, CGNKRTRGC (LyP-1) (28) also penetrates into tumors through the CendR/NRP mechanism (6). The primary receptor for this peptide is p32/gC1qR/HABP1, a mitochondrial protein expressed at the cell surface in tumors (29). Thus, our results show that at least 3 different primary receptors can initiate the sequence of events that leads to the NRP-dependent activation of the CendR pathway in tumors. Importantly, the difference in the primary receptors allows us to differentially target tumors or tumor areas based on receptor expression patterns, providing multiple options to enhance tumor therapy with tumor-specific CendR peptides.

The experiments with phage, fluorophore-labeled peptide, and nanoparticles showed the ability of iNGR to take coupled payloads into the extravascular tumor tissue. Our results further demonstrate that such enhanced delivery and tumor penetration also applies to compounds co-administered with iNGR. Importantly, we showed this for DOX, the anti-tumor activity of which was increased by injecting the drug together with iNGR.

The co-administration strategy has significant advantages. First, because chemical coupling is not needed, new chemical entities are not created, providing a faster route for clinical development. Second, unlike targeting of compounds chemically coupled to an homing

element, the co-administration process is not strictly dependent on the number of available receptors, which seriously limits the amount of a drug that can be delivered to a target (30).

Taken together, our results show that iNGR possesses the same targeting ability as CNGRC, supplemented with cell-internalizing and tumor-penetrating properties. This transformation suggests an important principle: a targeting peptide can be *ad hoc* improved by the addition of a CendR motif, which endows the peptide with tissue-penetrating properties and allows enhanced delivery of co-administered compounds into a target tissue. Rational optimization of targeting peptides in this manner may also have valuable applications in other diseases.

Authors' Contributions

LA, LR, KNS, TT, CT, GPR, CB and ER designed research; LA, LR, KNS, LAg and TT performed research; VRK and LAg contributed new reagents; LA, LR, KNS, LAg, TT and ER analyzed data. LA, KNS, TT and ER wrote the paper.

References

1. Ruoslahti E. Specialization of tumour vasculature. *Nat Rev Cancer* 2002;2:83-90.
2. Heldin CH, Rubin K, Pietras K, Ostman A. High interstitial fluid pressure - an obstacle in cancer therapy. *Nat Rev Cancer* 2004;4:806-13.
3. Teesalu T, Sugahara KN, Kotamraju VR, Ruoslahti E. C-end rule peptides mediate neuropilin-1-dependent cell, vascular, and tissue penetration. *Proc Natl Acad Sci U S A* 2009;106:16157-62.
4. Sugahara KN, Teesalu T, Karmali PP, Kotamraju VR, Agemy L, Girard OM, et al. Tissue-penetrating delivery of compounds and nanoparticles into tumors. *Cancer Cell* 2009;16:510-20.
5. Sugahara KN, Teesalu T, Karmali PP, Kotamraju VR, Agemy L, Greenwald DR, et al. Coadministration of a tumor-penetrating peptide enhances the efficacy of cancer drugs. *Science* 2010;328:1031-5.
6. Roth L, Agemy L, Kotamraju VR, Braun G, Teesalu T, Sugahara KN, et al. Transtumoral targeting enabled by a novel neuropilin-binding peptide. *Oncogene* 2012;31:3754-63.
7. Arap W, Pasqualini R, Ruoslahti E. Cancer treatment by targeted drug delivery to tumor vasculature in a mouse model. *Science* 1998;279:377-80.
8. Koivunen E, Gay DA, Ruoslahti E. Selection of peptides binding to the alpha 5 beta 1 integrin from phage display library. *J Biol Chem* 1993;268:20205-10.
9. Curnis F, Longhi R, Crippa L, Cattaneo A, Dondossola E, Bachi A, et al. Spontaneous formation of L-isoaspartate and gain of function in fibronectin. *J Biol Chem* 2006;281:36466-76.
10. Spitaleri A, Mari S, Curnis F, Traversari C, Longhi R, Bordignon C, et al. Structural basis for the interaction of isoDGR with the RGD-binding site of alphavbeta3 integrin. *J Biol Chem* 2008;283:19757-68.
11. Curnis F, Arrigoni G, Sacchi A, Fischetti L, Arap W, Pasqualini R, et al. Differential binding of drugs containing the NGR motif to CD13 isoforms in tumor vessels, epithelia, and myeloid cells. *Cancer Res* 2002;62:867-74.

12. Pasqualini R, Koivunen E, Kain R, Lahdenranta J, Sakamoto M, Stryhn A, et al. Aminopeptidase N is a receptor for tumor-homing peptides and a target for inhibiting angiogenesis. *Cancer Res* 2000;60:722-7.
13. Corti A, Curnis F. Tumor vasculature targeting through NGR peptide-based drug delivery systems. *Curr Pharm Biotechnol* 2011;12:1128-34.
14. Corti A, Pastorino F, Curnis F, Arap W, Ponzoni M, Pasqualini R. Targeted drug delivery and penetration into solid tumors. *Med Res Rev* 2012;32:1078-91.
15. Corti A, Curnis F, Arap W, Pasqualini R. The neovasculature homing motif NGR: more than meets the eye. *Blood* 2008;112:2628-35.
16. Curnis F, Sacchi A, Borgna L, Magni F, Gasparri A, Corti A. Enhancement of tumor necrosis factor alpha antitumor immunotherapeutic properties by targeted delivery to aminopeptidase N (CD13). *Nat Biotechnol* 2000;18:1185-90.
17. Agemy L, Sugahara KN, Kotamraju VR, Gujraty K, Girard OM, Kono Y, et al. Nanoparticle-induced vascular blockade in human prostate cancer. *Blood* 2010;116:2847-56.
18. Teesalu T, Sugahara KN, Ruoslahti E. Mapping of Vascular ZIP Codes by Phage Display. *Methods Enzymol* 2012;503:35-56.
19. Curnis F, Cattaneo A, Longhi R, Sacchi A, Gasparri AM, Pastorino F, et al. Critical role of flanking residues in NGR-to-isoDGR transition and CD13/integrin receptor switching. *J Biol Chem* 2010;285:9114-23.
20. Agemy L, Friedmann-Morvinski D, Kotamraju VR, Roth L, Sugahara KN, Girard OM, et al. Targeted nanoparticle enhanced proapoptotic peptide as potential therapy for glioblastoma. *Proc Natl Acad Sci U S A* 2011;108:17450-5.
21. Mayer LD, Dougherty G, Harasym TO, Bally MB. The role of tumor-associated macrophages in the delivery of liposomal doxorubicin to solid murine fibrosarcoma tumors. *J Pharmacol Exp Ther* 1997;280:1406-14.
22. Colombo G, Curnis F, De Mori GM, Gasparri A, Longoni C, Sacchi A, et al. Structure-activity relationships of linear and cyclic peptides containing the NGR tumor-homing motif. *J Biol Chem* 2002;277:47891-7.

23. Becker PM, Waltenberger J, Yachechko R, Mirzapoiazova T, Sham JS, Lee CG, et al. Neuropilin-1 regulates vascular endothelial growth factor-mediated endothelial permeability. *Circ Res* 2005;96:1257-65.
24. Corti A, Curnis F. Isoaspartate-dependent molecular switches for integrin-ligand recognition. *J Cell Sci* 2011;124:515-22.
25. Werle M, Bernkop-Schnurch A. Strategies to improve plasma half life time of peptide and protein drugs. *Amino Acids* 2006;30:351-67.
26. Haspel N, Zanuy D, Nussinov R, Teesalu T, Ruoslahti E, Aleman C. Binding of a C-end rule peptide to the neuropilin-1 receptor: a molecular modeling approach. *Biochemistry* 2011;50:1755-62.
27. Jubb AM, Strickland LA, Liu SD, Mak J, Schmidt M, Koeppen H. Neuropilin-1 expression in cancer and development. *J Pathol* 2012;226:50-60.
28. Laakkonen P, Porkka K, Hoffman JA, Ruoslahti E. A tumor-homing peptide with a targeting specificity related to lymphatic vessels. *Nat Med* 2002;8:751-5.
29. Fogal V, Zhang L, Krajewski S, Ruoslahti E. Mitochondrial/cell-surface protein p32/gC1qR as a molecular target in tumor cells and tumor stroma. *Cancer Res* 2008;68:7210-8.
30. Ruoslahti E, Bhatia SN, Sailor MJ. Targeting of drugs and nanoparticles to tumors. *J Cell Biol* 2010;188:759-68.

Figure legends

Fig. 1. iNGR shares the same receptor with CNGRC and, upon activation, strongly interacts with NRPs. (A) HUVECs were incubated for 2 hours at 4°C with FAM-labeled ARA (ARALPSQRSR;(28)), CNGRC, iNGR or iNGRt peptides. Cells were fixed and imaged with a Fluoview confocal microscope. Scale bars: 100 μ m. (B and D) Tenfold excess of UV-inactivated RPARPAR or RPARPARA phage, or 1 μ g/ml of control or neutralizing NRP-1 antibody was used to inhibit the binding (B) or the internalization (D) of CNGRC, iNGR or iNGRt phage in HUVECs. The results are shown as fold increase over insertless phage. * one way ANOVA < 0.05. Error bars: Standard Error. (C) Dose-dependent inhibition of iNGR phage binding to HUVECs by UV-inactivated phage. iNGR phage binding without inhibitors was considered as 100%. Error bars: Standard Error. (E and F) Dose-dependent binding of phage to purified NRP-1 (E) or NRP-2 (F) proteins. The number of phage bound to the proteins was quantified using a combination of a rabbit anti-T7 phage antibody and an HRP-labeled goat anti-rabbit antibody.

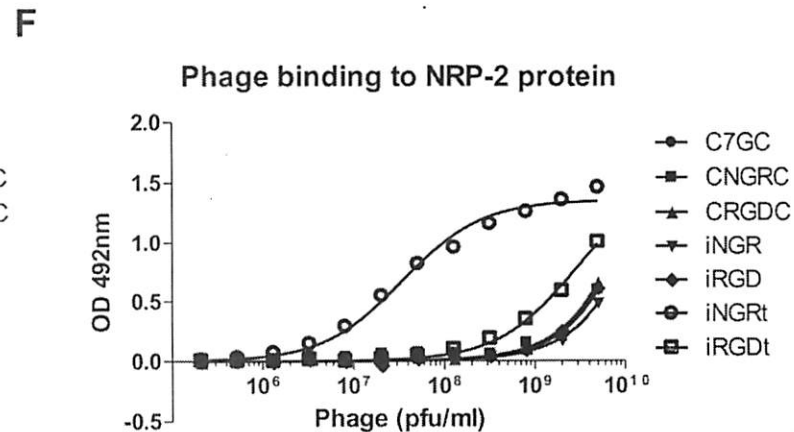
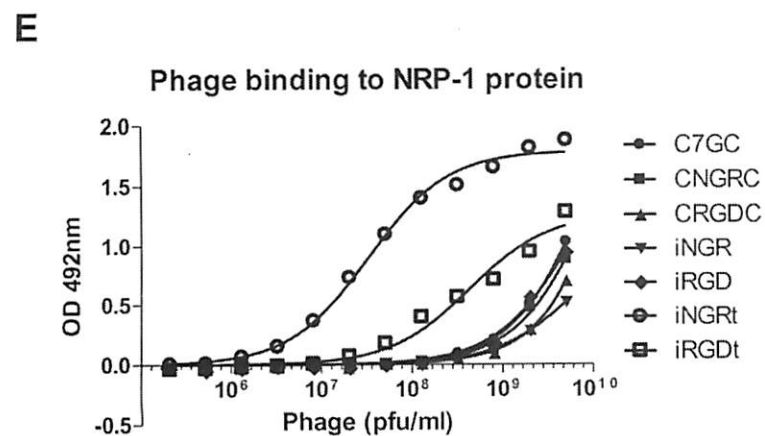
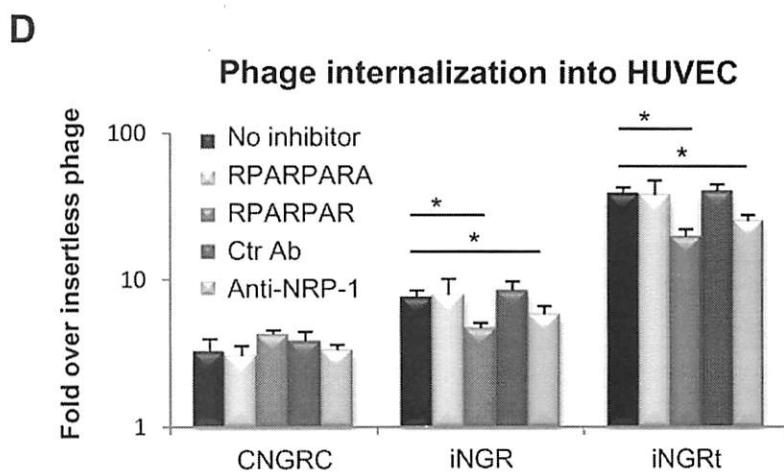
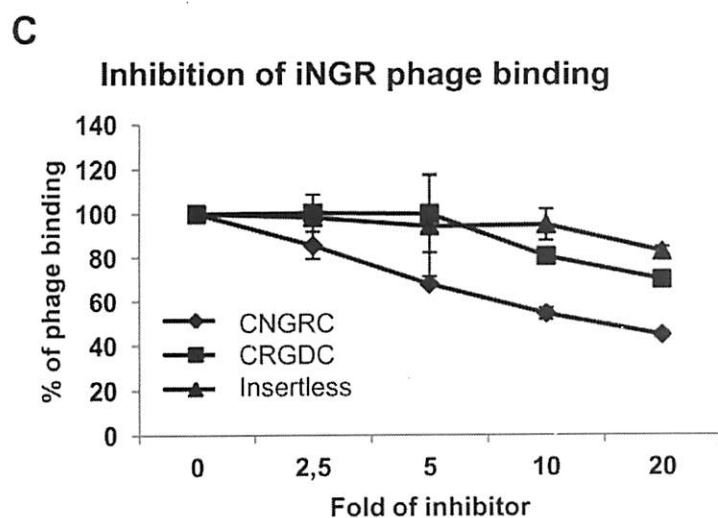
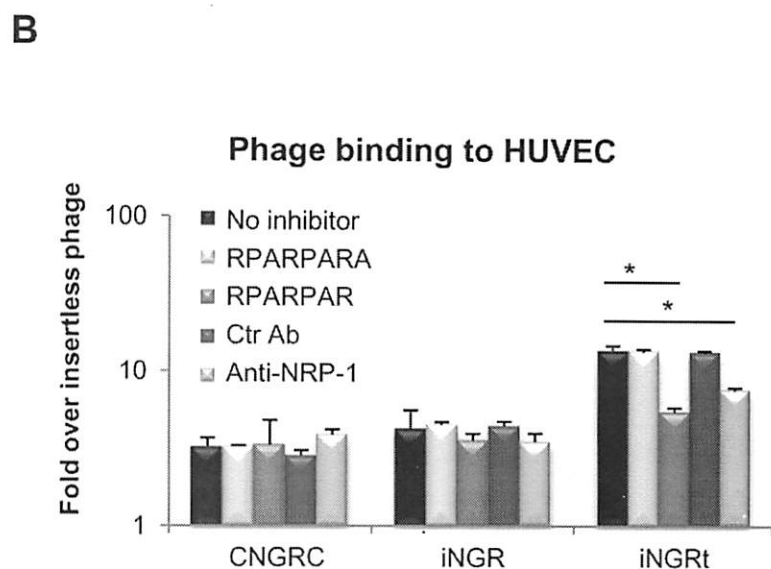
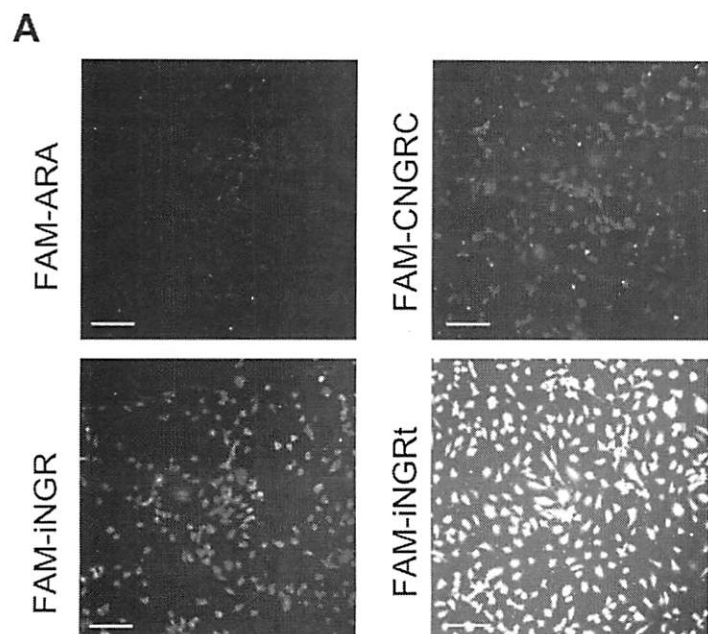
Fig. 2. iNGR penetrates deeper to tumors than NGR. (A) Expression of CD13, NRP-1, and NRP-2 on 4T1 cells analyzed by flow cytometry. The profiles represent the values of cells stained with appropriate antibodies (solid lines) or an isotype control (shaded). (B) Explanted 4T1 tumors were incubated with insertless, CNGRC, iNGR or iRGD phage. Phage bound to the tumor surface were removed with acid wash, and the number of phage particles that penetrated into the tumors was quantified by phage titration. Results are shown as fold increase over insertless phage. Each value was normalized against tumor weight. * one way

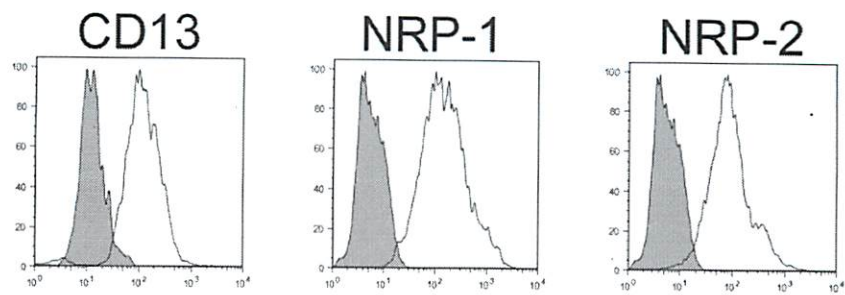
ANOVA < 0.05. Error bars: Standard Error. (C) Tumor dipping assays were performed as in (B), and frozen tumor sections were stained with an anti-T7 phage antibody (green) and DAPI (blue). Scale bars: 100µm.

Fig. 3. Systemic iNGR selectively accumulates and penetrates tumors. (A-B) *In vivo* phage homing to orthotopic 4T1 tumors. Phage were intravenously injected into 4T1 bearing mice and allowed to circulate for 40 minutes. After perfusion of the mice, tissues were collected and homogenized for phage titration (A) or processed for phage (green) and CD31 (red) immunostaining (B). Blue represents DAPI staining. In some cases, iNGR phage was co-injected with 50 µg of neutralizing NRP-1 or rabbit IgG antibody (B, lower panels). * one way ANOVA < 0.05. Scale bars: 50µm. Error bars: Standard Error (C-E) *In vivo* peptide homing to 4T1 tumors. One hundred micrograms of FAM-peptides (green) were intravenously injected into 4T1 bearing mice. One hour later, the mice were perfused, and tissues were collected and imaged under a UV light table (C and E). Then, the tissues were processed for CD31 (red) and nuclei (blue) staining (D) Scale bars: 50µm. (F) *In vivo* homing of NWs to 4T1 tumors. CNGRC- or iNGR-coated NWs (green) were injected into the tail vein of 4T1 tumor mice. After 4 hours, the mice were perfused, and tumors were collected and subjected to CD31 staining (red). Blue represents DAPI staining. Confocal images at 20x and 40x magnifications are shown. Scale bars: 100µm (20x), 50µm (40x). The arrows point to blood vessels positive for phage (B) or peptide (D). Note that the iNGR phage, peptides, and NWs effectively penetrated 4T1 tumors, and that the anti-NRP-1 antibody inhibited the tumor penetration of iNGR phage.

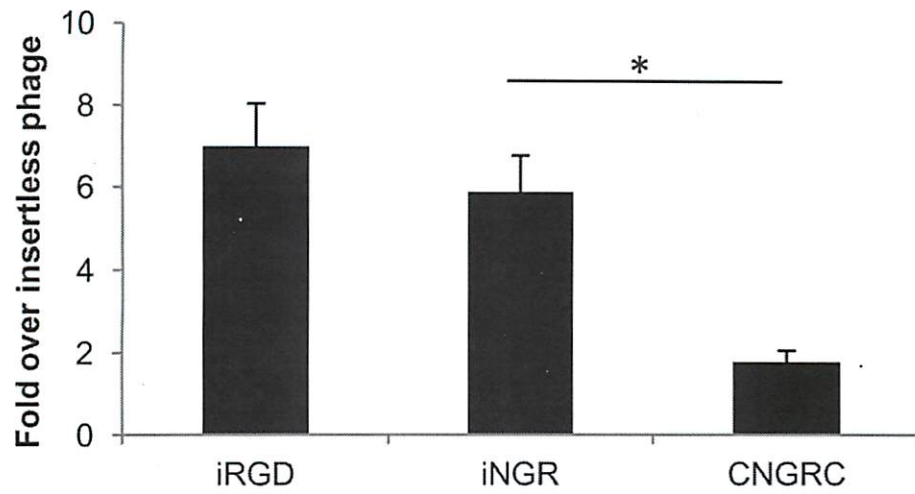
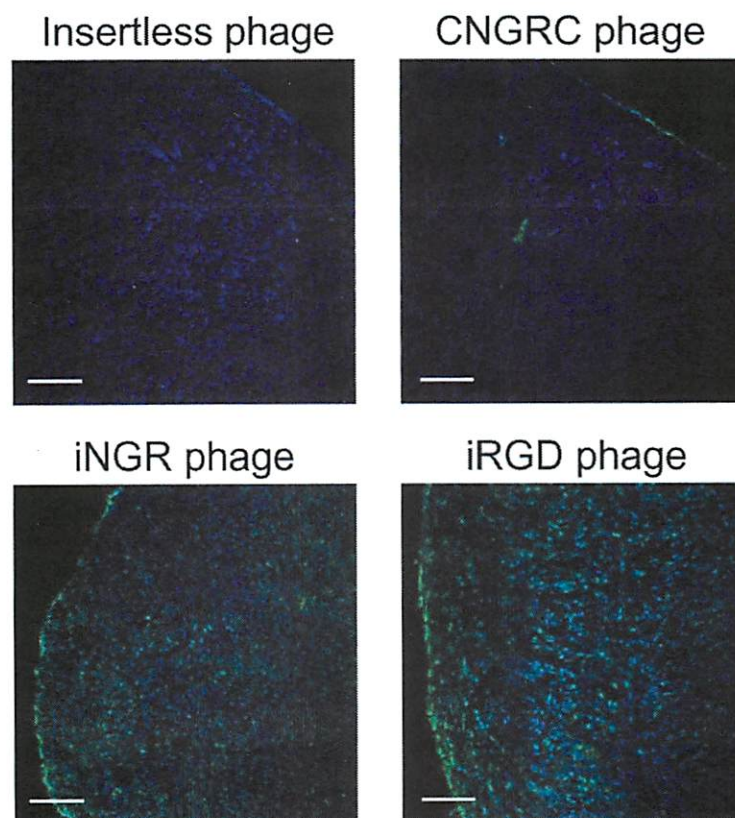
Fig. 4. iNGR triggers tumor-specific penetration of co-administered compounds. (A and B) One milligram of Evans Blue dye was intravenously co-injected with 4 $\mu\text{mol/kg}$ of peptides or PBS. After 40 minutes of circulation, the mice were extensively perfused, and tumors were collected for imaging under white light (A). Evans blue was extracted from the collected tumors and organs and quantified by OD₆₀₀ measurement (B). (C) Five mg/kg of FAM-CGKRK-conjugated NWs (green) were injected with or without 4 $\mu\text{mol/kg}$ of iNGR peptide into the tail vein of 4T1 bearing mice. After 5 hours of circulation, tumors were collected for CD31 immunostaining (red). Blue represents DAPI staining. Two representative images of three tumors are shown. Scale bars: 100 μm . (D) Ten mg/kg of DOX was intravenously co-injected with 4 $\mu\text{mol/kg}$ of the indicated peptides in 4T1-bearing mice. After 1 hour of circulation, the mice were extensively perfused, and the tissues were collected for DOX quantification. Results are shown as fold increase over DOX alone. * one way ANOVA < 0.05. Error bars: Standard Error.

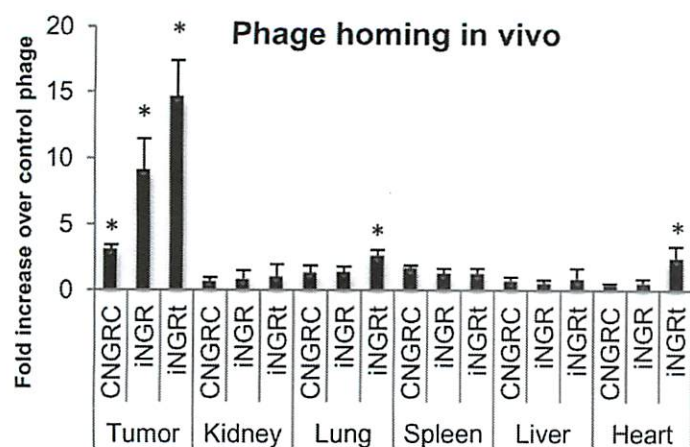
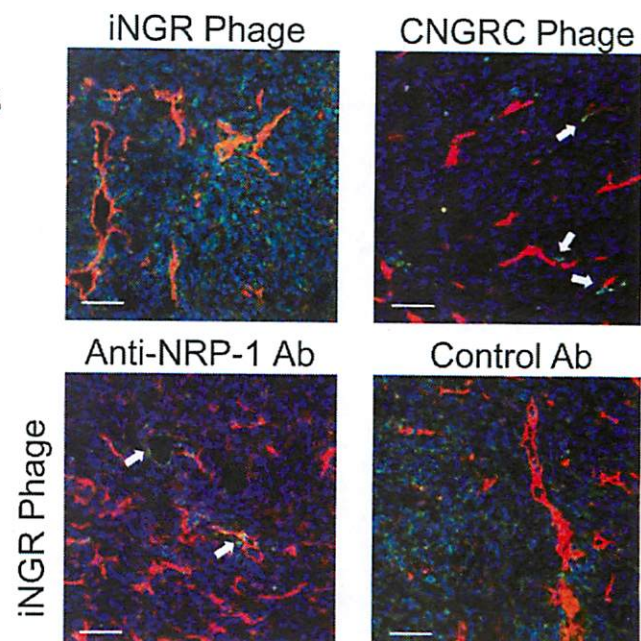
Fig. 5. iNGR enhances efficacy of anticancer drugs without affecting side effects. (A) Mice bearing orthotopic 4T1 tumors were treated every other day with PBS or 3 mg/kg of DOX combined with 4 $\mu\text{mol/kg}$ of CNGRC or iNGR peptide. Tumor growth was assessed every other day. (B) Body weight changes of the tumor mice from the treatment studies in (A). Percent body weight shift is shown. * two-way ANOVA < 0.05. *** two-way ANOVA < 0.001. Error bars: Standard Error.



A**B**

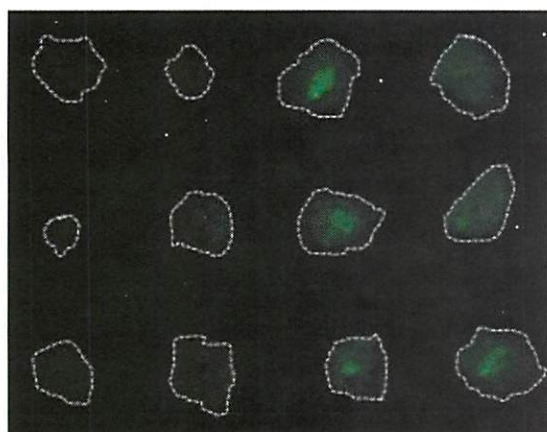
Dipping assay

**C**

A**B****C**

FAM- ARA CNGRC iNGR iNGRt

4T1 Tumors

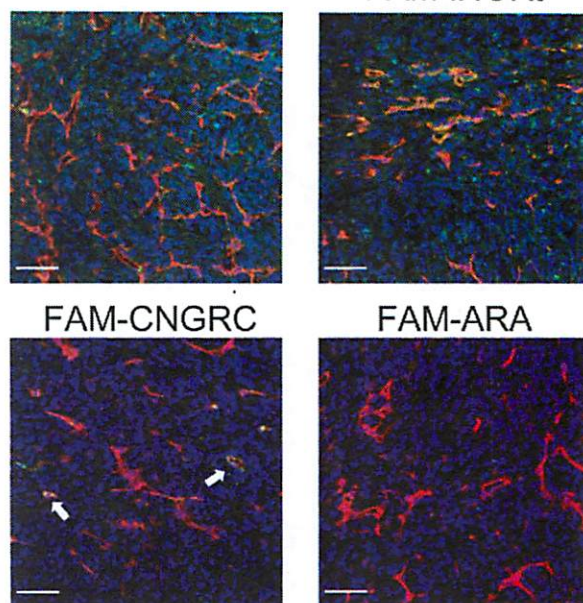
**D**

FAM-iNGR

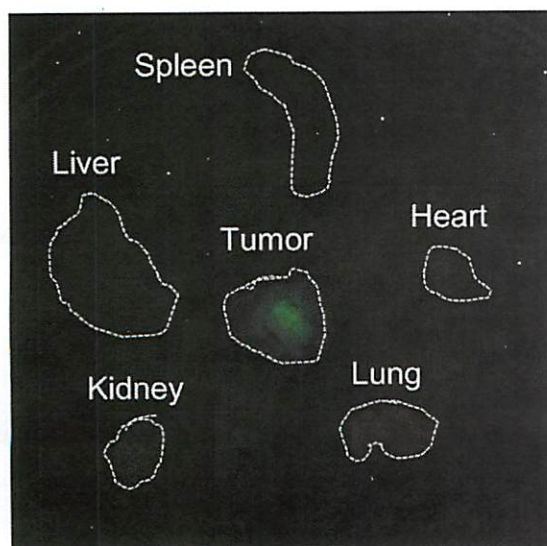
FAM-iNGRt

FAM-CNGRC

FAM-ARA

**E**

FAM-iNGR

**F**

20x

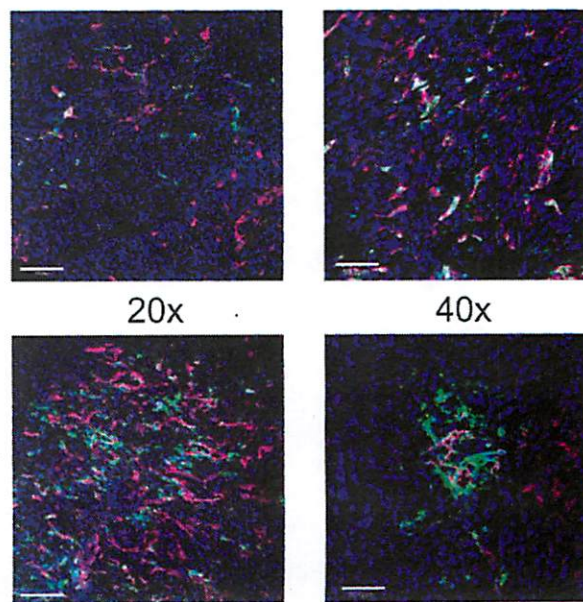
40x

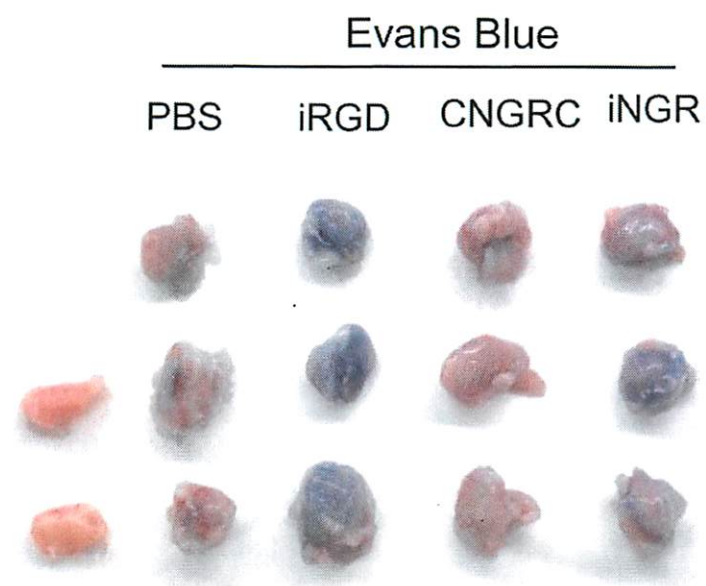
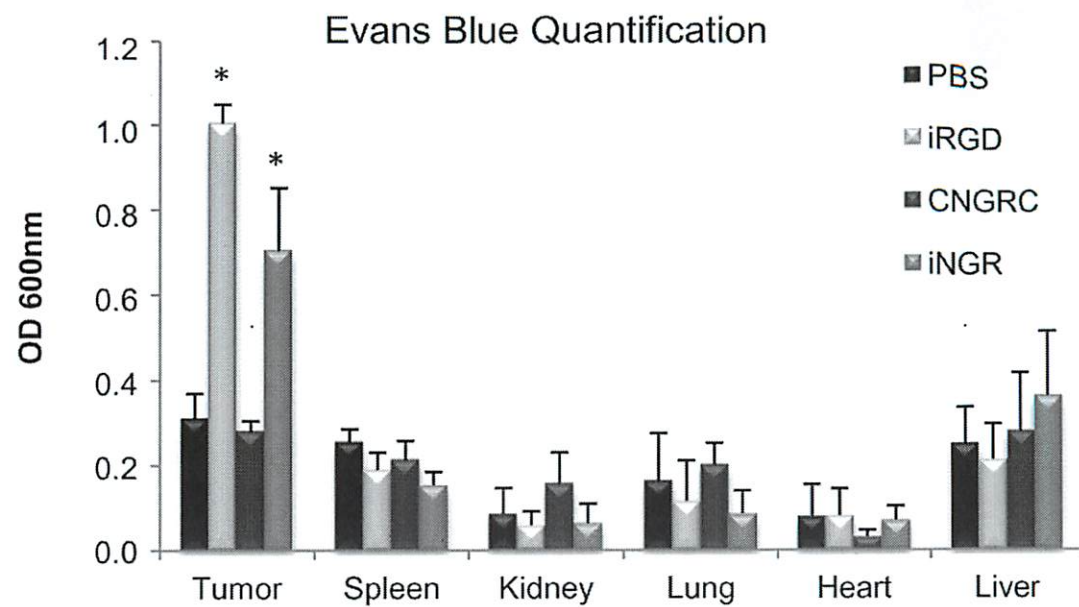
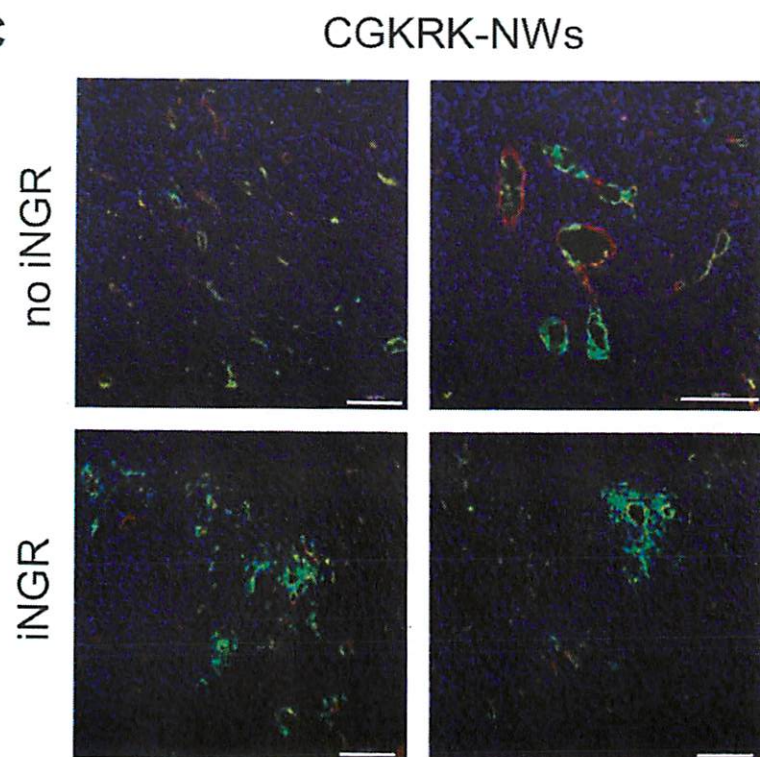
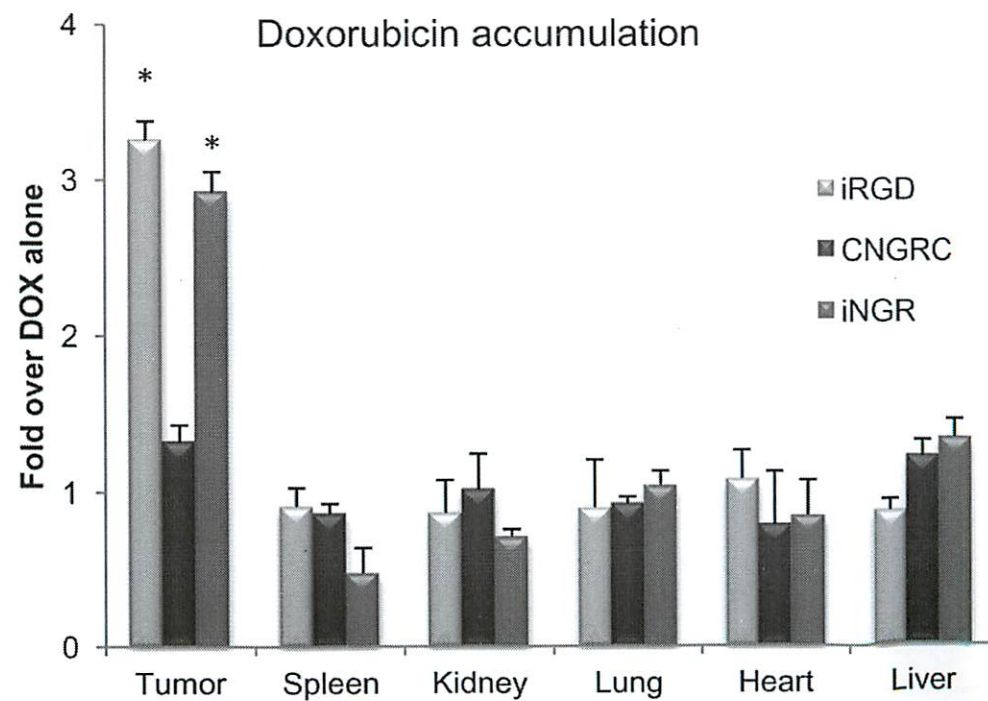
CNGRC-NW's

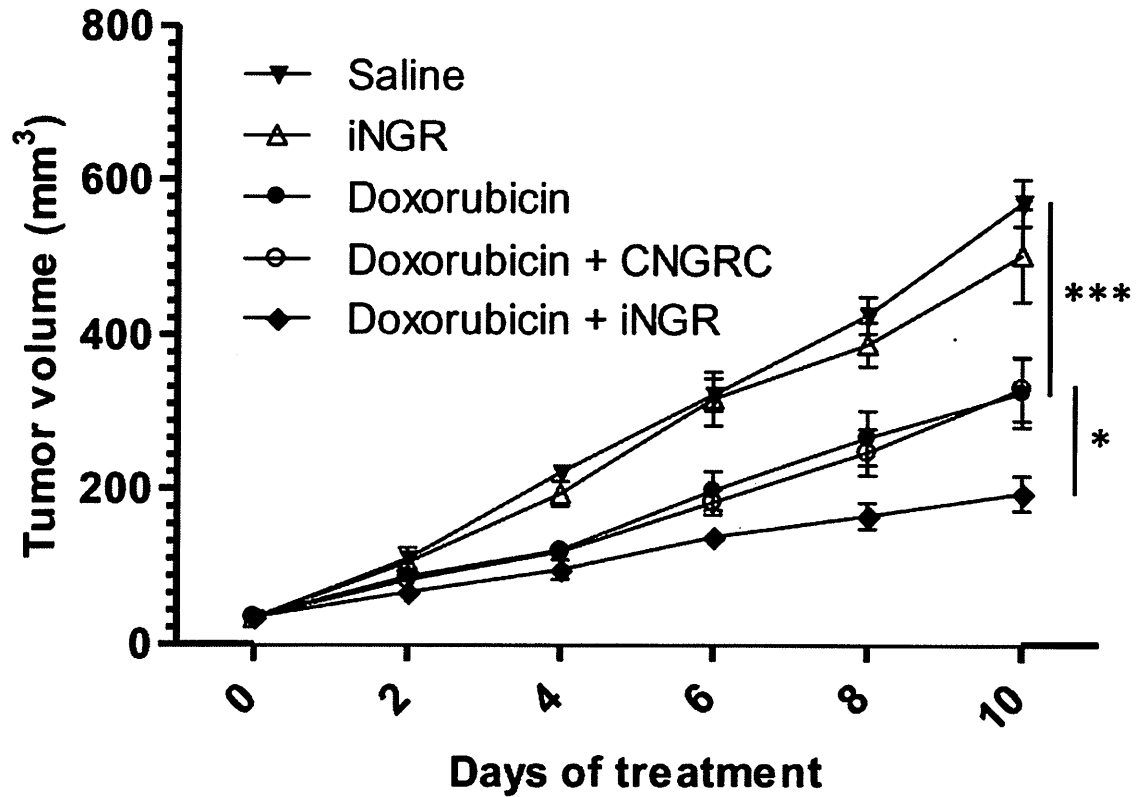
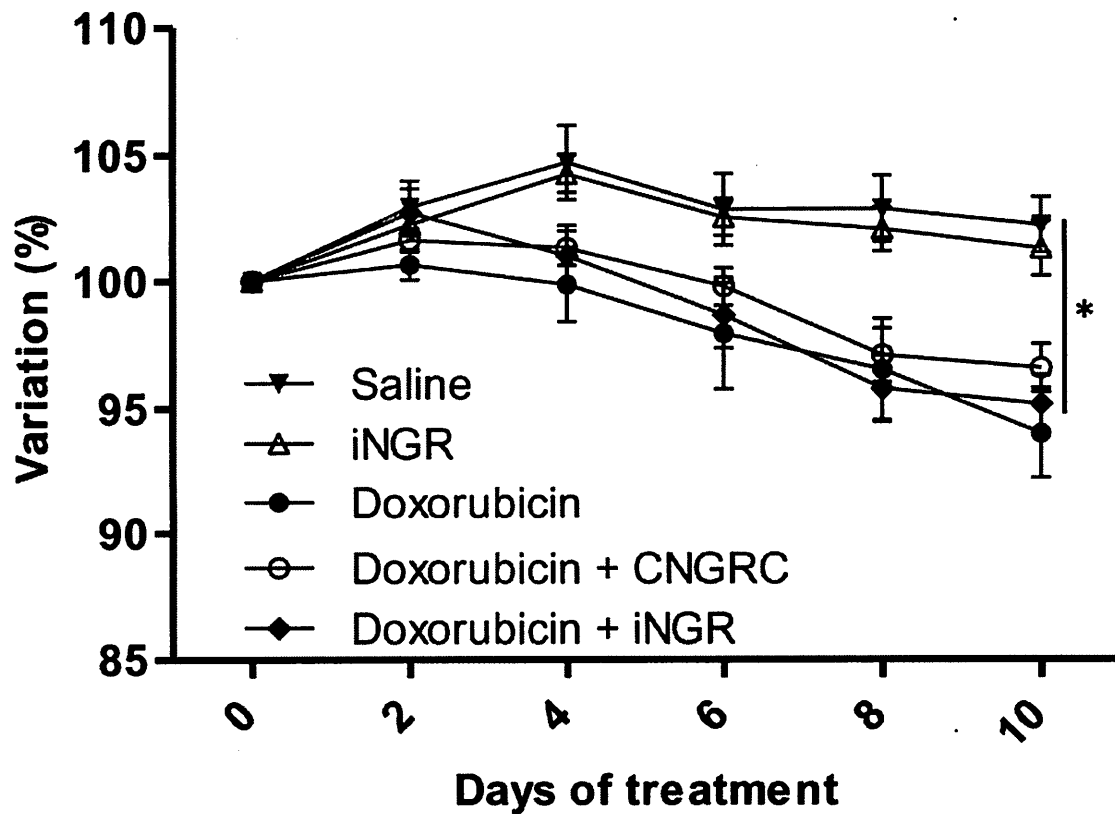
20x

40x

iNGR-NW's



A**B****C****D**

A**4T1 tumor treatment****B****Body weight**

De Novo Design of a Tumor-Penetrating Peptide

Luca Alberici^{1,2,3}, Lise Roth⁴, Kazuki N. Sugahara¹, Lilach Agemy¹, Venkata R. Kotamraju¹, Tambet Teesalu¹, Claudio Bordignon^{2,3}, Catia Traversari², Gian-Paolo Rizzardi², Erkki Ruoslahti¹

Materials and Methods

ELISA. MicroTest III Flexible assay plates (BD, San Jose, CA) were coated with 5 µg/ml of recombinant human NRP-1 (R&D Systems, Minneapolis, MN), recombinant human NRP-2 Fc chimera (R&D Systems), or recombinant human integrin $\alpha v \beta 3$ (R&D Systems). The coated plates were blocked with 0.5% BSA in PBS for 1 hour, and incubated with serial dilutions of phage for 2 hours at 4°C. The wells were washed with PBS containing 0.05% Tween20, and incubated with a rabbit anti-T7 phage antibody (3). After 1 hour at 4°C, the wells were washed and incubated with an HRP-labeled anti-rabbit antibody (Sigma-Aldrich) for 1 hour at 4°C. o-Phenylenediamine dihydrochloride (SigmaFast OPD; Sigma-Aldrich) was used as a substrate to quantify the amount of the HRP-labeled antibody captured on the microtiter wells. The reaction was stopped using 3 M H₂SO₄ and the absorbance at 492 nm was measured using a Labsystems Multiskan Plus (Fisher Scientific, Pittsburgh, PA).

Flow Cytometry: Adherent cells were detached using enzyme free dissociation buffer (Gibco). Incubations and washes were performed in PBS containing 3% FBS with the following antibodies at the dilution of 1:100. Primary antibodies: rat IgG (Santa Cruz Biotechnology, Santa Cruz, CA), rat anti-mouse CD13 (R363, GeneTex, Irvine, CA), rabbit IgG (Santa Cruz Biotechnology), rabbit anti-mouse NRP-1 (Millipore, Billerica, MA), rabbit anti-mouse NRP-2 (Millipore), mouse IgG (AbD Serotech, Raleigh, NC), mouse anti-human CD13 (WM15, Santa Cruz Biotechnology, Santa Cruz, CA), mouse anti-human NRP-1 (Miltenyi Biotec, Bergisch Gladbach, Germany) and mouse anti-human NRP-2 (R&D Systems). Secondary antibodies: FITC-labeled goat anti-rabbit (Invitrogen, Grand Island, NY), Alexa-488-labeled goat anti-rat (Invitrogen) antibodies and PE-labeled goat anti-mouse (Southern Biotech, Birmingham, AL).. Fluorescence was detected using a FACSort (BD Bioscience, San Jose, CA).

Cell lines and tumor models: The human leukemic monocyte lymphoma cell line U937 was cultured in RPMI supplemented with 10% FBS and penicillin/streptomycin. The Human pancreatic cell line BxPC-3 was cultured in DMEM supplemented with 10% FCS and penicillin/streptomycin. Ectopic BxPC3, tumors were generated by s.c. injection of 10^6 cells into athymic nude mice. Mouse Lewis Lung Carcinoma (LLC) and CT26 colon carcinoma were cultured in standard conditions. LLC (1×10^5) and CT26 (4×10^5) cells were s.c. injected into syngeneic C57BL/6 mice and BALB/c mice (Charles River Laboratories), respectively.

Peptide fragment isolation and analyses: Peptide fragment isolation and mass spectrometry analyses were performed using the protocol provided for FAM-iRGD isolation from cells (Sugahara et al. Cancer Cell, 16: 510-520, 2009).

Figure legends

Supplementary Table 1. Peptide description. ID and sequence in single letter amino acid code of each peptide is shown.

Supplementary Fig. 1. HUVECs express NGR and CendR motif receptors. Expression of CD13, NRP-1, and NRP-2 on HUVECs analyzed by flow cytometry. The profiles represent the values of cells stained with appropriate antibodies (solid lines) or an isotype control (shaded).

Supplementary Fig. 2. iNGR does not bind to CD13⁺ monocytes. (A) Expression of CD13, NRP-1, and NRP-2 on U937 monocytes analyzed by flow cytometry. The profiles represent the values of cells stained with appropriate antibodies (solid lines) or an isotype control (shaded). (B) Binding and (C) internalization of indicated T7 phage into U937 cells. Results are reported as fold increase over insertless phage binding/internalization. Error bars: Standard Error.

Supplementary Fig. 3. iNGR binding is not mediated by αv integrins. (A) Dose-dependent inhibition of iRGD phage binding to HUVECs by UV-inactivated phage. iRGD phage binding without inhibitors was considered as 100%. Error bars: Standard Error. (B) Dose-dependent binding of phage to purified $\alpha v \beta 3$ integrin. Some of the phage were pre-incubated in 0.1 M ammonium bicarbonate for 6 hours at 37°C to induce deamidation of asparagine into isoaspartic acid in the peptides and then probed on $\alpha v \beta 3$ coated plates. The number of phage that bound to the protein was quantified with ELISA using a combination of a rabbit anti-T7 phage antibody and an HRP-labeled goat anti-rabbit antibody.

Supplementary Fig. 4. iNGR is cleaved upon entering the cells. Mass-Spectrometry of intact FAM-NGR and FAM-iNGR peptides (first 2 lanes) and peptide fragments isolated from inside HUVECs (lanes 3 to 5). HUVECs were incubated without any peptides or with FAM-CNGRC or FAM-iNGR for 1 hour in the presence of a proteasome inhibitor MG132. The cells were lysed, and FAM-peptide fragments were recovered by immunoprecipitation with an anti-FAM antibody from the cell lysates. Note the presence of FAM-CRNGR peptides (m/z : 1076.527) only in the bottom panel. X: 6-aminoesanoic acid used as linker.

Supplementary Fig. 5. iNGR penetrates into extravascular tumor tissue. (A) Peptide accumulation in human pancreatic BxPC3 tumors. FAM-peptides (100 μ g; green) were intravenously injected into BxPC3-bearing mice. One hour later, the mice were perfused, and tissues were collected and imaged under a UV light table. Tum, Tumor; B, brain; K, kidney; Lu, lung; H, heart; P, pancreas; S, spleen. (B) FAM-NGR and FAM-iNGR NWS penetration into the tumor was quantified. Results are expressed as μm^2 of NW positive area per field. * $p < 0.05$.

Supplementary Fig. 6. iNGR does not increase the penetration of co-administered Evans blue dye into normal organs. Mice bearing 4T1 tumors were intravenously injected with 1 mg of Evans blue combined with PBS or 4 $\mu\text{mol/kg}$ of the indicated peptides. After 40 minutes of circulation, the mice were extensively perfused, and the organs were collected for imaging under white light. T, tumor; S, spleen; K, kidney; Lu, lung; H, heart; Liv, liver.

Supplementary Fig. 7. iNGR enhances tumor penetration of Evans Blue dye. Evans Blue (1 mg) was intravenously co-injected with of peptides (4 $\mu\text{mol/kg}$) or PBS into mice bearing either LLC (A) or CT26 (B) tumors. After 40 minutes of circulation, mice were extensively perfused and tumors were collected. Evans Blue was extracted from the

De Novo Design of a Tumor-Penetrating Peptide

tumors and kidneys and quantified by OD₆₀₀ measurement. Error bars: Standard Error. *

$p < 0.05$. ** $p < 0.005$.

Table S1

Peptide ID	Complete amino acid sequence
ARA	ARALPSQRRSR
Insertless	SSVDKLAAALE
NGR	CNGRC (cyclized between the cysteines)
iNGR	CRNGRGPDC (cyclized between the cysteines)
iNGRt	CRNGR
RGD	CRGDC (cyclized between the cysteines)
iRGD	CRGDKGPDC (cyclized between the cysteines)
iRGDt	CRGDK
RPARPAR	RPARPAR
RPARPARA	RPARPARA

Figure S1

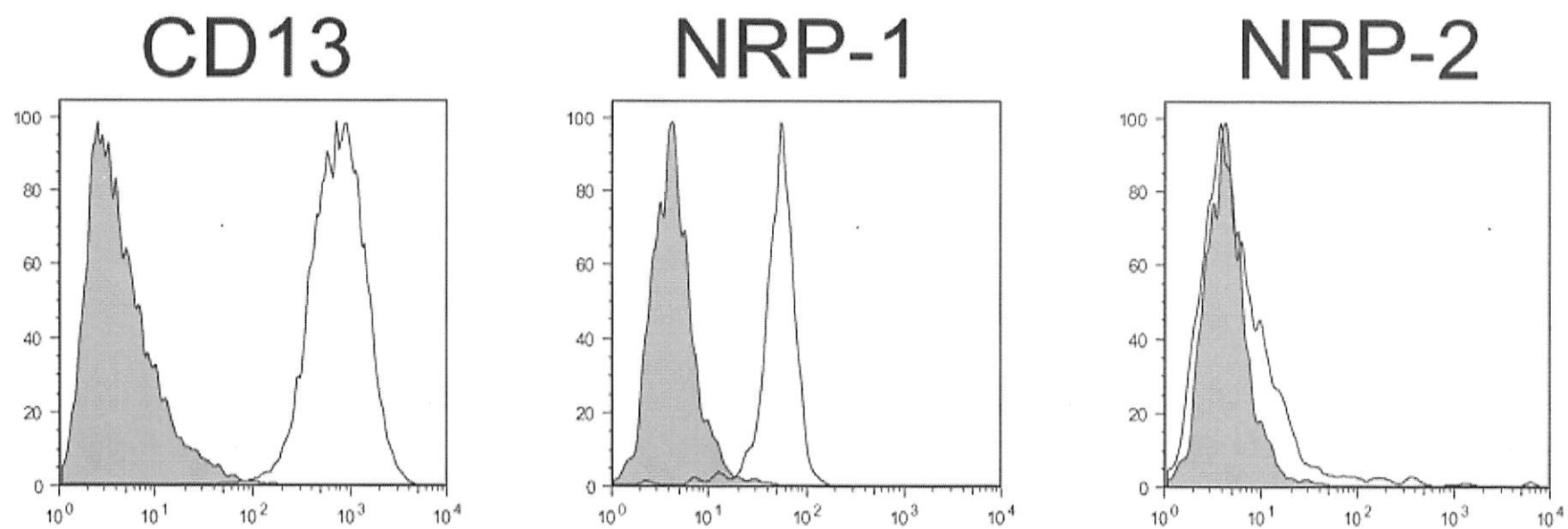
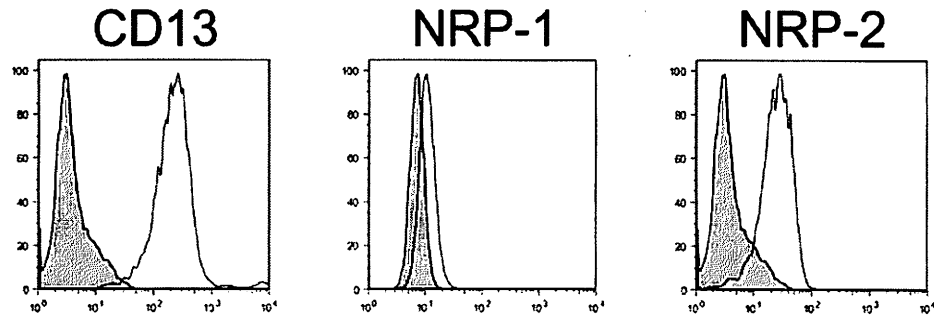


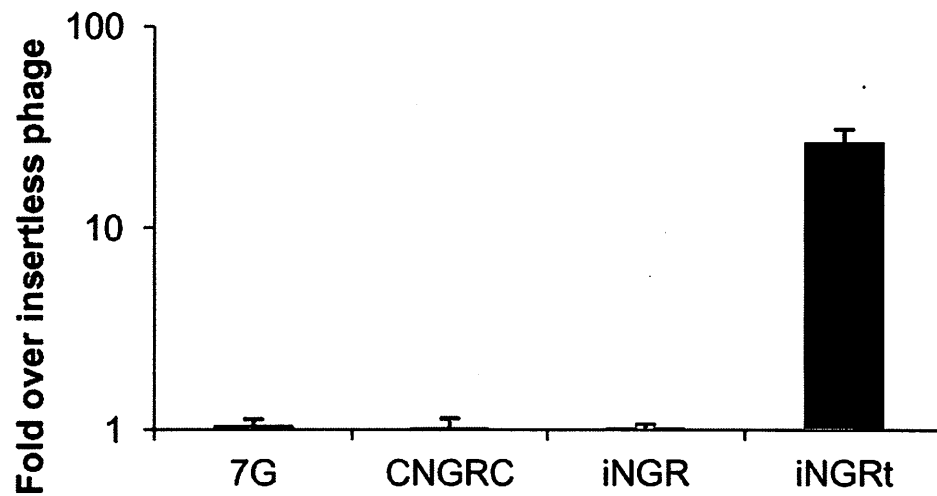
Figure S2

A



B

Phage binding to U937



C

Phage internalization into U937

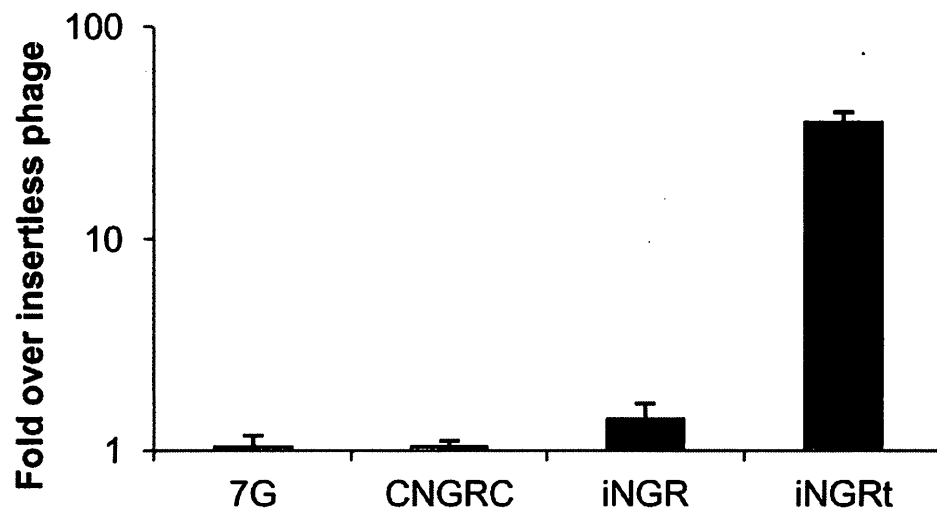
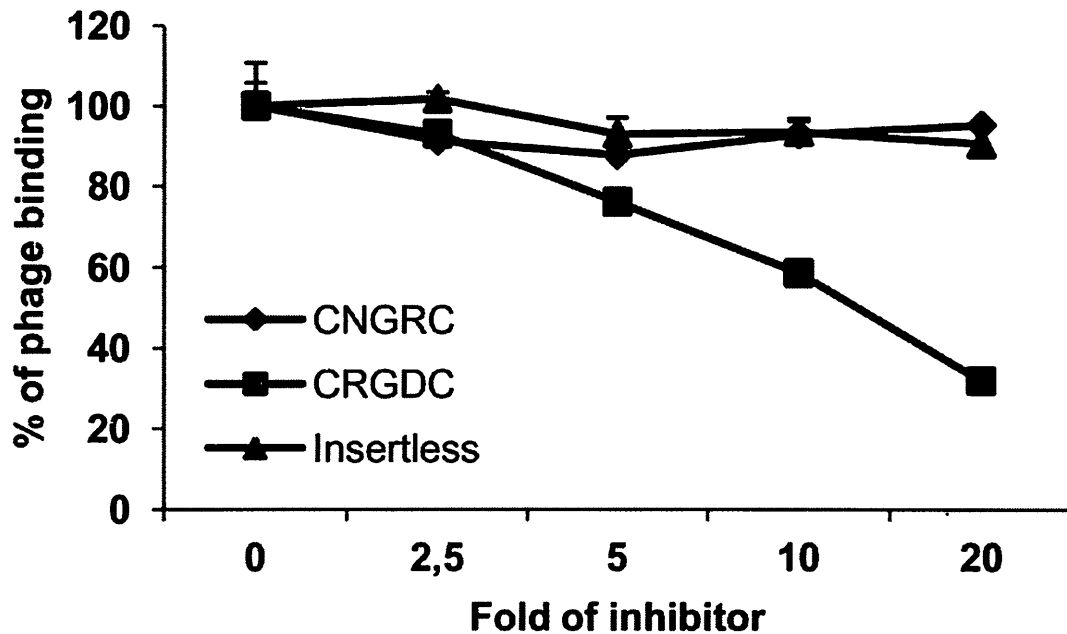


Figure S3

A

Inhibition of iRGD phage binding



B

Phage binding to $\alpha v\beta 3$ integrin

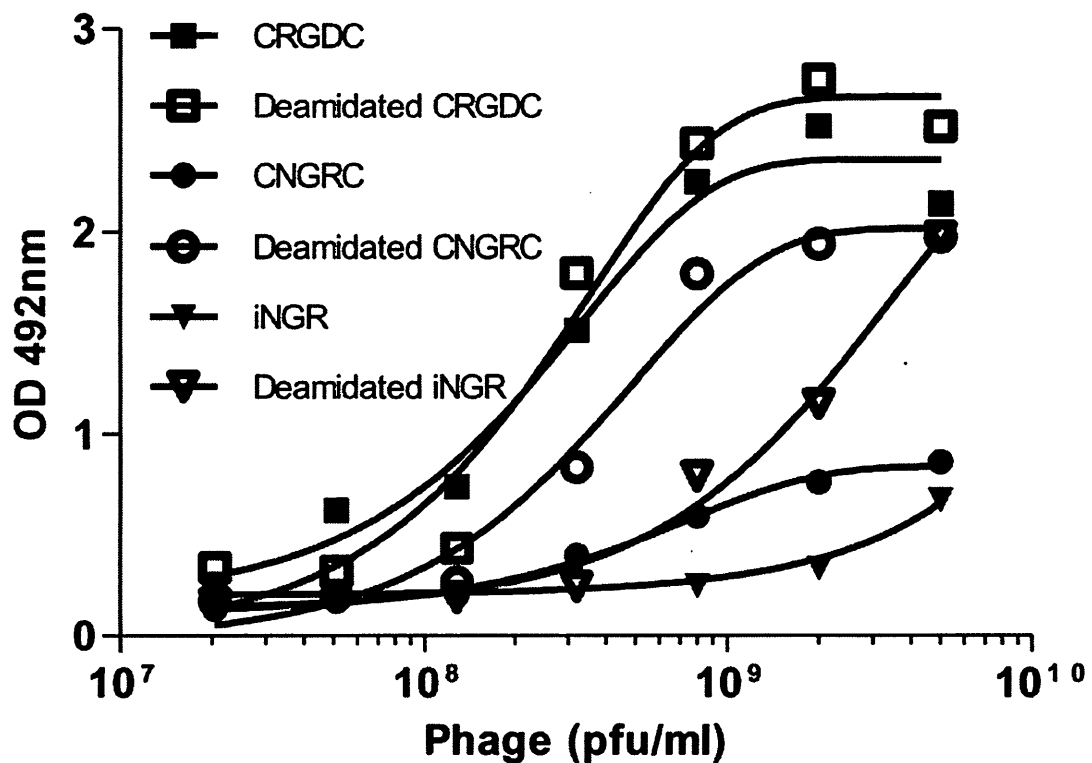


Figure S4

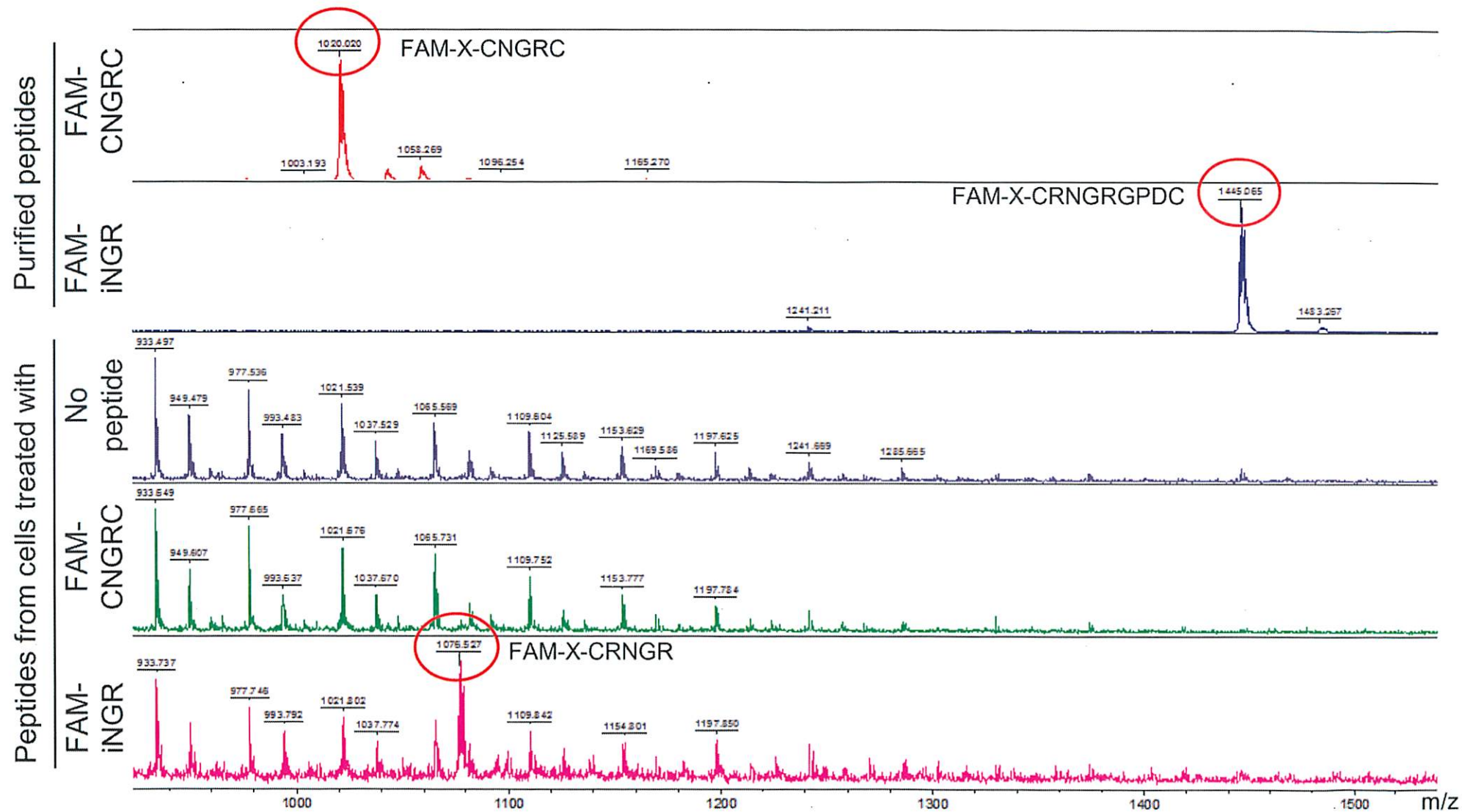
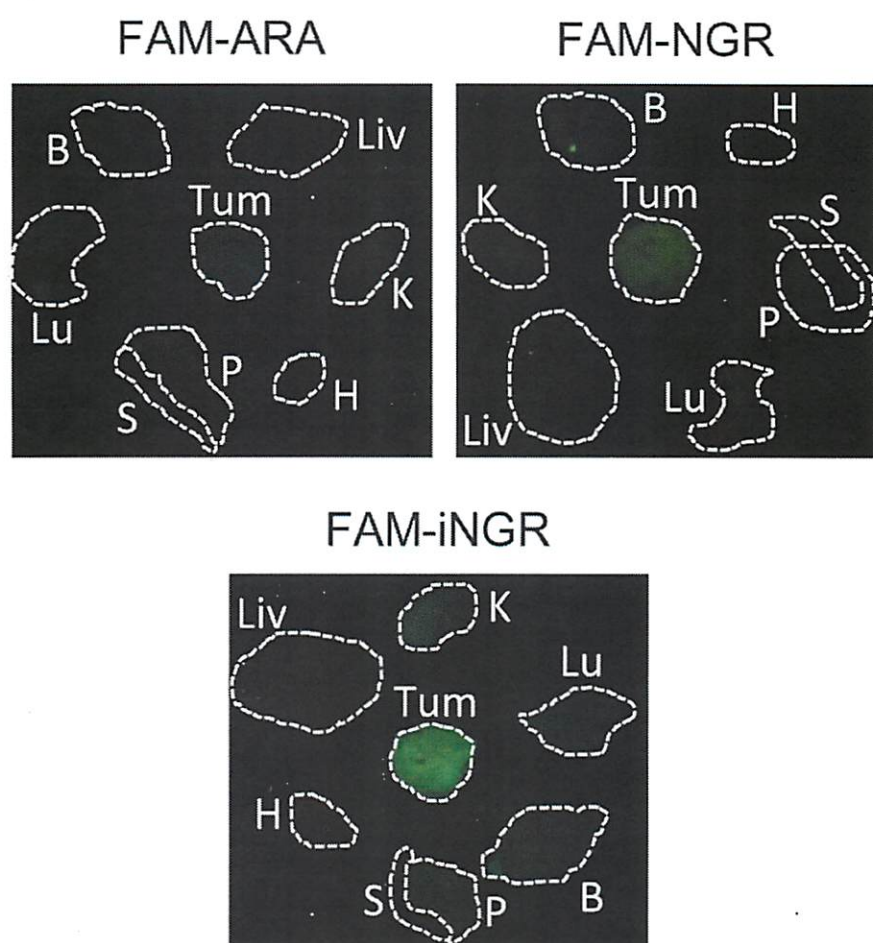


Figure S5

A



B

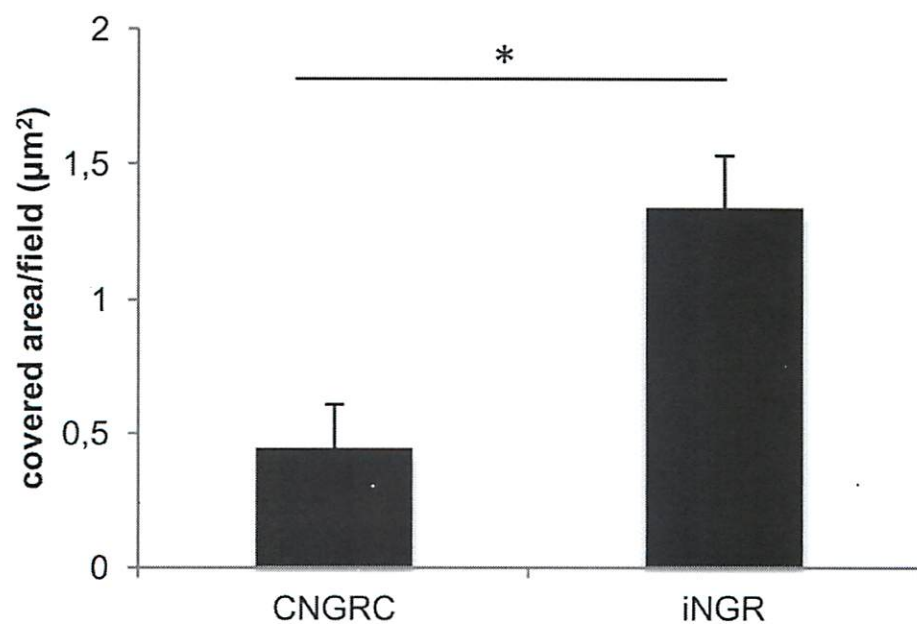


Figure S6

Evans Blue

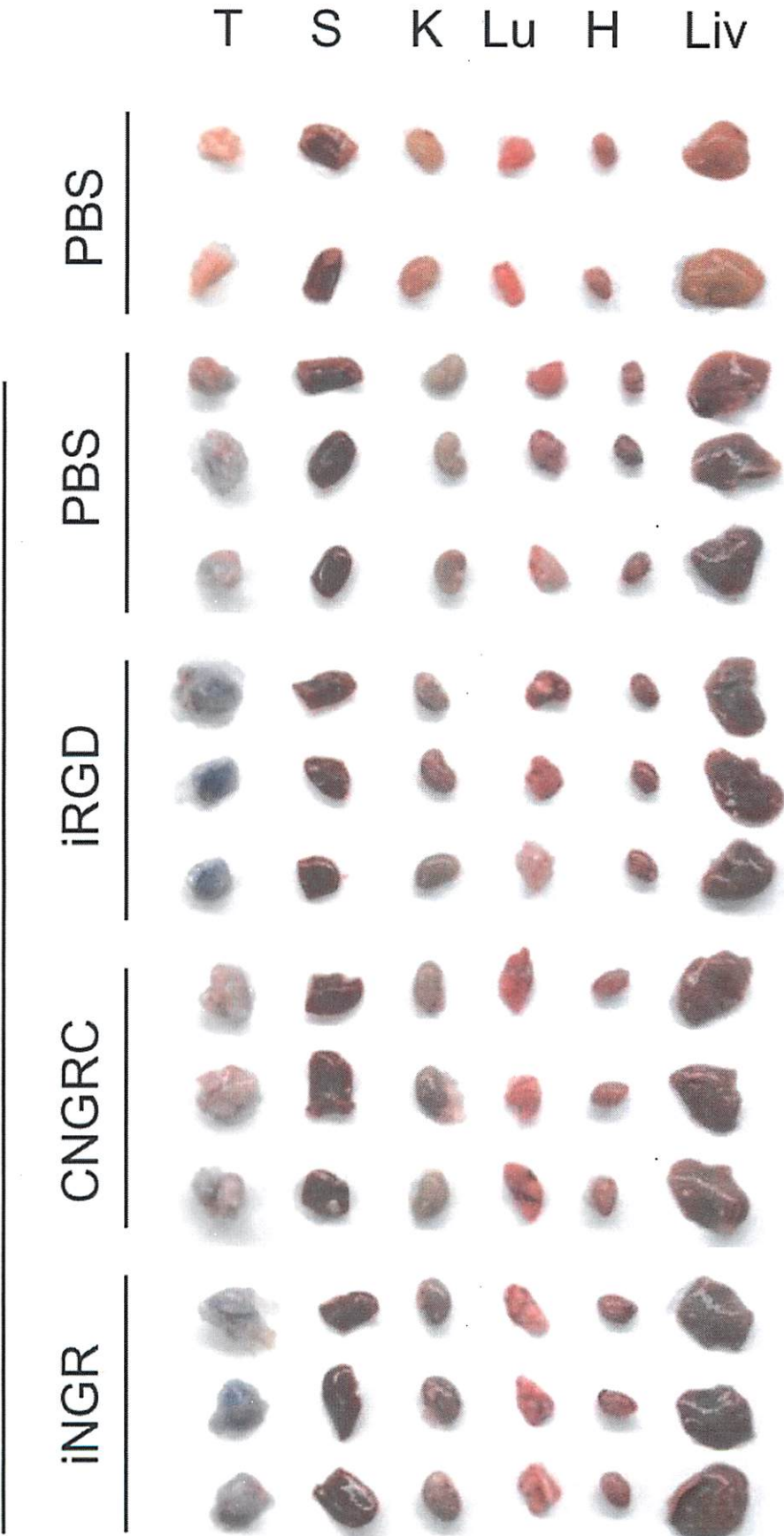


Figure S7

